ISSN 0915-6364

NATIONAL INSTITUTE FOR FUSION SCIENCE

Present Status on Atomic and Molecular Date Relevant to Fusion Plasma Diagnostics and Modeling

H. Tawara (Ed.)

(Received - Dec. 25, 1996)

NIFS-DATA-39 Jan. 1997

RESEARCH REPORT
NIFS-DATA Series

NAGOYA, JAPAN

Present Status on Atomic and Molecular Data Relevant to Fusion Plasma Diagnostics and Modeling

edited by

H.Tawara

National Institute for Fusion Science,

Nagoya 464-01, Japan

Dec., 1996

[keywords : divertor plasmas, CR-model, plasma diagnostics, elastic collisions, excitation, ionization, charge transfer, dissociative recombination, surface interactions]

Preface

This volume contains a series of the reports on the present status on atomic and molecular data relevant to fusion plasma diagnostics and modeling which have been given at

"International Symposium on Atomic and Molecular Processes in Fusion Plasmas"

held at National Institute for Fusion Science, Nagoya, over September 17 - 19, 1996.

The Symposium was organized as one of the satellite meetings for "International Conference on Plasma Physics (ICPP)" held over September 9 - September 13 in Nagoya and was intended to coordinate to exchange information on atomic and molecular as well as surface data need and availability for fusion plasma research among plasma physicists who attended ICPP and atomic and molecular physicists who joined "International Conference on Physics of Highly Charged Ions (HCI)" held over September 23 - September 26 in Ohmiya, Saitama.

The main topics during the Symposium were :

1) To discuss the need and availability of atomic and molecular collision data and surface data as well as their databases relevant to diagnostics and modeling of fusion plasmas.
2) To emphasize those involving the excited species, which are noted to be particularly important in the gas divertor physics.
3) To discuss how to organize the collaboration between collision physicists who in principle can provide accurate collision data and plasma physicists who need such data

The Symposium was opened by the welcoming address of Prof. A. Iiyoshi, Director General of NIFS, followed by 12 lectures and 14 posters, with the participation of about 60 scientists.

The editor would like to thank all the contributors who wrote reports on the recent progress and the present status on atomic and molecular data relevant to fusion plasma research. The support by Prof. A. Iiyoshi as well as the staffs of NIFS and PhD students who helped run the Symposium smoothly, in particularly K. Hosaka, F. Krok and T. Imai, is highly acknowledged.

The Inoue Foundation for Science (Tokyo) and Daiko Foundation (Nagoya) had provided generous financial support, without which the Symposium could not have been successful.

Dec. 25, 1996

H. Tawara

The editor

Contents

ATOMIC AND MOLECULAR PROCESSES IN FUSION PLASMAS

R.K. Janev

International Atomic Energy Agency, Vienna, Austria

ABSTRACT

The role of atomic and molecular processes in achieving and maintaining the conditions for thermonuclear burn in a magnetically confined fusion plasma is described. Emphasis is given to the energy balance and power and particle exhaust issues. The most important atomic and molecular processes which affect the radiation losses and impurity transport in the core plasma, the neutral particle transport in the plasma edge and the radiative cooling of divertor plasmas are discussed in greater detail.

1. INTRODUCTION

The energy generation by nuclear fusion reactions of hydrogenic isotopes in a magnetically confined thermonuclear plasma takes place in an ambient ionized atomic gas limited by certain material boundaries. A generic aspect of this situation is that, besides undergoing nuclear reactions, the charged nuclei interact also electromagnetically among themselves and with the other plasma constituents (electrons, impurities) as well. While the nuclear fusion reaction generate energy in the system, the electromagnetic interactions dissipate energy from the system (e.g. bremsstrahlung, other radiative processes). The reaction rates of nuclear and electromagnetic ("atomic") processes are by orders of magnitude different and this poses the problem of energy balance in the system. For instance, the rate coefficient of D-T fusion reactions at temperatures in the range of 10-20 keV are of the order of 10^{-16} cm^3/s, while the rate coefficients of atomic processes (e.g. charge transfer, or electron-ion excitation) are of the order of 10^{-8}-10^{-10} cm^3/s at the same plasma temperatures. This indicates that the energy generating nuclear processes take place in the background of much more intense energy loss atomic processes. A positive energy balance in a D-T plasma in the above temperature range can be obtained only due to the fact that the energy released per one nuclear fusion event (17.6 MeV) is about 10^6-10^8 times larger than the energy lost per one "atomic collision" event. However, this positive energy balance can easily be destroyed if the plasma is contaminated by high-Z impurities even on a percentage (or smaller) level.

Even in a perfectly pure D-T plasma, the electron bremsstrahlung on the hydrogen nuclei produces a negative energy balance for plasma temperatures below ~ 5 keV and above ~ 60 keV. The presence of plasma impurities with a charge q, enhances the bremsstrahlung radiation by a factor of q^2. In a plasma with temperatures in the range 10-20 keV the high-Z impurities may not be completely stripped and, therefore, the plasma electrons may lose energy in excitation, ionization and recombination collision processes with these ions. The excitation and recombination energy losses are converted into radiation, which freely escapes from the optically thin thermonuclear plasma (of a density ~ 10^{14}-10^{15} cm^{-3}). The rate coefficients of radiative processes scale strongly with the ionic charge (as ~ q, for line radiation, and ~ q^4, for dielectronic recombination), producing detrimental effects on the plasma energy balance. An unavoidable plasma impurity in a D-T fusion plasma is the alpha particle, generated in the $D+T \rightarrow \alpha+n$ fusion reactions. The imperfect plasma confinement, caused by the radial plasma transport, leads ultimately to certain degree of plasma-wall interaction, which generates impurities penetrating the plasma. Impurity concentrations of Fe on the level of 1%, or of W on the level of 0.1%, produce radiative plasma losses which prevent achievement of plasma burn conditions.

Another fundamental impact of atomic processes on a thermonuclear fusion plasma is related to its particle and energy confinement properties. As well known, a magnetically confined plasma is inherently far from thermodynamic equilibrium, a fact which follows directly from its quasi-neutrality. The long-range Coulomb interactions between plasma particles tend to restore the thermodynamic equilibrium and thereby destroy the confinement. This is achieved through multiple Coulomb collisions which produce particle diffusion across the confining magnetic field lines. This cross-field transport process represents one of the basic mechanisms for plasma particle and energy losses from the confinement region.

In a more formal context, the origin of the impact of atomic processes on the plasma properties and dynamics lies in the collisional term of the Boltzmann equation, describing the space-time evolution of the distribution function of plasma particles. Even in a fluid approximation of Boltzmann kinetic equation, the effects of atomic processes remain in form

of source/sink terms in the corresponding moment equations (describing the conservation of plasma particles, momentum and energy) and provide coupling between them. All this demonstrates that the atomic physics aspects of controlled thermonuclear fusion have a fundamental character and are intrinsically imbedded both in the function plasma energetics and dynamics. On a less fundamental level, but still in an essential form, the critical role of atomic physics processes appears in various fusion research areas, such as plasma heating (e.g. by neutral beams), plasma diagnostics, design of the impurity control and thermal power exhaust systems, etc. The research in these areas requires accurate account of the most important atomic, molecular and plasma-surface interaction processes, as well as of their collisional (or radiative) characteristics (cross sections, reaction rates, etc).

In the present review we shall discuss the atomic and molecular processes in thermonuclear tokamak fusion plasmas in the context of their effects on certain plasma properties (e.g. radiative losses, impurity transport) and plasma dynamics. We shall consider both the central and the periphery plasma regions, and outline the most important specific processes which influence the plasma properties in these regions.

The atomic and molecular processes in fusion plasmas have been reviewed on many occasions [1-7]. The present review will concentrate on the recent developments in this area, and will emphasize those processes which have been recently identified as playing important role in certain plasma regions (e.g. gas-target divertor plasmas) or in certain plasma studies (e.g. active and passive plasma diagnostics).

2. MAIN TOKAMAK PLASMA REGIONS AND THEIR PHYSICAL CHARACTERISTICS

The plasma volume in a toroidal magnetic confinement device, such as the tokamak, can conveniently be divided into two main regions: an inner (central) region, in which the magnetic field lines are closed and form nested magnetic flux surfaces, and an outer region (outside the last closed magnetic flux surface, LCFS) in which the magnetic field lines are open and strike the material walls. This second region is usually referred to as plasma edge region and it includes both the plasma beyond the LCFS which extends up to the containment vessel walls (scrape-off region) and the plasma in the divertor (if it is added as part of the magnetic configuration, as is usually the case with the recent tokamak designs). These two

plasma regions are characterized by significantly different plasma compositions, plasma parameters and plasmas dynamics. The differences in the plasma composition and plasma parameters (temperature and density) are also reflected in the types of atomic processes taking place in these two regions, as well as on their influence on the plasma properties and dynamics.

The plasma temperature in the central (main) plasma region of a reactor level fusion device has a radial distribution which on the magnetic axis of the torus (r=0) has values in the range T(0) ~ 10-20 keV, while at the LCFS (r=a) it attains values in the range T(a) ~ 300-500 eV. The radial plasma density distribution n(r) in this region spans values from n(0) ~ 10^{14}-10^{15} cm^{-3} at the magnetic axis down to n(a) ~ 10^{13} cm^{-3} at the LCFS. With this plasma temperature distribution, the low-Z impurities ($Z \gtrsim 10$) are completely in the core plasma region ($r \leq a/2$), while the medium-Z ($10 \lesssim Z \lesssim 30$) and high-Z ($Z \gtrsim 30$) impurities may be only partially stripped. In the LCFS region (r ~ a), the degree of ionization of plasma impurities is obviously lower and only impurities with $Z \lesssim 5$ are fully stripped.

The impurity composition of the main plasma obviously depends on the materials used for the first wall and other plasma facing components (such as divertor plates, antennas for radio-frequency heating, etc). The selection of the materials for plasma facing components is dictated by many, frequently contradicting criteria, which include considerations related to the impurity radiative power losses (which favours low-Z materials), lifetime of plasma facing components (which favours materials with low plasma-interaction induced erosion rates), thermomechanical response to high-heat and high-particle plasma fluxes, safety aspects (low tritium inventory and material activation), etc. In the presently operating large and medium size tokamak devices (such as JET, TFTR, JT-60U, DIII-D, ASDEX, Tore Supra, Alcator C-Mod, Textor, etc), the most abundant typical plasma impurities are (or have been): Be, B, C, O, Al, Si, Ti, Cr, Fe, Ni, Cu, and in some cases (e.g. Alcator C-Mod) even Mo. The materials favoured (or contemplated) for the next step devices (such as ITER) will also produce plasma impurities from the above list, possibly including some additional species (e.g.

W and Ta).

The plasma temperature and density in the scrape-off region decrease radially from their respective values ~ 300-500 eV and ~ 10^{13} cm^{-3} at the LCFS down to 10-12 eV and 10^{12} cm^{-3}, respectively, near the vessel walls. In the divertor region, the plasma temperature may vary in the range 5-50 eV, with values as low as about 1-3 eV near the divertor plates (or divertor side walls). The plasma density in the divertor region, generally, retains its value at the divertor throat, and may even increase near the divertor plates in a high recycling regime. The edge plasma region as a whole is characterized by high impurity concentrations and a high neutral gas density, resulting from plasma-surface interaction and particle recycling processes. The low temperatures in the plasma edge region keep the impurities in relatively low charge states ($q < 5$ for low-Z, and $q < 8$ for high-Z impurities) and even support the existence of molecular species in the cold divertor regions. The atomic impurity species present in the edge plasma are the same as those mentioned earlier (Be, B, C, O..., metallic impurities), while the main molecular impurities are the hydrocarbons and the carbon oxides. The principal molecular species in the divertor region are, obviously, the molecular hydrogen and its ions.

We shall now discuss the atomic collision processes occurring in the central and edge plasma regions separately.

3. ATOMIC PROCESSES IN THE CENTRAL PLASMA REGION

Under the temperature and density conditions prevailing in the central plasma region the most important collision processes are those between plasma electrons and impurity ions. If the impurity ion is fully stripped, the only possible electron-ion collision processes are the bremsstrahlung

$$e + A^{q+} \rightarrow e' + h\nu \qquad (1)$$

and the radiative recombination

$$e + A^{q+} \rightarrow A^{(q-1)+} + h\nu \, . \qquad (2)$$

The bremsstrahlung is a powerful radiative process at high temperatures T, with a rate coefficient proportional to $q^2 T^{1/2}$. In contrast to this, the radiative recombination has a rate

coefficient proportional to $q^2\ T^{-1/2}$, and its importance in the central plasma region is negligible. If the impurity ion is incompletely stripped, the following electron-ion processes become possible:

- excitation

$$e + A^{q+}(n\ell) \rightarrow e' + A^{q+*}(n'\ell'), \tag{3}$$

- ionization

$$e + A^{q+} \rightarrow e' + A^{(q+1)+} + e'' \tag{4}$$

- dielectronic recombination

$$e + A^{q+} \rightarrow A^{(q-)+**} \rightarrow A^{(q-1)+*} + h\nu \tag{5}$$

The process of direct electron-impact excitation (3) is an important energy loss mechanism in the central plasma region since it results in line radiation of excited A^{q+*} ion. The intensity of this radiation is proportional to q. For Li-like ions, and ions of higher isoelectronic sequences, excitation of an inner-shell electron can also occur, producing a doubly excited A^{q+**} ion. This doubly excited state can either decay radiatively or autoionize by Auger electron emission. At high temperatures, the rate coefficient of the described excitation-autoionization process may significantly exceed the rate coefficient of the direct ionization, Eq. (4).

Dielectronic recombination, Eq. (5), is also a powerful energy loss mechanism in the central plasma region. The electron capture in the first step of this process is accompanied by simultaneous excitation of a valence ion electron. The stabilization of the resulting doubly excited state by a radiative decay may still leave the ion in an excited state (as indicated in Eq. (5)), which is subject to further radiative decay. The radiated power due to this process is, therefore, very large and is proportional to q^4. This strong q-dependence of the dielectronic recombination radiative power losses indicates how undesirable the high-Z impurities in the central plasma region are.

The electron-ion collision processes, (3)-(5) determine to a large degree the ionization state distribution of individual impurity species in the main plasma. A more complete picture of the ionization equilibrium is obtained, however, only when the multi step processes (such as excitation followed by ionization) are taken into consideration (collisional-radiative models).

Moreover, due to the neutral hydrogen beam plasma heating and hydrogen pellet injection for plasma fueling, certain level of "residual" hydrogen atom concentration (n_H) is always present in central plasma region. The electron capture process

$$A^{q+} + H \rightarrow A^{(q-1)+} (n\ell) + H^+ \qquad (6)$$

in the energy range below 10-20 keV/amu has cross sections of about $5q\times10^{-16}$ cm^2 (rate coefficients about $q\times10^{-7}$ cm^3/s) and leads to population of ionic states with high principal quantum number (around $n_m \sim q^{0.78}$) [8]. For neutral atom concentration $n_H/n_e \gtrsim 10^{-5}$ (n_e being the plasma electron density), the electron capture process may significantly affect the ionization equilibrium and increase the plasma radiation. In the case when A^{q+} is a completely stripped ion, the radiation of excited product ions in reaction (6) can be used for diagnostic purposes ("charge exchange recombination spectroscopy" [9]) and, in fact, this is the only way to determine the radial distribution of completely stripped ions in a fusion plasma. The charge exchange recombination spectroscopy, which uses external neutral hydrogen and helium beams has been widely used for measuring also many other plasma parameters (e.g. Ti, Z_{eff}, etc) [10]. It should be noted that the charge exchange between the "residual" hydrogen atoms and the energetic plasma ions, which also has enormous cross sections in the energy range below ~ 20 keV (see above for q=1), is an important particle loss process. Even more important are the effects charge-exchange neutrals in producing plasma impurities when they hit the wall of the containment vessel (via the process of physical sputtering).

Some collision processes of incompletely stripped impurity ions with plasma protons and fusion-born alpha particle may also be very important. For instance, the proton-impact excitation of fine-structure components of incompletely stripped impurities

$$H^+ + A^{q+} (J) \rightarrow H^+ + A^{q+} (J+1) \qquad (7)$$

may be a significant plasma ion energy loss process, competing with and sometimes exceeding, the plasma power loss due to electron impact processes [11]. This process has been very little studied so far. The charge exchange processes

$$H^+ + A^{q+} \rightarrow H + A^{(q+1)+} \qquad (8)$$

and

$$He^{2+} + A^{q+} \rightarrow He^{+} + A^{(q+1)+} \quad (9a)$$

$$He^{+} + A^{q+} \rightarrow He + A^{(q+1)+} \quad (9b)$$

$$He^{2+} + A^{q+} \rightarrow He + A^{(q+2)+} \quad (10)$$

may also be important particle loss processes from the fusion plasma. Particularly important in this context could be the processes (9) and (10) which, under certain conditions, may lead to alpha particle escape from the central plasma before their complete thermalization. Therefore, these processes may impair the alpha particle heating. These processes have also been very little investigated and their impact on plasma properties is still not clear.

4. ATOMIC AND MOLECULAR PROCESSES IN THE PLASMA EDGE

The diversity of atomic and molecular species in the plasma edge makes the collision physics phenomena in this region extremely complex. On the other hand, the plasma edge region plays a critical role for the thermal power and helium exhaust from the reactor and a detailed knowledge of all collision and radiative processes which are related to the exhaust problem is required. The atomic physics of edge plasmas is further complicated by the particle-surface interaction processes which are part of the entire reaction kinetics picture.

There are three major aspects of the role of atomic and molecular processes in the plasma edge. These processes influence the plasma and impurity transport in this region, they determine almost completely the neutral particle transport (and, thereby, the helium exhaust) and they provide the basic (radiative and momentum transfer) mechanisms for power exhaust from this region. The divertor region of the edge plasma plays a specific role in this respect since it is the region from where the major portion of thermal power can be exhausted. We consider below the atomic and molecular processes in the plasma edge with the above three contexts in mind.

In the class of electron-atomic ion collision processes, the most important ones in the plasma edge are excitation and ionization, (3) and (4), the former in the radiative cooling of the plasma, and the latter in establishing the ionization equilibrium. Because of the low plasma temperatures and low ionic charge states, dielectronic recombination is not an important process in this region. In contrast, the radiative electron-ion recombination becomes

important in the divertor regions with temperatures below ~ 5 eV. Since electron recombination with singly charged ions is not an important process in the edge plasma, the electron-impurity atom collision processes are also of low importance (except for ionization).

The high neutral atom density in the edge plasma region makes the e-H collision events fairly frequent. Because of this high collision frequency, even electron-impact processes with excited hydrogen atom are important. Therefore, the e-H collision kinetics includes the processes

$$e + H(n) \rightleftarrows e' + H(n') \, , \; n' > n \geq 1 \, , \tag{11}$$

$$e + H(n) \rightarrow e' + H^+ + e'' \, , \; n \geq 1 \tag{12}$$

$$e + H^+ \rightarrow H(n) + h\nu \tag{13}$$

Hydrogen atoms in the plasma edge are produced mainly by electron-impact dissociation of hydrogen molecules entering the plasma from the walls (hydrogen recycling), or deliberately introduced in this region for fueling or plasma cooling purposes (gas puffing). The main collision processes of electrons with hydrogen molecules and molecular ions are:

$$e + H_2 \rightarrow e' + H + H \tag{14}$$

$$e + H_2 \rightarrow e' + H_2^+ + e'' \tag{15}$$

$$e + H_2^+ \rightarrow e' + H_2^{+*}(2p\sigma_u) \rightarrow e' + H + H^+ \tag{16a}$$

$$\rightarrow e' + H_2^{+*}(2p\pi_u) \rightarrow e' + H^*(n=2) + H^+ \tag{16b}$$

$$e + H_2^+ \rightarrow H + H^*(n) \qquad , \; n \geq 2 \, . \tag{17}$$

For plasma temperatures below 10 eV the molecular dissociation via the process (14) prevails, yielding ground state neutral atoms with average kinetic energy of ~ 3 eV. For temperatures above 10 eV the electron-impact ionization process (15) dominates, producing vibrationally excited H_2^+ (v) ions (with a vibrational level distribution maximized around v_m ~ 3-4). The H_2^+ ions in this temperature region are subject to the intense electron impact dissociation channels, (16a) and (16b), the first (dominant) one producing products with mean kinetic energy of about 4.3 eV, while the second produces an excited neutral, H^* (n=2), (with

mean kinetic energy of 1.5 eV), the Doppler shifted radiation from which can be used for diagnostic purposes.

An important aspect of electron-molecule and electron-molecular kinetics is the role of vibrationally excited states. It is well known [12] that the cross sections of processes (14)-(17) vary strongly with the vibrational state of the target giving a substantial increase of their reaction rates. The thresholds of processes (14)-(17) decrease with increasing the target vibrational quantum number, which leads to an increase of the mean kinetic energy of dissociation products. All these changes make a significant difference in the overall electron-molecule reaction kinetics and require accurate knowledge of the vibrational state distribution of both H_2 and H_2^+. This means that all collision processes which determine the vibrational level populations of H_2 and H_2^+ have also to be included in the kinetic scheme. The most important among these processes are:

$$e + H_2(v) \rightleftarrows e' + H_2(v') \tag{18}$$

$$H^+ + H_2(v) \rightleftarrows H^+ + H_2(v') \tag{19}$$

$$H + H_2(v) \rightleftarrows H + H_2(v') \tag{20}$$

$$H_2^+(v_1) + H_2(v_2) \rightleftarrows H_2(v_1') + H_2^+(v_2') \tag{21}$$

$$H_2(v_1) + H_2(v_2) \rightleftarrows H_2(v_1') + H_2(v_2') \tag{22}$$

$$H^+ + H_2(v) \rightarrow H + H_2^+(v') \tag{23}$$

The charge exchange process (21) has a quasi-resonant character for $v_1 \approx v_2$ and, therefore, very large cross sections ($\sim 10^{-16}$-10^{-15} cm^2) at low collision energies. In the energy region around 4 eV, the cross section of the ion-conversion reaction (23) has also a large cross section ($\sim 10^{-16}$ cm^2) [13]. This reaction, therefore, rapidly converts the plasma ions$^+$(H) in molecular ions (H_2^+), which are further either dissociated by electron impact (reaction (16)) if the plasma temperature is above ~ 10 eV, or recombined with the plasma electrons (reaction (17)) if the plasma temperature is below ~ 3 eV. The reaction chain involving the processes (15), (21), (23) and (17) probably plays a very important role in the "volume" plasma

recombination in cold divertor regions and is possibly responsible for the phenomenon of "plasma detachment" near divertor plates, observed in several operating tokamak devices.

For still lower plasma temperatures ($T_e \lesssim 1$ eV), negative ion formation and existence in the cold divertor regions becomes possible, via the process

$$e + H_2 (v) \rightarrow (H_2^-)^* \rightarrow H + H^- \quad , v \geq 4 \tag{24}$$

where $(H_2^-)^*$ is a short-living dissociative state. While for v=1-3, the cross section of reaction (24) is small, for $v \geq 4$ it becomes very large [14] increasing by almost an order of magnitude with each increase of v by unity. (The total reaction rate for the process (24) for $T \leq 1$ eV is about 10^{-7} cm^3/s [14].) For $T \geq 2$ eV, the H^- ion is rapidly destroyed by electron impact, but for $T \leq 1$ eV, the rate coefficient of the ion-ion recombination

$$H^+ + H^- \rightarrow H (n=3) + H \tag{25}$$

is $\sim 3 \times 10^{-8}$ cm^3/s and is more than three times larger than the rate coefficient for electron detachment. The reaction chain (24)-(25) may also be an important volume plasma recombination mechanism at plasma temperature below ~ 1.5 eV.

While the electron-ion collision processes in the plasma edge provide a major mechanism for radiative plasma edge cooling, and the electron-molecule/molecular ion processes, together with the ion-conversion and ion-ion neutralization processes, provide the most probable mechanism for volume plasma recombination, the charge-exchange, elastic and momentum transfer collision processes between plasma ions and plasma edge neutrals, as well as between the charge-exchange hydrogen atoms and other edge plasma neutrals provide the basic mechanism for plasma momentum dissipation and exhaust in the divertor region. Dissipation of the plasma ion momentum on divertor channel walls is a necessary condition for reducing the plasma particle flux impinging on the divertor plates along the magnetic field lines. The most important elastic and momentum transfer processes are those occurring in the $H^+ + H$, $H^+ + H_2$, $H + H$, $H + H_2$ and He^+, $He^{2+} + H$, H_2. A systematic study of these collision system and the generation of corresponding cross section information have recently been initiated [15].

In the problem of helium exhaust from the divertor region, all the processes changing the energy, charge state and the momentum of helium ions (He^+, He^{2+}) and atoms are of obvious importance. Resonant charge exchange processes

$$He^+ + He \rightarrow He + He^+ \quad (26)$$

$$He^{2+} + He \rightarrow He + He^{2+} \quad (27)$$

have large cross sections and have significant importance for the helium removal. Elastic and momentum transfer collisions of He^+, He^{2+} and He with the abundant hydrogen neutrals H and H_2 also have a significant impact on the helium exhaust.

The plasma edge region contains a significant amount (on the level of few percents) of molecular impurities, such as C_mH_n, CO, CO_2, H_2O, Be- and B-hydrides. These are, generally, formed on the surfaces and then released in the plasma by various particle-impact processes or by thermal desorption. The hydrocarbons, particularly CH_4 and C_2H_2, are by far the most abundant plasma edge molecular impurities, produced mainly by chemical erosion of plasma facing carbon materials. The election-impact processes involving molecular impurities are similar to those for molecular hydrogen (and its ion), and their rate coefficients are of the same order of magnitude as for the hydrogenic molecular species. The dissociation channels for the multi-atom molecular impurities are evidently much more numerous than in the hydrogenic case.

Apart from the impurities generated by plasma-wall interaction processes, atomic and molecular impurities may be deliberately introduced in the plasma edge region to enhance the plasma radiative power losses from this region. These impurities should have good recycling and radiating properties, and not very high atomic numbers. In the current large tokamak experiments and divertor design concepts, N_2, Ne and Ar are the favoured radiating impurities for injection in the divertor region. In order to evaluate precisely the radiative plasma power losses due to these impurities construction of the complete collisional-radiative model for each of them is necessary.

5. CONCLUSION

The presented brief account of atomic and molecular processes in fusion plasmas has focussed only on a limited number of issues in which these processes play an important role.

Other areas of fusion energy research in which atomic processes have a significant impact include the neutral beam heating and current drive, plasma fueling, various spectroscopic schemes of plasma diagnostics, and certain aspects of the plasma dynamics in the edge or near edge region. The emphasis within the present overview was given on those atomic and molecular processes which have a strong effect on radiative properties and neutral particle transport in the plasma edge. New aspects of the atomic physics of divertor plasmas, related to the implementation of gas-target divertor concept, have been highlighted. These include the role of collision processes involving vibrationally excited hydrogenic molecular species in achieving efficient "volume" plasma recombination in the near divertor plate region, and the elastic and momentum transfer processes in dissipating the plasma power over the side walls of divertor chamber.

The questions of availability and needs of atomic and molecular cross section data for the fusion energy research has not been discussed in the present review. These questions have been addressed in several other reviews [16].

REFERENCES

1. M.F.A. Harrison, in: Atomic Processes in Electron-Ion and Ion-Ion Collisions, ed:, F. Brouillard (Plenum Press, New York, 1986) p. 421.
2. R.K. Janev, J. de Physique 50, C1-421 (1989).
3. R.K. Janev, M.F.A. Harrison and H.W. Drawin, Nucl. Fusion 29, 109 (1989).
4. H.W. Drawin, in: Atomic and Plasma-Material Interaction Processes in Controlled Thermonuclear Fusion, eds.: R.K. Janev and H.W. Drawin, (Elsevier, Amsterdam, 1993), p.45.
5. R.K. Janev, Comments At. Mol. Phys. 26, 83 (1991).
6. R.K. Janev, in: Review of Fundamental Processes and Applications of Atoms and Ions, ed.: C.D. Lin (World Scientific, Singapore, 1993) p. 1.
7. R.K. Janev, in: Atomic and Molecular Processes in Fusion Edge Plasmas, ed.: R.K. Janev (Plenum Press, New York, 1995), p. 1.
8. R.K. Janev and H.P. Winter, Phys. Rep. 117, 265 (1985).
9. V.V. Afrosimov et al JETP Lett. 28, 501 (1979); see also: R.C. Isler, Phys. Rev. Lett. 38, 1359 (1977).

10. See, e.g., A. Boileau et al. Nucl. Fusion 29, 1449 (1989) and references therein.

11. V.A. Abramov, private communication (1996).

12. M. Capitelli and R. Celiberto, in: Atomic and Molecular Processes in Fusion Edge Plasmas, ed.: R.K. Janev (Plenum Press, New York, 1995) p. 195.

13. F. Linder et al, in: Atomic and Molecular Processes in Fusion Edge Plasmas, ed.: R.K. Janev (Plenum Press, New York, 1995) p. 397.

14. R.K. Janev, W.D. Langer, K. Evans and D.E. Post, Elementary Processes in Hydrogen-Helium Plasmas, (Springer-Verlag, Berlin, 1987).

15. D.R. Schultz et al, in: Atomic and Molecular Processes in Fusion Edge Plasmas, ed.: R.K. Janev (Plenum Press, New York, 1995), p.279.

16. See the reviews of R.A. Hulse (p. 165), A. Pospieszczyk (p. 213), D. Reiter (p. 243), D. Post (p. 267), M.F.A. Harrison (p. 285) and R.A. Phaneuf and R.K. Janev (p. 371) in: Atomic and Plasma-Material Interaction Processes in Controlled Thermonuclear Fusion, eds.: R.K. Janev and H.W. Drawin (Elsevier, Amsterdam, 1993).

Atomic and molecular processes in JT-60U Divertor Plasmas

H. Takenaga, K. Shimizu, K. Itami, H. Kubo, N. Hosogane, T. Sugie,
S. Higashijima, N. Asakura, A. Sakasai, M. Shimada and JT-60 team

Naka Fusion Research Establishment,
Japan Atomic Energy Research Institute,
Naka-machi, Naka-gun, Ibaraki 311-01, Japan

Atomic and molecular data are indispensable for the understanding of the divertor characteristics, because behavior of particles in the divertor plasma is closely related to the atomic and molecular processes. In the divertor configuration, heat and particles escaping from the main plasma flow onto the divertor plate along the magnetic field lines. In the divertor region, helium ash must be effectively exhausted, and radiation must be enhanced for the reduction of the heat load onto the divertor plate. In order to exhaust helium ash effectively, the difference between behavior of neutral hydrogen (including deuterium and tritium) and helium in the divertor plasma should be understood. Radiation from the divertor plasma generally caused by the impurities which produced by the erosion of the divertor plate and/or injected by gas-puffing. Therefore, it is important to understand impurity behavior in the divertor plasma. The ions hitting the divertor plate recycle through the processes of neutralization, reflection, absorption and desorption at the divertor plates and molecular dissociation, charge-exchange reaction and ionization in the divertor plasma. Behavior of hydrogen, helium and impurities in the divertor plasmas can not be understood without the atomic and molecular data.

In this report, recent results of the divertor study related to the atomic and molecular processes in JT-60U were summarized. Behavior of neural deuterium and helium was discussed in section 2. In section 3, the comparisons between the modelling of the carbon impurity transport and the measurements of C II and C IV were discussed. In section 4, characteristics of the radiative divertor using Ne puffing were reported. The new diagnostic method for the electron density and temperature in the divertor plasmas using the intensity ratios of He I lines was described in section 5.

1. Introduction

Control of heat and particles escaping from the main plasma is a one of the most important issues to realize thermonuclear fusion reactors. The divertor is the most promising method for the control of heat and particles. In the divertor configuration, heat and particles escaping from the main plasma flow onto the divertor plate along the magnetic field lines. Helium ash must be effectively exhausted in the divertor region. Also, the heat load onto the divertor plate must be reduced, since the high heat load causes the erosion of the divertor plate. In order to reduce the heat load onto the divertor plate, radiation must be enhanced in the divertor plasmas. Radiation from the divertor plasma generally is caused by the impurities which are produced by the erosion of the divertor plate and/or are injected by gas-puffing. The produced and/or injected impurities must be shielded from the main plasma by the divertor plasma, because the impurities increase radiative losses and dilute the nuclear reaction in the main plasma. Therefore, it is important for the divertor study to understand behavior of hydrogen (including deuterium and tritium), helium and impurities. The ions hitting the divertor plate recycle through the processes of neutralization, reflection, absorption and desorption at the divertor plate and molecular dissociation, charge-exchange reaction and ionization in the divertor plasma. Behavior of particles in the divertor plasma is closely related to atomic and molecular processes. Thus, atomic and molecular data are indispensable for understanding of the divertor characteristics.

In this report, recent results of the divertor study related to the atomic and molecular processes in JT-60U were summarized. Behavior of neural deuterium and helium was discussed in section 2 [1.1]. The results of the analyses for the spectra and emission profiles of Dα and He I lines were presented. In section 3, the comparison between the modelling of the generation and transport for the carbon impurity and the measurements of C II and C IV were discussed [1.2]. In section 4, characteristics of the radiative divertor using Ne gas-puffing were reported [1.3]. The new diagnostic method for the electron density and temperature in the divertor plasmas using the intensity ratios of He I lines was described in section 5 [1.4].

References

[1.1] H. Takenaga, et al., in International Conference on Plasma Physics (Nagoya, 1996).

[1.2] K. Shimizu, et al., Proc. 15th International Conference on Plasma Physics and Controlled Nuclear Fusion Research, (1994, Seville) Vol. 3, IAEA, Vienna, (1994) 431.

[1.3] K. Itami, et al., "Review of JT-60U Experimental Results from February to October, 1995" JAERI-Research, 96-018, 96.

[1.4] H. Kubo, et al., ibid, 104.

2. Neutral Deuterium and Helium Behavior in JT-60U Divertor Plasmas

2. 1. Introduction

Control of neutral deuterium and helium particles in the divertor plasmas is a critical issue for the steady state operation of a fusion plasma, because it directly affects the density of both main and divertor plasmas and helium ash exhaust. In order to reduce helium density in the main plasma, the penetration probability of neutral helium into the main plasma should be smaller than that of neutral deuterium. In addition, for the compatibility of high neutral deuterium density in the divertor plasma with helium ash exhaust, the pumping rate of neutral helium should be larger than that of neutral deuterium. In order to understand the difference between neutral deuterium and helium behavior in the divertor plasma, their velocity and density distributions should be investigated. The velocity distribution determines the penetration depth of the neutral particle into the plasma and also gives information on the recycling processes. The ions hitting the divertor plates recycle through processes of neutralization, reflection, absorption and adsorption at the divertor plate and molecular dissociation and charge-exchange reaction in the divertor plasma. Each process modifies velocity distribution of neutral particles, and then the velocity distribution influences the penetration depth and density distribution.

In JT-60U, Dα and He I (λ=667.8 nm) spectra have been measured so as to estimate the velocity distributions of both deuterium and helium atoms, and absolute intensities of Dα and He I have also been measured so as to estimate the density distributions of the deuterium and helium atoms. In this paper, neutral deuterium and helium behavior was analyzed using a Monte-Carlo simulation code based on these measurements. In section 2. 2, the diagnostics related to this study and the methods of analysis are described. The results of the comparison between the measured and calculated velocity distributions are presented in section 2. 3. The results of comparison between the measured and calculated emission intensity profiles are presented in section 2. 4, and conclusions are described in section 2. 5.

2. 2. Methods of analysis

JT-60U is a large tokamak with a major radius of 3.4 m and an aspect ratio of 4. The divertor discharges are formed with a single null point at the bottom. The divertor plates were made of carbon-fiber composite (CFC) tiles. Figure 1 shows a schematic drawing of the cross-section of JT-60U divertor and sight lines for the spectroscopic measurements. The Dα and He I emission intensity profiles were measured with an optical fiber array. There were 60 viewing chords with a spatial resolution of about 1.2 cm. The light transmitted through the optical fibers was divided into 4 branches, and the 4 wavelengths could be simultaneously measured using interference filters with a time resolution of 50 ms [2.1].

The Dα and He I spectra were measured using a high resolution spectrometer [2.2] with 10 viewing chords as shown in fig. 1. The wavelength resolution was 11 pm for Dα measurements and 14 pm for He I measurements. The wavelength was calibrated against that of a He-Ne laser and the error was smaller than 3 pm. Langmuir probes were placed at 15 positions on the divertor plates as shown in fig. 1, and each yielded the electron density and temperature at the divertor plates.

In order to interpret the experimental data, behavior of neutral deuterium and helium was simulated using the neutral particle transport simulation code DEGAS [2.3] which includes atomic and molecular processes and wall reflection model. Franck-Condon energy was taken into account for each dissociation process of deuterium molecules. The electron density, electron temperature and ion temperature in the scrap-off layer and divertor plasmas were calculated using a simple divertor code [2.4], and these were used as input parameters for the DEGAS code. The simple divertor code solved 1-D fluid equations along the magnetic fields using the boundary condition of the electron density and temperature at the divertor plates.

2. 3. Analysis of Dα and He I spectra

In fig. 2, open circles show the measured Dα spectrum around the outboard strike point for the L-mode plasma with plasma current I_p=2 MA, magnetic field B_T=3.5 T, line averaged density $\bar{n}_e=2\times10^{19}$ m^{-3}, NBI input power P_{NB}=6 MW, divertor density $n_e^{div}=3\times10^{18}$ m^{-3} and divertor electron temperature T_e^{div}=80 eV. The spectrum splits into three components due to the Paschen-Back effect. The effect of Hα was observed around $\Delta\lambda$=0.18 nm. As can be seen from this figure, the spectrum shows a symmetrical profile and the contribution of the reflected particles with high energy was not observed. The peak of the spectrum shifted about 6 pm toward the short wavelength side, and this shift corresponds to the energy of 0.068 eV. The solid line shows the Dα spectrum calculated with the DEGAS code, where the presently available atomic and molecular data were used. The split due to the Paschen-Back effect and the device function of the spectrometer were taken into account. In this calculation, deuterium was released from the divertor plates as a molecule having the same temperature as the divertor plate. This means that all ions hitting the divertor plates are once absorbed and then desorbed as a molecule. The calculated Dα spectrum consisted of a narrow component ascribed to Franck-Condon atoms and a broad component ascribed to charge-exchanged atoms. The broad component agrees with the measurement. However, the peak shift of the narrow component is larger than that of the measurement. In order to adjust the calculation to the measurement, the simulation was performed where the Franck-Condon energy was taken as a free parameter. In fig. 2, the dashed line shows the Dα spectrum which was produced as a sum of the calculated spectra in the cases that the Franck-Condon energy was

set to 0.03, 2, 5 and 10 eV for all dissociation processes. The low energy component at 0.03 eV was necessary to decrease the amount of the calculated peak shift, and the components of 2, 5 and 10 eV were necessary to adjust the extent of the narrow component. Here, the ratios of each contribution for 0.03, 2, 5 and 10 eV were selected to be 0.11, 0.35, 0.28 and 0.26, respectively. The small contribution of the low energy deuterium affects the Dα spectrum, because the low energy deuterium has a sharp spectrum. One of the reasons that the deuterium has the low energy could be dissociative excitation.

In fig. 3, the measured He I spectrum around the outboard strike point is shown for the L-mode plasma with I_p=1.2 MA, B_T=3.5 T, $\bar{n}_e$=1.5×10^{19} m^{-3}, P_{NB}=10 MW, $\bar{n}_e^{div}$=3×10^{18} m^{-3} and T_e^{div}=100 eV. The discharge was operated in deuterium with small amounts of helium gas-puffing. The spectrum can be reproduced as a sum of narrow and broad Gaussian functions. The broadening of the narrow component was almost the same as the wavelength resolution of the spectrometer. In this measurement, the wavelength resolution corresponds to the Doppler width of helium at a temperature of 0.2 eV. The width of the broad component was equal to the Doppler width of helium at a temperature of 1-2 eV. The peak shifts of the narrow and broad components were in the range of uncertainty of the wavelength. The contribution of the broad and narrow components are also shown in fig. 3 by dashed and thin lines, respectively. In this case, the intensity of the broad component integrated over the wavelength was almost the same for the narrow component.

The narrow component is ascribed to the helium desorbed from the divertor plates with the temperature of divertor plates. The broad component can not be explained by helium reflected at the divertor plates, since the peak was not shifted toward the short wavelength side. In the simulation where the helium atoms were released at 2 eV, the peak of spectrum appeared at $\Delta\lambda$=0.02 nm. The charge-exchange reaction, recombination and neutral-neutral reaction between deuterium and helium can be considered as the candidate mechanism for the broad component. However, these reaction rates are too small to explain the intensities of the broad component. Further work remains to be made to determine the source of the broad component.

2. 4. Analysis of Dα and He I emission profiles

The Dα and He I emission profiles were simultaneously measured for the discharge where the He I spectrum was analyzed in section 3. The measured Dα emission intensity profile and the calculated profile are shown in fig. 4. The calculated profile was produced as a sum of the calculation in the cases that Franck-Condon energy was set to 0.03, 2, 5 and 10 eV for all dissociation processes. The ratio of each contribution was selected to be the same as in section 3. The neutral particles were released as molecules with the same profile as the particle flux to the divertor plates, and the absolute value of the particle source was adjusted

to the measurement. From this analysis, the deuterium source at the divertor plates was estimated to be $3.3\times10^{22}\,s^{-1}$. The deuterium density was estimated to be $1.6\times10^{17}\,m^{-3}$ around the outboard strike point, and also the penetration probability was estimated to be 2%. Because the charge-exchange reaction rate is comparable to the ionization rate for deuterium, the calculated deuterium density and the penetration probability do not strongly depend on the Franck-Condon energy. When the Franck-Condon energy was set to be 0.03 and 10 eV for all dissociation process, the deuterium density was evaluated to be 2.9×10^{17} and 1.2×10^{17} m^{-3}, respectively, and also the penetration probability was evaluated to be 1.8 and 2.5%, respectively.

The measured He I emission intensity profile and the calculation are shown in fig. 5. The profile was calculated as the sum of two components with a similar amount: one released at the divertor plate temperature and the other released at 2 eV. It is noted that the calculated He I spectrum of the helium atom released at 2 eV does not agree with the broad component of the measurement as described in section 3. We assumed that the width of the helium flux profile released from the divertor plates was a factor of 3 smaller than that of the deuterium flux profile and the outboard helium flux was enhanced by 2.5 compared with the deuterium flux profile, so as to adjust the calculated emission profile to the measurement. The calculation disagrees with the measurement in the ranges of R=2.8-2.9 and 3.3-3.4 m. In order to adjust the calculation to the measurement in these ranges, the helium flux which has the extended tails should be considered. The total helium source was estimated to be $3.2\times10^{21}\,s^{-1}$. Also the helium density around the outboard strike point and the penetration probability was estimated to be $4.7\times10^{17}\,m^{-3}$ and 1.3 %, respectively. Although the total helium source was one order of magnitude smaller than the deuterium source, the helium density becomes larger than the deuterium density because the helium source was localized around the outboard strike point compared with the deuterium source. The fact that the helium density was higher than the deuterium density is advantageous for the helium exhaust. Because the charge-exchange reaction rate is smaller than the ionization rate for helium, the dependence of the helium density on the released energy was strong. The helium density was estimated to be 7.2×10^{17} and $2.3\times10^{17}\,m^{-3}$ for the cases that the released energy was set to 0.05 and 2 eV, respectively. The penetration probability strongly depends on the released energy. The penetration probability was estimated to be 0.1 and 2.7% for the cases that the released energy was set to 0.05 and 2 eV, respectively.

2. 5. Summary

Neutral deuterium and helium behavior in JT-60U divertor plasmas has been studied based on measurements of the spectra and emission intensity profiles of Dα and He I in combination with computer simulations. The calculated peak shift of the Dα spectrum was

larger than that of the measurement. In order to adjust the calculation to the measurement, the Franck-Condon energies of 0.03, 2, 5 and 10 eV were taken into account. The measured He I spectrum consisted of broad and narrow components. The narrow component can be ascribed to the desorbed helium. However, the mechanism which produces the broad component is yet to be understood. The deuterium and helium density and the penetration probability into the main plasma were estimated based on the measurements of absolute Dα and He I emission intensity profiles and simulations. It was found that the total helium source released at the divertor plates was one order of magnitude smaller than the deuterium source. However, the helium density was higher than the deuterium density. The penetration probability of the helium strongly depends on its energy, and it is important for helium control to understand the mechanism which is responsible for the production of the high energy helium.

Acknowledgments

The authors wish to thank Dr. M. Shimada for valuable discussions. They are also grateful to JT-60 team for the support in the experiments.

References

[2.1] H. Kubo et al., Plasma Phys. Control. Fusion 37 (1995) 1133.

[2.2] H. Kubo et al., 7th Int. Toki Conf., 1995

[2.3] D.B. Heifetz, in Physics of Plasma-Wall Interactions in Controlled Fusion, eds. D.E. Post and R. Behrisch (Plenum, New York, 1986) p. 695.

[2.4] K. Shimizu, et al., J. Nucl. Mater. 196 & 198 (1992) 476.

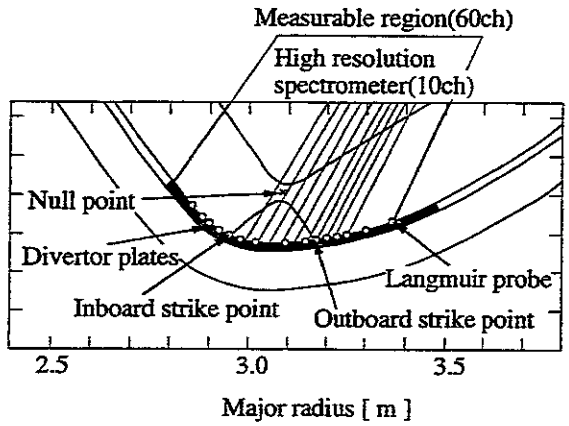

fig. 1 Schematic drawing of JT-60U divertor and viewing chords of diagnostics.

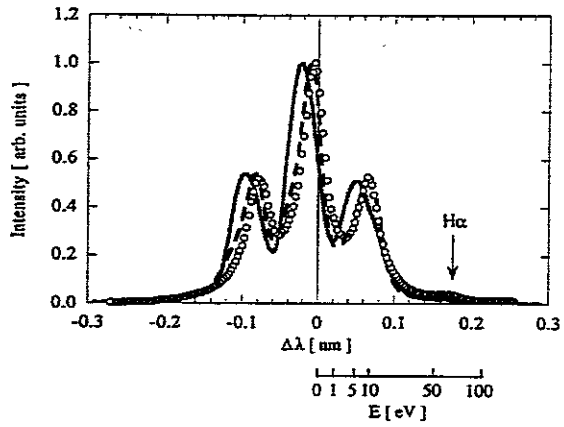

fig. 2 Open circles show measured Dα spectrum. Solid and dashed lines show calculated Dα spectrum. In the calculation shown by dashed line, Franck-Condon energy was modified.

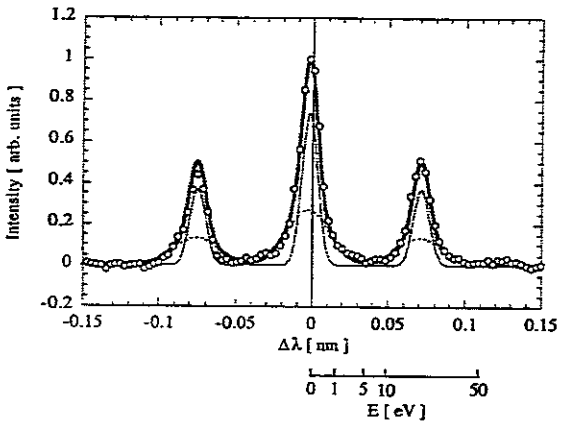

fig. 3 Open circles show measured He I spectrum. Solid thick line shows fitted curve using two Gaussian functions. Thin and dashed lines show the contribution of two Gaussian functions.

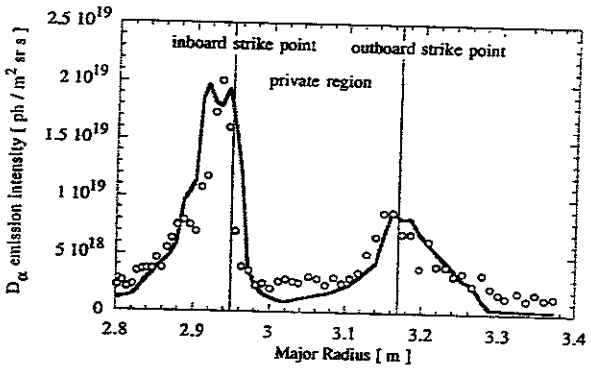

fig. 4 Open circles and solid line show measured and calculated Dα emission intensity profile, respectively.

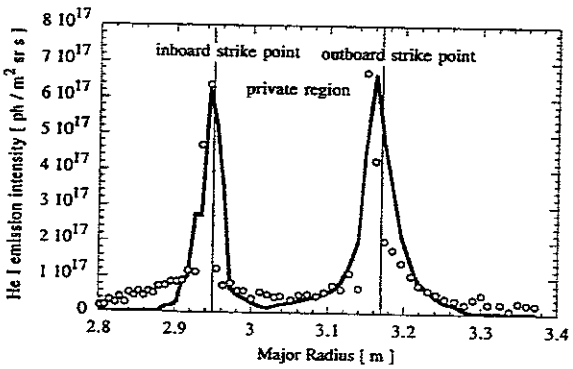

fig. 5 Open circles and solid line show measured and calculated He I emission intensity profile, respectively.

3. Modelling of Impurity and Plasma Transport for Radiative Divertor

3. 1. Introduction

The high heat load onto divertor plates is one of the most crucial issues for the design of a tokamak fusion reactor. Remote radiative cooling by cold and dense divertor plasmas is the most promising method for reducing the heat load onto the divertor plates. However, in discharges with such divertor plasmas, radiation near the X-point is enhanced locally and often leads to a MARFE. The main plasma is cooled directly due to deterioration of the impurity shielding effect, occasionally leading to a density limit disruption. Therefore, it is necessary to investigate the conditions of the formation of a cold and dense divertor plasma without triggering a MARFE.

A two-dimensional impurity code based on Monte Carlo techniques (IMPMC) which did not include chemical sputtering has been developed to study the impurity behavior in the divertor plasma. The calculated profile of the C II line (6580Å) emission reproduced the experimentally measured profile except in the private region in the case of low density divertor plasmas [3.1]. The plasma parameters were calculated with an interpretative divertor code [3.2]. Carbon chemical sputtering has been incorporated into the IMPMC code to investigate the effects of chemical sputtering in high density divertor plasmas close to the MARFE onset.

3. 2. Impurity Transport Modelling

The IMPMC code [3.1] includes the following processes: (1) impurity generation, (2) atomic / molecular processes, (3) parallel motion of impurity ions along the field lines, (4) anomalous diffusion across the flux surfaces, and (5) Coulomb scattering. Impurity neutrals are originally sputtered from a divertor plate by physical sputtering of deuterium ions. Some of the sputtered impurities return to the plate and cause self-sputtering. Taking account of the sputtering yields and incident fluxes onto the target plates, the sputtered outfluxes are determined self-consistently. In order to incorporate the angular dependence of the sputtering, the normal incidence yields are enhanced by a factor of 2.0 and 1.5 for physical and self-sputtering, respectively. These values correspond to an incidence angle of about 30 degrees [3.3]. In a simple model which is widely used for self-sputtering, the incident energy of impurity onto the target plates is assumed to be $E_0^{simple} = (5/2)T_i + (1/2)m_i c_s^2 + eZ\phi_s$, where c_s is the sound speed and ϕ_s is the sheath potential. This simple model overestimates the flux of self-sputtering by 5 ~ 6 times that of the self-consistent calculation because of overestimation of E_0^{simple}. The impurity ions which return to the target plates cannot gain a flow velocity close to that of the background plasma, because the dominant ions hitting the plates are C^{2+} and the ion thermal force directed upstream overcomes the friction force. This result indicates

that the Monte Carlo approach is indispensable for evaluation of the self-sputtering process.

The neutral particles which hit the wall cause physical sputtering or chemical sputtering depending on the incident energy. The chemical sputtering yield strongly depends on the wall temperature (T_w) and the incident energy (E_0). As shown later, the methane sputtered from the wall in the private region is the most important for penetration of carbon impurity into the X-point region. The wall temperature in the private region is about 300°C and the mean energy of neutral particles which sputter methane is about 50 eV. In such condition of T_w = 600K and E_0 < 50 eV, the chemical sputtering yield by deuterium neutrals is in the range of 0.04 ~ 0.06 [3.3]. Hence the chemical sputtering yield is set at 0.05. The dissociation process of methane sputtered by chemical sputtering and the dynamics of dissociation products, such as CD_4^+, CD_3, and CD_3^+, are also included in our model.

3. 3. Simulation Results and Comparison with Experiments

3. 3. 1 Experimental observations in high density plasma

An interesting phenomenon of a drastic change in the profile of C II line radiation before and after the start of a MARFE was observed in high density divertor plasmas of JT-60U [3.4] as shown in Fig. 3.1. The profile becomes broader as the density increases. The electron temperature in front of the plates measured with Langmuir probes is around 20 eV before the MARFE onset at 7.8 sec. The ionization rate in the SOL plasma with parameters of $n_e \geq 10^{19}$ m^{-3} and $T_e \geq 20$ eV indicates that all the carbon impurities are ionized to C^{3+} ions before they reach near the X-point. Therefore, the change in the C II line radiation profile observed in discharges with strong gas-puffing can not be explained by physical sputtering at the target plates alone.

3. 3. 2 Impurity generation in high density plasma

Simulations have been carried out with the new IMPMC code including chemical sputtering. Figure 2 shows the spatial distribution of the calculated carbon flux density by physical and chemical sputtering in low and high density plasmas. The physical sputtering in the high density plasma is reduced because of the low incident energy of deuterium ions. On the other hand, the charge exchange process becomes dominant in the neutral transport and the influx of neutral to the wall increases with the plasma density. The neutral particles which hit the wall cause physical sputtering or chemical sputtering depending on the incident energy. The fraction of the particle flux with the incident energy of above 100 eV is less than 10% and the mean energy of the influx is about 20 eV on the target plates and 50 eV on the wall in the private region. The energy is small for physical sputtering. Thereby, it can be assumed that the neutral particles cause only chemical sputtering which produces methane (CD_4). Chemical sputtering becomes dominant in the high density plasma, as shown in Fig.

3.2(b). The rate coefficients for CD_4 dissociation processes in Ref. [3.5] are used. Only 10% of CD_4 released from the target plates can become C^+ ions. Dissociation and ionization events of CD_4 take place at the vicinity of the plates and the ions, such as CD_4^+ and CD_3^+, quickly return to the plates through the diffusion process. In addition, some of the remaining neutral hydrocarbons return to the wall since the velocity direction is randomized at neutralization. It should be noted that small fraction of the methane released from the target plates make a contribution to the C II line radiation. In contrast, half of CD_4 released from the wall in the private region is dissociated to C^+ ions finally, because they are ionized and dissociated

Figure 3.3 shows the calculated profiles of C II line radiation. The agreement with the measured profile is fairly good. The intensity near the X-point cannot be explained without chemical sputtering, as shown in Fig. 3.3(b). Figure 3.4 displays the radiation distribution of carbons originating from physical sputtering at the target plates (a) and chemical sputtering at the wall in the private region (b). The radiation of physically sputtered carbon ions is localized at the target plates, while the radiation of carbon ions originating from chemical sputtering has peaks between the X-point and the separatrix strike points. This result is consistent with the experimental observation that the radiation peaks appear between the X-point and the strike points before the start of a MARFE.

3. 3. 3 Impurity generation in low density plasma

The carbon impurity transport in a low density divertor plasma was reanalyzed with the IMPMC code including chemical sputtering. The calculated C II profile agrees fairly well with the experimentally measured profile even in the private region as shown in Fig. 5(a). We confirmed the conclusion in Ref. [3.6] that the carbon generation is principally caused by deuterium physical sputtering and self-sputtering and that the contribution of chemical sputtering is small in low density plasmas. The profile of the calculated C IV line emission indicates that the cross-field diffusion coefficient is around 1 m^2/s as shown in Fig. 3.5(b).

3. 4. Conclusions

A two-dimensional impurity code based on Monte Carlo techniques (IMPMC) has been developed to investigate impurity behavior in diverted plasmas. Using this model, carbon impurity behavior in JT-60U NB heated plasmas has been investigated. The impurity source profiles in the low density plasma can be explained by deuterium ion physical sputtering and self-sputtering. In contrast, in high density plasmas, the physically sputtered impurities from target plates are reduced because of the low incident energy of deuterium ions. In high density plasmas, chemical sputtering by neutral particles which strike the wall in the private region becomes dominant and enhances the radiation near the X-point. This enhanced

radiation near the X-point is considered to trigger a MARFE. Since the shielding is less effective for the carbon originating from the private region, it is necessary to reduce the neutral flux to the wall in the private region to avoid a MARFE. One method is to close the private region with a dome-like structure [3.7]. The effectiveness of this structure is now under investigation with the present code.

Acknowledgment

The authors would like to thank Dr. H. Tawara of NIFS for useful discussions related to the dissociation process of methane.

References

[3.1] SHIMIZU, K., et al., to be published in J. Nucl. Mater.

[3.2] SHIMIZU, K., et al., J. Nucl. Mater 196-198 (1992) 476.

[3.3] ROTH, J., et al., Supple. J. Nucl. Fusion (1991) 64.

[3.4] HOSOGANE, N., J. Nucl. Mater 196-198 (1992) 750.

[3.5] EHRHARDT, A.B., LANGER. W.D., "Collisional Processes of Hydrocarbons in Hydrogen Plasmas", PPPL-2477 (1987).

[3.6] SAKASAI, A., Plasma Physics and Controlled Nuclear Fusion Research 1992 (Proc. 14th Int. Conf. Wurzburg, 1992), IAEA, Vienna, Vol. 1 (1993) 195.

[3.7] TSUJI, S., et al., to be published in J. Nucl. Mater.

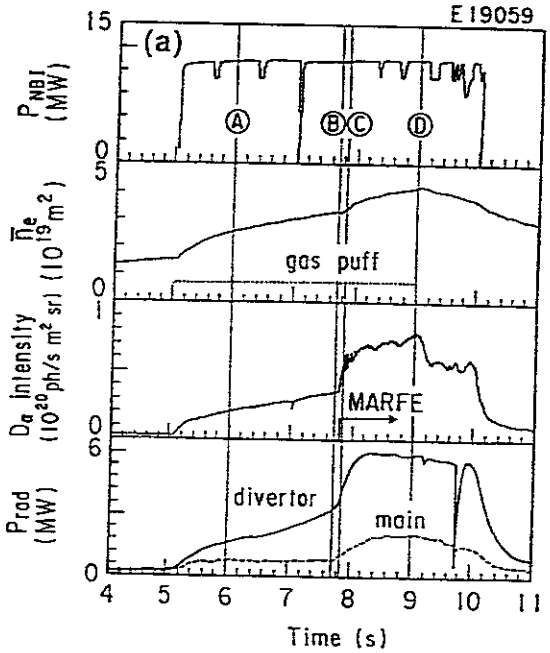

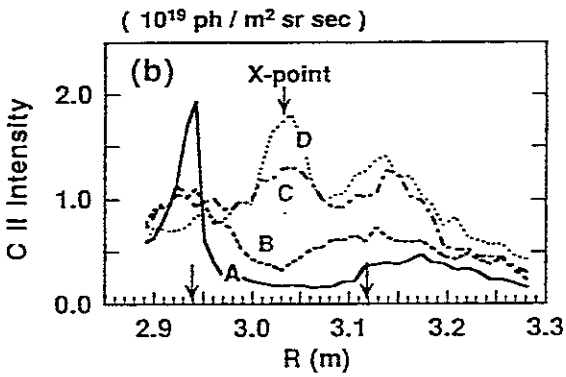

Fig. 1 (a) Time evolution of plasma parameters in an NB-heated discharge with a MARFE. The MARFE started at 7.8 sec. (b) Time evolution of C II line intensity profiles in the divertor region. The inner and outer separatrix strike points are shown by arrows. The peak at the inner separatrix strike point drops and the intensity near the X-point increases gradually as the plasma density increases due to the gas puff. After a MARFE starts at 7.8 sec, the intensity at the vicinity of the X-point increases rapidly within 0.1 sec.

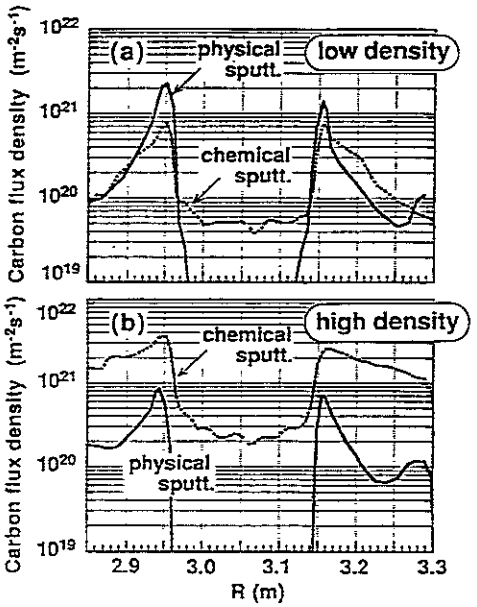

Fig. 2 Carbon flux density for deuterium ion physical sputtering (solid line) and chemical sputtering (dashed line) in a low density (a) and a high density plasma (b). They are flux density normal to the target plate and the wall, i.e. they are multiplied by the pitch of magnetic field line.

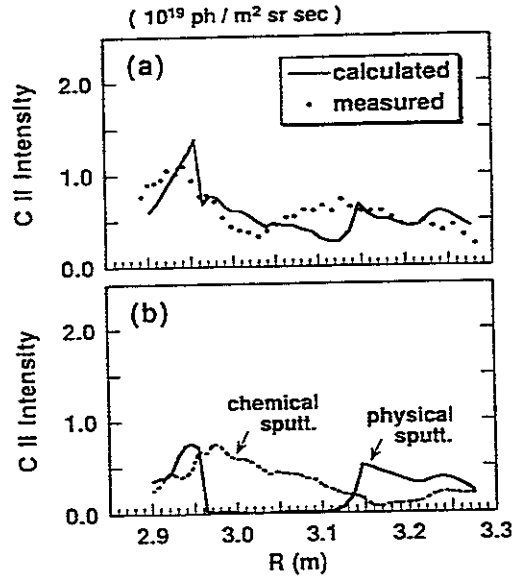

Fig. 3 (a) Calculated profile of C II line intensity in a high density plasma. The measured profile is plotted with closed circles. (b) Calculated profile of C II line intensity due to physical and chemical sputtering. The experimentally measured intensity near the X-point cannot be explained without chemical sputtering.

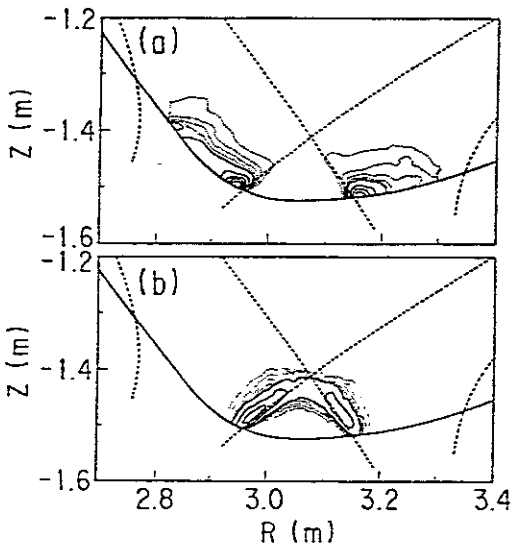

Fig. 4 Contour map of radiation of carbon originating from physical sputtering (a), and chemical sputtering at the wall in the private region (b). The increment between broken contours is 0.1 MW/m^3, and the increment between solid lines is 0.5 MW/m^3. The radiation of the physically sputtered carbon ions is localized near the target plates, while the radiation of the chemically sputtered carbon ions has peaks between the X-point and the separatrix strike points.

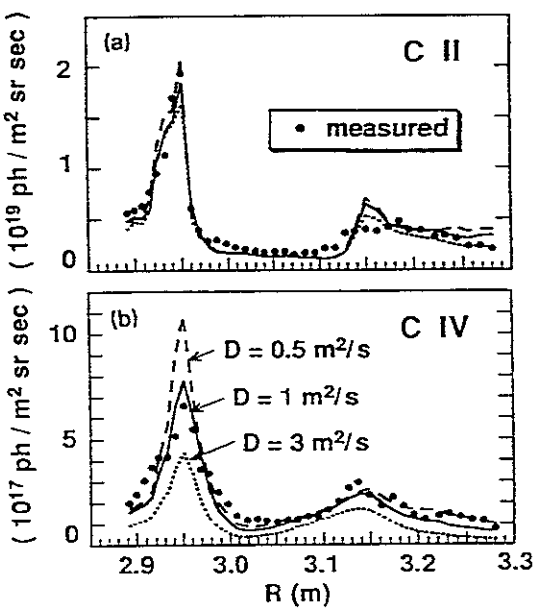

Fig. 5 (a) Calculated profile of C II line intensity in a low density plasma. The measured profile is plotted with closed circles. (b) C IV line intensity profiles calculated with various values of cross-field diffusion coefficient, $D_\perp$. Comparison with the measured profile indicates that $D_\perp$ is around 1 m^2/s.

4. Radiative divertor plasma with Neon injection

4. 1. Introduction

In order to obtain the core plasmas with high ion temperature, it is important to suppress particle recycling to a low level around the main plasma , as well as operating plasmas in improved confinement mode. It is becoming difficult to produce cold, dense and radiative divertor plasmas due to high heat flux density to the divertor and high temperature in the scrape off layer under such conditions. Major part of efforts in divertor study in recent tokamak devices are recently devoted to the radiative divertor experiment by impurity gas puff. In ASDEX Upgrade tokamak, complete detachment at the divertor plasma was obtained during ELMy H-mode without degradation of the core plasma confinement. Demonstration of significant reduction of heat flux at the divertor due to the enhanced radiation loss from the boundary attracted attention and the concept of radiative divertor by impurity puffing is recognized as an alternative of gas target divertor concept of ITER. Radiative divertor experiments by impurity gas puffing were carried out in March, July and September, in 1995. A part of the results was presented at the 22nd EPS conference at Bounemouth, UK.[4.1].

4. 2. Experimental results

The purpose of this study is to investigate the compatibility of high ion temperature in ELMy H-mode plasmas that are produced at the low particle recycling conditions and the radiative divertor plasmas by utilizing neon as seed impurity to enhance radiation loss from the plasma. In order to compare effects on divertor plasma parameters by a various Neon gas and D_2 gas puff sequences, ELMy H-mode plasmas with Ip = 1.2MA, B_T = 2T and P_{NB} = 15MW were produced at the low particle recycling conditions as target discharges. A synergistic effect of the neon gas puff followed by deuterium gas puff was found on the enhancement of radiation loss and particle flux at the divertor . In Fig. 4.1(a), the increment of the radiation loss from the main and divertor plasmas after four kinds of the gas puff sequences is shown. These sequences indexed as "Neon Only", "D_2 Only", "Neon + D_2" and "D_2 + Neon" in the figure mean neon gas puff, deuterium gas puff, neon gas puff followed by deuterium gas puff and deuterium gas puff followed by neon gas puff, respectively. Total injection of neon gas and deuterium gas were 1.2Pam^3 and 9.6Pam^3, respectively. As shown in the figure, the increment of radiation loss by "Neon + D_2" gas puff is much larger than the sum of the radiation loss by the "Neon Only" gas puff and that by "D_2 Only" gas puff from both the main and divertor plasmas. Such a synergistic effect is not seen for the "D_2 + Neon" gas puff. In Fig. 4.1(b) and Fig. 4.1(c), the increment of deuterium particle flux to the divertor and the increment of the electron density in the main plasma by the same gas puff sequences are shown, respectively. While the synergistic effect was again observed for the "Neon +

D_2" gas puff, no synergistic effect was observed for "Neon + D_2" gas puff. In other words, the effect of the "D_2 + Neon" gas puff on the divertor particle flux and electron density is the same with or less than the sum of the effect by the "Neon Only" gas puff and that by "D_2 Only" gas puff. It was clearly demonstrated that the "Neon + D_2" gas puff was effective in producing the radiative divertor plasmas.

With the synergistic effect of neon and deuterium gas puffing, radiative divertor plasmas were obtained in ELMy H-mode plasmas with P_{NB} = 23MW while the H-factor was maintained to 1.5. The discharge was produced at the low particle recycling condition (Φ_{main}= 2 x 10^{22}/s) and particle recycling was increased by a factor of five and radiation loss was increased by a factor of two at the divertor. Change of Z_{eff} due to Neon was about 1 and total dilution of Deuterium due to impurity ions was estimated to be 50%. This discharge is compared with the reference plasma of ELMy H-mode which was produced at the high particle recycling condition in Table 4.1. Since the high T_{i0} that was produced at the low recycling phase was maintained in the case 1 until the radiative divertor phase, the neutron rate was even larger than the case 2, irrespective of the dilution of deuterium due to neon in the case 1.

By increasing radiation loss at the divertor further, the radiative divertor plasma which dissipates 80% of incoming heat flux was produced in ELMy H-mode plasmas with P_{NB} = 20MW. (See Fig. 4.2.) In such a discharge, the total radiation loss from the plasma increased from 6MW to 14MW of the NB power. Profiles of heat flux density to the divertor at the initial phase and at the radiative divertor phase are shown in Fig. 4.2(b). Detachment at the strike point of the separatrix occurred when the heat flux density vanished at t = 9.0 s. The detachment was maintained for two seconds until the end of the NB heating. Degradation of the main plasma confinement due to the radiation enhancement is shown in Fig. 4.3. H-factors of the main plasma are plotted against P^{rad}_{TOT}/P_{ABS} . Data points are taken from ELMy H-mode plasmas with $P_{NB} < 23$MW. Here P^{rad}_{TOT} is the total radiation power and P_{ABS} is NB absorption power.

4. 3. Summary

A synergistic effect of the neon gas puff followed by deuterium gas puff was found on the enhancement of radiation loss and particle flux to the divertor . With the synergistic effect, radiative divertor plasmas were obtained with relatively high ion temperature in the main plasma.

Reference

[4.1] K. Itami et al. Plasma Phys. Control. Fusion 37 (1995) A235-A265.

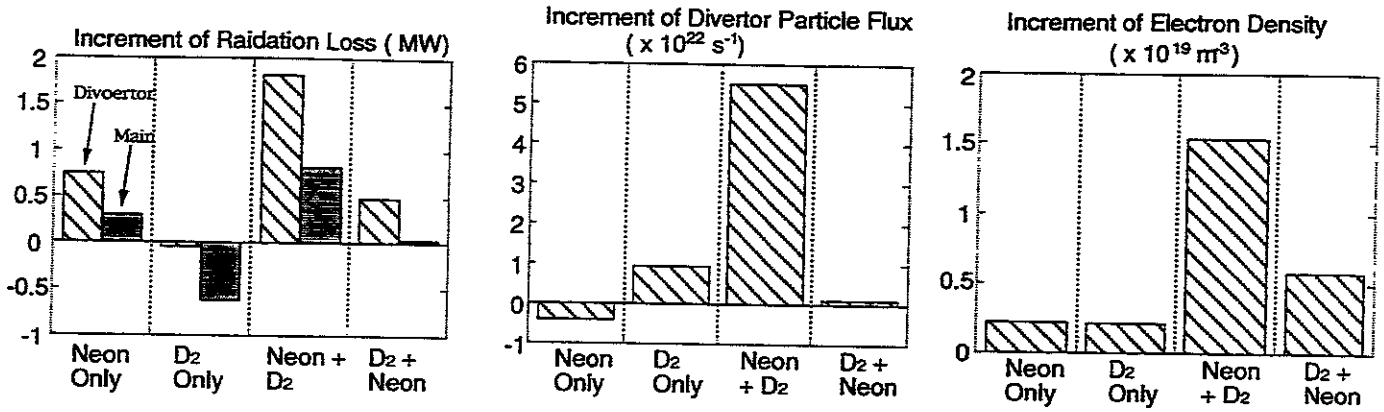

Fig. 1
(a) Increment of the radiation loss from the main and divertor plasmas
(b) Increment of Divertor Particle Flux
(c) Increment of Electron Density
after four kinds of the gas puff sequence

	conditions	Φ_{MAIN} (s^{-1})	$\overline{n_e}$ (m^{-3})	Prad/PNB	Ti0 (keV)	$n_{DD}(s^{-1})$
case 1	Low Recycling + Ne & D2 puff	$5x10^{22}$	$3.2x10^{19}$	50%	7	$3.8x10^{15}$
case 2	High Recycling + No gas puff	$2x10^{22}$	$2.8x10^{19}$	30%	5	$3.1x10^{15}$

Table. 1

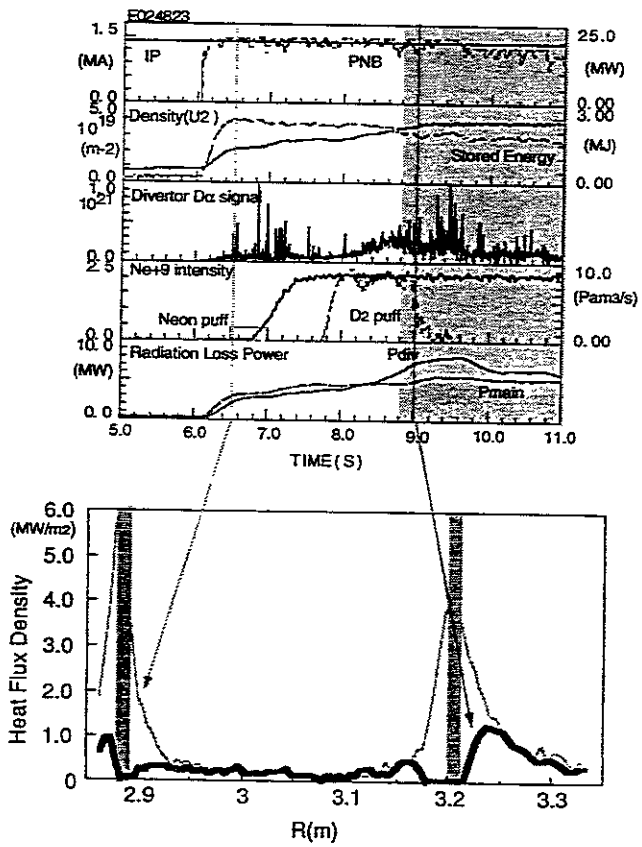

Fig. 2
(a) Waveforms of ELMy H-mode discharge with radiative divertor
(b) Heat flux density profiles.
(Before and after the radiative divertor .)

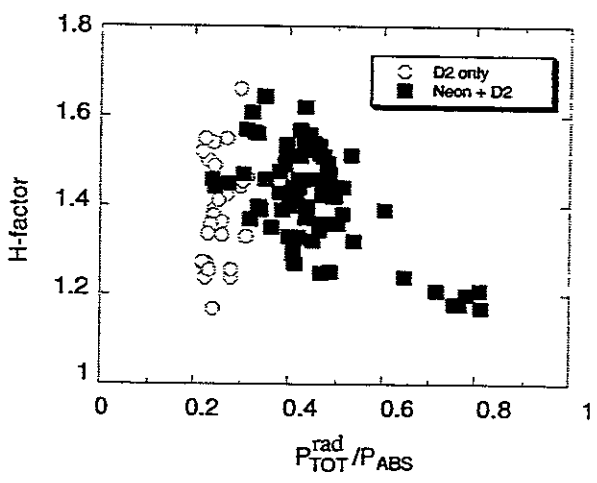

Fig. 3
H-factor vs P_{TOT}^{rad}/P_{ABS} in ELMy H-mode plasmas with neon and deuterium gas puff.
(P_{NB}<23MW)

5. Measurement of Electron Temperature and Density in Divertor Plasmas Using Intensity Ratios of He I Spectral Lines

5. 1. Introduction

Electron temperature and density in divertor plasmas has usually been measured with Langmuir probes located at divertor plates so far. However, high heat flux damages the probe and then it is difficult to measure the density. On the other hand, the method using line intensity ratios does not suffer such a problem. To use He line emission is favorable, because He injection has little effect on fusion plasma performance and He atoms are produced by the nuclear reaction in fusion reactors. In TEXTOR, He I lines: $2p\ ^1P$ - $3s\ ^1S$ (728 nm), $2p\ ^3P$ - $3s\ ^3S$ (706 nm) and $2p\ ^1P$ - $3d\ ^1D$ (668 nm), from an injected He-atom beam have been used for measuring the temperature and density profiles in the plasma edge [5.1]. This paper describes the spatial profile measurement of the temperature and density in the JT-60U divertor using the line intensities.

5. 2. Experiment

Figure 5.1 shows the diagnostics for this investigation in a schematic diagram of the JT-60U divertor. We have simultaneously measured the three He I line emissions from the divertor plasmas with a spatial resolution of 1 cm using a 38-channel optical fiber array [5.2]. The temperature and density at the divertor plates are measured with Langmuir probes and the radiative losses are measured with bolometers.

Figure 5.2 shows a time evolution of a discharge for this study. During NB heating, He gas was puffed for 300 ms and the electron density was raised by a continuous H_2 puff. From the increase in the electron density, the ratio of the helium ion density to the hydrogen ion density was estimated to be 0.34 and 0.068 at 6.5 s and 10 s, respectively. A MARFE occurs in the vicinity of the null point at 9.1 s and the radiative losses measured with the bolometer viewing the null point increases drastically. Then the outboard divertor became partially detached.

5. 3. Results and Discussion

The intensity ratios around the outboard strike point are compared with those calculated by TEXTOR group [6.1] and Kyoto group [6.3] in Fig. 5.3. In the calculations, the electron density was assumed to be 1×10^{19} m^{-3} for the temperature measurement and the electron temperature is assumed to be 50 eV for the density measurement. The error bar in Fig. 5.3(a) indicates the change in the calculated intensity when the density changes from 0.2 to 5×10^{19} m^{-3}. And the error bar in Fig. 5.3(b) indicates the change in the calculated intensity when the temperature changes from 10 to 100 eV. We cannot identify the discrepancy between the two

calculations. The Kyoto group has recently updated the atomic data and considered more energy levels than the TEXTOR group did. The scattering of the measured data is ascribed to the error in the probe measurement. Although the measured intensity ratio increases with the temperature as expected, the temperature is smaller than calculation. The discrepancy cannot be ascribed to the assumption of the density in the calculations. The measured intensity is closer to that calculated by the TEXTOR group than that calculated by the Kyoto group. For the density measurement, the measured intensity ratio agrees with that calculated by the TEXTOR group. The discrepancies between the measurement and the calculations might be attributed to ion collision effect, which was ignored in the calculations. It is expected that the ion collision effect decreases the intensity ratio for the temperature measurement and increases the intensity ratio for the density measurement.

The fifth and sixth rows in Fig. 5.2 show the time evolution of the temperatures and densities around the outboard strike point obtained by the probe measurement and spectroscopic measurement. Here the TEXTOR data were used to derive the temperature and density from the spectroscopic measurement. Although the temperature derived from the spectroscopic measurement decreases with the increase in the electron density in the main plasma as the temperature measured with the probe, it is about half of that measured with the probe. The density derived from the spectroscopic measurement agrees with the density measured with the probe.

Fig. 5.4 shows the spatial distributions of He I 728 nm intensity, the temperature and density derived from the spectroscopic measurement. We discuss the distributions between the outboard strike point and the null point. In this region, the angle between the viewing chords of the spectroscopic measurement and the separatrix surface is rather large and the viewing chords change along the field line. Under the attached divertor condition, the intensity profile has a clear peak at the outboard strike point. The intensity profile becomes flat as a MARFE occurs. As the electron density in the main plasma increases, the temperature decreases and the density increases in the divertor. During the MARFE, the temperature decreases down to 10 eV and the profile becomes flat. Then the density near the divertor plates to which the plasma is attached is twice the density around the null point.

The optical fiber viewing the strike point observes the line emission from the vicinity of the strike point, where He atoms recycle dominantly. It is expected that the temperature and density at the strike point are reliably derived from the intensity ratios. Assuming that the electron density is 1×10^{19} m^{-3} and the energy of the He atoms is 600K, the ionization length of the He atoms is estimated to be 20 and 1.4 cm at electron temperatures of 10 and 50 eV, respectively. Under the attached divertor condition, it is expected that the He atoms cannot penetrate the scrape-off layer because the temperature is high. Then the line emission measured with the fibers viewing the range between the strike point and the null point comes from the

two boundaries of the scrape-off layer: the outboard boundary and the private-region boundary. Therefore it is difficult to obtain the correct profiles of the temperature and density between the strike point and the null point from the spectroscopic measurement. As the density increases and the temperature decreases, the He atoms penetrate deeper into the scrape-off layer, and the density obtained by spectroscopy increases and the temperature obtained by spectroscopy decreases. When the MARFE occurs and the temperature is low, the measurement is useful in deriving temperature and density profiles because the He atoms penetrate the scrape-off plasma and the peripheral region of the main plasma.

5. 4. Summary

The intensity ratios of the He I spectral lines can be used for estimating the electron temperature and density profiles in divertor plasmas, although more precise atomic data are necessary. Around the strike point, the temperature and density derived from the spectroscopic measurement agreed with those measured with probes within a factor of two. On the other hand, it is difficult to obtain correct profiles of the temperature and density between the strike point and the null point. However, when a MARFE occurs and the temperature is low, the measurement is useful in deriving the temperature and density profiles. The spectroscopic measurement suggested that the temperatures around the divertor plates to which the divertor plasma attached and around the null point were about 10 eV.

Acknowledgment

The authors are grateful to Dr. M. Goto and Prof. T. Fujimoto of Kyoto university for providing the atomic data.

References

[5.1] B. Schweer et al.; J. Nucl. Mater. 196 - 198 (1992) 174.
[5.2] H. Kubo et al.; Plasma Phys. Control. Fusion 37 (1995) 1133.
[5.3] M. Goto et al.; private communication.

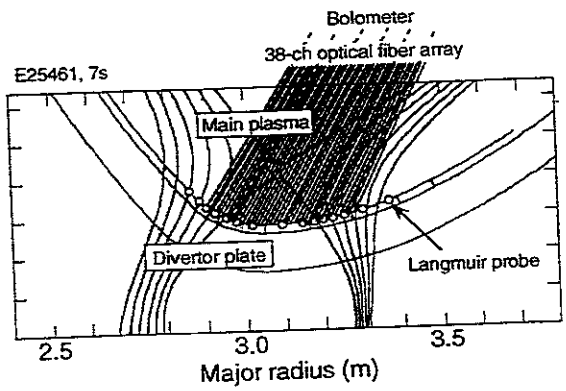

Fig.1 Schematic diagram of the JT-60U divertor.

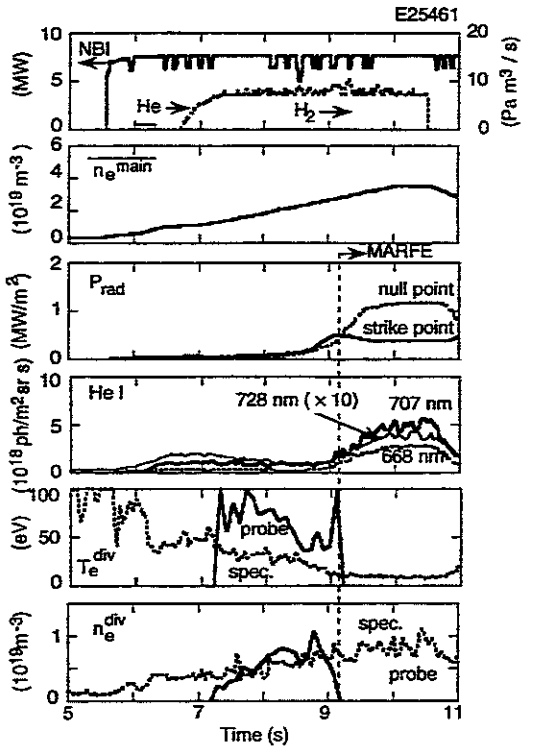

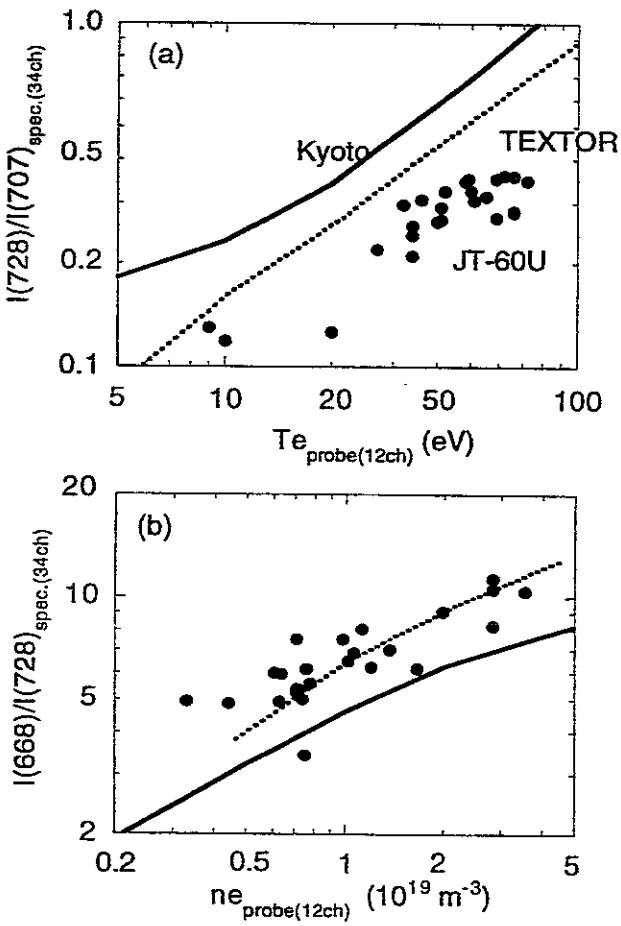

Fig. 3 Intensity ratios for (a) the temperature measurement and (b) the density measurement. The solid points indicate the ratios measured around the outboard strike point in JT-60U and the lines indicate those calculated by TEXTOR group and Kyoto group.

Fig. 2 Time evolution of a discharge with a He puff. The NBI power and the puff rates of He and H_2 are shown in the first row. The line-averaged electron density in the main plasma is shown in the second row and the radiative losses measured with the bolometers viewing the null point and the outboard strike point are shown in the third one. The forth row shows line intensities of He I 728 nm, 707 nm and 668 nm around the outboard strike point. The fifth and the sixth shows the temperatures and densities around the outboard strike point obtained by the probe measurement and spectroscopic measurement.

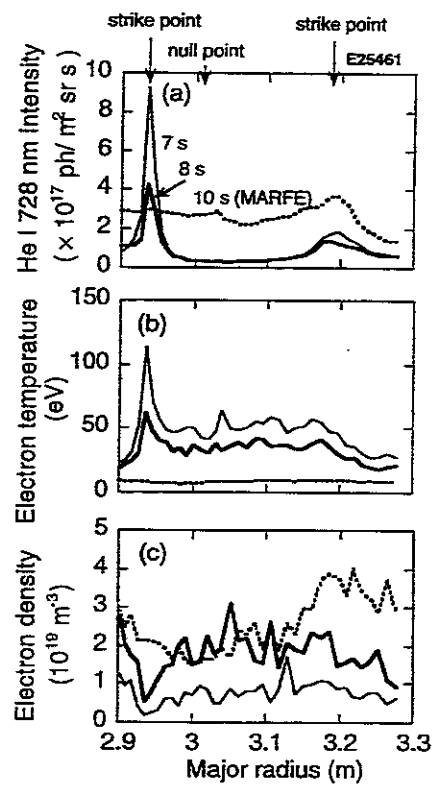

Fig. 4 Spatial distributions of (a) He I 728 nm intensity, (b) the temperature and (c) density derived from the spectroscopic measurement using the TEXTOR data.

Collisional-Radiative Model: A Plasma Spectroscopy Theory for Experimentalists

Takashi Fujimoto
Department of Engineering Science, Graduate School of Engineering, Kyoto University, Kyoto 606-01

Keiji Sawada
Department of Applied Science, Faculty of Engineering, Shinshu University, Nagano 380

Introduction

The population $n(p)$ of an excited (and the ground-state) level p of ions immersed in plasma is described by the rate equation,

$$\begin{aligned} dn(p)/dt = & \sum_{q \neq p} [C(q, p)\, n_e + A(q, p)]\; n(q) \\ & - [\{\sum_{q \neq p} C(p, q) + S(p)\}\; n_e + \sum_{q < p} A(p, q)]\; n(p) \\ & + [\alpha(p)\, n_e + \beta(p)]\; n_z\, n_e \end{aligned} \qquad (1)$$

which is coupled with similar equations for other levels, where n_z is the density of the ions in the next ionization stage, and the rate constants are

$C(p, q)$: Excitation or deexcitation rate coefficient for transition $p \rightarrow q$ by electron collisions,
$S(p)$: Ionization rate coefficient from level p,
$A(p, q)$: Spontaneous radiative transition probability for $p \rightarrow q$,
$\alpha(p)$: Three-body recombination rate coefficient to level p, and
$\beta(p)$: Radiative recombination rate coefficient to level p.

In eq. (1) $q < p$ means level(s) q lying energetically lower than level p.

In 1962 the method of the quasi-steady-state solution (the collisional-radiative model) was proposed [1]. Its idea is: for excited levels the

relaxation time is much shorter than the typical time constant for ionization and recombination of the plasma itself, so that an xcited level population readily adjust itself to the ionization state of the plasma. In other words, under normal plasma conditions, the positive quantity on the r.h.s. of eq. (1) and the negative quantity almost cancel out each other, leaving a small time derivative. To retain this small quantity will not make much sense. Thus we put

$$dn(p)/dt = 0 \qquad \text{for } p \neq 1 \tag{2}$$

where $p = 1$ is understood to denote the ground state. Thus the coupled differential equations (1) reduce to a set of coupled linear equations for excited levels. It turned out later [2] that the situation concerning the excited-level population is not so straightforward as originally assumed. Approximation (2), however, appears to be valid in a wide range of conditions. Now, $n(1)$ and n_z enter into this set of equations (2) as parameters. The solution of this coupled equations may be expressed as

$$n(p) = r_0(p) Z(p) n_z n_e + r_1(p) [Z(p)/Z(1)] n(1) \tag{3}$$

$$\equiv \quad n_0(p) \quad + \quad n_1(p)$$

where $Z(p)$ is the Saha-Boltzmann coefficient that gives the LTE population as $n(p) = Z(p) n_z n_e$. Instead of $n(p)$, the population coefficients $r_0(p)$ and $r_1(p)$ are now unknown quantities to be solved for eq. (2). They are functions of n_e and T_e.

For the ground-state density $n(1)$ and the ion density n_z, we have to retain the time derivative of eq. (1), and these equations give ionization and recombination of this system of ions under consideration. These equations are described in terms of the effective rate coefficients

$$dn(1)/dt = -dn_z/dt$$

$$= -S_{CR} n(1) n_e + \alpha_{CR} n_z n_e \tag{4}$$

where the collisional-radiative ionization and recombination rate coefficients are expressed in terms of the population coefficients for $p > 1$, which have been obtained above,

$$S_{CR} = S(1) + \sum_{p>1} C(1, p) - [1/Z(1)\, n_e] \sum_{p>1} Z(p)\, r_1(p)\, [C(p, 1)\, n_e + A(p, 1)] \quad (5a)$$

$$\alpha_{CR} = \alpha(1)\, n_e + \beta(1) + \sum_{p>1} Z(p)\, r_0(p)\, [C(p, 1)\, n_e + A(p, 1)] \quad (5b)$$

where $p > 1$ means all the excited levels. It should be noted that the

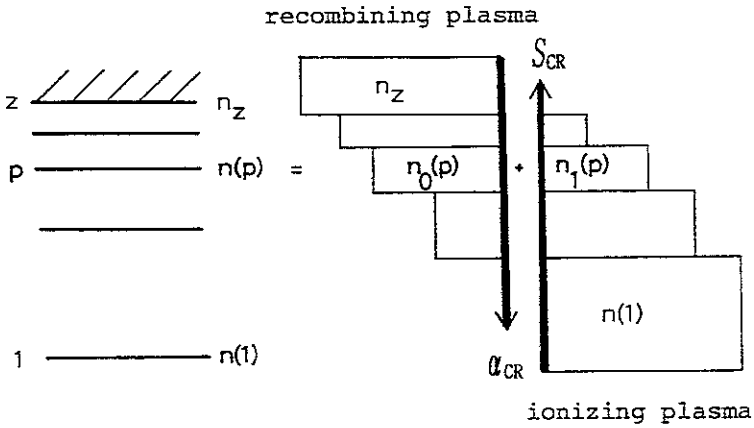

Fig. 1

ionization rate coefficient, eq. (5a), includes only $r_1(p)$, not $r_0(p)$, and *vise versa* for the recombination rate coefficient. This is an important

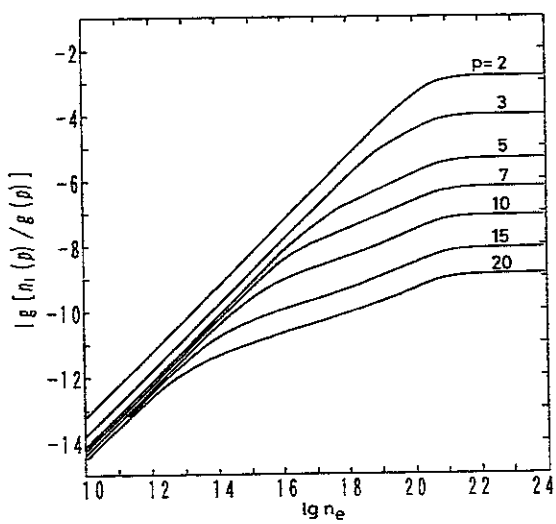

Fig. 2

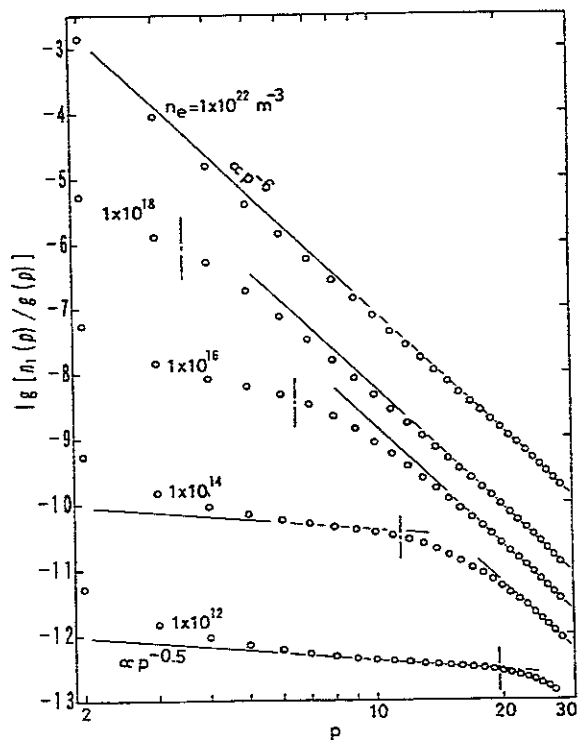

Fig. 3

point to remember.

Equations (3), (4) and (5) suggest that we may decompose the excited-level population and the process of ionization-recombination into two components: the ionizing plasma component that is proportional to $n(1)$ and the recombining plasma component proportional to n_z. [3] This situation is depicted schematically in Fig. 1.

Ionizing plasma

In the following we take neutral hydrogen as an example of atoms and ions in plasma. The different-l sublevels are assumed to be populated according to their statistical weights, so that we specify a level with its principal quantum number. Thus p or q is understood to denote the p.q.n. of the level. We assume T_e = 1.28 x 10^5 K and $n(1)$ = 1 m^{-3}. [4] Figure 2 shows the excited level populations against n_e. Figure 3 shows the population distribution among the excited levels. We may divide whole the region of n_e or all the excited levels into two regimes, the corona phase for the

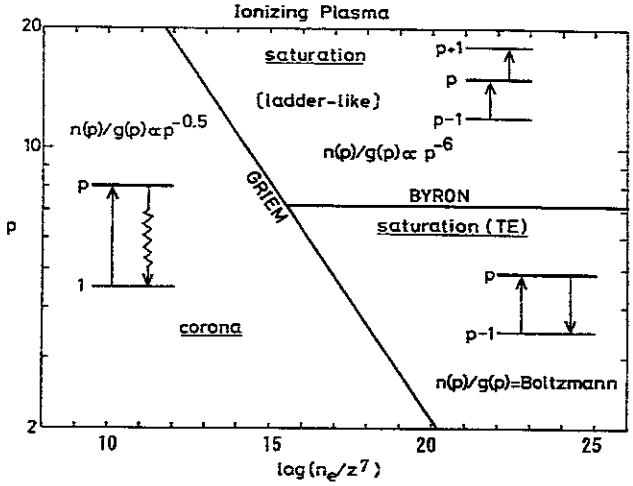

(a)

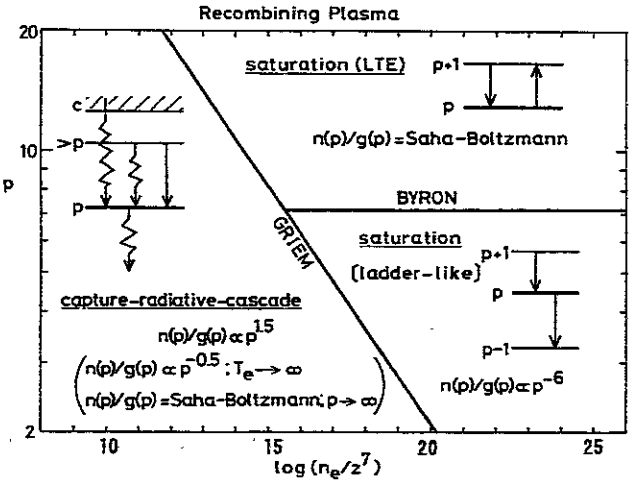

(b)

Fig. 4

low density regime and the saturation phase for the high density regime. Figure 4(a) shows schematically these regimes and the boundary between them: Griem's boundary. This boundary is given from comparison, for a particular level p, of the collisional depopulation rate and the radiative

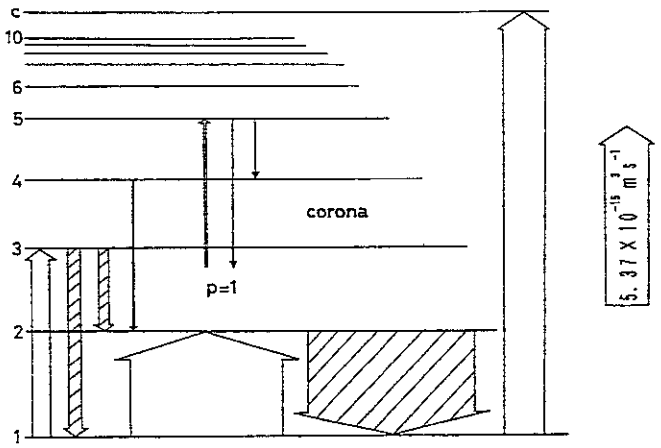

Fig. 5

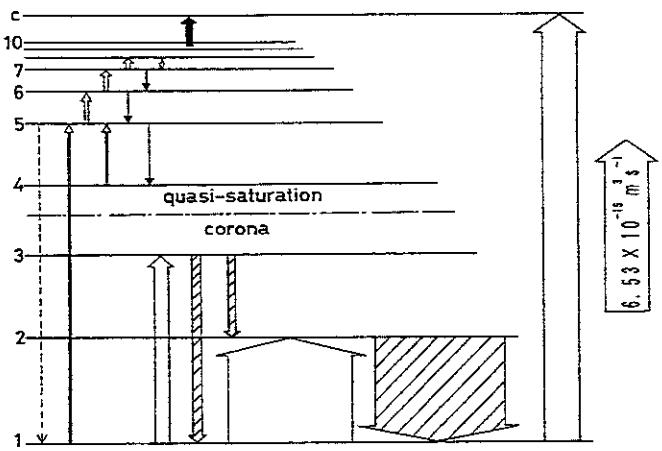

Fig. 6

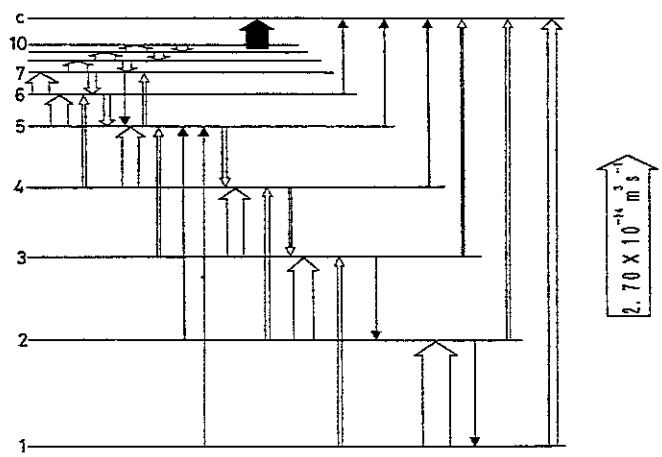

Fig. 7

decay rate

$$\sum_{q<p} A(p, q) \sim [\sum_{q\neq p} C(p, q) + S(p)]\, n_e \qquad (6)$$

Numerically the boundary may be given approximately by

$$p_G \sim 480\,(n_e/z^7)^{-2/17} \qquad (6a)$$

where n_e is measured in m^{-3} and z is the effective core charge felt by the excited electron. (In the figure another boundary is given. Under ordinary conditions this boundary lies much lower than $p = 2$, and does not appear in this diagram.)

Figures 5, 6 and 7 give sketches of the dominant flows of electrons among the levels for $n_e = 1 \times 10^{12}$ m^{-3}, 1×10^{18} m^{-3} and 1×10^{22} m^{-3}, respectively. The width of an arrow represents the magnitude of the flow. The blank arrow denotes the collisional transition and the hatched one the radiative transition.

From these figures it is obvious that in the low density regime, or the corona phase, an excited level population is given by the balance relation

$$n_1(p) = [C(1, p)\, n(1)\, n_e + \sum_{q>p} n_1(q)\, A(q, p)] / \sum_{q<p} A(p, q) \qquad (7)$$

It has been shown that, in the numerator, the second term, the cascading contribution from higher-lying levels, should be almost 20 %, which depends little on p. [5] Thus, eq. (7) is consistent with our nomenclature, the corona phase.

In the high-density regime, another balance is established (Figs. 6 and 7);

$$n_1(p-1)\, C(p-1, p)\, n_e \sim n_1(p)\, C(p, p+1)\, n_e \qquad (8)$$

We call this mechanism the ladderlike excitation. An important consequence appears in the population distribution: Equation (8) indicates that the flow of electrons between the adjacent levels is independent of p. Since

the excitation rate coefficient to the adjacent higher-lying level, $C(p, p+1)$ is, roughly apeaking, proportional to p^4, the population $n_1(p)$ should be proportional to p^{-4}, or

$$n_1(p)/g(p) \propto p^{-6} \tag{9}$$

where $g(p) = 2p^2$ is the statistical weight of level p. We call this feature the minus sixth power distribution. Figure 3 compares eq. (9) with the numerical calculation.

Since this ladderlike flow results in ionization, this may be called the ladderlike excitation-ionization. With an increase in n_e Griem's boundary lowers (Fig. 4a), and levels lying above this boundary enter into the high density regime, or are engulfed by the ladderlike excitation-ionization scheme. This results in an increase in the effective ionization rate coefficient. Figure 8 shows the rate coefficient and its breakdown

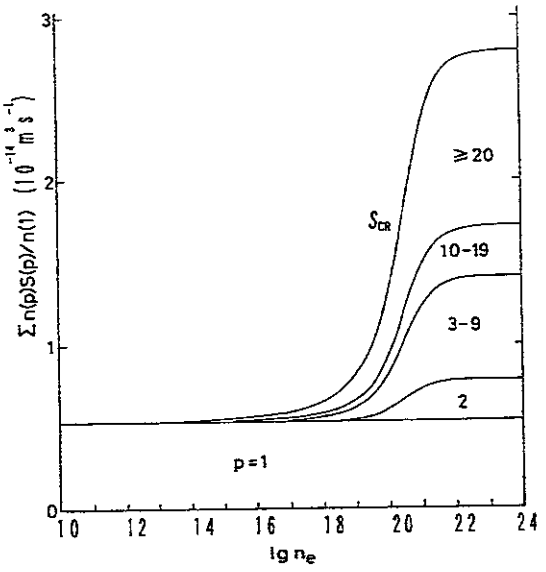

Fig. 8

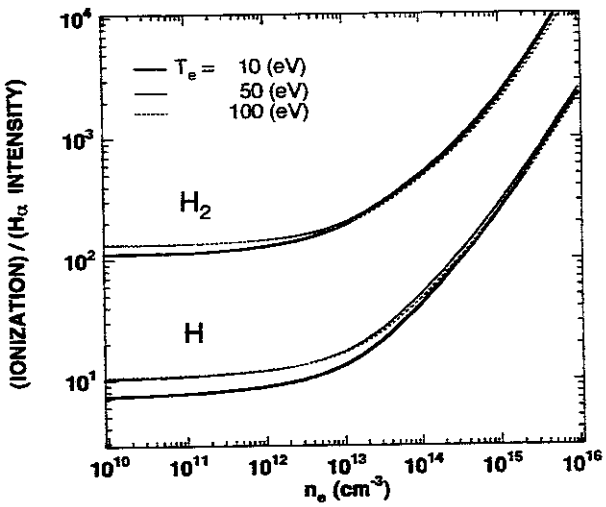

Fig. 9

into the individual processes of ionization: the number indicates the level from which the final step of ionization takes place.

In our experiment on a particular plasma, if we measure excited-level populations, $n(p)$, and if we identify them to the ionizing plasma component, $n_1(p)$, a flow of ionization accompanies these populations, as is indicated as the upward flow at the right in Figs. 5, 6 and 7. This suggests

that, by combining Fig. 2 and Fig. 8, we may determine the effective ionization flow from a measurement of populations in the ionizing plasma. Figure 9 shows the ratio of the number of ionization events to the number of the Balmer α photons emitted. [6] It is noted that $n_1(p)$ would have a temperature very close to the atom temperature.

Recombining plasma

We assume low temperature, T_e = 1 x 10^3 K. Figure 10 shows the excited level populations against n_e, and Fig. 11 shows the population distribution among the excited levels. [7] Here the population per unit statisti-

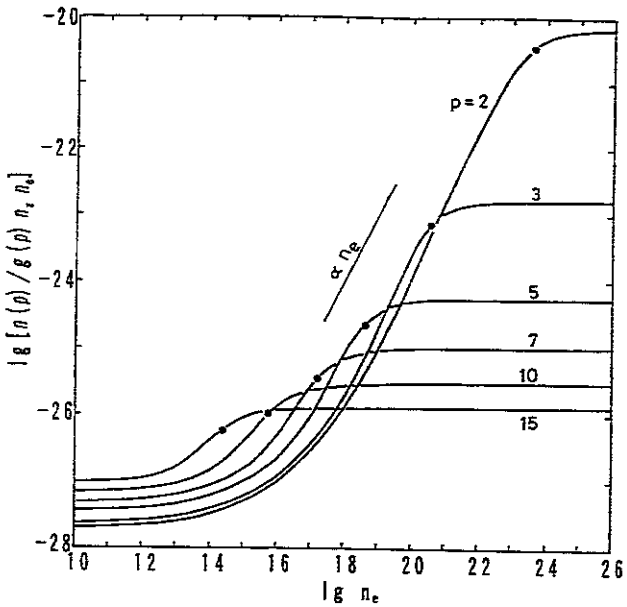

Fig. 10

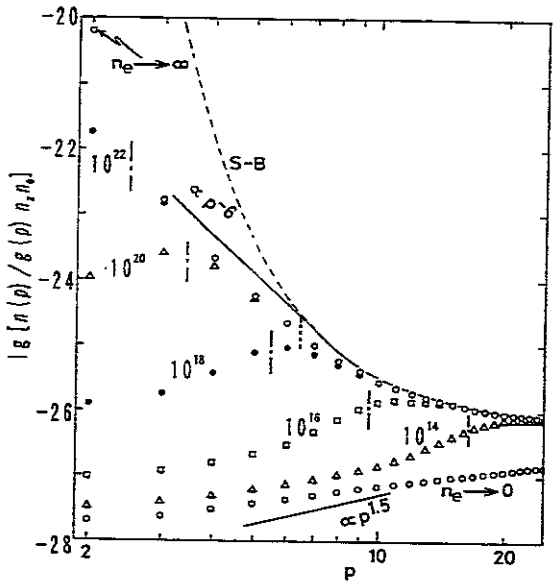

Fig. 11

cal weight, $n(p)/g(p)$, has been further divided by $n_z n_e$. In Fig. 11, the solid-dashed curve denoted as "S-B" indicates the LTE population, *i. e.*, $n(p) = Z(p)\, n_z n_e$. Figure 4b shows the phase diagram for the populations. We can divide the n_e region or the excited levels into the low density regime and the high density regime. The boundary between them is the same as in the case of the ionizing plasma, Griem's boundary. This boundary is given in Fig. 10 with the closed circles and in Fig. 11 with the dash-dotted lines. Figure 12, 13 and 14 show the sketch of the dominant flows of electrons in the energy level diagram for the low-density limit, n_e = 1 x 10^{20} m^{-3}, and the high-density limit, respectively. Griem's boundary is given by the dash-dotted line in Fig. 13.

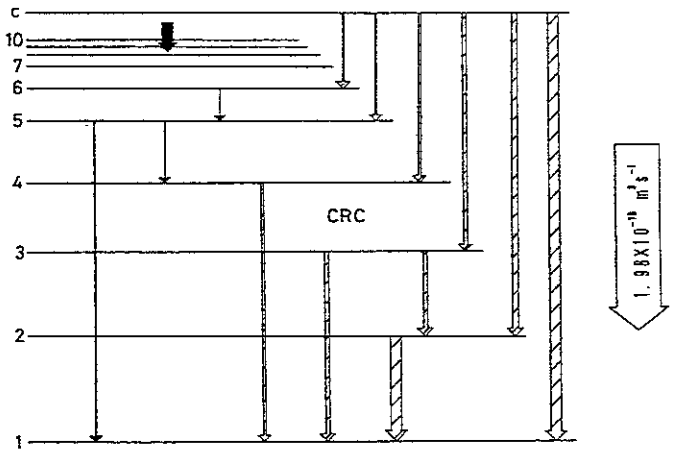

Fig. 12

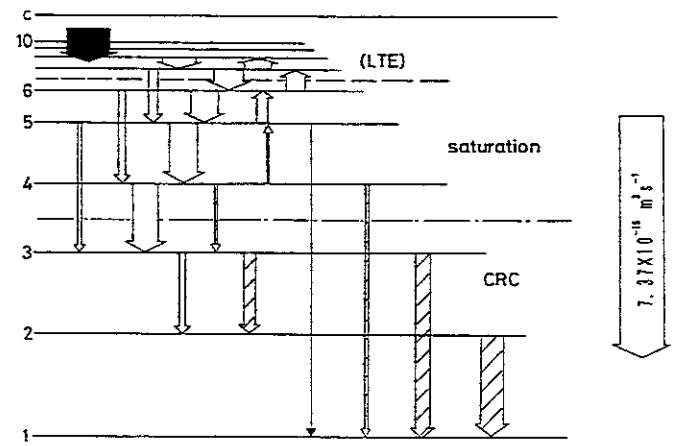

Fig. 13

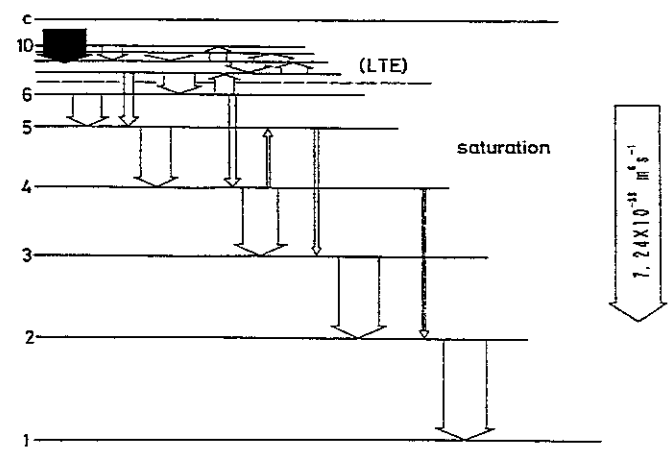

Fig. 14

From these figures it may be concluded that, in the low density regime, or the CRC phase, excited levels are populated by the processes of radiative recombination plus cascade. This results in population inversion. (Fig. 11)

The excited levels in the high density regime are further divided into

the high lying levels and the low lying ones by Byron's boundary, p_B, which is given in Fig. 4(b). This is also given in Figs. 11, 13 and 14 with the dotted line. For levels lying above p_B, excitation is more frequent than deexcitation, $C(p, p+1) > C(p, p-1)$, and for levels below that *vise versa*. Thus the boundary is given by the level at which

$$C(p, p+1) = C(p, p-1) \tag{10}$$

holds. This level may be given approximately by

$$p_B = (z^2 R/3kT_e)^{1/2} \tag{11}$$

where R is one rydberg (13.6 eV). For a level p lying above p_B population coupling with the adjacent higher lying level $(p+1)$ is strong, resulting in the Boltzmann population ratio. It is noted that the direct coupling of the excited-level population with the continuum, or ionization-three-body-reocmbination, is rather weak. These high-lying excited levels as a whole couple with the continuum states, and have populations in LTE. If an electron originally belonging to one of these levels leaves them across p_B and goes down, it cannot return to these levels, because the energy separation between the lower lying levels is too large for the plasma electrons having rather low energies to excite this electron back. Thus, for these low lying levels $p < p_B$, only the ladderlike deexcitation

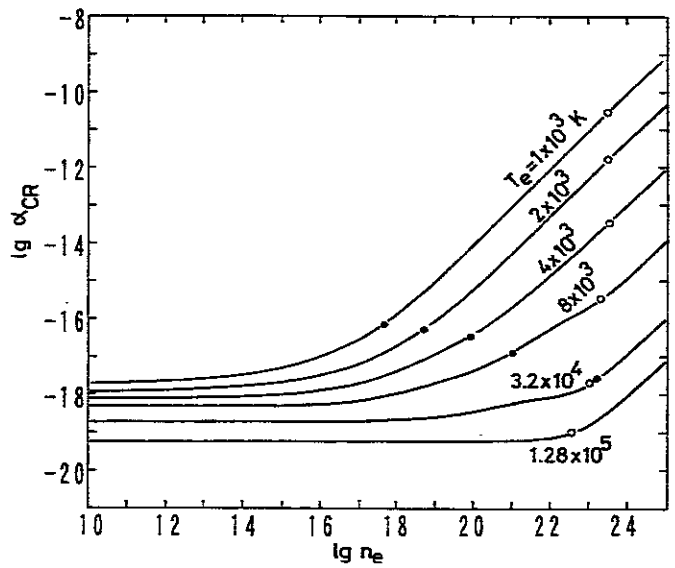

Fig. 15

$$C(p+1, p)\, n_0(p+1)\, n_e \sim C(p, p-1)\, n_0(p)\, n_e \qquad (12)$$

is possible (Fig. 14). Again the minus sixth power ditribution is established. See Fig. 11. It has been shown that, in the high density limit, the population distribution is well approximated for $p > p_B$ by the LTE populations, and for $p < p_B$ by smooth extrapolation of the LTE populations from p_B with the slope of minus six (Fig. 11). [5]

We note that, in our experiment, if we identify the observed populations, $n(p)$, to the recombining plasma component, $n_0(p)$, these atoms should have temperatures very close to the ion temperature. Furthermore, these populations are accompanied by the corresponding recombination flow as given on the right of Figs. 12, 13 and 14.

Figure 15 shows the collisional-radiative recombination rate coefficient for several temperatures. For a temperature, whole the n_e range may be divided into two regions: the low density region where α_{CR} is almost independent of n_e, and the high density region where it is proportional to n_e. In the former region α_{CR} is given from Fig. 12 by

$$\alpha_{CR} = \sum_{p \geq 1} \beta(p) \qquad (13)$$

and thus may be called "radiative recombination". In the latter, the situation is completely different in high temperature and low temperature. On each curve in Fig. 15, the open circle shows the n_e at which radiative transitions become comparable in magnitude with the corresponding collinal transitions, *i.e.*, $A(2, 1) = C(2, 1)\, n_e$. Thus, in high temperature, *e.g.*, $T_e = 1.28 \times 10^5$ K, to call the recombination mechanism in high density plasma "three-body recombination" may not be entirely incorrect.

In low temperature, at much lower density than the above boundary, the recombination rate coefficient has entered into the high density limit value. (Fig. 15) How is this possible ? The density of Fig. 13, $n_e = 10^{20}$ m^{-3}, falls in this region. If we compare this figure with Fig. 14, the high density limit, we understand the reason. Difference between these figures is in the transitions among the levels below p_B. In the latter case they are the ladderlike deexcitation, and in the former they are the ladderlike deexcitation between p_B and p_G, and radiative decay for levels

below p_G. Both the cases give almost exactly the same recombination flow (proportional to n_e, of course). This means that the effective recombination rate does not depend on the details of deexcitation among the levels below p_B, so long as p_B plays its role in the population kinetics. Thus, starting from low density, with an increase in n_e, Griem's boundary p_G lowers, and when it reaches Byron's boundary p_B, the recombination rate coefficient enters into the high density limit. In Fig. 15 the closed circles show n_e at which

$$p_G = p_B \tag{14}$$

holds, giving the bounday between the low density region and the high density region. The key process that determine the effectrive recombination rate is the population at p_B and the collisional deexcitation from this

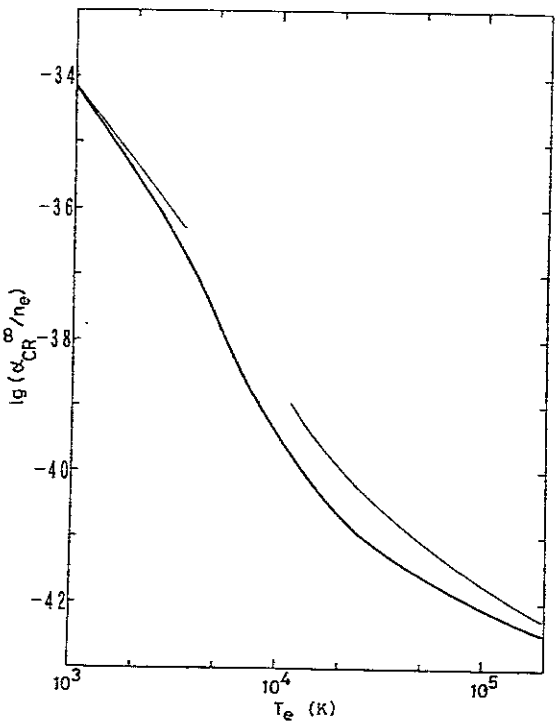

Fig. 16

level to the adjacent lower-lying level. Thus, the effective recombination rate coefficient may be approximated as

$$\alpha_{CR} \sim Z(p_B)\, C(p_B, p_B{-}1)\, n_e \tag{15}$$

where the population at p_B has been approximated to be that in LTE. Figure

16 shows the approximation (15) with the numerical calculation.

As we have seen the recombination mechanism in low temperature is far from straightforward. To call this recombination the "three-body recombination" [8] is misleading.

Ionization balance plasma

We may consider a plasma in ionization balance as a reference standard for real plasmas which we encounter in experiment. It is defined by

$$n_z/n(1) = S_{CR}/\alpha_{CR} \qquad (16)$$

and the excited-level populations are accordingly given by eq. (3).

At low density where all the coefficients, $r_0(p)$, $r_1(p)$, S_{CR} and α_{CR}, are in the low density limit, it has been shown that, in eq. (3), the ionizing plasma component of the population is about one order of magnitude larger than the recombining plasma component. This conclusion is rather general for a wade range of T_e: For T_e = 8 x 10^3 K, the ratio is $n_z/n(1)$ = 3 x 10^{-5}, and the ratio of the recombining plasma component to the ionizing plasma comonent $n_0(p)/n_1(p)$ is 0.1 - 0.7 for $p > 5$. For T_e = 1 x 10^6 K, the ratio is $n_z/n(1)$ = 2 x 10^7, more than 10 orders of magnitude higher. Still $n_0(p)/n_1(p)$ is 0.2 - 1.

In the high density limit the following interrelations hold, *i.e.*,

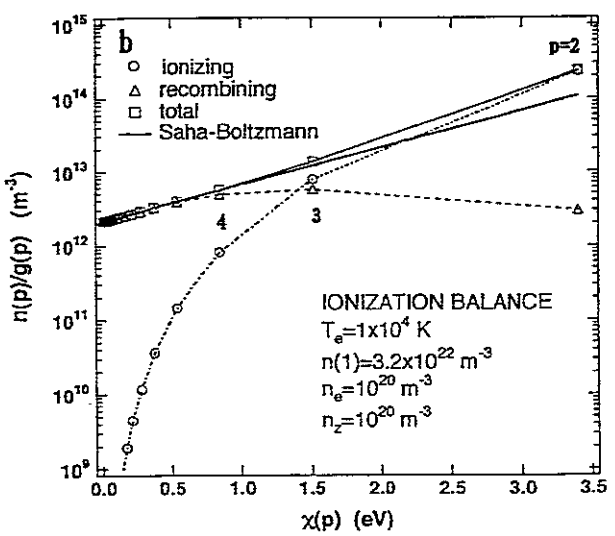

Fig. 17

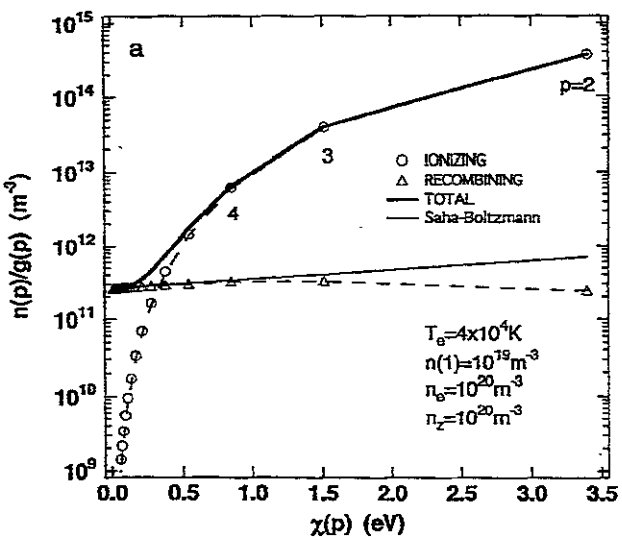

Fig. 18

$$r_0(p) + r_1(p) = 1 \tag{17}$$

and

$$\alpha_{CR} = Z(1)\, n_e S_{CR} \tag{18}$$

Equation (18) ensures the ionization ratio $n_z/n(1)$ to be in the Saha-Boltzmann relationship, and, under this condition, eq. (17) leads to the LTE population in all the excited levels. [3] Figure 17 shows a situation rather close to this case. The LTE population is given by the straight line. The boundaries are $p_B = 2.3$ and $p_G = 2.1$. For higher-lying levels than p_B the recombining plasma component gives the LTE population, while for the lower lying level $p = 2$ the ionizing plasma component is predominant. For level $p = 3$, both the components have similar magnitudes, resulting in a near LTE population.

Ionizing plasma and recombining plasma

It is usual for many real plasmas encountered in our experiment to be out of ionization balance. The above arguments suggest the following: For an ionizing plasma where $n_z/n(1) \ll S_{CR}/\alpha_{CR}$ holds, the ionizing plasma component, $n_1(p)$, tends to predominate over the recombining plasma component, $n_0(p)$. At the same time, the flow of ionization is larger than that of recombination by a factor $[n(1)/n_z] \times [S_{CR}/\alpha_{CR}]$. For a recombining plasma with $n_z/n(1) \gg S_{CR}/\alpha_{CR}$, exactly the opposite statements are valid.

Figure 18 shows an example of a slightly ionizing plasma: $[n(1)/n_z] \times [S_{CR}/\alpha_{CR}]$ is about 10^2. The lower lying levels reveal the ionizing plasma component, as suggested above. On the other hand, for levels lying higher than $p = 7$, the recombining plasma component predominates over the ionizing plasma component. This is because the the minus sixth power distribution, eq. (9). decreases very rapidly with an increase in p. If we measure these populations $n_0(p)$ we can estimate the recombination flow, Fig. 15. However, from the measured populations $n_1(p)$ in the low lying levels, we may estimate the flow of ionization, and we will find that this is 10^2 times larger than the recombination flow, in this example.

As we have suggested earlier, from a measurement of a profile of an

emission line, the excited atoms in level p, $n(p)$, may be decomposed into $n_0(p)$ and $n_1(p)$ according to their temperatures; atoms $n_0(p)$ should have a temperature very close to the ion temperature, while $n_1(p)$ should reflect the atom temperature.

References

1. D.R. Bates, A.E. Kingston and R.W.P. McWhirter, Proc. R. Soc. (London) **267**, 297 (1962).
2. K. Sawada and T. Fujimoto, Phys. Rev. E **49**, 5565 (1994).
3. T. Fujimoto, J. Phys. Soc. Jpn. **47**, 265 (1979).
4. T. Fujimoto, J. Phys. Soc. Jpn. **47**, 273 (1979).
5. T. Kawachi and T. Fujimoto, Phys. Rev. E **51**, 1440 (1995).
6. K. Sawada, K. Eriguchi and T. Fujimoto, J. Appl. Phys. **73**, 8122 (1993).
7. T. Fujimoto, J. Phys. Soc. Jpn. **49**, 1561 (1980); **49**, 1569 (1980).
8. Ya.B. Zel'dovich and Yu.P. Razier, *Physics of Shock and High Temperature Hydrodynamic Phenomena* (Academic Press, New York, 1966) vol.1,

Elastic, excitation, ionization and charge transfer cross sections of current interest in fusion energy research

D.R. Schultz and P.S. Krstić

Physics Division, Oak Ridge National Laboratory, Oak Ridge, Tennessee 37831-6373

Abstract

Due to the present interest in modeling and diagnosing the edge and divertor plasma regions in magnetically confined fusion devices, we have sought to provide new calculations regarding the elastic, excitation, ionization, and charge transfer cross sections in collisions among relevant ions, neutrals, and isotopes in the low- to intermediate-energy regime. We summarize here some of our recent work.

1 Introduction

In pursuit of ever more realistic, accurate models and diagnostic methods for fusion energy research, complete databases of heavy particle cross sections for excitation, ionization, charge transfer, and recombination have been sought for many years. While great progress has been made along these lines, the type of reactions and the collision energy range has been dictated primarily by the need to understand the physics of the central, core plasma in such magnetically confined plasma devices as tokamaks. Contemporary interest in developing so-called "next-step" experimental reactors, such as ITER, however, has highlighted the needed for the study of new atomic and molecular collision regimes. As described in great detail elsewhere [1], engineering and physics issues are focussed on (*i*) the edge plasma, which must be tailored to suppress the ingress of impurities into the core and to entrain them, and (*ii*) the divertor, which will be used for hydrogen recycling and heat (power) and particle (impurities, helium ash) exhaust. Since these plasma regimes are characterized by greatly lower temperatures and higher densities than the core, correspondingly different atomic, and even molecular, reactions play crucial roles.

2 Elastic scattering

Due to these necessarily lower temperatures and higher densities in the edge and divertor regions, significant amounts of neutrals will be present. Since the cross section for elastic ion-ion, ion-neutral, and neutral-neutral scattering can be large compared to the

Figure 1. Comparison of the elastic (Q_{el}) and momentum transfer (Q_{mt}) cross sections for collisions of H^+ with H. Displayed are the present semiclassical method, the fit made by Bachmann and Belitz to their classical approach, and the Massey-Mohr approximation.

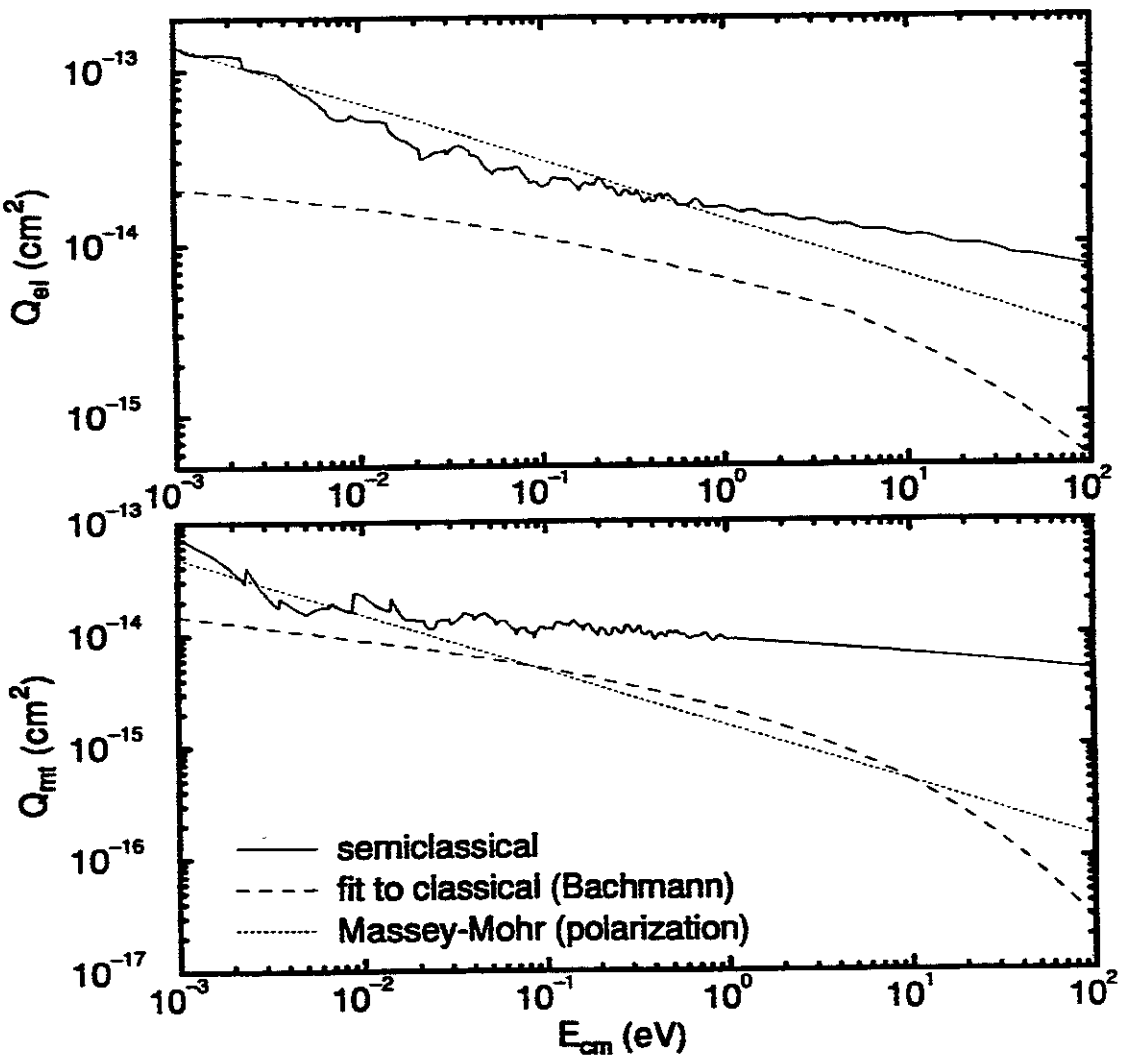

inelastic channels at very low collision energies, these processes play a dominant role in the momentum balance of these regions. In the production of atomic data relevant to fusion energy research, a database for elastic and other cross sections related to transport properties has not been compiled in light of the heretofore heavy emphasis on inelastic, intermediate to high energy collisions. In particular, these slow, neutral particles are important due to their role in radiating and dissipating power and in providing a high recycling region which shields plasma facing components from the high heat and particle fluxes. (For a description of various aspects of modeling neutral gas transport in edge and divertor plasmas, see for example Ref. [2]).

It was therefore our purpose in a recent work [3] to tabulate in a useful way data that can be found in the literature and to provide new calculations of the relevant cross sections where the data is not available, or when it has not be presented in a way which can be readily utilized. A significant contribution to such efforts has been made as well by Bachmann and Belitz [4] who utilized a classical approximation to compute cross sections for proton impact of H, H_2, and He, and for collisions of He^+ with He.

Since the edge and divertor regions will be rich in neutral atomic hydrogen, and molecular hydrogen recycled after recombination at the walls or introduced for fueling, these species have been of primary interest. In addition, since the ash of the fusion process must also be removed at the divertor, significant amounts of helium should also be present. Thus, we considered collisions among the various relevant ions and isotopes of H, H_2, and He. Since the edge plasma temperature is on the order of, say, 10 to 300 eV, and that of the divertor 1-50 eV, we consider center mass collision energies in the range $0.001 \leq E_{cm} \leq 100$ eV. This range accommodates the fact that often the cross sections must be averaged over Maxwellian distributions so that knowledge of the cross section over a slightly larger range is useful. In addition, the extent of this range to the low end often allows a point of comparison to be made with data of astrophysical interest, and thus an additional benchmark.

For example, in Figure 1 we present the result of our (semiclassical) calculation of the elastic cross section compared with the classical approach of Bachmann and Belitz noted above and with the simple Massey-Mohr approximation. A very accurate quantum mechanically solution to the elastic scattering and charge transfer problem in the energy range of interest has been provided for $H^+ + H$ and [5, 6] and for $H^+ + D$ and $D^+ + H$ [7] by Hunter and Kuriyan. These works provided a benchmark for the development of our semiclassical approach, and we find very good agreement with the phase shifts they tabulated extensively [5]. In addition, we find good agreement with the elastic and charge transfer total and differential cross sections contained in these works. In addition, quite recently, Hodges and Breig [8] have performed numerical integrations of the radial Schrödinger equation for Hunter and Kuriyan's potential energy curves, and confirm their results independently. Our semiclassical results agree very well with their published elastic, momentum transfer, and charge transfer cross sections.

Furthermore, other related cross sections are actually of greater practical use. They

Figure 2. The elastic, momentum transfer, viscosity, and charge transfer cross sections for $H^+ + H$ along with smooth fits.

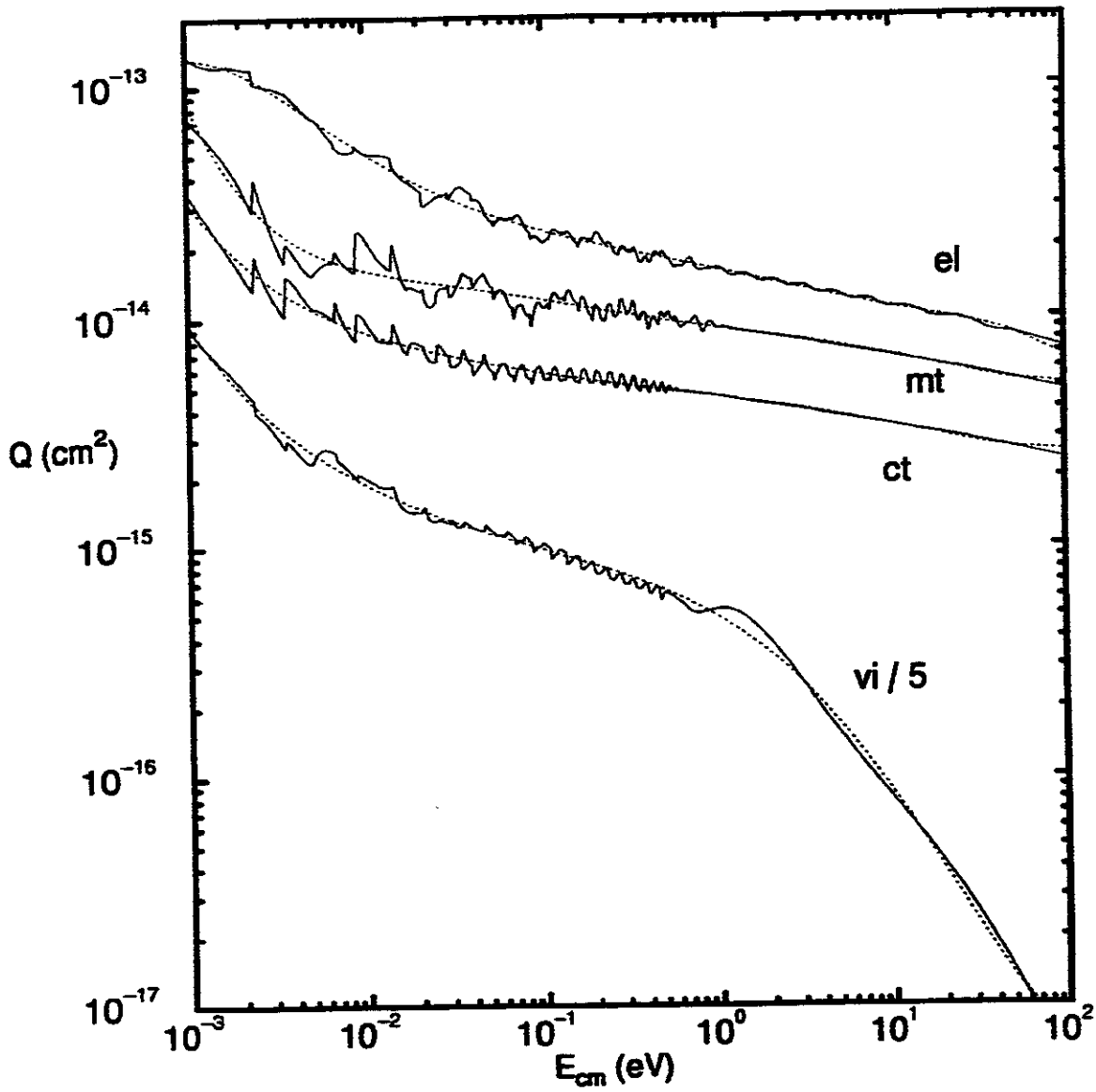

may be measured through various parameters of the gas or plasma transport (see e.g. Ref. [9]) or calculated from the elastic differential cross section. Of these, we will be particularly concerned with the momentum transfer (Q_{mt}) and viscosity (Q_{vi}) cross sections.

One of the most important fundamental quantities in the study of the mobility and diffusion of neutral or charged particles in a gas or plasma is the momentum transfer cross section, Q_{mt}, defined by

$$Q_{mt} = \int (1 - cos\theta) \frac{d\sigma_{el}}{d\Omega} d\Omega \tag{1}$$

$$= 2\pi \int_0^{\pi} (1 - cos\theta) \frac{d\sigma_{el}}{d\Omega} sin\theta d\theta \ . \tag{2}$$

To see how this quantity is related to momentum transfer, consider the elastic collision between two particles a and b. The linear momentum of particle a is simply μv_a. If θ is again the center of mass scattering angle, the change in the forward momentum of the particle is $\mu v_a(1 - cos\theta)$. Thus, Q_{mt} is a measure of the average forward momentum lost in such collisions. Since backscattering retards the diffusion of particles in a gas or plasma, this loss of forward momentum thus determines the rate of diffusion and therefore Q_{mt} is often referred to as the "diffusion cross section." Other important measures may be defined in terms of Q_{mt}, such as the momentum transfer mean free path, collision frequency, and fractional energy loss per collision [9].

If the elastic differential cross section is dominated by forward scattering, then owing to the factor $(1 - cos\theta)$ in the definition of the momentum transfer cross section, $Q_{el} > Q_{mt}$. Conversely, if backscattering dominates, $Q_{mt} > Q_{el}$. If the elastic cross section diverges as $\theta \rightarrow 0$, this factor may lead to a finite value of Q_{mt}.

Inversely related to the heat conductivity and viscosity of a gas or plasma is the "viscosity cross section." It too is defined as the integral over solid angle of the elastic differential cross section, weighted by a factor of $sin^2\theta$ instead of $(1 - cos\theta)$. Thus,

$$Q_{vi} = \int sin^2\theta \frac{d\sigma_{el}}{d\Omega} d\Omega \tag{3}$$

$$= 2\pi \int_0^{\pi} sin^3\theta \frac{d\sigma_{el}}{d\Omega} d\theta \ . \tag{4}$$

Since the $sin^2\theta$ factor is maximum at $\theta = \pi/2$ and goes to zero for $\theta \rightarrow 0$ or π, this factor emphasizes scattering near $\pi/2$ while deemphasizing either forward or backward scattering. Collisions resulting in scattering to center of mass angles near $\pi/2$ are more effective in inhibiting conductivity since such collisions tend to equalize the energy, and therefore, the greater the rate of collisional equalization of energy, the smaller the viscosity and heat conduction. Clearly, if the elastic differential cross section is dominated by forward scattering, the viscosity cross section is much smaller than the elastic total cross section.

Figure 2 shows our computed elastic, momentum transfer, viscosity, and charge transfer cross sections, along with smooth fits which are needed by modeling codes. These fits

Figure 3. The potential energy curves, elastic differential cross section, and the elastic and related transport total cross sections for Be^{2+} + H.

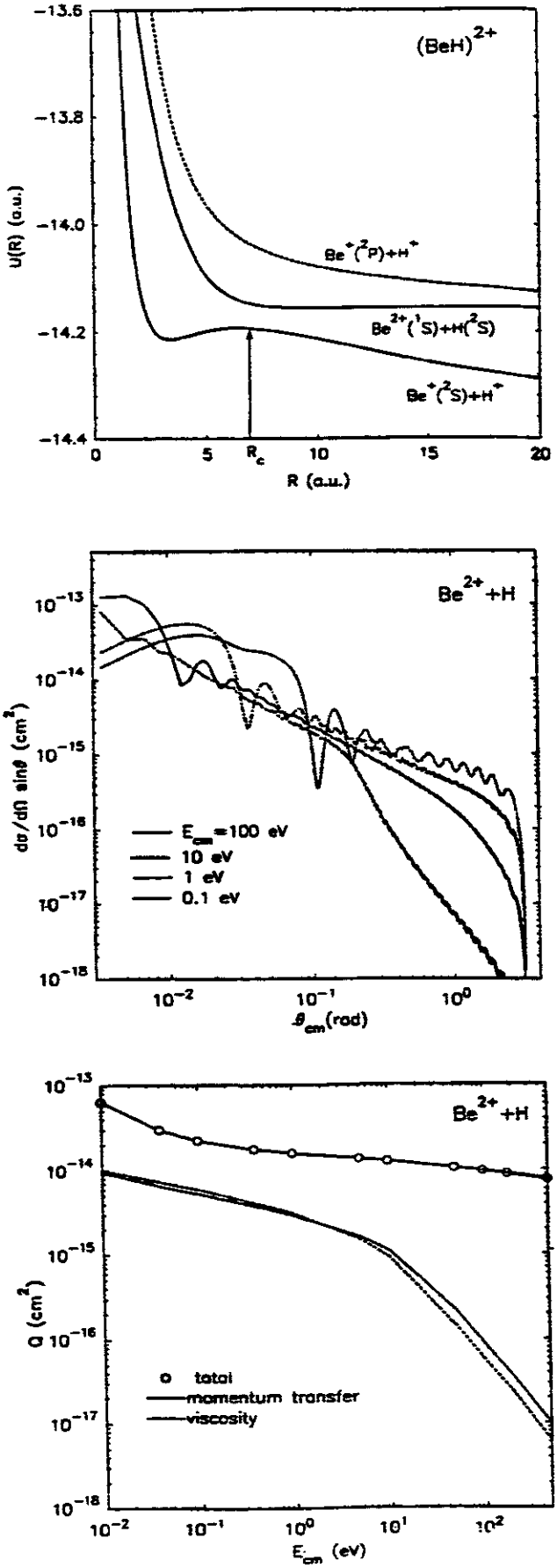

Figure 4. Preliminary result for elastic scattering from the ground and low-lying vibrationally excited states of H_2 by proton impact.

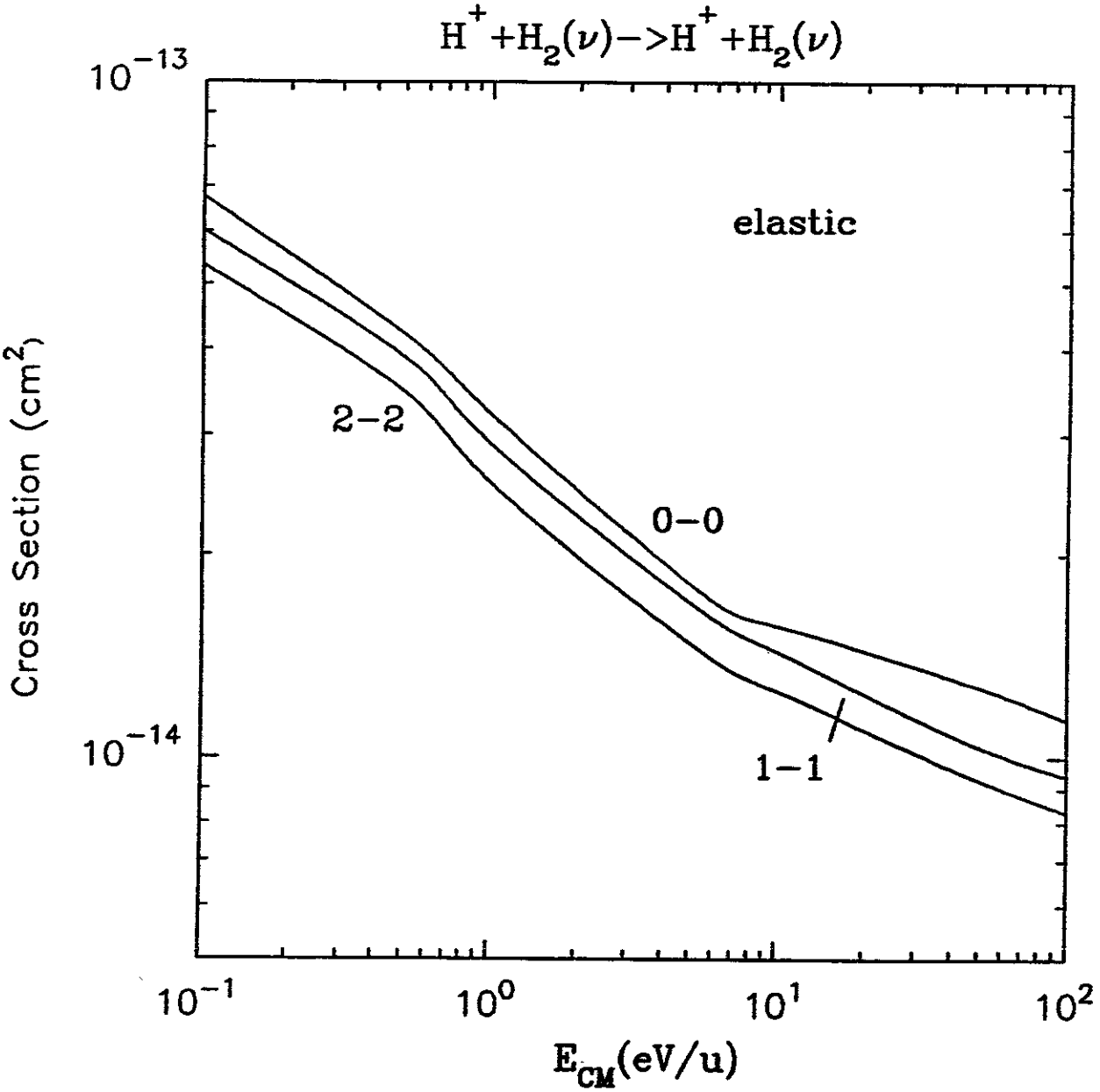

are tabulated, along with similar results for H + H, H + He, and other systems in Refs. [3, 4].

Other collision systems of current interest involve beryllium and its ions. Beryllium is a potentially useful plasma facing component since it is of low-Z, and therefore engenders low deleterious radiation losses, and has good physical/chemical properties. Therefore, beryllium neutrals and ions will be present in the divertor which may be lined with this material. Calculation of the elastic and transport cross sections requires accurate potential energy curves for the ground and low-lying states of $(BeH)^{q+}$. Such calculations are presently the object of state-of-the-art approaches. Therefore, we have applied an unrestricted Hartree-Fock calculation using Gaussian bases and a subsequent single configuration interaction approach to fill in the gaps in existing accurate data for these potentials. Finally, to facilitate our one- and two-state calculations of the elastic phase shifts, we have fit these potentials using a 6-parameter formula. This procedure and our results for scattering of Be^{2+}, Be^{+}, and Be from H are given in a recent article [10] and in Figure 3 we display the potential energy curves, typical differential cross sections, and the total elastic, momentum transfer, and viscosity cross sections for Be^{2+} + H.

Also of particular interest recently is the elastic and related transport cross sections for protons colliding with H_2. Slow collisions of these species will be quite prevalent in the divertor as hydrogen plasma is neutralized, partly through recombination on the walls. In order to calculate elastic cross sections for scattering of protons on H_2 molecules in various initial vibrational states, an Infinite Order Sudden Approximation (IOSA) was used. In effect, rotational motion of the H_2 molecule is considered frozen during the collision, allowing averaging of the cross sections obtained for fixed H_2 orientations. Adiabatic surfaces $U(R, \rho, \gamma)$ were calculated *ab initio* using the quantum chemistry program package GAMESS in its RHF-Full CI options, with 54 S, P Gaussian basis states. The calculation is done for 5200 geometrical configurations of H_3^+, varying R in the range from 60 to 0 a.u., and ρ from 0.6 to 5.4 a.u., for $\gamma = 0°, 30°, 60°$, and $90°$. The semiclassical phase shifts η_l were calculated for each fixed (ρ, γ) combination $(0 \leq l \leq 3000)$, thus forming the ρ—dependent scattering amplitude. For each H_2 orientation, the amplitude was averaged over the normalized wave function of the relevant vibrational state ν. Finally, the resulting differential and total elastic cross sections were averaged over the full solid angle of the H_2 orientations. Results of these calculations will be published soon and in Figure 4 we present our preliminary result for the elastic cross section.

3 Ionization in collisions of H with H

Owing to the relatively low plasma temperatures of the edge and divertor regions and to conditions present in certain astrophysical environments, recent interest has turned to ionization in slow collisions of H with H. To treat this collision system, we have generalized the method of hidden crossings [11] to treat mutlielectron, multicenter systems utilizing molecular Hartree-Fock and single configuration interaction methods extended into the

Figure 5. Single ionization in H + H collisions. Displayed are results of the multicenter, multielectron hidden crossings approach (solid line), measurements by Gealy *et al.* (diamonds) and by McClure (squares), theoretical results of Shingal *et al.* (dash-dot line), and Shingal *et al.*'s correction for simultaneous ionization of one electron and excitation of the other (dashed line).

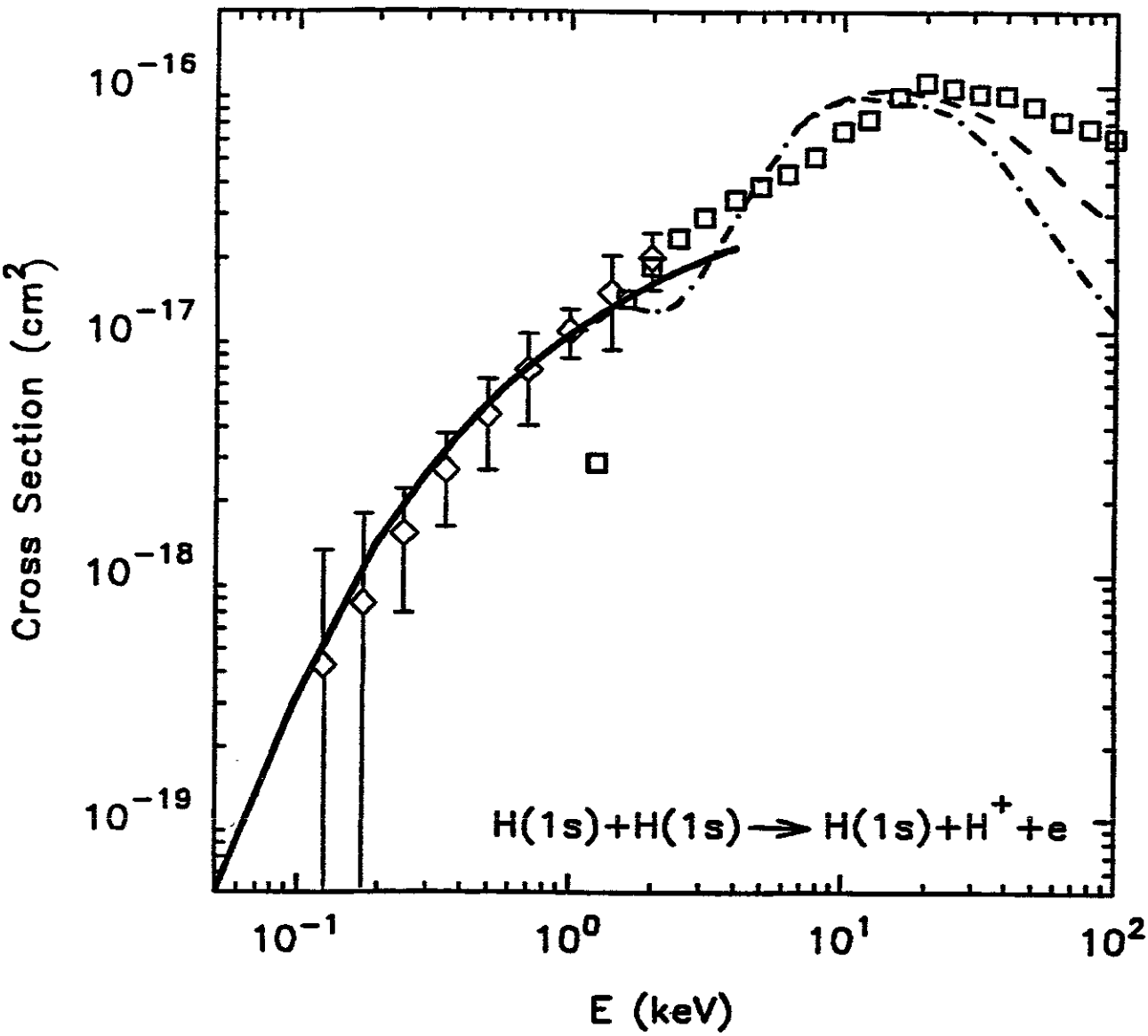

Figure 6. Excitation to the n=2 level of H by He^{2+} impact. Along with our CTMC result (dashed line), shown are atomic orbital (solid line, Fritsch *et al.*) and molecular orbital (dotted line, Errea *et al.*) results. Arrows indicate the peak positions predicted on the basis of a simple timing model presented in a forthcoming manuscript.

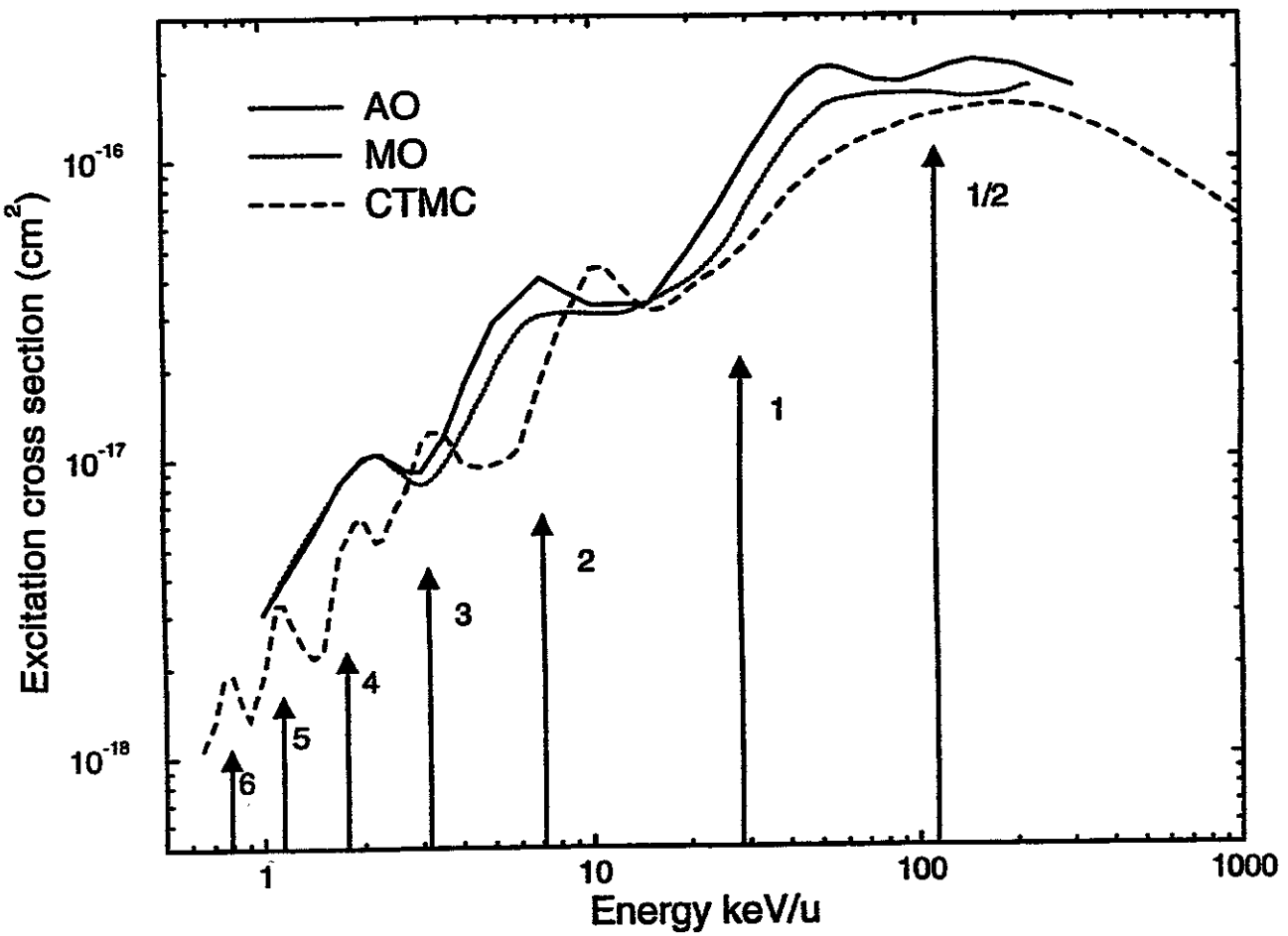

complex plane of internuclear separation. In brief, this method identifies the positions in the complex plane at which the promotion between electronic states (possibly the continuum) is strongly isolated, and thus can predict the probability of transitions. This recent work was the first in which diabatic promotion to the continuum in a two-center, two-electron system was shown. Excellent agreement with experiment was found regarding ionization in 50 to 1000 eV H + H collisions (see Figure 5).

4 Other inelastic collisions

As mentioned above, since beryllium is often used and proposed for plasma-facing components, its inelastic collisions with principle plasma species are important to quantitatively understand so that they maybe taken into account in plasma models. Furthermore, since charge exchange recombination spectroscopy has proven extremely useful in diagnosing the transport properties of the plasma and other characteristics, tabulations of the state-selective charge transfer cross section are often required by diagnostians. Thus, we have recently computed over a wide range of energies the excitation, ionization, and state-selective charge transfer cross sections for Be ions colliding with atomic and molecular hydrogen [12]. We have also carried out a similar study for neon ions [13] since this species may be puffed into the divertor in order to beneficially increase the radiated energy, thereby decreasing the power load directly on the divertor plates. In addition, frozen pellets of moderate-Z materials such as neon have been proposed as so-called "killer pellets" to quench the plasma quickly in the event of a disruption.

In these recent works we tabulate extensively the state-selective charge transfer cross section and compare our inelastic cross sections computed with the classical trajectory Monte Carlo (CTMC) technique with other available theoretical results and with experiment. By and large such other data does not exist. In addition to the rather routine tabulation of needed results, these works often provided surprises which proved quite interesting. For example, in both works we found oscillations of the excitation cross section at around 10 keV/u with the CTMC method which to our knowledge have never been seen before. We found that previous atomic orbital close coupling calculations also displayed this feature, but left the physical mechanism underlying its formation essentially undetermined. This has lead to much more detailed work to elucidate such a mechanism and is the subject of a manuscript in preparation. In Figure 6 we illustrate this oscillation for excitation in He^{2+} + H collisions where extensive atomic orbital calculations have been made by Fritsch *et al.* [14].

Acknowledgements

The authors gratefully acknowledge the support for this work by the U.S. D.O.E, Office of Fusion Energy Sciences in a grant to Oak Ridge National Laboratory, managed by Lockheed Martin Energy Research Corp. under contract number DE-AC05-96OR22464.

References

[1] R.K. Janev, in: *Review of Fundamental Processes and Applications of Atoms and Ions* (C.D. Lin, ed.), World Scientific, Singapore (1993).

[2] D. Reiter, in: *Atomic and Plasma-Material Interaction Processes in Controlled Thermonuclear Fusion* (R.K. Janev and H.W. Drawin, eds.), Elsevier Science Publishers (1993).

[3] D.R. Schultz, S.Yu. Ovchinnikov, and S.V. Passovets, *Elastic and Related Cross Sections for Low-Energy Collisions among Hydrogen and Helium Ions. Neutrals, and Isotopes*, in: *Atomic and Molecular Processes in Fusion Edge Plasmas*, edited by R.K. Janev (Plenum, New York, 1995) p. 279.

[4] P. Bachmann and H.J. Belitz, *Elastic Processes in Hydrogen-Helium Plasmas: Collision Data*, Max Planck Institut für Plamsaphysik Report IPP 8/2 (1993).

[5] G. Hunter and M. Kuriyan, Proc. Roy. Soc. (London) A **353**, 575 (1977).

[6] G. Hunter and M. Kuriyan, At. Data. Nucl. Data Tables **25**, 287 (1980).

[7] G. Hunter and M. Kuriyan, Proc. Roy. Soc. (London) A **358**, 321 (1977).

[8] R.R. Hodges and E.L. Breig, J. Geophysical Res. **95**, 7697 (1991).

[9] E.W. McDaniel, *Collision Phenomena in Ionized Gases*, John Wiley, New York (1964); *Atomic Collisions: Electron and Photon Projectiles*, John Wiley, New York (1989); *Atomic Collisions: Heavy Particle Projectiles*, John Wiley, New York (to be published).

[10] P. Krstić, D.R. Schultz, and G. Bent, Physica Scripta **T62**, 21 (1996).

[11] P. Krstić, G.Bent, and D.R. Schultz, Phys. Rev. Lett. **77**, 2428 (1996).

[12] D.R. Schultz, P.S. Krstić, and C.O. Reinhold, Physica Scripta **T62**, 69, (1996).

[13] D.R. Schultz and P.S. Krstić, Atomic and Plasma-Material Interaction Data for Fusion **6** (1996).

[14] W. Fritsch, R. Shingal, and C.-D. Lin, Phys. Rev. A **44**, 5686 (1991).

Low energy heavy particle collisions relevant to gas divertor physics

Kunizo Onda

Science University of Tokyo

Abstract

Cross sections for rotational and vibrational excitations of H_2 molecules caused by impact of electron, proton, H atom, H_2, H_2^+, or H^- are compared with one another and reviewed for rotational excitations by examining an interaction potential between collision partners. It is pointed out what are difficulties in theoretical approaches to collision of atoms with H_2 molecules initially in vibrationally and rotationally excited states. A theoretical approach developed by our group, which aims quantum mechanically to investigate vibrationally inelastic scattering, exchange reaction, or dissociation of molecule in vibrationally excited states collided with an atom or its ion, is presented. Newly obtained dissociation cross sections of H_2 in vibrationally excited states by He impact are presented and compared in magnitude with those of H_2 caused by electron impact.

1. Introduction

It is estimated[1] that gas temperature is in the range of several eV and number density of particles is in the order of $10^{15} \sim 10^{16}$ cm^{-3} at the most interesting part in gas divertor plasmas. In these physical conditions, atomic and molecular collision processes play crucial roles in exhausting enormous power flowed from edge or scrape-off layer(SOL) plasmas. Hydrogen atoms in these relatively high density regions are easily recombined into molecular form on divertor plates. It is expected that newly formed hydrogen molecules are predominantly abundant in number density over any other molecules, and are in rotationally and vibrationally excited states. Radiative lifetime of these excited states is known to be $10^5 \sim 10^6$ s, because the hydrogen molecule has no permanent electric dipole moment.

According as the rotational or vibrational states are excited higher, so a size of the molecule extends larger. Thus, it is easily imagined that any cross section is large for collision of molecules in excited states with any kind of projectiles. Therefore, it is very important to investigate collision processes related to hydrogen molecules, which are most abundant in number density among many species of molecules and are to be in rotationally and vibrationally excited states. The energy range in these collision processes interested in gas divertor plasmas is specifically below several tens of eV. In section 2, we review collision cross sections for rotational and vibrational excitations of the molecular hydrogen caused by impact of different kind of projectiles, such as electron, H atom, H_2, H_2^+, or H^-, and these cross sections are compared in magnitude with one another. In section 3, we

point out difficulties in theoretical approaches to nonreactive, reactive, and dissociative collisions between atoms and diatomic molecules in vibrationally highly excited states and present our new theoretical procedure to overcome these difficulties. Cross sections for dissociative collision of the hydrogen molecule with electrons are compared in magnitude with those caused by impact of He atoms in section 4. Concluding remarks are made in section 5.

2. Review of cross sections for rotational and vibrational excitations of molecular hydrogens

Reliable collision cross sections seem to be available as compiled by Phelps[2] for the hydrogen molecule in the rotationally and vibrationally ground state caused by impact of different kind of projectiles. These cross sections are very important to estimate the amount of reliable energy transfer through collisions between atoms, molecules, or their ions and molecular hydrogens. In order to grasp the magnitude of these cross sections, we review in this section rotational and vibrational excitation cross sections of the molecular hydrogen caused by impact of electron, proton, hydrogen or helium atom, molecular hydrogen, or molecular hydrogen ion.

2.1. Rotational excitations

Rotational excitation cross sections of para hydrogen molecules caused by impact of different projectiles are compared with one another in Fig. 1. Data of the electron impact are most reliable, because the experimental values[3,4] (shown by a dashed line with a character e) agree well with theoretical results.[5,6]

As can be seen from Fig. 1, protons are most effective in exciting rotational states from its ground state at the collision energy below several eV in a laboratory frame. The magnitude of proton impact cross sections (recommended values compiled by Phelps[2] based on the very limited experimental results obtained by Linder[7]) is bigger than those caused by other projectiles by a factor of about $10^2 \sim 10^3$ at the collision energy of 0.1 eV and by a factor of about 10 at 1 eV. The results of the proton impact (shown by solid circles) are theoretically obtained by Gianturco and Tritella.[8]

Cross sections of the He impact (represented by symbols + along with a character He) are theoretically obtained by McGuire and Kouri[9] and McGuire.[10] Data of the H_2 impact (shown by a long dashed line along with a character H_2) are theoretically obtained by

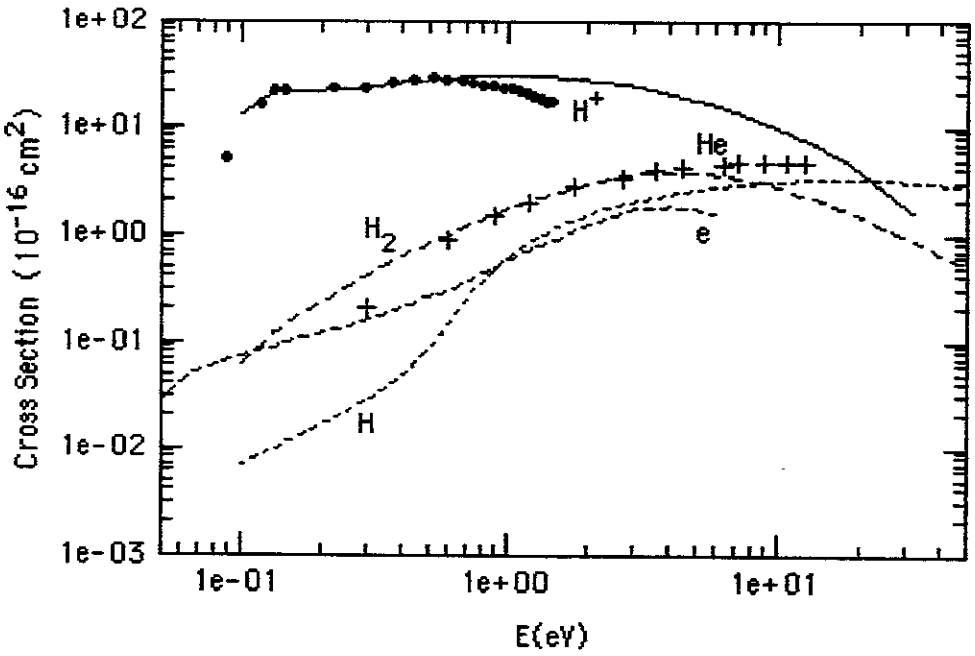

Figure 1. Rotational Excitation of H_2(J=0->2)

Green, Ramaswamy, and Rabitz[11] in the energy range below 4 eV and are estimated by Phelps[2] above 4 eV. It is worthwhile to point out that the magnitude of cross sections for rotational excitation caused by the He impact is almost the same as that caused by the H_2 impact above about 0.6 eV. Buck's group[12] intensively studied rotational excitations of H_2 molecules by impact of H_2 and those caused through collision between their isotopic variants. Cross sections of the H atom impact (shown by a dotted line along with a character H) are theoretically obtained by Green and Truhlar.[13]

Cross sections for rotational excitation of ortho molecular hydrogens are represented in Fig.2. At the collision energy below 1 eV, the biggest cross section is brought by the proton impact (recommended values[2] based on the experimental results[7]) shown by a solid line as the case of the para hydrogen molecule. Results obtained theoretically by Schinke[14] are shown by open squares. Both results reasonably agree with each other, and establish confidence of these data.

Data of the H^- impact represented by solid squares are determined experimentally by Müller, Zimmer, and Linder,[15] whose results are summed over final rotational states, that is, the total rotational excitation cross section. As they mentioned in their paper,[15] the absolute magnitude is not completely settled yet.

Cross sections of the electron impact obtained by Gibson[16] are represented by a dashed line and those determined by Linder and Schmidt[4] are denoted by open circles. These

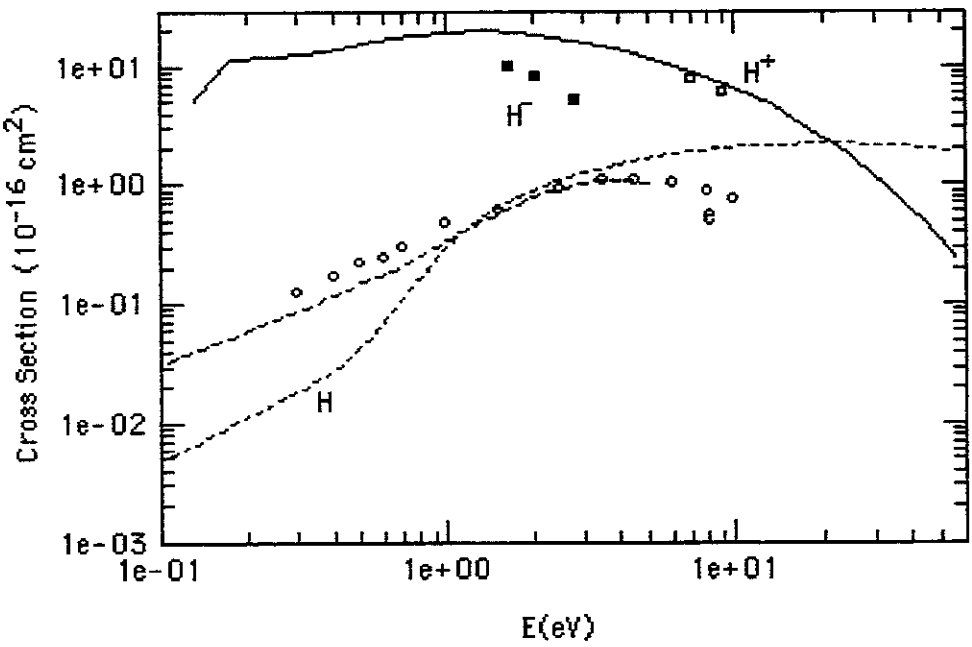

Figure 2. Rotational Excitation of H_2(J=1->3)

results agree reasonably well with theoretical ones.[5,6] Therefore, these cross sections are reliable.

Data of the H atom impact are theoretically obtained by Green and Truhlar.[13] It is expected in gas divertor plasmas that the hydrogen atoms and molecules are most abundant in number density and collisions between them are very frequent. Since this collision system should be important in gas divertor plasmas and astrophysical application, it is highly desirable to investigate further, and to compile reliable cross sections for rotational excitations.

In order to understand the magnitude of these cross sections from the physical point of view, we examine the magnitude of an interaction potential between the proton, atomic hydrogen, or electron and the molecular hydrogen. The interaction potential is expanded in terms of Legendre polynomials, and its lowest three coefficients are compared with one another as a function of the radial distance between the center of mass of the hydrogen molecule and the projectile. The bond length of H_2 in the ground state is fixed at its equilibrium value of 1.4 a_0. For the proton and molecular hydrogen system,[8,14,17] V_0 term has a well of depth about 3.5 eV at the radial distance 1.8 a_0, which shows existence of a stable H_3^+ molecular ion. In the outer region beyond the radial distance of 5.5 a_0, V_2 term becomes positive because of the interaction between a positive charge and a permanent electric quadrupole moment, though an interaction potential between a charge

and an induced electric dipole moment is attractive in this region. On the other hand, in the hydrogen atom and molecule system,[18] the major three components V_0, V_2, and V_4 are almost entirely repulsive except for very weak attractive parts seen in the expansion coefficients of Legendre polynomials higher than 0, and a long range interaction is negligibly weak compared with the one between the charged particle and the molecular hydrogen. The interaction potential between the electron and molecular hydrogen[5,6] is much stronger than that between the proton and hydrogen molecule. A reduced mass between the electron and H_2 is much smaller than the one between an atom and H_2. Therefore, the number of partial waves contributing to rotational excitations of H_2 by electron impact is not so many compared with that for the atom and H_2 system.

The cross section of rotational excitation of H_2 caused by the proton impact has the very weak energy dependence at the energy below about a few eV as seen from Figs. 1 and 2 above. Since such energy dependence can be estimated by applying the Born approximation to the long range interactiont between the charge and electric quadrupole moment, it seems that this long range interaction dominates over any other interactions. If this interpretation is true, it is very probable that much larger cross sections for rotational excitations of the molecular hydrogen are brought by impact of a hydrogen negative ion. The reason is that the long range interaction between the charge and quadrupole moment is the same as the one between the electron and molecular hydrogen and is stronger than the one between the proton and molecular hydrogen. Although it is not fully investigated yet experimentally or theoretically for rotational excitations of the hydrogen molecule by impact of the hydrogen negative ion, Müller, Zimmer, and Linder[15] measured the total rotational excitation cross sections at three impact energies as shown by solid squares in Fig. 2. The cross sections of the H^- impact are smaller than those of the H^+ impact. This means that the long range interaction is not the main interaction.

The results obtained by Gianturco and Tritella[8] tell us that the strong anisotropic interaction is effective to excite the rotational state for partial waves below about 40 in the unit of $\hbar$. It is possible that the strong isotropic attractive V_0 term pulls the proton inside the strong anisotropic interaction region. In these cases, it is understandable that many higher partial waves contribute to the cross sections for rotational excitations compared with cases of collision systems with other partners, in which a strong isotropic attractive well does not exist. Since these rotational excitation cross sections are so large, it is important to reinvestigate rotational excitation of H_2 caused by impact of the proton or

the hydrogen negative ion.

2.2. Vibrational excitations

We now turn to vibrational excitations of the molecular hydrogen. Cross sections for the vibrational excitation from $v = 0$ to $v\prime = 1$ of H_2 caused by different kind of projectiles are shown in Fig. 3. Cross sections of the H atom impact represented by a dotted line

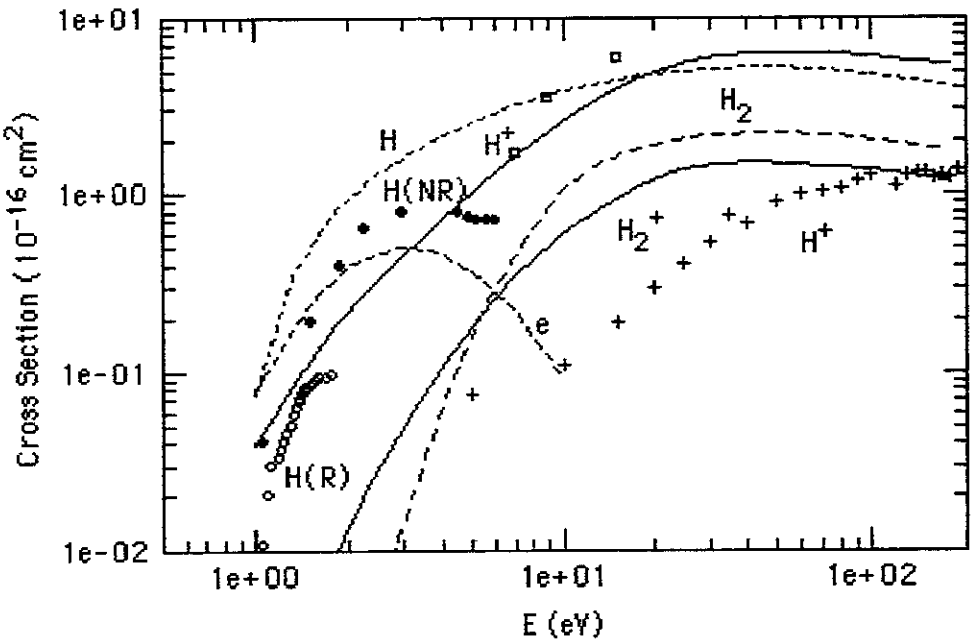

Figure 3. Vibrational Excitation of H_2 (v = 0->1)

along with a character H are recommended values of Phelps.[2] Reactive cross sections are the results obtained by Zhang and Miller,[19] whose results are represented by open circles along with a character H(R). Their results are partly confirmed by other theoretical works.[20,21] Cross sections for nonreactive vibrational excitations are obtained theoretically by Onda, Iwai, and Wada,[22] whose results are shown by solid circles along with a character H(NR). The magnitude of reactive cross sections is smaller than that of nonreactive cross sections by a factor of $2 \sim 4$. Therefore, it is probable that coupling between different arrangement channels is weak. Rearrangement channels are not considered in their treatment and coupling among rotational states is also neglected. Therefore, their results can be overestimated, even if it is expected that coupling among different arrangement channels and the one among rotational states in different vibrational states are not so effective to nonreactive vibrational excitations.

Data of the H^+ impact shown by a solid line along with a character H^+ are recom-

mended values of Phelps[2] based on the results experimentally obtained by Gentry and Giese.[23] These results are reasonably reproduced at three impact energies by Schinke,[14] whose results are represented by open squares. Symbols + along with a character H^+ show the experimental results measured by Herrero and Doering,[24] but it seems that their results are too small compared with the results[2,14,23] mentioned above for the H^+ impact.

Cross sections of the electron impact are represented by a dashed line along with a character e. These results are experimentally determined by Ehrhardt *et al.*,[25] and the magnitude of these cross sections is theoretically confirmed.[26,27] As pointed out by Morrison *et al.*,[28] the difference between the results of Crompton *et al.*[3] and those of Morrison *et al.*[28] is not disregarded, and causes unsolvable problems in swarm analyses.

Results of the H_2 impact (shown by a long dashed line along with a character H_2) and those of the H_2^+ impact (represented by a solid line with H_2^+) are estimated by Phelps.[2] Since these collision systems should be important in gas divertor plasmas, more works are surely required for collision of H_2 with H_2 or H_2^+. In the collision of H_2^+ with $H_2(v)$ as measured by Shao and Ng,[29] the formation cross section of H_3^+ in the energy range below several eV seems to reach the maximum value predicted by Langevin[30] and Gioumousis and Stevenson[31] models. As the collision energy is increased above about 10 eV, the cross section for the charge transfer $H_2(v\prime) + H_2^+$ dominates over those for any other processes. Therefore, it is understandable that the cross sections of rotationally and vibrationally inelastic scattering can be small for collision of H_2 with H_2^+. But, it is not well understood yet what are the physically meaningful branching ratios among energetically accessible channels, such as H_3^+ formation, charge transfer, rearrangement, and nonreactive inelastic scatterings. Although it is thought that this is qualitatively understood by examining potential energy surfaces, it must be answered quantitatively by taking into account collision dynamics between $H_2^+ + H_2(v)$.

Cross sections for the vibrational excitation from $v = 0$ to $v\prime = 2$ of H_2 caused by different kind of projectiles are represented in Fig. 4. Cross sections of the H^+ impact represented by a solid line along with a character H^+ are recommended values of Phelps,[2] and open squares are results theoretically obtained by Schinke.[14] Symbols + along with a character H^+ show the experimental results measured by Herrero and Doering,[24] but it seems that their results are too small compared with two results[2,14] of the H^+ impact mentioned above.

Solid circles along with a character H(NR) are results of the H atom impact obtained

by Onda, Iwai, and Wada.[22] Although coupling among rearrangement channels seems weak as mentioned before, it is probable that their results are overestimated for these cross sections.

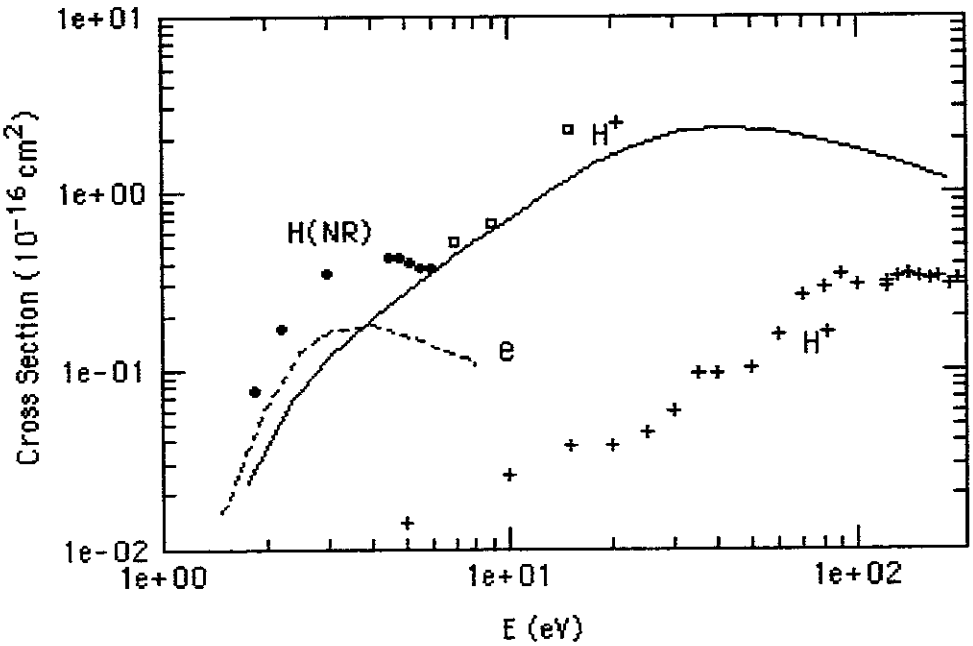

Figure 4. Vibrational Excitation of H_2 (v=0->2)

Results of the electron impact measured by Ehrhardt*et al.*[25] are represented by a dashed line along with a character e. The magnitude of the experimental results[25] does not agree with those obtained theoretically[27] for this excitation. In order to settle the absolute magnitude of these cross sections, it is desirable to investigate further experimentally and also theoretically.

As can be understood from comparison of this figure with Fig. 3, more works are surely required for the other projectiles not being presented here.

3. Review of theoretical approach to collision of atoms with diatomic molecules in vibrationally highly excited states

We very briefly review theoretical approaches based on quantum mechanics to collision of an atom with a diatomic molecule in the electronically ground state and the vibrationally and rotationally excited states. Although there are many investigations (see review articles[32]) of nonreactive scattering and exchange reaction for the target molecule initially in the vibrational ground state or its first excited state, there is few works of

these collision processes for the target molecule initially in vibrationally highly excited states and of collision induced dissociation as well. In order to clarify what are difficulties in theoretical approaches to these collision processes, let us consider vibrational and rotational excitation processes of diatomic molecules caused by the atom impact at the collision energy below the dissociation threshold of the molecule. The number of coupled channels in vibrational and rotational states is calculated by the expression

$$\sum_{v=0}^{v_{max}} \sum_{j=0}^{j_{max}^{v}} (2j+1) = \sum_{v=0}^{v_{max}} (j_{max}^{v}+1)^2,$$

where v_{max} is the quantum number of the highest vibrational state energetically accessible at some collision energy and j_{max}^{v} is the quantum number of the highest rotational state in the vibrational state of the quantum number v. We take up the simplest collision system such as H + H_2 as an example at the collision energy close to the dissociation threshold. It is known that the number of coupled states is more than 1500, if reaction channels through exchange of atoms are included. If we make use of the close coupling method to investigate these collision processes, we have to solve numerically these coupled equations. It is impracticable at this moment to solve such a huge number of coupled equations. This is one reason why collision of atoms with molecules in the vibrationally highly excited states is theoretically not fully studied yet.

In order to understand how strong the coupling among vibrational states is, we studied vibrationally inelastic scattering without taking account of coupling among different rearrangement channels[22,33] for the collision system of H + H_2, in which the interaction potential surface is accurately represented in an analytic form.[18] In cases of the target molecule in vibrationally highly excited states, we have to include continuum states to obtain converged results for vibrational excitation processes as made clear separately by Scherzinger and Secrest[34] and Onda,[33] even if the collision energy is below the dissociation threshold of the molecule. This is another reason why collision dynamics of molecules in the vibrationally highly excited states is very rarely investigated. As shown by Onda,[33] the total cross sections for vibrationally inelastic scattering are in the order of 10^{-15} cm^2 for H + $H_2(v)$ with $v \geq 8$ at the collision energy above about 1 eV. Since these cross sections are to be large, it is important to investigate thoroughly collisions related to H_2 in vibrationally excited states and to determine the magnitude of cross sections for elastic and inelastic scattering and exchange reactions.

Now let us mention very briefly the works of dissociation of molecules caused by

impact of atoms. Previous quantum mechanical studies for collision induced dissociation are divided into two categories, that is, a time-dependent method[35] and a time-independent one.[36] Theoretical studies are not matured yet for collision induced dissociation of molecules initially in vibrationally excited states. Although there are a few quasi-classical trajectory calculations[37,38,39] for realistic collision systems, reliable theoretical investigations are very rare. On the other hand, there are several experimental studies,[40] in which vibrational enhancement is one of noticeable characteristics, and the vibrational state investigated in experiments is up to $v = 7$. Vibrational enhancement in reactive cross sections at the collision energy below the dissociation threshold is partly reproduced by the theoretical work made by Miller's group.[41]

In order to overcome the difficulties mentioned in the first two paragraphs of this section, we developed a new approach[42] to investigate quantum mechanically collision between the atom and diatomic molecule, in which channels of elastic and inelastic scattering, atom exchange reaction, and dissociation of the molecule strongly couple with one another during collision. We briefly introduce our theoretical procedure here. Schrödinger equation describing the collision system is represented by using mass scaled Jacobi coordinates. This Schrödinger equation is transformed into the one represented by hyperspherical coordinates. Dissociative continuum states are automatically discretized in the hyperspherical coordinates, even if the dissociative states of the molecule are continuum in the Jacobi coordinates. This is one advantage of the hyperspherical coordinates over the Jacobi ones in treating collision processes including double continuum states as pointed out by Delves.[43] A two variable partial differential equation (PDE) is derived from Schrödinger equation describing the collision dynamics. In order to solve directly the PDE, we make use of a finite difference formula[44] combined with a discrete variable representation.[45] This method intends to overcome the difficulties encountered with the close coupling method in the Jacobi coordinates, in which the number of coupled channels is in principle infinite and by which collision dynamics cannot be studied, because nonreactive, reactive, and dissociative channels couple strongly with one another. This new approach is applied to collision of He with $H_2^+(v)$ in a collinear configuration, and numerical accuracy of this method is confirmed by comparison of our results with those obtained by previous investigations at the collision energy below dissociation threshold (see ref. 46 in detail).

4. Dissociation cross sections of H_2 molecules

Electron impact dissociation of H_2 molecule in the vibrationally excited states are investigated theoretically by Rescigno and Schneider.[47] The complex Kohn variational method is applied to this collision. Dissociation of H_2 is caused by direct excitation to the electronically excited state b $^3\Sigma_u^+$ from $H_2(v)$ with $v = 0 \sim 9$ in the electronic ground state. The magnitude of cross section is 5.6×10^{-17} cm^2 for the initial state of $v = 0$, 7.4×10^{-17} cm^2 for $v = 3$, 8.9×10^{-17} cm^2 for $v = 6$, and 1.0×10^{-16} cm^2 for $v = 9$ at the impact energy of 12 eV being the lowest impact energy investigated by Rescigno and Schneider. Since dissociation of H_2 is induced through excitation of the electronic state, the internal vibrational energies are not effectively converted into the one promoting dissociation of the molecule. This means that the magnitude of dissociation cross sections depends weakly on the initial vibrational states, although vibrational enhancement is observable in these results.

Atems and Wadehra[48] investigated the dissociation of $H_2(v)$ by a slow electron impact through resonance states of $H_2^-(B\ ^2\Sigma_g^+)$ and $H_2^-(X\ ^2\Sigma_u^+)$. The dissociation cross sections through the $H_2^-(X\ ^2\Sigma_u^+)$ resonance state reach the maximum about 3×10^{-23} cm^2 for $v = 0$ at the impact energy of $5 \sim 6$ eV, 6×10^{-20} cm^2 for $v = 3$ at $3.5 \sim 4.5$ eV, 3×10^{-18} cm^2 for $v = 6$ at $2.5 \sim 3.5$ eV, 3×10^{-17} cm^2 for $v = 9$ at $2 \sim 3$ eV, and 8×10^{-17} cm^2 for $v = 12$ at $1.5 \sim 3$ eV. The maximum dissociation cross section through the resonance state $H_2^-(B\ ^2\Sigma_g^+)$ is 2.5×10^{-17} cm^2 for $v = 0$ at the impact energy of about 11 eV, 3.2×10^{-17} cm^2 for $v = 5$ at about 4 eV, 2.8×10^{-16} cm^2 for $v = 12$ at about 1 eV. It is highly probable that the contribution of this resonance to dissociation cross sections is dominant over the one through any other electronic excitation processes and much larger dissociation cross sections are obtained for the initial vibrational states being higher than $v = 12$ at their resonance energies. Vibrational enhancement is really magnified by existence of the resonance state $H_2^-(B\ ^2\Sigma_g^+)$. Accoring as the impact energy is increased above 10 eV, dissociation cross sections through resonance states become considerably smaller than those of direct excitation obtained by Rescigno and Schneider.[47]

Very recently, Nobusada and Sakimoto[49] studied quantum mechanically dissociation of $H_2(v)$ by impact of He atom. In this collision system, a channel of exchange reaction through rearrangement of the atom and molecule is energetically closed in the electronic ground state of He + H_2. Since the interaction potential is essentially of short ranged,

the infinite-order sudden (IOS) approximation employed successfully by Schinke[14] (see further references therein) is applicable to this dissociation process at collision energies above about 5 eV. Nobusada and Sakimoto employed our new approach[42] to solve directly the PDE in the hyperspherical coordinates for each of different arrangements of He + H_2 and applied the IOS approximation to obtain dissociation cross sections. Representative results at the collision energy of 8 eV show the magnitude of dissociation cross sections to be 5×10^{-20} cm^2 for $v = 0$, 5×10^{-18} cm^2 for $v = 3$, 7×10^{-17} cm^2 for $v = 9$, and 1.2×10^{-15} cm^2 for $v = 14$. Vibrational enhancement is clearly demonstrated in their results. It is made clear by their investigation that internal vibrational energies compared with impact energies are much more effective to promote dissociation of H_2. Dissociation cross sections in this collision system are also obtained by quasi-classical trajectory calculations.[37] Since both results agree with each other within a factor of 2, these new results are valuable for understanding the order of magnitude for dissociation cross sections of molecules in vibrationally highly excited states.

The magnitude of dissociation cross sections of H_2 brought by the atom impact is larger than that of electron impact except for the case of slow electron impact through resonance states of $H_2^-(B\ ^2\Sigma_g^+)$ at the resonance energies. Although the results obtained by Nobusada and Sakimoto are one example for dissociation of H_2 induced by the atom impact, it is probable for impact of atoms and molecules to be more effective to dissociate H_2 in vibrationally excited states at collision energy of several eV.

5. Concluding remarks

Although it is not experimentally confirmed yet that H_2 molecules in gas divertor plasmas are in rotationally and vibrationally excited states, it is highly probable for the H_2 molecules, which are newly formed on divertor plates, to be in rotationally and vibrationally excited states.

Since the magnitude of collision cross sections for H_2 molecules in these excited states is in the order of $10^{-16} \sim 10^{-15}$ cm^2 as mentioned in sections 3 and 4, H_2 molecules in vibrationally highly excited states are easily quenched and also produced by collision of atoms and molecules. In order to establish the amount of reliable energy transfer through collisions between atoms, molecules, or their ions and molecular hydrogens and to determine the population of rotational and vibrational states of H_2 molecules in gas

divertor plasmas, it is very important to investigate thoroughly collision processes related to the H_2 molecules in rotationally and vibrationally highly excited states.

References

1. D. E. Post, J. Nucl. Mater. **220-222**, 143 (1995).
2. A. V. Phelps, J. Phys. Chem. Ref. Data **19**, 653 (1990).
3. R. W. Crompton, D. K. Gibson, and A. I. McIntosh, Aust. J. Phys. **22**, 715 (1969).
4. F. Linder and H. Schmidt, Z. Naturforsch. **26a**, 1603 (1971).
5. R. J. W. Henry and N. F. Lane, Phys. Rev. **183**, 221 (1969).
6. S. Hara, J. Phys. Soc. Japan **27**, 1009 (1969).
7. F. Linder, in *Electronic and Atomic Collisions*, edited by N. Oda and K. Takayanagi (North-Holland, Amsterdam, 1980), p. 535.
8. F. A. Gianturco and P. Tritella, Phys. Rev. **A16**, 542 (1977).
9. P. McGuire and D. J. Kouri, J. Chem. Phys. **60**, 2488 (1974).
10. P. McGuire, J. Chem. Phys. **62**, 525 (1975).
11. S. Green, R. Ramaswamy, and H. Rabitz, Astrophys. J. Suppl. **36**, 483 (1978).
12. U. Buck, F. Huisken, J. Schluesener, and J. Schaefer, J. Chem. Phys. **74**, 535 (1981);
    U. Back, F. Huisken, G. Maneke, and J. Schaefer, *ibid.* **78**, 4430 (1983);
    U. Back, F. Huisken, A. Kohlhase, D. Otten, and J. Schaefer, *ibid.* **78**, 4439 (1983).
13. S. Green and D. G. Truhlar, Astrophys. J. (Letters) **231**, L101 (1979).
14. R. Schinke, J. Chem. Phys. **72**, 3916 (1980).
15. H. Müller, M. Zimmer, and F. Linder, J. Phys. B: At. Mol. Opt. Phys. **29**, 4165 (1996).
16. D. K. Gibson, Aust. J. Phys. **23**, 683 (1970).
17. R. Schinke, M. Dupuis, and W. A. Lester, Jr., J. Chem. Phys. **72**, 3909 (1980).
18. A. J. C. Varandas, F. B. Brown, C. A. Mead, D. G. Truhlar, and N. C. Blais, J. Chem. Phys. **86**, 6258 (1987).
19. J. Z. Zhang and W. H. Miller, Chem. Phys. Letters, **153**, 465 (1988).
20. D. E. Manolopoulos and R. E. Wyatt, Chem. Phys. Letters, **159**, 123 (1989).
21. J. M. Launay and M. Le Dournef, Chem. Phys. Letters, **163**, 178 (1989).
22. K. Onda, M. Iwai, and T. Wada, J. Phys. Soc. Japan, **60**, 3327 (1991).
23. W. R. Gentry and C. F. Giese, Phys. Rev. **A11**, 90 (1975).
24. F. A. Herrero and J. P. Doering, Phys. Rev. **A5**, 702 (1972).

25. H. Ehrhardt, L. Langhans, F. Linder, and H. S. Taylor, Phys. Rev. **173**, 222 (1969).
26. R. J. W. Henry and E. S. Chang, Phys. Rev. **A5**, 276 (1972).
27. A. Klonover and U. Kaldor, J. Phys. B: Atom. Molec. Phys. **12**, 3797 (1979).
28. M. A. Morrison, R. W. Crompton, B. C. Saha, and Z. Lj. Petrovic, Aust. J. Phys. **40**, 239 (1987).
29. J. D. Shao and C. Y. Ng, J. Chem. Phys. **84**, 4317 (1986).
30. P. Langevin, Ann. Chim. Phys. **5**, 245 (1905).
31. G. Gioumousis and D. P. Stevenson, J. Chem. Phys. **29**, 294 (1958).
32. D. G. Truhlar and R. E. Wyatt, Ann. Rev. Phys. Chem. **27**, 1 (1976); M. Kneba and J. Wolfrun, *ibid.* **31**, 47 (1980); R. B. Walker and J. C. Light, *ibid.* **31**, 401 (1980); G. W. Flynn and R. E Weston, Jr., *ibid.* **37** 551, (1986); L. D. Levine, *Fifty Years of* $H + H_2$ *Kinetics*, Int. J. Chem. Kinet. **18**, 919 (1986); G. C. Schatz, Ann. Rev. Phys. Chem. **39**, 317 (1988); W. H. Miller, *ibid.* **41**, 245 (1990).
33. K. Onda, J. Phys B: At. Mol. Opt. Phys. **24**, 4509 (1991).
34. A. L. Scherzinger and D. Secrest, J. Chem. Phys. **73**, 1706 (1973).
35. L. W. Ford, d. J. Diestler, and A. W. Wanger, J. Chem. Phys. **63**, 2-19 (1975); K. C. Kulander, *ibid.* **69**, 5064 (1978); J. C. Gray, G. A. Fraser, and D. G. Truhlar, *ibid.* **73**, 5726 (1980); C. Leforestier, Chem. Phys. **87**, 241 91984); C. Leforestier, in *the Theory of Chemical Reaction Dynamics*, edited by D. C. Clary (Reidel, Dordrecht, 1985); C. Leforestier, Chem. Phys. Lett. **125**, 373 (1986); V. Mohan and N. Sathyamurthy, Comput. Phys. Rep. **7** 213 (1988).
36. J. Manz and J. Römelt, Chem. Phys. Lett. **77**, 172 (1981); J. A. Kaye and A. Kuppermann, Chem. Phys. Lett. **78**, 546 (1981); *ibid.* **115**, 158 (1985); Chem. Phys. **125**, 279 (1988).
37. J. E. Dove and S. Raynor, Chem. Phys. **28**, 1113 (1978).
38. N. C. Blais and D. G. Truhlar, *Potential Energy Surfaces and Dynamics Calculations*, edited by D. G. Truhlar (Plenum, New York, 1981) p. 431.
39. J. E. Dove and M. E. Mandy, Int. J. Chem. Kinet. **18**, 993 (1986).
40. W. A. Chupka and M. E. Russell, J. Chem. Phys. **49**, 5426 (1968); W. A. Chupka, J. Berkowitz, and M. E. Russell, *VI-th International Conference on the Physics of Electronic and Atomic Collisions* (MIT Press, Cambridge, 1969), p. 71; D. V. Pijkaren, E. Boltjes, J. V. Eck, and A. Niehaus, Chem. Phys. Lett. **86**, 20, (1983); D. V. Pijkaren, J. V. Eck, and A. Niehaus, *ibid.***91**, 293, (1984);

T. Turner, O. Dutuit, and Y. T. Lee, J. Chem. Phys. **81**, 3475, (1984).
41. J. Z. H. Zhang, D. L. Yeager, and W. H. Miller, Chem. Phys. lett. **173**, 489 (1990).
42. K. Sakimoto and K. Onda, J. Chem. Phys. **100**, 1171 (1994).
43. L. M. Delves, Nucl. Phys. **9**, 391 (1959); *ibid.* **20**, 275 (1960).
44. E. C. Sullivan and A. Temkin, Comput. Phys. Commun. **25**, 97 (1982).
45. J. C. Light, I. P. Hamilton, and J. V. Lill, J. Chem. Phys. **82**, 1400 (1985).
46. K. Sakimoto and K. Onda, Chem. Phys. Lett. **226**, 227 (1994).
47. T. N. Rescigno and B. I. Schneider, J. Phys. B: At. Mol. Opt. Phys. **21**, L691 (1988).
48. D. A. Atems and J. M. Wadehra, J. Phys. B: At. Mol. Opt. Phys. **26**, L759 (1993).
49. K. Nobusada and K. Sakimoto, to be published.

Fine structure of charge exchange lines observed in laboratory plasmas

K.Ida, S.Nishimura[1)], K.Kondo[2)]

National Institute for Fusion Science
Nagoya 464-01 Japan

1) The Graduate University for Advanced Studies

2) Graduate School of Energy Science, Kyoto University

Abstract

The influence of the fine structure of charge exchange lines appears only at the plasma edge or in the recombining phase where the ion temperature is low enough. The observed spectra in Li III and C VI are consistent with the sum of fine-structure components populated by statistical weights (assuming complete l-mixing) not by direct charge exchange cross sections. Some discrepancy was observed in the intensity ratio of fine-structure components between the observation and calculation for C VI in the recombining phase. The fine-structure of charge exchange lines gives an apparent Doppler shift in plasma rotation velocity measurement using charge exchange spectroscopy.

1. Introduction

The charge-exchange reaction between fully stripped carbon and atomic hydrogen becomes an important subject, since charge exchange spectroscopy (CXS) has been applied to measure ion temperature and plasma rotation profiles in magnetically confined plasmas [1,2]. Hydrogen neutral beam (NB) in the energy range of 20 - 40 keV, which is usually equipped to heat plasmas, is used also for CXS diagnostic. This technique also provides the fully stripped impurity radial profile and concentration with the use of the calculated charge exchange cross section [3]. Recently most measurements have been done with the use of a line of transition between high n-levels in the visible region taking advantage of the use of a optical fiber array to obtain multi-point simultaneous measurements [4]. Charge-exchange collisions typically between fully stripped ions of a light impurity $[A^{Z+}]$ and hydrogen atoms in a heating fast neutral beam $[H^0]$ result in an excited ion with one more electron in an excited state (n,l). This charge-exchange recombination process is expressed as

$$A^{Z+} + H^0 \rightarrow A^{(Z-1)+}(n,l) + H^+ \qquad (1)$$

The resulting ion $A^{(Z-1)+}$ in an excited state (n,l) subsequently decays through photon emission by which the velocity distribution of the original fully stripped ions $[A^{Z+}]$ can be obtained. Generally,

impurity ions are in an ionizing phase and the recombination process is not so important in the steady state for magnetically confined high temperature plasmas. A recombining phase of impurity ions is generally ignored in the core plasma. However, when the plasma temperature drops rapidly, for instance after the NB heating is turned off, the radiative recombination process for fully stripped ions

$$A^{z+} + e \rightarrow A^{(z-1)+}(n,l) \tag{2}$$

can be important. This process is considered to be dominant in the recombining phase.

The energy of a given level in a hydrogen-like ion with nuclear charge Z is given by

$$E(n,j) = -\frac{Z^2}{n^2}\left[1 + \frac{(\alpha Z)^2}{n}\left(\frac{1}{j+1/2} - \frac{3}{4n}\right)\right]R_y \tag{3}$$

where Ry is the Rydberg energy, α is the fine structure constant, and n is the principal quantum number and j is the total angular momentum. The observed intensities for each fine-structure component in the charge exchange line are determined by the cascade of the excited electrons from their initial distribution produced by the charge-exchange reaction. Since energy splitting between high n levels is only few eV, ion-ion collisions cause transfers between l levels (l-mixing) before an electron drops to lower states via photon radiation. When the plasma density is high enough, each l-level is repopulated to the statistical weights as $(2l + 1)$ by ion-ion collisions[1].

Each fine-structure component of high n-levels in the hydrogen-like ions is not observed in the magnetically confined high temperature plasmas, because energy splitting of $\Delta\lambda < 1$ Å is much smaller than the Doppler broadening. In contrast, the fine structure for Be-like ions was studied in the visible region relatively easily because of large energy splitting ($\Delta\lambda \sim 10$ Å). The line intensity ratio of Be-like OV multiplet lines for $2s3s\ ^3S_1$ - $2s3p\ ^3P_{2,1,0}$ (λ = 2781.04Å, 2787.03Å, 2789.86Å, $\Delta\lambda$ = 8.82Å) transitions was measured in the reversed field experiments Extrap-T1 and T2. The measured line intensity ratios deviate from the predictions of the model assuming a population in the l levels with statistical weights[5]. In this paper, the fine structure of hydrogen-like Li III ions (λ =4498 26- 4499 15Å, $\Delta\lambda$ = 0.89Å) measured in Heliotron-E plasmas and hydrogen-like C VI ions (λ = 3433 02- 3433 90Å, $\Delta\lambda$ = 0.88Å) in CHS heliotron/torsatron plasmas are compared with the predictions of the model assuming a population in the l levels with statistical weights.

2. Fine structure of hydrogen-like Li III ions observed in Heliotron-E

The Heliotron-E is an axially asymmetric heliotron/torsatron with poloidal period number L=2, toroidal period number M=19, major radius R=2.2m, magnetic field B=1.9T, averaged minor radius a=0.21 m. Heliotron-E has several nearly perpendicular neutral beams with 0 degree (5 ion sources : 1.5MW), 11 degree (3 ion sources : 1.1MW), and 28 degree injection angles (2 ion sources : 0.6MW). The neutral beams are injected into a low density target deuterium plasma produced by 53GHz fundamental electron cyclotron heating (ECH)[6]

Li impurities generally do not exist in the plasma and Li impurities were injected by means of

pellets to study the fine structure of hydrogen-like Li ions. A Li pellet injector consists of a magazine for pellets, gun barrel, guide tubes and differential pumping system with a buffer tank of 0.1 m^3 [7]. A Li pellet is injected into a plasma, which is initiated by a 106GHz gyrotron and further heated by neutral beams of 3.5MW power[8]. The acceleration voltage of the neutral beams is 23 kV. The magnetic field strength is 1.9 T. A 1.26 m visible spectrometer with a 2-dimensional detector (Hamamatsu,C3554X) [4] is employed to analyze the spectral profiles of the charge exchange recombination line of Li^{3+} ion. The time resolution is 20 ms. The sight-lines of 40 fiber optics cross the plasma column from 1.98 m to 2.42 m on the major radius and the spatial resolution is 0.013 m.

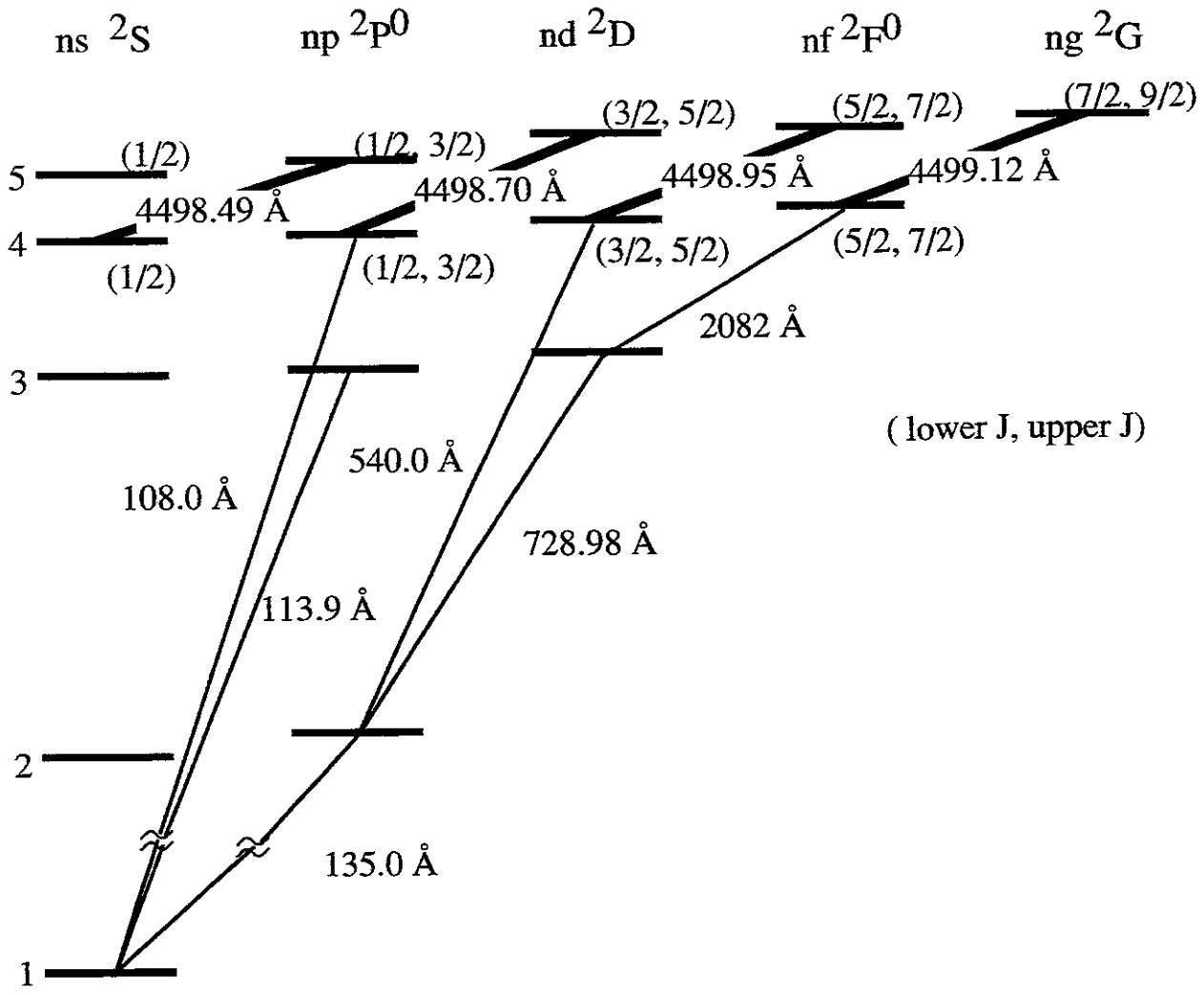

Fig.1 Grotrian diagram of Li III Wavelengths indicated in this diagram are mean values of each transitions with different J levels

Figure 1 shows a Grotrian diagram of Li III. The Li III line emissions for the $\Delta n = 5 - 4$ transition (4498 26 - 4499 15Å) are measured with visible spectrometer, while the Li III line emissions for the $\Delta n = 2 - 1$ transition (135 Å) is measured with a VUV spectrometer as a monitor of concentration on Li ions. Wavelengths indicated in this diagram are mean values of each transition with different j levels. The line emission for the $\Delta n = 4 - 3$ transition can not be measured in Heliotron-E charge exchange spectroscopy , because the wavelength of this emission is below the transmission cut off of the optical fiber array used.

Figure 2 shows a spectra of charge exchange line of carbon for the $\Delta n = 5 - 4$ transition measured at the plasma center ($R = 2.18$ m : $\rho = 0.0$), half radius ($R = 2.09$ m : $\rho = 0.6$) and plasma edge ($R = 2.03$ m : $\rho = 0.8$). The charge-exchange plus background spectra (CXS + BKG) are measured at t = 370 ms (~ 30ms after the Li pellet injection), while the background spectra (BKG) are measured when no Li pellet is injected into the plasma. The pure charge-exchange spectra (CXS) is given by subtracting background spectra from (CXS + BKG) spectra. The background line emission at $\lambda = 4497.8$ Å has not been identified yet in Heliotron-E. The intensity of this background line emission is relatively constant in space, while the intensity of the charge-exchange signal has a peak at the plasma center, which indicates that Li density profile is peaked at the plasma center. Therefore the ratio of charge-exchange signal to the background increases toward the plasma center. The pure charge-exchange spectra (CXS) extracted is compared with the calculations with a single component and with the fine-structure components.

Figure 3 shows the spectra of charge exchange lines of Li ions for the the $\Delta n = 5 - 4$ transition measured at R = 2.18m for the charge exchange recombination [(a), (b)] and the radiative recombination [(c), (d)]. The charge exchange recombination spectra are measured at t=370 ms (30 ms after the Li pellet injection) with neutral beam injection (NBI), while the radiative recombination spectra are measured in the recombining phase (t = 450 ms) after the NBI is turned off. Although the selection rules for spontaneous radiative transition are $\Delta l = \pm 1$ and $\Delta j = \pm 1, 0$, with the statistical weighted l level population, main components are $j \rightarrow j-1$ in $\Delta n = 1$ lines. The height of lines indicates the intensity of emissions of transition(s) of $j = 3/2 \rightarrow 1/2$, ($P_{3/2} \rightarrow S_{1/2}$ and $D_{3/2} \rightarrow P_{1/2}$), $j = 5/2 \rightarrow 3/2$, ($D_{5/2} \rightarrow P_{3/2}$ and $F_{5/2} \rightarrow D_{3/2}$), $j = 7/2 \rightarrow 5/2$, ($F_{7/2} \rightarrow D_{5/2}$ and $G_{7/2} \rightarrow F_{5/2}$), and $j = 9/2 \rightarrow 7/2$, ($G_{9/2} \rightarrow F_{7/2}$). Fine-structure components of charge exchange lines in Li III are typically masked by Doppler broadening. Fine-structure influence appears at the recombining phase as asymmetry of spectra. The calculated spectra (solid lines) in Fig (a) and (c) are the best fit of single (a) Gaussian or (c) Lorentz functions. When the ion temperature is high enough the Gaussian function is used, while the Lorentz function is used to represent the instrumental function of the spectrometer when the ion temperature is very low. The discrepancy between the measured spectra and calculation with a single component (ignoring the multiple lines due to fine structure effect) is observed. The calculated spectra in Fig (b) and (d) are the sum of all the fine-structure components, each having Gaussian (b) or Lorentz (d) functions. The amplitude of each component corresponds to the emission intensity ratio of fine-structure components assuming the population in the statistical weighted l distribution. The width of Gaussian or Lorentz functions is given to match the measured data but it is common for all components. The measured spectra have good agreement with the calculated spectra from the sum of fine-structure components with a statistical weights l distribution.

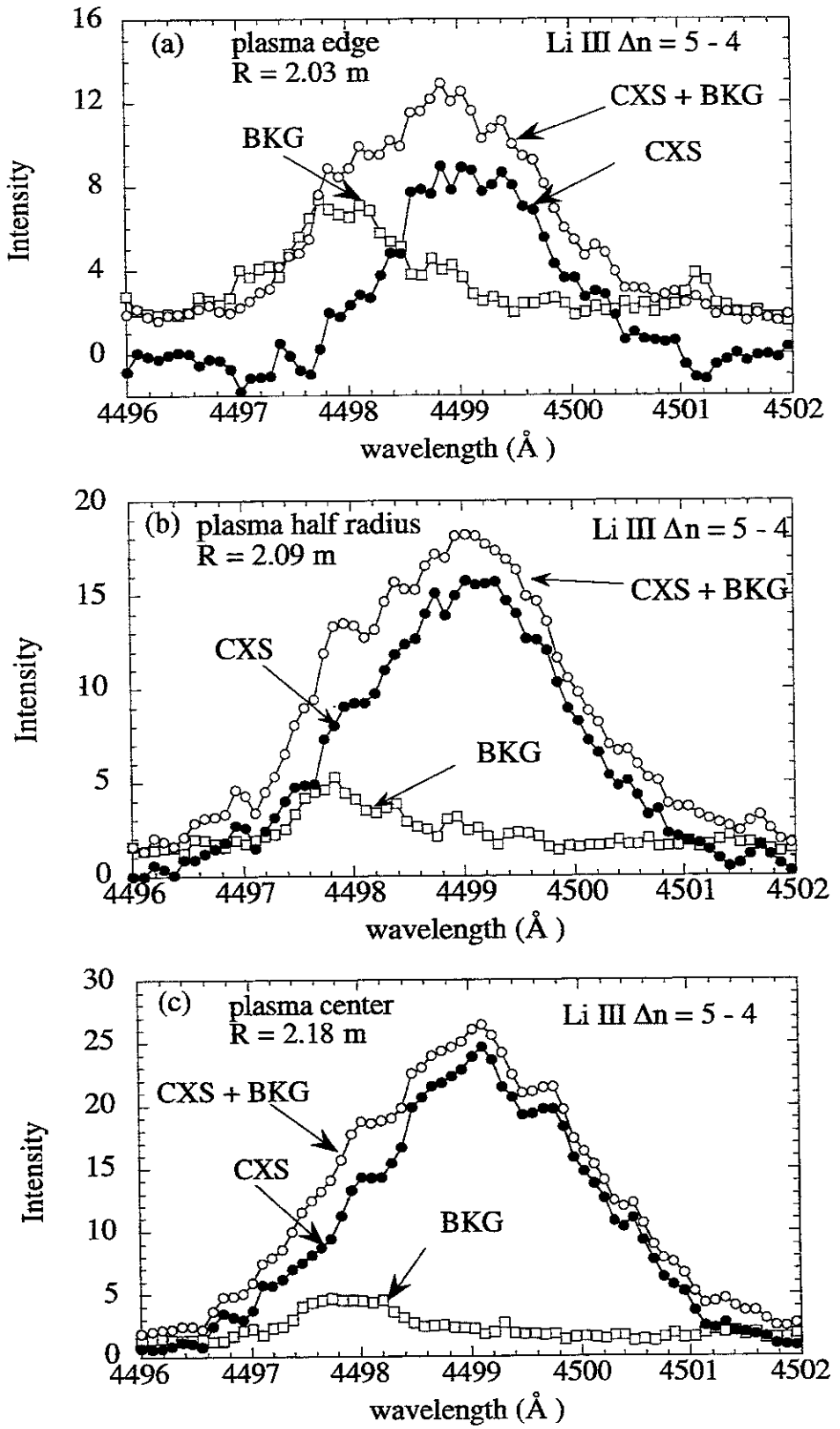

Fig.2 Spectra of the charge exchange recombination lines of Li III for $\Delta n = 5 - 4$ transition. (a), (b) and (c) are measured at the plasma edge, half radius and center. Charge exchange spectra (CXS) are derived by subtracting the background intensity (BKG) from the measured spectra (CXS + BKG).

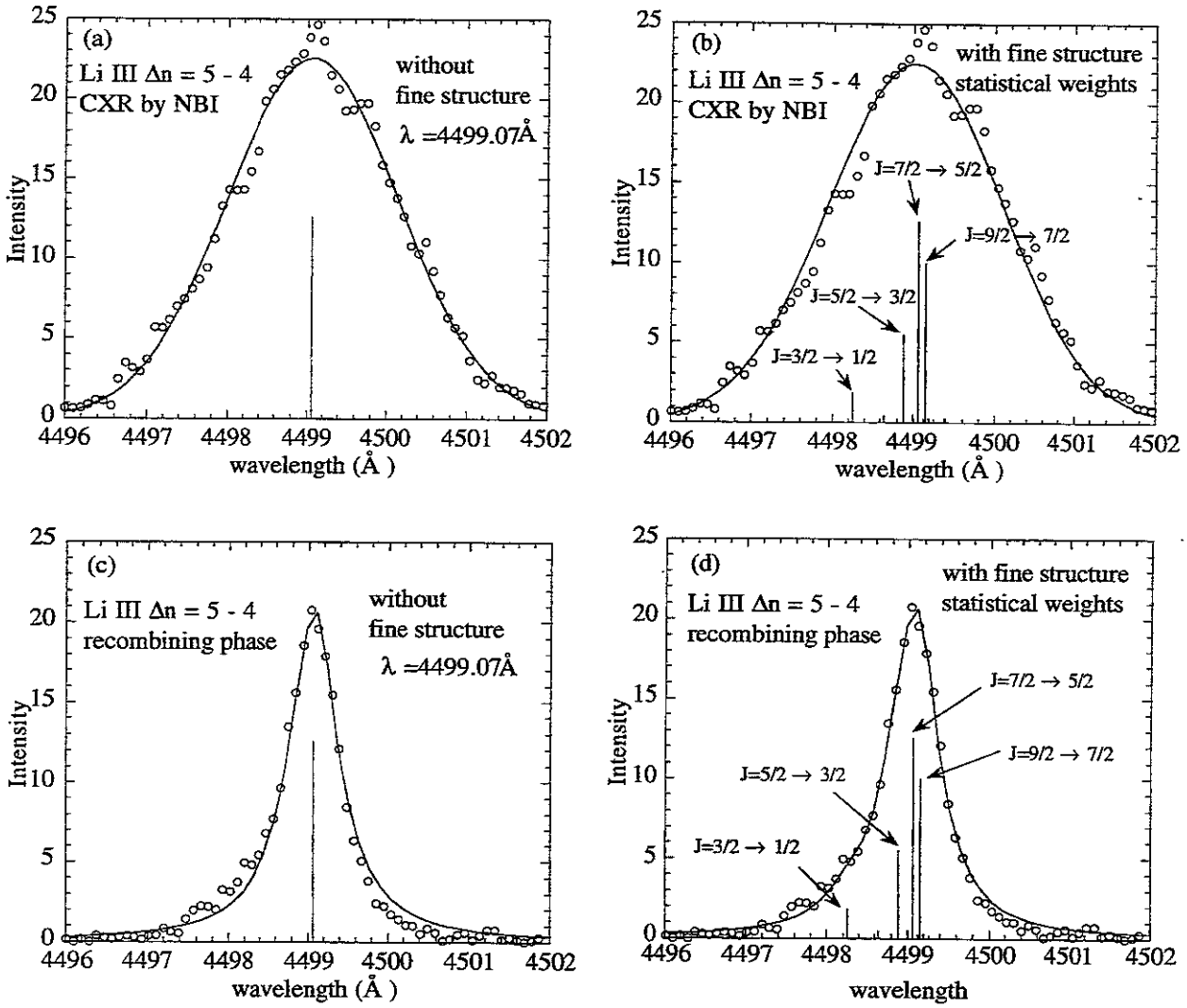

Fig.3 Spectral of charge exchange lines of Li III for $\Delta n = 5 - 4$ transition during NBI at the plasma center and the calculated spectral profiles without (a) and with (b) fine structure effect. Spectral profiles of Li III in the recombining phase after the neutral beams were turned off and the calculated spectral profiles without (c) and with (d) fine structure effect. The height of the lines indicates the intensity of the emissions of fine components.

3. Fine structure of hydrogen-like C VI ions observed in CHS

The Compact Helical System (CHS), is a poloidal period number L = 2 and toroidal period number M = 8 heliotron/torsatron device with a major radius of 1 m and an average minor radius of 0.2 m[9]. A 53 GHz gyrotron produces ECH plasmas with a low density below 1 x 10^{13} cm^{-3}, while the tangential NBI with 0.9 MW can sustain the plasma with high density up to 1 x 10^{14} cm-3. A 96 channel space resolved 1 m visible spectrometer system using a CCD detector coupled with an image intensifier has been developed to measure the ion temperature and poloidal/toroidal rotation velocities[10]. Three sets of optical fiber array have been installed in CHS. Two of them (one viewing from upper port and the other viewing from lower port) are viewing a fast neutral beam

poloidally and the other has a view which does not intersect the neutral beam line to subtract background radiation. These optical fibers with 132 μ mm diameter are led into the entrance slit of 1 m Czerny-Turner spectrometer with 2400 grooves/mm grating. At the exit plane, the light from each fiber gives the spectrum from one spatial position. The light from all of the fibers is focused onto the image intensifier tube coupled with a CCD TV camera. The resolution is ~ 0.1Å/ch (~100 spectral channels), while the time resolution is 20 ms.

Figure 4 shows the measured and calculated spectra of hydrogen-like carbon for the Δn = 7-6 transition measured for the charge exchange recombination [(a), (b) at the plasma center R = 0.97 m and (c),(d) at the plasma edge R = 1.07 m] and the radiative recombination [(e),(f) at the plasma center R = 0.97 m] in CHS. The height of lines for the transition indicated by j=3/2→1/2, j=5/2→3/2 , j=7/2→5/2 , j=9/2→7/2, j=11/2→9/2, and j=13/2→11/2 shows the intensity ratio of fine-structure components of ($P_{3/2}\rightarrow S_{1/2}$ and $D_{3/2}\rightarrow P_{1/2}$), ($D_{5/2}\rightarrow P_{3/2}$ and $F_{5/2}\rightarrow D_{3/2}$), ($F_{7/2}\rightarrow D_{5/2}$ and $G_{7/2}\rightarrow F_{5/2}$), ($G_{9/2}\rightarrow F_{7/2}$ and $H_{9/2}\rightarrow G_{7/2}$), ($H_{11/2}\rightarrow G_{9/2}$ and $I_{11/2}\rightarrow H_{9/2}$) and ($I_{13/2}\rightarrow H_{11/2}$). Fine-structure components of charge exchange lines in C VI are typically masked by Doppler broadening. However, the influence of fine-structure appears at the plasma edge where the ion temperature is low T_i< 200 eV or the recombining phase where the electron density n_e = 0.6 - $1.2\times10^{19}m^{-3}$ and ion temperature T_i = 40 eV. Figures (a) and (c) show that a single (a) Gaussian or (c) Lorentz function can not reproduce the measured spectra. As seen in Fig. (b) and (d), the measured spectra have good agreement with the calculated spectra from the sum of fine-structure components with a statistically weighted l distribution. However, a discrepancy between the measured and calculated spectra with fine-structure components in C VI was observed at the recombining phase.

The initial l - distribution produced by the charge exchange reactions differs depending on the calculations of the cross sections[11]. Many theoretical calculations have been proposed: molecular orbital (MO) calculation by Green et al. [12], the extended atomic orbital (AO) calculation of Fritsch and Lin [13,14], and the unified atomic-molecular orbital (AO-MO) calculation of Kimura and Lin [15], the unitarized distorted- wave approximation (UDWA) of Ryufuku [16,17], and continuous energy state model of Koike [18], have been proposed. However most calculations [12,13,15] give the partial cross sections for low n -levels below n =5, where X-ray or VUV emissions are produced. Few charge exchange cross sections for high n-level transitions above n =7 have been calculated and their values are quite different from each other[14,17,18]. The l -mixing is mainly caused by bulk ions and impurities since the energy gap between different l -levels is small [1], whereas the excitation among different n -levels is caused by electron excitation. The effect of l-mixing on emission cross section appears differently depending on the l-distributions of the cross section. For n = 7 levels, the partial cross section of the charge transfer have maximum values at l = 1 - 2 in Koike's, at l = 3 - 4 in Fritsch's, and at l = 5 in Ryufuku's calculation. In the limit of complete l -mixing, the l -distribution is re-distributed by l -mixing following the statistical weight. Figure 5 shows the spectra of charge exchange line of carbon for the Δn = 7-6 transition measured at the plasma edge with charge exchange recombination (CXR) by neutral beam injection (NBI) and predictions from different calculations of direct charge-exchange cross sections. As shown in the solid lines, calculated spectra from the sum of fine-structure components with the populations proportional to the direct charge exchange cross section predicted by Ryufuku show better agreement

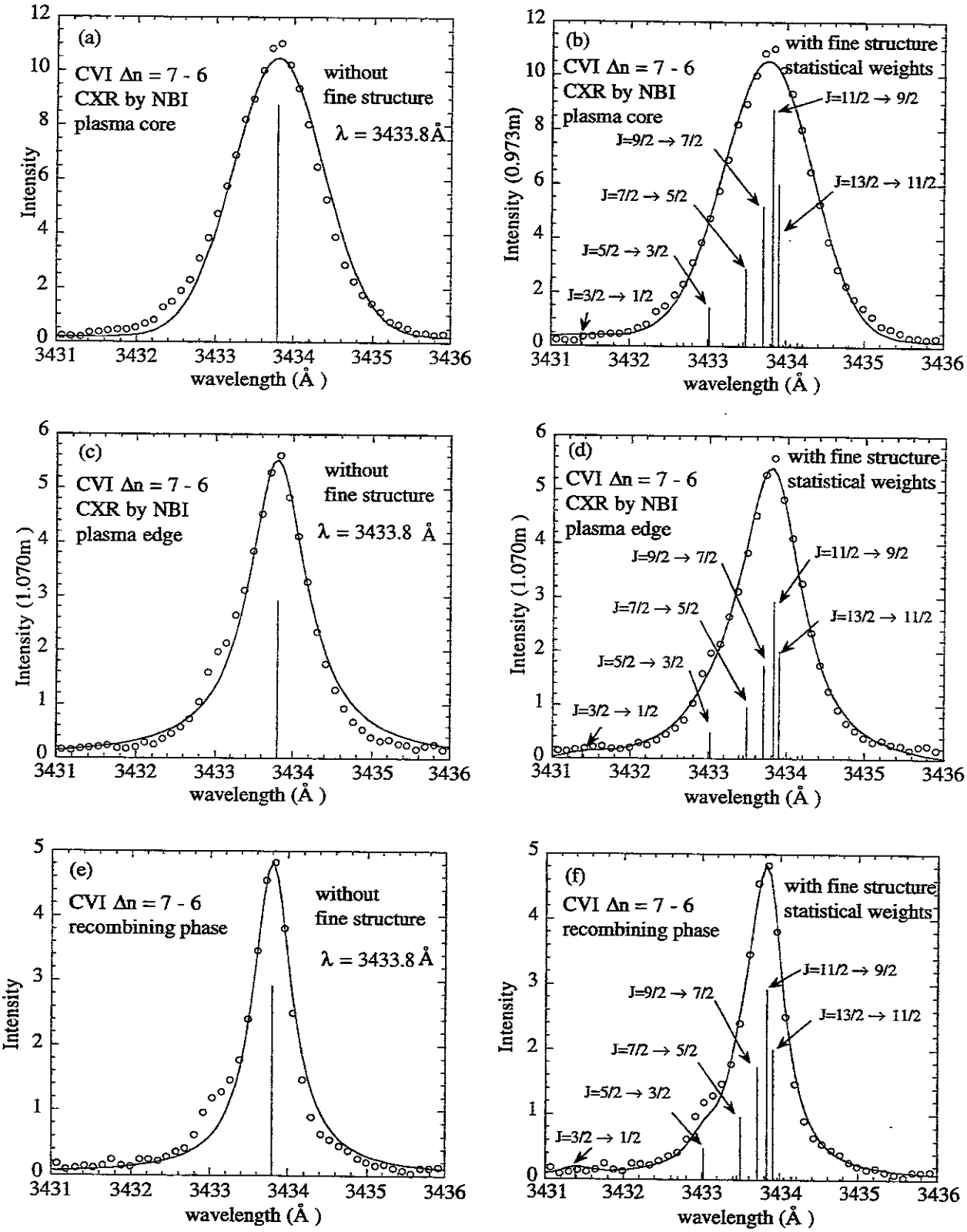

Fig.4 Spectra of charge exchange recombination line of C VI for $\Delta n = 7 - 6$ transition. (a) and (b) are spectra measured at the plasma core, while (c) and (d) are spectra measured at the plasma edge with charge exchange recombination (CXR) by neutral beam injection (NBI). (e) and (f) are the spectra measured at the recombining phase after the NBI is turned off. The solid lines are calculated spectra (a),(c),(e) without fine structure and (b),(d),(f) with fine structure in statistical weights.

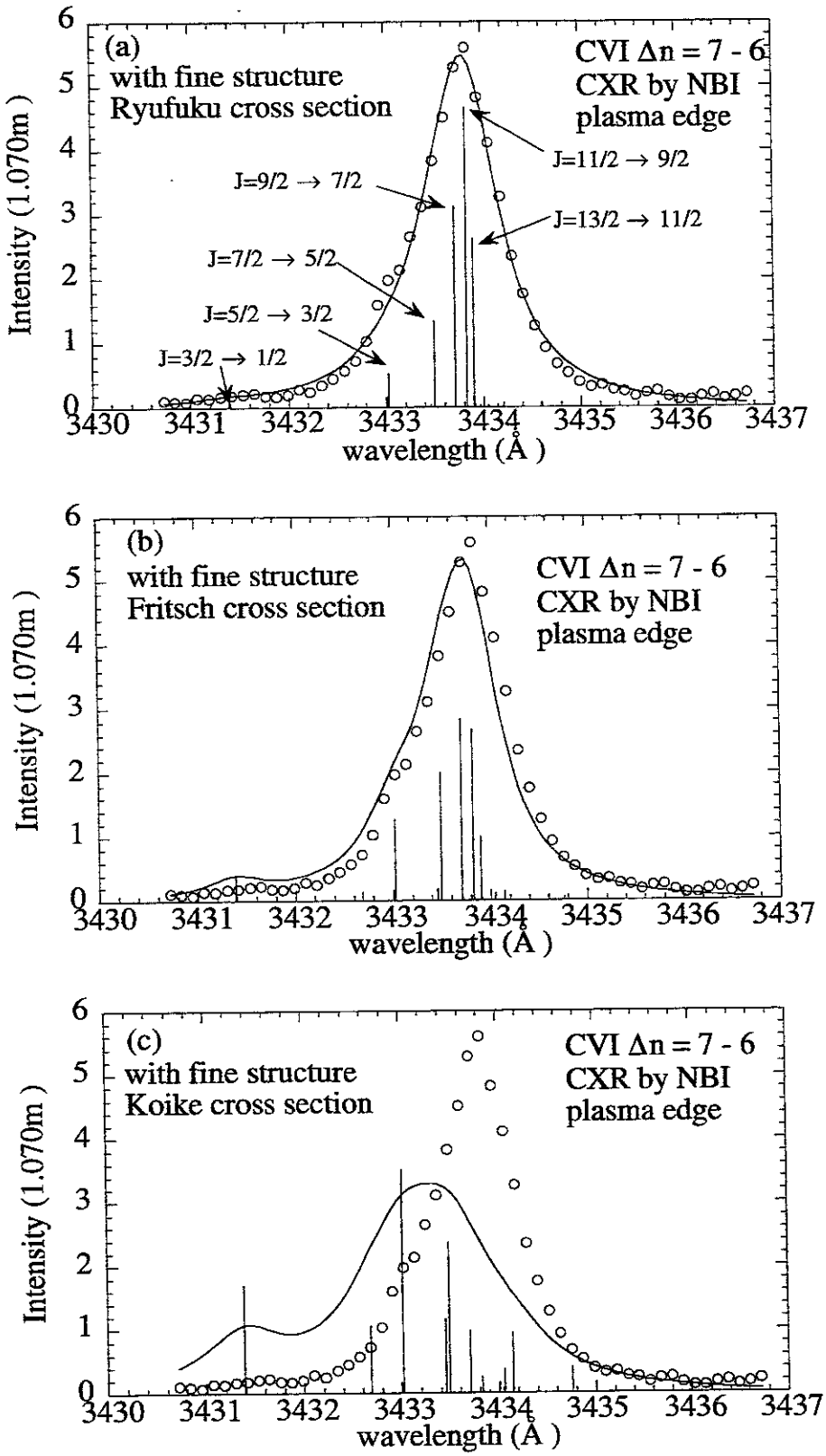

Fig.5 Spectra of charge exchange line of carbon for $\Delta n = 7 - 6$ transition measured at the plasma edge with charge exchange recombination (CXR) by neutral beam injection (NBI) in CHS. The solid lines are calculated spectra with fine structure in the weights proportional to the direct charge exchange cross section predicted by (a) Ryufuku, (b) Fritsch and (c) Koike calculations.

than that by Fritsch and Koike calculations. This is because, the initial l - distribution produced by the charge exchange reactions predicted by Ryufuku calculations is similar to that statistically weighted l - distribution. Since the plasma densities for those Li III and C VI spectra measurements are high enough to assume that those ions are in the complete l-mixing state, these measurements could not justify the validity of the charge exchange cross section calculations.

The splitting of lines in the visible range or of high n level associated with fine structure in hydrogen-like ions can not be measured in the hot plasma because the Doppler broadening is so large that it masks the splitting. Apparent Doppler broadening due to the fine-structure components causes an overestimation of the ion temperature of only < 20%, when the ion temperature exceeds over 100 eV for the transition of Δn = 7-6 in hydrogen-like Carbon ions. On the other hand, a distortion of the charge exchange spectra from a Gaussian profile due to the asymmetry of energy splitting in fine-structure components causes an apparent wave length shift. This apparent wave length shift in measurements can be distinguished from the wave length shift due to plasma rotations by viewing the plasma from two directions opposite each other. Figure 6 shows a radial profile of (a) ion temperature and (b),(c) wavelength shift ($\Delta\lambda$) of C VI Δn = 7 - 6 transition measured with (b) upper viewing array and (c) lower viewing array at t = 130 ms (during NBI) and at t = 170 ms (after the NBI is turned off). Because the Doppler shifts during NBI change their sign depending on the viewing direction (from the upper and lower viewing array), these wave length shifts are considered to represent mainly plasma rotation velocity. However, the wave length shifts after NBI do not depend on the viewing direction, and this wave length shift is considered to be the apparent shift associated with the asymmetry of energy splitting in fine-structure components. This apparent Doppler shift becomes most significant when the ion temperature is low (T_i = 30 - 40 eV) as is seen in the recombining phase. This observation suggests the importance of two arrays viewing from opposite directions from each other in the plasma rotation velocity measurements using charge-exchange spectroscopy.

4. Discussion

The observed fine structures for Li III and C VI are consistent with the calculated spectra with the l -distribution given by statistical weights (assuming complete l -mixing) not by direct charge exchange cross sections. However, some discrepancy was observed in the fine structure between the observation and calculation for C VI in the recombining phase. Since the plasma density is high enough to assume complete l -mixing, it is not clear what causes the discrepancy between measurements and calculations in the recombining phase. Although there are no interference impurity line(s) observed near the C VI Δn = 7 - 6 transition line in the NB injected phase, there might be some interference impurity line(s) when the electron temperature is low, such as during the recombining phase. C VI Δn = 8 - 7 transition in the recombining phase should be investigated in the future to study whether the l distribution for high n level transition in the hydrogen-like impurity is statistically weighted or not.

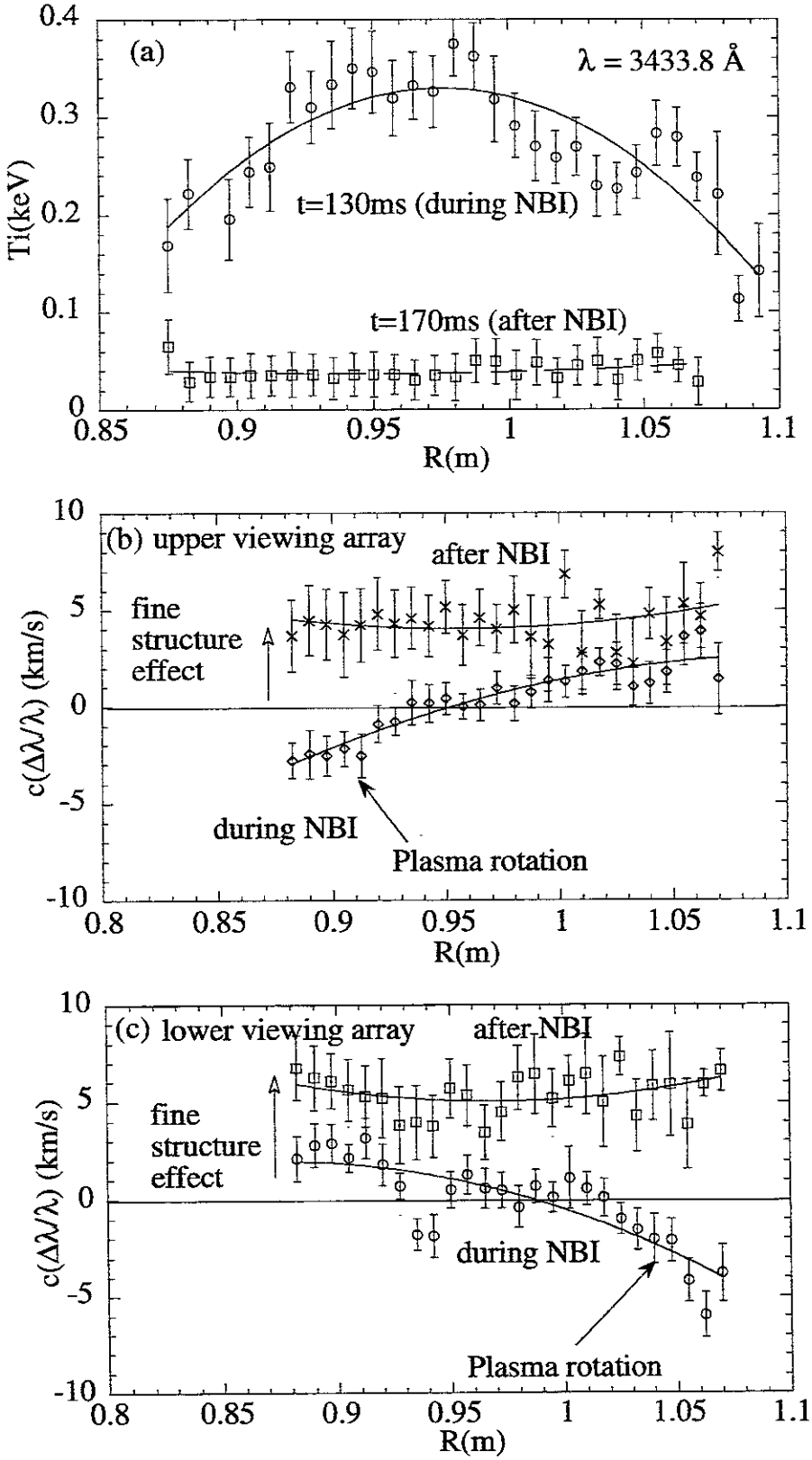

Fig.6 Radial profiles of (a) ion temperature and (b),(c) wavelength shift ($\Delta\lambda$) of $\Delta n = 7 - 6$ transition measured with (b) upper viewing array and (c) lower viewing array during NBI and after NBI was turned off

Acknowledgement

The authors acknowledge the experimental group of Heliotron-E and CHS group for their supports to do this work. Useful discussions with Dr. T.Fujimoto (Kyoto University) and Dr. T.Kato (NIFS) are appreciated.The authors thank Dr.B.J.Peterson for correcting the manuscript.

References

[1] R.J.Fonck, D.S.Darrow and K.P.Jaehnig, Phys. Rev. A29 , (1984) 3288.

[2] R.C.Isler, Plasma Phys. Control. Fusion **36** (1994) 171.

[3] R.J.Fonck, M.Finkenthal, R.J.Goldston, D.L.Herndon, R.A.Hulse, R.Kaita, D.D.Meyerhofer, Phys. Rev. Lett. 49 , (1982) 737.

[4] K.Ida and S. Hidekuma, Rev. Sci. Instrum. 60 , (1989) 876.

[5] T.Kato, E.Rachlew-Kallne, P.Horling and K.-D Zastrow, National Institute for Fusion Science Report, (1996) NIFS-436

[6] F.Sano, et. al., Nucl. Fusion **24** (1984) 1103.

[7] K.V.Khlopenkov, V.Yu.Sagdeev, S.Sudo et al., (in *Proc. 7th Int.Conf.on Plasma Physics and Controlled Nuclear Fusion, Toki, Japan, 1995*)

[8] K.Kondo, K.Ida, C.Christou, et. al., (in *Proc. th Int. Conf. on Plasma Surface Interactions in Controlled Fusion Devices*, 1996)

[9] K.Matsuoka et. al., in Plasma Physics and Controlled Nuclear Fusion Research (in *Proc. 12th IAEA Conf. Nice, 1988*) Vol.II (1989) 411.

[10] K.Ida, H.Yamada, H.Iguchi, S.Hidekuma, H.Sanuki, K.Yamazaki and CHS Group, Phys Fluids B3 (1991) 515

[11] K.Ida and T.Kato, Physics Letter **A166** (1992) 35

[12] T.A.Green, E.J.Shipsey, J.C.Browne, Phys. Rev. A25 , (1982) 1364.

[13] W.Fritsch and C.D.Lin, Phys. Rev. A29 , (1984) 3039.

[14] W.Fritsch, Phys. Rev. A30 , (1984) 3324.

[15] M.Kimura, D.C.Lin Phys, Rev. A32 , (1985) 1357 .

[16] H.Ryufuku and T.Watanabe, Phys. Rev. A20 , (1979) 1828.

[17] H.Ryufuku, Rep. JAERI-M-82-031 (1982).

[18] F.Koike, J. Phys. Soc. Jpn. 57 , (1988) 2344.

Recent theoretical studies of slow collisions between plasma impurity ions and H or He atoms

W. Fritsch[1] and H. Tawara[2]

[1]Bereich Theoretische Physik, Hahn-Meitner-Institut Berlin, D-14109 Berlin, Germany
[2]National Institute for Fusion Science, Nagoya 464-01, Japan

October 8, 1996

Abstract

We review recent progress in theoretical studies of slow collisions between light plasma impurity ions and atomic hydrogen or helium. We start with a brief overview of theory work that has been done by various groups in the past. We then proceed to discuss work that is published in the last two years. For the systems of Be^{2+}– He, Be^{4+}– He and C^{5+}– He we present yet unpublished work of our own. All of this work broadens our knowledge about systems that are of interest for the fusion community. Some of the new information is found to be at variance with what is known from other sources and hence needs further analysis

1 Introduction

After much development of the theory in the past two decades, electron transitions in atomic collision can now be addressed with a number of sophisticated descriptions. In slow collisions which are the subject of this report, the large transition probabilities require the use of non-perturbative methods. Close-coupling descriptions have been set up, in the past, first to predict the gross behaviour of the active electrons in the collision. Much refined versions are being used now to predict ever finer details, typically the population of weak channels, but also recently the quantum-mechanical phases of the population amplitudes and their dependences on the scattering angle. The success of these descriptions confirms the basic picture beneath the various close-coupling models, the movement of the active electrons between mainly a limited number of molecular or atomic configurations. The number of needed configurations can be rather large, however, when interest is in weak transitions, sometimes larger than computing facilities would allow to accommodate. It is then that simpler models are not only convenient but necessary. The fully classical description of such collisions has been demonstrated to predict reliable cross sections at not-too-low energies or in situations when the level density is large. There are other, simple semiclassical models available which allow to assess a given collision process at least qualitatively.

Many of the theoretical developments have been stimulated, as have been accompanying experimental studies, by the needs of the fusion plasma community for a wide-ranging data base on atomic collisions. For example, studies of the weak transitions to highly excited ionic states would be considered a merely academic exercise if there was not the method of fusion plasma diagnostics by charge exchange or beam emission spectroscopy. For a recent description of this application of atomic collision data, see the report by Hoekstra [1]. Ten years ago, beryllium ions were not seriously considered in theoretical collision studies as experiments on such toxic material were considered unlikely. After the planning and actual appearance of beryllium as a plasma facing material in fusion devices, quite a few studies on beryllium ions have been undertaken.

In this report we review recent theoretical work on slow collisions of light plasma impurity ions with hydrogen or helium targets. We base our report on the recent review by Janev et al. [2], which summarizes the situation of both theory and experiment as of 1994. Theoretical work that has been published in the last two years is summarized and referenced. We also present work of our own, a portion of which is not yet available in press.

In the next section we start with a short summary of the data basis as it is presented in more detail in ref. [2]. References to original work is given only if such work is *not* included in ref. [2], as in the case of target excitation processes. In the following section, we present new work that has appeared in the last two years. Any unpublished work of our own is discussed here too. In a final section, we summarize the progress that has been achieved and the status of the data base.

2 Status of theoretical work up to 1994

The large body of theoretical work on A^{q+}– H, He collisions, up to 1994, has been reviewed by Janev et al. [2]. Earlier reviews, like the one on collisions between Be^{q+} and B^{q+} with H, H_2 and He [3], are cited there. For details and further references, we refer to that compilation. Fully quantummechanical close-coupling models have been applied to a few systems in the eV/u energy regime up to energies of fractions of keV/u,[1] for predicting total transfer and sometimes a few partial transfer cross sections to the main final channels. Semiclassical close-coupling models, with molecular-orbital or atomic-orbital expansions, have been applied at higher energies, typically from fractions of keV/u up to 100 keV/u. In very few of these latter investigation, also trans-

[1]In this report, we use the notation *u* for the atomic mass unit which is often called *amu*.

fer into final states with large orbital quantum numbers $n\ell m$ has been considered. Such detailed work needs to include the consideration of target excitation processes as these may interact with the weaker transfer processes. Some theoretical work is also based on an analysis of the molecular energy diagram of a system for "hidden crossings", i.e. crossings of energy levels at complex values of the interatomic separation. There is no space here to delve into these theoretical model descriptions as this is already covered in ref. [2].

2.1 Collisions with atomic hydrogen

2.1.1 Total transfer cross sections

From theoretical work of this type, along with experimental data, a "recommended" set of total transfer cross sections has been given for Be^{4+}, B^{5+}, C^{6+} and O^{8+}– H collisions at energies of 0.01 – 100 keV/u. For incompletely stripped ions, recommended total transfer cross sections exist for Be^{2+} and Be^{3+}– H collisions at 0.05 – 10 keV/u (transfer in the case of Be^{+} ions is very weak), and for B^{3+} and B^{4+}– H collisions at 0.1 – 100 keV/u. Some limited information on B^{+} and B^{2+}– H collisions is available from experiment only. Recommended transfer cross sections exist also for C^{q+}– H collisions (q = 1 – 5) and for O^{8+}– H collisions (q = 1 – 7). For N^{q+}– H collisions, there exists a fair amount of information in the literature, notably in theory work for the charge states of q = 6, 5, and 7.

Theoretical work for the heavier impurity ions like Si, Ti, V, Fe, Ni, and other metallic ions, is very limited. It does not exist for charge states $q = 1-2$ where it would be needed most since, for low charge states, the ionic core does make a decisive difference between various equicharged ions. On the other hand, for $q \geq 3$ and energies above some 1 keV/u, existing work shows that total transfer for equicharged ions is essentially the same and hence, for an assessment of total transfer, there is no need for dedicated calculations for each individual system.

2.1.2 Partial transfer cross sections

In theory work within the close-coupling description, there is always some information on the final state distribution in electron transfer, at least for the particular shell n_0 that is most likely to be populated and sometimes also for $n_0 + 1$. Beyond that, there are studies that have been aimed particularly at the determination of the final state distribution for states with higher quantum numbers $n \geq n_0 + 2$. The most advanced of these studies predict partial transfer cross sections for Be^{4+}– H collisions ($n_0 = 3, n \leq 8$), B^{5+}– H collisions ($n \leq 8$), C^{6+}– H collisions ($n_0 = 4, n \leq 8$), N^{7+}– H collisions ($n \leq 8$), and O^{8+}– H collisions ($n_0 = 5, n \leq 9$). There is no similarly detailed study for systems that involve any of these elements in an incompletely stripped form, or any of the heavier impurity ions.

2.1.3 Excitation cross sections

Target excitation processes have not been considered in ref. [2]. There is indeed very little information, theoretical or experimental, on the weak excitation process in slow collisions of any system except for the H^{+}– H system. In ref. [4], calculated excitation cross sections are given, for $n = 2, 3$ target states, for Be^{4+}– H and C^{6+}– H collisions. It is shown that these cross sections as well the cross sections for H^{+} and He^{2+} projectiles do scale at scaled energies E/q above 10 keV/u (q is the charge state of the ion), but they are rather different for each system at the lower energies. At low energies, there are seen to be structures in the energy dependencies of the calculated excitation cross sections.

2.1.4 Collisions involving an excited hydrogen target

For electron transfer from an excited hydrogen target, classical (CTMC) calculations have been performed with a number of projectile charge states q and initial target excitation states n. From these results, as well as from purely geometrical considerations, a scaling relation for the total transfer cross section σ has been derived for scaled energies $En^2/q^{0.5}$ larger than 10 eV/amu,

$$\frac{\sigma}{n^4 Z} = \mathcal{F}\left(\frac{n^2 E(\mathrm{keV/u})}{\sqrt{Z}}\right), \qquad (1)$$

i.e. the scaled cross section on the left-hand side of eq. (1) is a universal function $\mathcal{F}$ of the scaled energy. This scaling works best for large quantum numbers n of the initial state of the hydrogen electron and high energies. For $n = 2$, it is documented down to a scaled energy of 20 keV/u only.

2.2 Collisions with helium

2.2.1 Transfer of one electron

For Be^{q+}– He collisions, close-coupling studies have been done only for Be^{4+} projectiles and the population of the states in the main principal shell ($n = 2$). There is more theoretical information on B^{q+} projectiles, for $q = 3 - 5$, but only little in known on partial transfer cross sections for these systems, see also the evaluation by Phaneuf et al. [5].

For C^{q+} projectiles, close-coupling studies exist for $q = 4, 6$ only, but recommended total transfer cross sections exist for all charge states $q \geq 2$. For O^{q+}– He collisions, theoretical studies exist for $q = 1, 6, 8$, and recommended total transfer cross sections exist for all charge states q. For heavier impurity ions, there is only scarce information, e.g. for the ions Si^{4+}, Ti^{4+}, and, from CTMC calculations, for the full set of Fe^{q+} ions.

As of 1994, there exist no theoretical study of target excitation for the systems of interest here.

2.2.2 Two-electron processes

Close-coupling calculations exist on double-electron transfer in A^{q+}– He systems for projectiles Be^{4+}, B^{4+}, C^{6+}, N^{7+} and O^{8+}, as well as for transfer-ionization for C^{6+} and O^{8+} ions. For these latter ions as well as for Ne^{10+} and Si^{14+} ions, there is also information from CTMC calculations. Transfer-excitation processes have not been much studied. The little available information can be shown, however, to

ie on a universal curve after applying some phenomenological scaling procedure.

3 Recent theoretical work

In this section we present work that has been done after previous reviews [2, 5] have completed.

3.1 *Collisions with atomic hydrogen*

3.1.1 *Be^{q+} – H collisions*

The bare-ion system of Be^{4+}– H collisions has been investigated with the molecular-orbital close-coupling method [6], with the method of hidden adiabatic crossings [7], and with the CTMC method [8]. In the CTMC work [8], Be^{2+} and Be^{3+} ions are also considered along with excitation and ionization cross sections for all these systems. The Be^{4+}– H system has also been studied with a Gaussian-basis close-coupling method, in a systematic investigation of the Z^{Z+}– H systems (Z=2–8) at 0.25–800 keV/u [9].

Electron transfer in Be^{4+}– H collisions. In Figure 1, we

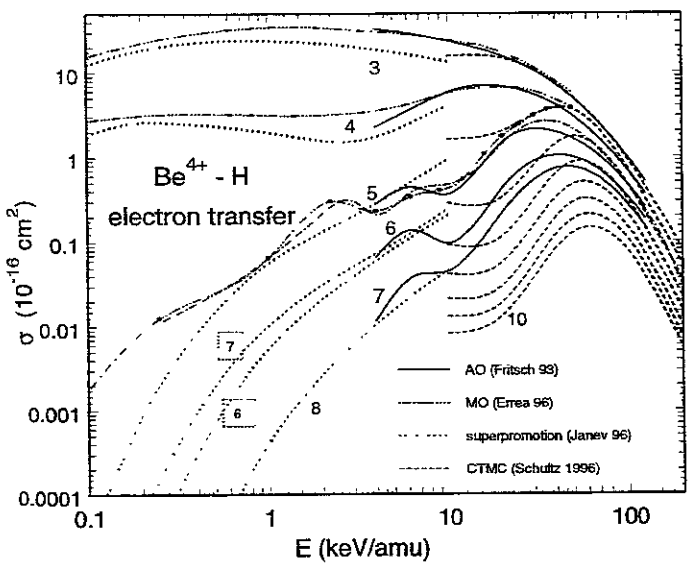

FIG. 1: Calculated electron transfer cross sections into B^{3+} n shells in Be^{4+}– H collisions, from close-coupling calculations with an AO [4] (full lines) expansion, with a Gaussian expansion [9] (dash-dotted line, shown here only for n=5, see text) and with an MO [6] (dash-triple-dotted lines) expansions, from the superpromotion model [7] (dotted lines), and from a CTMC calculation [8] (dashed lines).

show the calculated partial transfer cross sections into complete n shells of Be^{3+} from these calculations, along with the results from the earlier AO-expansion study [4]. Note that the results from the Gaussian expansion calculation [9] agrees very closely with the MO results at low energies and with the AO results at the higher energies, they are hence left out for n=3,4 in order to avoid clutter in the figure. These results show a few features which illustrate the merits and the limitations of the various theoretical models:

- Various versions (MO, AO, Gaussian) of close-coupling calculations agree very well among each other at overlapping energies.
- Typically and justifiably, MO calculations extend to lower energies and AO calculations to higher energies.
- Large-scale Gaussian basis calculations are perfectly suited for covering both the low- and the high-energy regime.
- MO calculations are not easily adapted to the determination the population of high-n states. This is less of a problem for AO calculations.
- For n=5, the MO results still agree closely with the results from the Gaussian expansion but both results deviate somewhat from the curve by the hidden-crossing model. It is not clear whether the results from both the MO and the Gaussian expansion suffer from a common problem, the trapping of electron flux that would go into other states if they existed in the calculation, or whether the description by hidden crossings becomes less reliable for n=5 and higher n shells.
- The method of hidden crossings treats the basic physics of slow collisions very well. Some deviations exist, however, to the results of close-coupling calculations.
- The CTMC is readily adapted to the determination of the population of high-n states.
- The results from the classical (CTMC) calculations links with the results from the close-coupling calculations at higher energies (above 50 keV/u). Large deviations exist at lower energies.

A unique feature of the hidden crossing theory in this case is a reversal of the order in which the n-shells are populated. According to ref. [7], the n=7 shell is more strongly populated than the n=6 shell. The authors of that work argue that this is due to the particular topology of the energy diagram of this collision system. On the other hand, the AO basis used in ref. [4] does include all states that are needed to represent this energy diagram in an approximate manner. It is hence not clear at this point why these two descriptions disagree on the relative population of n=6,7 shells.

Electron excitation in Be^{4+}– H collisions. Calculated excitation cross sections for the Be^{4+}– H system are displayed in Figure 2. It is seen that the undulatory structure of low-energy excitation cross sections from the earlier AO expansion calculation [4] is now confirmed qualitatively and also near-quantitatively in the new close-coupling calculations [6, 9]. This structure is also seen in the CTMC calculation [8] which, for excitation cross section, appears to hold to lower energies than in the case of electron transfer.[2]

[2]Schultz et al. [8] discuss also results from "another AO calculation by Fritsch" that is quoted by Krstić et al. [10]. We note that these results have been shown at an informal IAEA experts' meeting as preliminary. Their use in a publication has never been authorized.

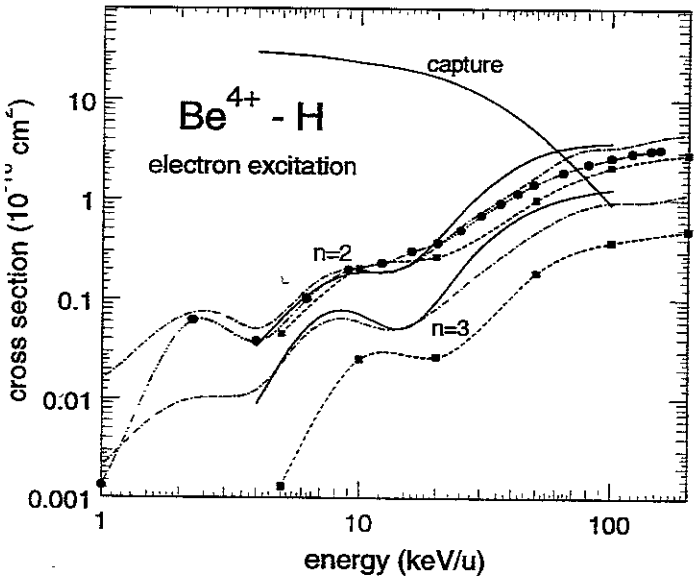

FIG. 2: Calculated excitation cross sections in Be^{4+}– H collisions, from close-coupling calculations with AO [4] (full lines), with Gaussian [9] (dash-dotted lines), and with MO [6] (dash-triple-dotted lines) expansions, and from a CTMC calculation [8] (dashed lines).

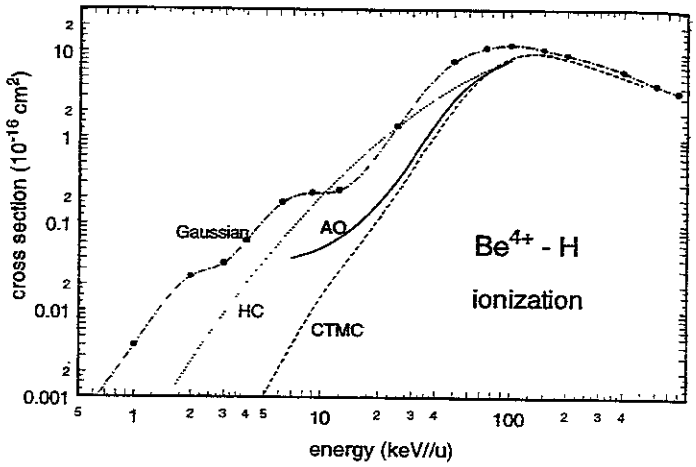

FIG. 3: Calculated ionization cross sections in Be^{4+}– H collisions, from close-coupling calculations with AO [4] (full lines) and with Gaussian [9] (dash-dotted lines) expansions, from the hidden crossing model [10] (dotted lines), and from a CTMC calculation [8] (dashed lines).

We hence note that the behavior of the excitation cross sections from the AO expansion work for a few A^{q+}–H systems, see the discussion in ref. [4], is now more plausible than before. At the higher energies, close-coupling calculations for excitation may become less certain when couplings to ionization sets in. On the other hand, the CTMC results should hold there and, at any rate, the various calculations in Figure 2 confirm each other mutually within an error band of some 40 percent.

The CTMC cross sections for excitation to the H n=3 states are about a factor of two smaller than both the results from the AO and the Gaussian expansion study. Because the states interact with more highly excited states in the transfer channel, the close-coupling results are less reliable than for the n=2 excitation channel. One may hence give preference to the CTMC results here. There are excitation cross sections up to the H n=8 shell in the CTMC work.

Ionization in Be^{4+}– H collisions. Calculated ionization cross sections are depicted in Figure 3. There is seen to be a wide gap between the cross sections from the hidden-crossing theory [10] and from the CTMC calculation which, however, closes at the higher energies. On the assumption that the CTMC is appropriate at higher energies and the hidden-crossing theory at lower energies, one would expect an interpolating curve between the two to be a good guess of the actual ionization cross section. The cross section from the AO expansion work [4], which is not published in ref. [4] but has been taken out from the population of pseudostates in that work, happens to look like such interpolating curve. On the other hand, the Gaussian expansion calculation shows a similar structure as the AO expansion calculation for ionization but the cross sections at low energy are about a factor of four larger. At even lower energies, the ionization cross sections from the Gaussian expansion calculation are distinctively larger than those from the hidden-crossing theory.

In this situation it is difficult to recommend a preferred curve for ionization cross sections at low energies. It is not clear whether the undulations in the results from the close-coupling calculations, notably thoses seen in the results from the Gaussian expansion, are real, or whether the ionization cross sections from the hidden-crossing theory should be preferred at low energies.

Errea et al. [6] argue that electronic flux into the highest states of their large-scale MO calculation, together with the cross section for the dominant transfer states, may be taken as total electron loss, due to a trapping effect into these high-lying states. This does not allow, however, to extract ionization cross sections at low energies where electron loss is essentially given by electron transfer processes.

Electron transfer in Be^{q+}– H collisions (q=2,3). The partial transfer and the excitation and ionization cross sections from the CTMC work [8] for these systems constitute new information, for energies and the range of n levels like in the case of Be^{4+}– H collisions. Based on the observations for the Be^{4+}– H system, the accuracy of these results at low energies may be only up to a factor of two. But these new results pose a challenge that other theories still have to meet.

3.1.2 B^{q+}– H collisions

The systems B^{q+}– H ($q = 1, 3, 5$) have been studied by Hansen et al. [11] with the AO expansion model. They present partial transfer cross sections for a few n shells and the respective ℓ subshells. For the singly charged B^+ projectile, transfer cross sections are also given for an excited H ($2s$) target. The system with $q = 5$ is included in the study by Errea et al. [6] within the MO expansion model, it also deals with the excited target state of H ($2s$). Shimakura et

al. [12] have studied a number of systems with a multistate MO expansion, among those they show results for the B^{3+}– H system.

In Figure 4 we show total transfer cross sections for the B^{3+} projectile. Also included is a curve that is generated

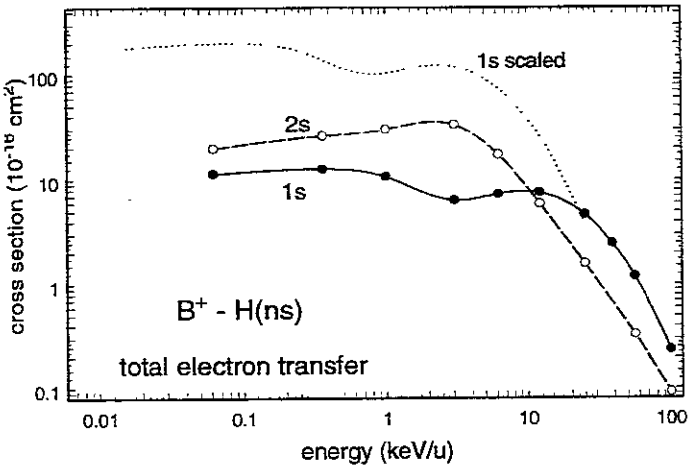

FIG. 4: Calculated total transfer cross sections in collisions between B^+ ions and H ($1s$) (full line) and H ($2s$) (broken line) targets, from close-coupling calculations with AO expansions [11]. The dotted line is the result of scaling the full line for a simple prediction of cross sections from an excited H (n=2) target.

from the cross sections for B^+– H ($1s$) collisions by dividing its energies by 4 and multiplying the cross sections by 3. This would be a simple but inadequate prediction of the B^+– H (n=2) cross section from the scaling rule [2], cf. eq. (1), which, however, is seen not to hold at this low charge state of the projectile, and not at low energies where transfer is dominated by the population of very few final states. This is why the calculation by Hansen and Dubois may be considered particularly useful. On the other hand, it is not clear how accurate the calculation is for H ($1s$) targets when multi-electron effects lead to final configurations like B ($1s^2 2s 2p^2$). Core-excited final states are not included in this calculation nor in any other calculation, but they may be excited in collisions with lowly charged ions.

About the B^{3+}– H system, we note that the total transfer cross sections from the MO calculations by Shimakura et al. [12] agree well with the results from the AO expansion calculation [11]. In the latter work, also partial transfer cross sections are given.

In Figure 5, we show the calculated total transfer cross sections for B^{5+}– H($1s$) and B^{5+}– H($2s$) collisions, from the close-coupling calculations with an AO expansion [11], a Gaussian expansion [9], and with an MO expansion [6], and from the hidden-crossing theory [10]. There is good agreement between the theories for the H ($1s$) target. The result for the H (n=2) target from the hidden crossing theory is seen to deviate largely from the result for a H ($2s$) target from the MO description. Note that these latter cross sections include only the n=6,7,8 states. The scaled cross sections, taken from the MO cross sections for an H ($1s$) target is reasonably close to the MO cross sections for a H ($2s$) target, lending support to that result. At the higher energies, this comparison suggests that the calculated transfer cross section for the H ($2s$) target underestimates the actual total transfer cross section into all states of the projectile.

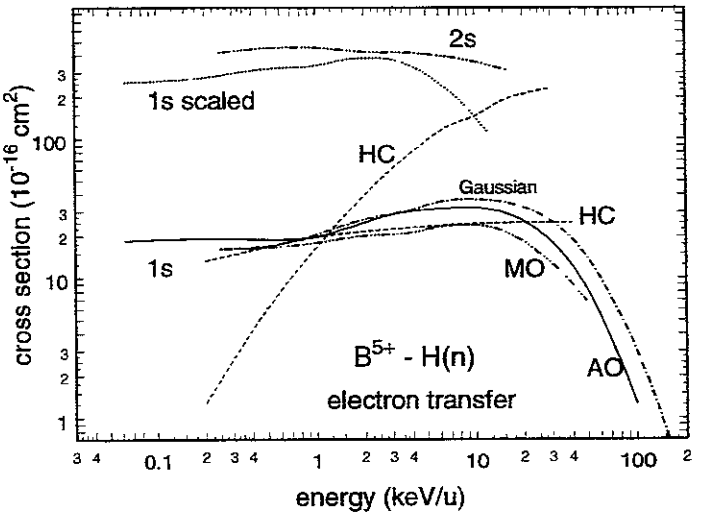

FIG. 5: Calculated total transfer cross sections in collisions between B^{5+} ions and H ($1s$) and H ($2s$) targets, from close-coupling calculations with an AO expansion (full line) [11], with a Gaussian expansion [9] (dash-dotted line), with an MO expansion (triple-dot-dashed line) [6], and from the hidden-crossing theory (broken line) [10]. The dotted line is the result of scaling the MO curve for a H ($1s$) target, for a simple prediction of cross sections from an excited H (n=2) target. The MO curve for the excited H ($2s$) target indicates the transfer cross section to the n=6–8 states only.

3.1.3 Si^{4+}– H collisions and other systems

Pieksma et al. [13] have studied the Si^{4+}– H collision system, for both hydrogen and deuterium targets, with quantal molecular-orbital close-coupling calculations. They find that below an energy of 1 eV/amu, the cross sections become dependent on the target isotope species, due to the effect of the attractive interatomic potential on the nuclear trajectory. At 0.01 eV/amu, the total transfer cross section for a deuterium target is predicted to be a factor of 2 smaller than the cross section for a hydrogen target. Absolute experimental data from the same group, taken with a deuterium target, confirm the calculations quantitatively at energies of 0.01 - 1000 eV/amu.

This work is an impressive example of the accuracy of state-of-the-art quantal close-coupling calculations at very low energies. A similar effect has been found in calculations for collisions between C^{3+} [14] and N^{4+} [15] ions and hydrogen and deuterium targets at energies below 10 eV/amu but the status of the experiments has yet precluded a confirmation of these predictions.

The C^{4+}– H system has been investigated [16] with a semiclassical molecular-orbital model at energies of 0.02 – 1 keV/u. The calculated state-specific cross sections agree with results from an earlier quantal calculation and with data.

The N^{2+}– H system has been investigated [14] with an improved quantal molecular-orbital calculation at energies of

0.1 - 100 eV/amu. The transfer cross sections are found to be significantly, and at the low energies actually drastically, reduced from what is known from previous calculations, see the discussion in ref. [14]

Finally, the C^{6+}– H, N^{7+}– H and O^{8+}– H systems have all been studied with Gaussian expansions [9], and electron transfer cross sections have been determined for the respective dominant capture shell n_0 up to n_0+2, along with excitation and ionization cross sections. A careful analysis of these results with respect to results from other investigations is still outstanding.

3.2 Collisions with helium

3.2.1 The role of transfer-excitation in slow collisions

Transfer-excitation processes have not been much investigated in the last two years. We take up this point because, in low-energy collisions, the population of a particular state in the transfer channel may be significantly altered when contributions from transfer-excitation processes are not considered.

An example is the case of slow He^{2+}– He collisions. As discussed in ref. [17], the population of He^+ $(n\ell)$ states in these collisions can be effected by single transfer (in the projectile) and by transfer-excitation processes (in the target). The molecular-orbital picture of the system suggests that, in slow collisions, both process are equally likely and hence the line emission cross section for the n=4 → n=3 line contains almost equal contributions from both processes. The total line emission cross section, thus calculated with the atomic-orbital expansion model, turns out to agree nicely with data [18].

In ref. [19], an assessment is given of the transfer-excitation cross section in the Be^{4+}– He and in C^{6+}– He systems. In these system, transfer-excitation is comparable in magnitude to the single-transfer process to, respectively, the second most and the third most important n shell of the projectile. It is well conceivable that for another system, under favourable conditions, transfer-excitation is more important, i.e. when the energy of transfer-excitation states closely matches the energy of the initial state at interatomic separations of 4 ~ 6 a.u.

In the recent work by Wang et al. [20], one- and two-electron processes in Be^{q+}– He and B^{q+}– He collisions ($q \geq 2$) are investigated with a one-electron model. For the two-electron transitions, the probabilities for two independent one-electron transitions are taken and multiplied, where these probabilities are determined in separate calculations fo the 'first' and the 'second' electron. This model description is expected to work well when a two-electron transition can be visualized as the sequential transition, in one collision event, of two electrons. On the other hand, this description will not work when, at low energies, the two-electron transition is driven predominantly by a favourable energy matching condition and hence both electrons may be visualized to move jointly. In Figure 6, this is illustrated for the process of transfer-excitation in Be^{4+}– He collisions, which has been investigated earlier with a two-electron AO description [19] and now also with the one-electron AO description by Wang et al. [20]. The transfer-excitation cross

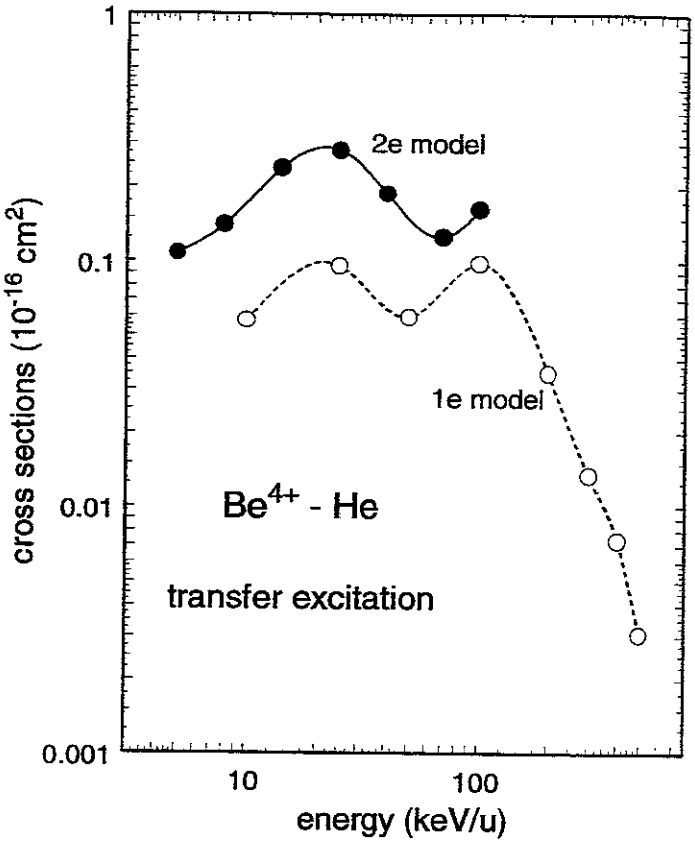

FIG. 6: Calculated cross sections for total transfer excitation to Be^{3+} $n\ell$ He^+ $n'\ell'$ configurations in Be^{4+}– He collisions, from close-coupling calculations with a two-electron AO expansion (full line) [19] and with a one-electron AO expansion (dashed line) [20].

sections from the two-electron model are seen to be much larger than the cross sections from the one-electron model at the lower energies but the gap appears to close at the higher energies. Curiously, the shape of the cross sections is about the same from both calculations.

3.2.2 Be^{q+} – He collisions

Be^{2+}–He collisions. The Be^{2+}– He collision system has been investigated now, for the first time, in three independent appproaches. A two-electron AO expansion [21] has been used for the determination of total and partial transfer cross sections. Total transfer cross sections have also been determined with a one-electron AO expansion [20] and with an MO expansion [12]. Wang et al. [20] investigate also the weaker cross sections for two-electron transitions. The total transfer cross sections from the two AO calculations turn out to agree nicely except at the higher energies, see Figure 7. The cross sections from the MO work are, however, much lower than from the AO works.

The probable reason for this drastic and unusual disagreement is a difference in the potentials adopted for the Be^{2+} core and hence a difference in the level structure of the collision system. For weak transitions, a slight change of the energy separation can lead to a large change of the tran-

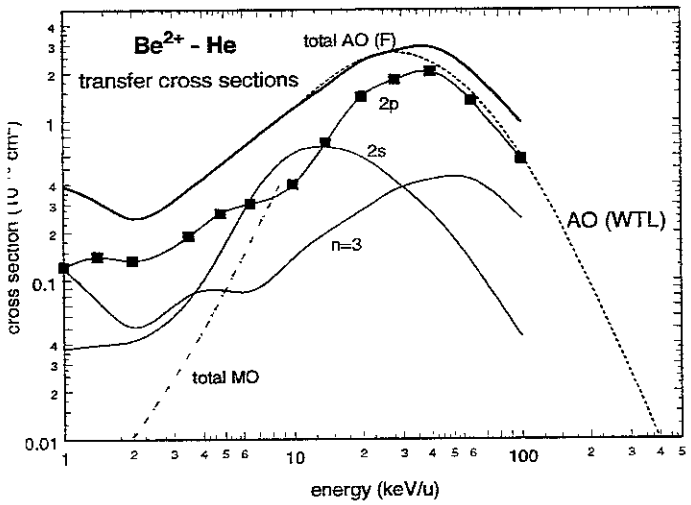

FIG. 7: Calculated total transfer cross sections in Be^{2+}– He collisions, from close-coupling calculations with a two-electron AO expansion (full line) [21] and with a one-electron AO expansion [20] (dashel line), and with an MO expansion (triple-dot-dashed line) [12]. The other lines are partial single transfer cross sections [21] to projectile states as specified in the figure.

ition probability in slow collisions. In the AO work [21], he experimental $2s$ binding energy of the Be^+ ion has been natched and the $2p$ energy reproduced to 1 percent. In the AO work, the authors state that they matched the expermental binding energies "generally within a few percent". Without knowledge of further details, it is hard to understand more closely the discrepancy at low energies.

As is seen in Figure 7, the single transfer is predicted in he AO calculation [21] to go predominantly into the Be^+ $2p$) state except in a narrow energy range where the $2s$ state lominates. An assessment of transitions to the n=3 shell s also given. The total two-electron transfer cross section s estimated to be roughly 2–7 $\times 10^{-18}$ cm^2 at 1–100 keV/u nergies [21]. According to the one-electron study [20], the ransfer-excitation and transfer-ionization cross sections are ctually the stronger two-electron channels. Both investigations with the AO expansion schemes derive excitation ross sections, Wang et al. [20] also show cross sections for onization.

Be^{3+}– He collisions. Shimakura et al. [12] show total single transfer cross sections for the Be^{3+}– He system in the same energy range as for the Be^{2+}– He system, which are rather flat and uneventful at about 1×10^{-15} cm^2. They connect with the cross sections by Wang et al. [20] above 10 keV/u from where on they become smaller with increasing energy. Again, Wang et al. [20] give also cross sections for excitation, ionization, and the transfer-excitation and transfer-ionization processes.

Be^{4+}– He collisions - electron transfer. The Be^{4+}– He system has been investigated with a two-electron AO expansion [19] and with a one-electron AO expansion [20], and with an MO expansion [12]. There is also earlier work on this system with an AO expansion [22] and with an MO expansion [23]. The results for single and for double electron transfer from these calculations are displayed in, respectively, Figures 8 and 9. For single electron transfer, all result

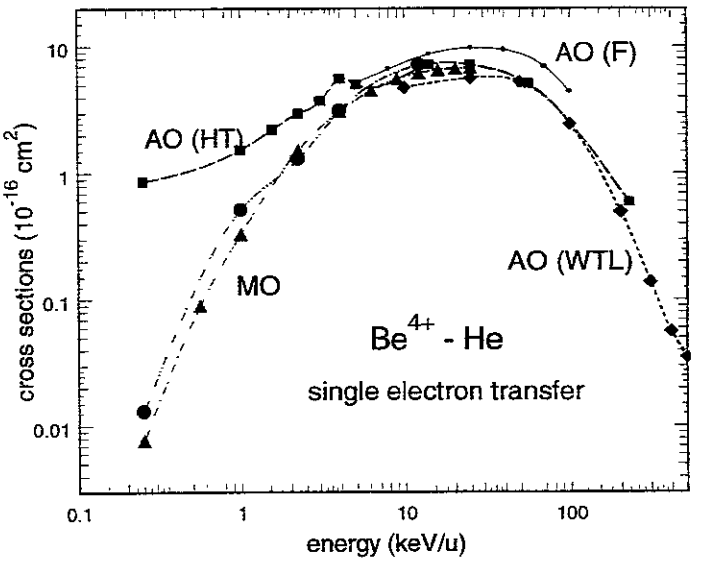

FIG. 8: Calculated single electron transfer cross sections in Be^{4+}– He collisions, from close-coupling calculations with two-electron AO expansions [19] (full line) and [22] (dashed line with squares), with a one-electron AO expansion [20] (dashed line with diamonds), and with MO expansions [12] (circles) and [23] (triangles).

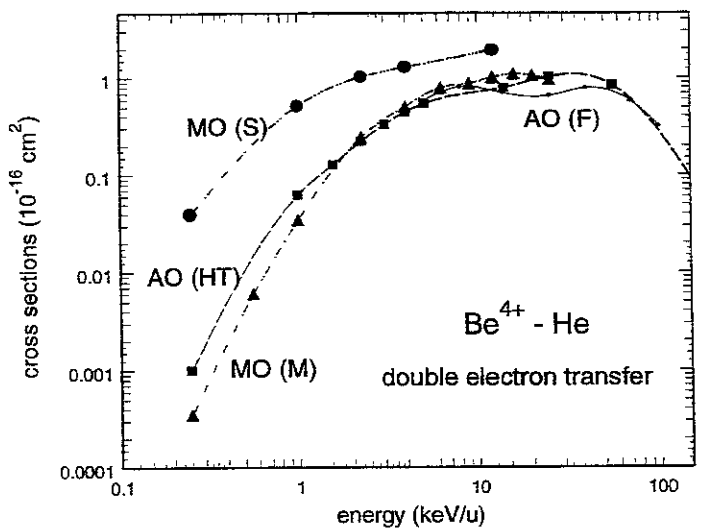

FIG. 9: Calculated double electron transfer cross sections in Be^{4+}– He collisions, from close-coupling calculations with AO expansions [19] (full line) and [22] (dashed line), and with MO expansions [12] (circles) and [23] (triangles).

are seen to agree reasonably well, except for the low-energy part of the curve due to Hansen and Taulbjerg [22] which not only deviates from the two MO curves but also shows an uncharacteristically flat behavior. Note that the two-electron AO calculation by Fritsch [19] contains many more n capture shells than the other calculations. The deviation between the transfer cross section from this work and the

other works at the higher energies, up to about a factor of two, is surprising and not accounted for.

The double transfer cross section from the MO calculation by Shimakura et al. [12] appears to be too large in comparison to the results in the other studies. As these authors do not state all the details of their calculations, it is hard to understand this discrepancy. On the other hand, the other studies agree well on double electron transfer.

Partial transfer cross sections have been determined not only for the leading capture channels of Be^{3+} (n=2,3) [22] but also for the higher n shells up to n=6 [19]. For the purpose of plasma diagnostics, information on the population of even higher n states is needed [1]. With present computation facilities, it seems hardly feasible to include that many states in a full two-electron close-coupling calculation.

We have therefore set up to determine partial transfer cross sections to high-n states in a *one-electron calculation* and to include effects of the second electron in a second step. The dynamics of the electron is hence studied in the field of the He^+ core and the Be^{4+} nucleus. We have adopted a conventional exponentially screened Coulomb potential for the He^+ core, and a basis of all AO capture states for n=1–9, as well as a set of states at the target which represent the He ground state, the first excited states and pseudostates.

The partial transfer cross sections from this new one-electron calculation are compared, in Figure 10, with the results from the earlier two-electron calculation [19]. The general features from both calculations are about the same, except that the cross over between the curves for n=2 and n=3 in the two-electron calculation does not occur in the one-electron calculation. Also, there is a slightly different behavior between the curves for n=4–6 at low energies.

There are a few ways in which one can try to correct the results of the one-electron calculation for the presence of a 2nd electron that can undergo transitions. A purely statistical argument would lead to strong two-electron transfer cross sections, it would be unphysical since the second electron sees less attraction by the projectile. A separate determination of the transition probability for the second electron, after the first electron has transferred, like in the work by Wang et al. [20], would lead to another large calculation. For the purpose of improving on the cross sections for the high-n transfer states, we observe that the *ratio* of partial transfer cross sections σ_n for adjacent shells n, σ_{n+1}/σ_n, is very close between the one-electron and the two-electron calculation. A simple raise of the partial transfer cross section from the one-electron calculation by a factor of 1.5 would hence bring all cross sections from the one-electron model to a close agreement with the results from the two-electron calculation. Taking a simple overall factor would also reflect the expectation that the main deficiency on the one-electron model occurs in a first step when the electron changes partner. The rearrangement of the electron between the final states in the projectile should be one-electron process that is correctly described in the one-electron calculation.

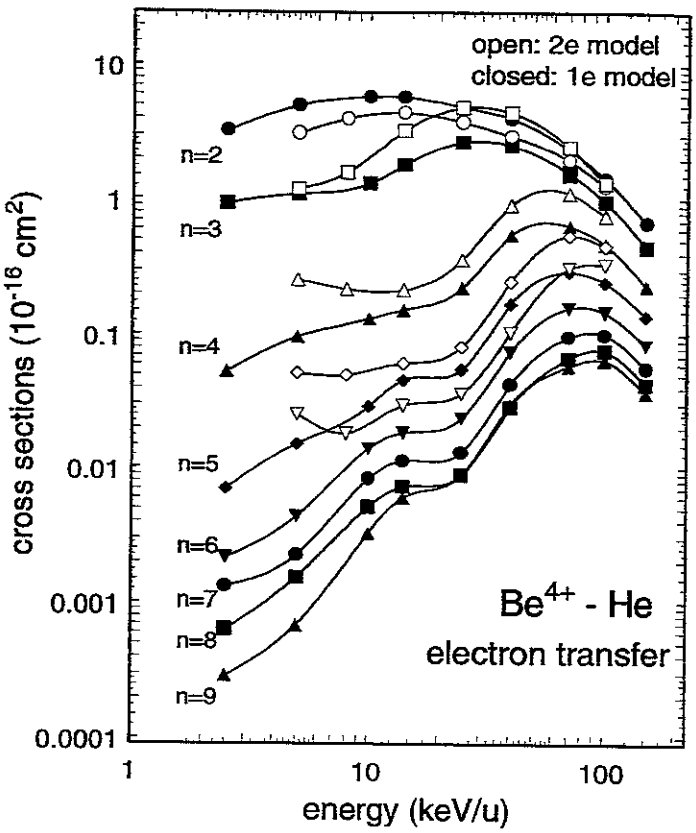

FIG. 10: Calculated electron transfer cross sections to Be^{3+} n shells in Be^{4+}– He collisions, from close-coupling calculations with two-electron AO expansions [19] (open symbols), and with one-electron AO expansions [24] (closed symbols). Note that these latter results from the one-electron model are not yet corrected for the presence of a 2nd electron, they need to be raised by a factor of 1.5, see text.

Be^{4+}– He(1s2s) collisions - electron transfer. In this one-electron calculation for Be^{4+}– He collisions, electron transfer cross sections have also been determined for an initially excited He ($1s2s$) 2^1S target. The results are displayed in Figure 11. The transfer cross sections are seen now to peak

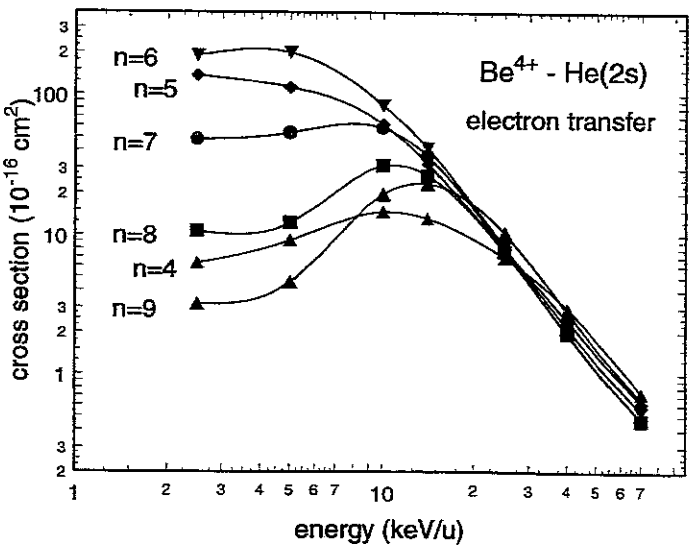

FIG. 11: Calculated electron transfer cross sections to Be^{3+} n shells in Be^{4+}– He($2s$) collisions, from close-coupling calculations with a one-electron AO expansion [24].

it n=6 at the low energies. The transfer cross sections to he high-n states are 1~2 orders of magnitude larger than he corresponding cross sections for ground-state He. A mall admixture of metastable He in the neutral beam can ience considerably change the spectra of charge-exchange pectroscopy.

In Figure 12, we compare the calculated n-distribution n Be^{4+}– He($2s$) collisions, at 10 keV/u, with the result rom a CTMC study [25] which has been performed for a umber of A^{Z+}– He(n = 2) systems. The agreement is

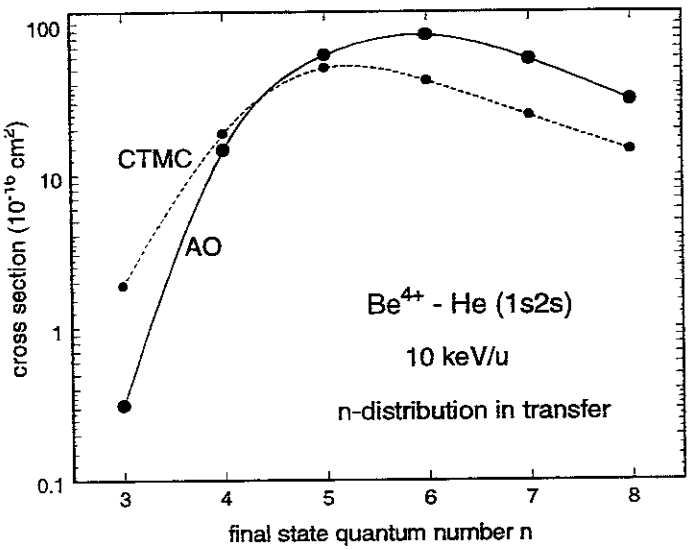

FIG. 12: Calculated n-distribution of electron transfer cross sections in Be^{4+}– He($2s$) collisions, from close-coupling calculations with a one-electron AO expansion [24] (full line), and from a CTMC study [25] (dashed line).

only qualitative. A plausible explanation would be that this energy is too low for the CTMC calculation to be fully reliable.

In Figure 13, we present, in a scaled plot, cf. eq. (1), the total transfer cross sections from the CTMC study [25], for a He(n=2) target, together with the results from the AO studies for Be^{4+} [24] and for He^{2+} [17] projectiles, the latter two for a He($2s$) target. The total transfer cross sections from the CTMC study for bare ions between Z=3 and 8 are all seen to lie, within a factor of two error, on a common curve. The two results from the respective AO studies are also very close to each other and slightly below the CTMC results at the high energies. At the low energies below some 25 keV/u scaled energy, the cross sections from the AO studies lie above the results from the CTMC study, suggesting that the CTMC description is less appropriate there.

One may wonder whether the results for a He($2s$) target (AO) and for a He(n=2) target (CTMC) can be expected to be reasonably close. Figure 14 shows that this is indeed the case. It shows calculated total transfer cross sections in H^+– H(2ℓ) collisions for a $2s$ target and for a statistical mixture of 2ℓ targets, from an AO close-coupling study [26]. The cross sections with both choices of target configuration are seen to be rather close, and certainly closer than the discrepancies that have been discussed for the low energies in the case of an excited He target, cf. Figure 12.

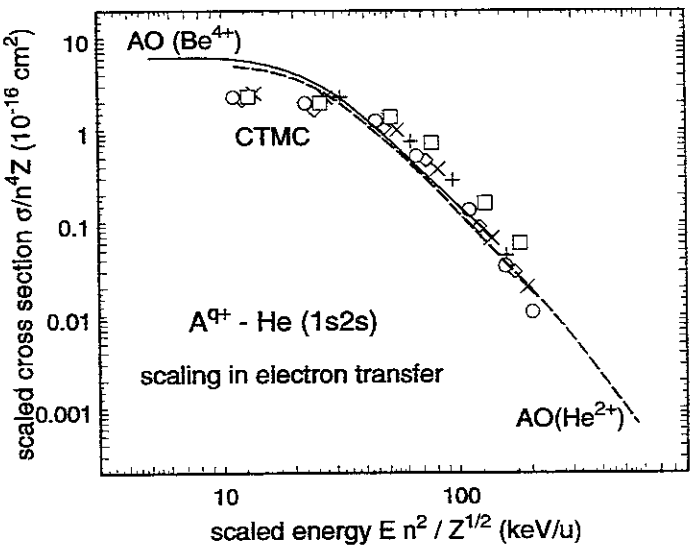

FIG. 13: Scaled plot of calculated electron transfer cross sections in A^Z– He($2s$) collisions, from close-coupling calculations for Be^{4+} [24] (full line) and He^{2+} [17] (dashed line) projectiles, and from a CTMC study [25] for Li^{3+} (+), Be^{4+} (×), B^{5+} (◇), C^{6+} (○), and O^{8+} (□) projectiles.

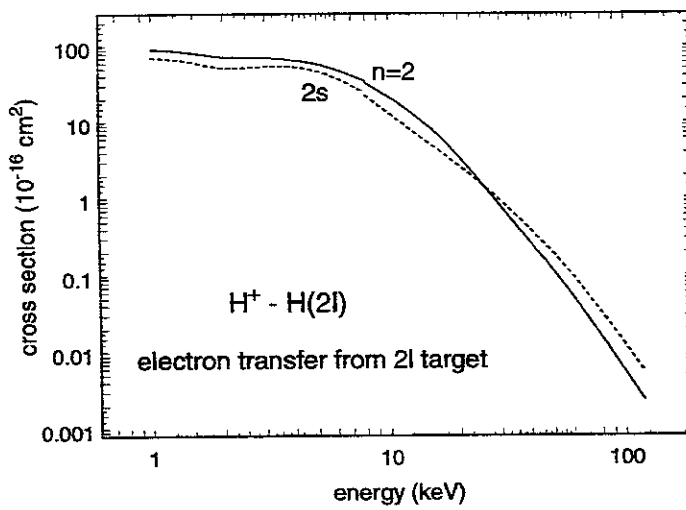

FIG. 14: Calculated cross section for total electron transfer in collisions between a H^+ ion and an excited H (n=2) target (solid line) and an excited H ($2s$) target (broken line) [26].

Be^{4+}– He(n) collisions - electron excitation. The excitation process in Be^{4+}– He(n = 2, 3) collisions has been studied with the Born and Glauber high-energy theories [27]. The authors state in their work that they are not convinced of the accuracy of their results at the lower energies of their investigation. In Figure 15 we compare their result for the He (n=2) initial configuration with the results from the AO expansion study [24], for a He ($2s$) initial state. The results from both independent studies are found to confirm each other mutually, if the Glauber theory is adopted at the higher energies.

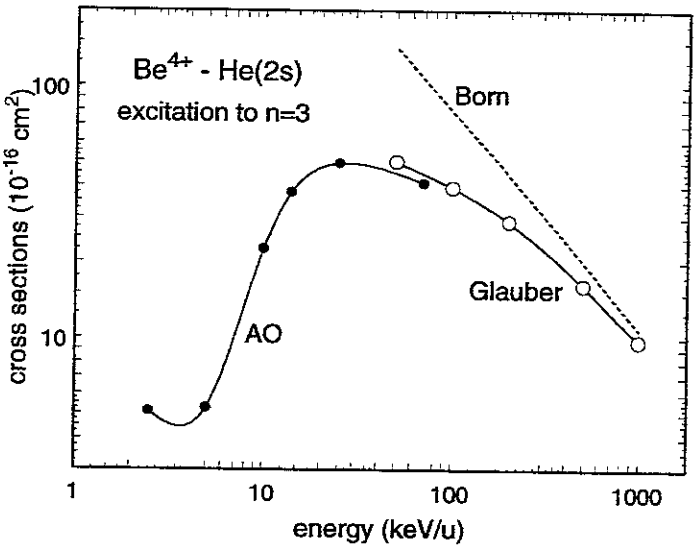

FIG. 15: Calculated electron cross sections for electron excitation to the He (n=3) shell in Be^{4+}– He($2s$) collisions, from close-coupling calculations with a one-electron AO expansion [24], and from the Born and the Glauber approximations [27]. Note that the latter calculations assume an initial He (n=2) configuration.

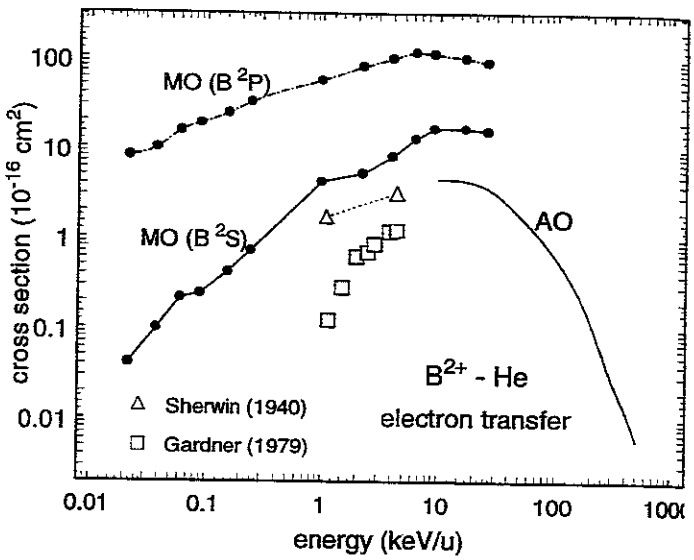

FIG. 16: Calculated electron cross sections for total electron transfer in B^{2+}– He collisions, from MO close-coupling calculations [28] for the B^{2+} ^2S ground state (solid line with dots) and the B^{2+} ^2P excited state (dash-dotted line), and from a one-electron AO calculation [20] (solid line). Data are by Sherwin [30] (triangles) and by Gardner et al. [29] (boxes).

3.2.3 B^{q+}– He collisions

The B^+– He system has been investigated for the first time now, in the AO expansion work by Hansen and Dubois [11], at energies of 0.1 – 100 keV/u. The total transfer cross sections are rather small and originate predominantly from the population of the B ground state. It is not known how accurate the one-electron description is in this case but the calculated cross sections are certainly a good estimate of what a much more involved theory might give.

Total and state-specific cross sections are also given in ref. [11] for electron transfer from the initially excited He ($2s$) state.

The B^{2+}– He system has been studied with an MO expansion scheme [12, 28] at energies of 0.02 – 10 keV/u, and with a one-electron AO expansion scheme at 10 – 500 keV/u [20]. The total electron transfer cross sections from the MO work turn out to be much larger than the data by Gardner et al. [29], and a little larger than the previous, rather old data by Sherwin [30], see Figure 16. On the other hand, the transfer cross section from the AO work is about a factor of four smaller than from the MO work, it can be thought to connect to either of sets of experimental data.

It is hard to understand the discrepancy between the results from these two theories. The MO investigation uses a consistent two-electron expansion scheme and energies that closely match the experimental binding energies. The AO expansion work, while addressing the systematics of a number of systems, may be thought inferior for this particular system on both counts, it uses a one-electron expansion and slightly less realistic energies. In another restriction, the AO work uses a B^{2+} potential that is taken to represent the *singlet* capture states, not the triplet states which are statistically more probable. Still the AO expansion work leads to transfer cross sections that are in harmony with the data. More work is needed to resolve this puzzling situation.

In the MO study, the transfer cross section for an initially excited projectile of B^{2+} ($1s^2 2p\ ^2P$) is also studied and found to be much larger than the cross section for the ground-state projectile. In ref. [28], the cross section for exciting the projectile from its ground state to its excited ^2P state is also given.

The B^{3+}– He system has also been investigated in refs. [12, 28, 20], in another MO work [31], and in the AO expansion work by Hansen and Dubois [11]. These studies agree largely with previous work on total electron transfer at energies of 0.05 – 200 keV/u, except for the data by Gardner et al. [29]. The theories [28, 11] also agree on the relative cross sections of the predominantly populated final states of B^{2+} ($2s$) and ($2p$). In the AO expansion work [11], the partial transfer cross sections into the n=3 states are also given, and so are excitation, ionization, transfer-excitation and transfer-ionization cross sections in ref. [20].

The B^{4+}– He system is included in the systematic investigation by Wang et al. [20], which again covers the energy range of 10 – 500 keV/u.

The B^{5+}– He system has been investigated with the AO expansion models by Hansen and Dubois [11] at energies of 0.06 – 220 keV/u, and by Wang et al. [20] at 10 – 500 keV/u. In the work by Hansen and Dubois, single-electron transfer to the n=3 states is seen to dominate here but double electron transfer to doubly excited states is also given and shown to be of the order of 10 percent of the single transfer cross section. Wang et al. agree on the total single electron transfer cross section, they also give the excitation, ionization, transfer-excitation and transfer-ionization cross sections.

Igarashi and Shirai [27] have determined the electron excitation cross sections in B^{5+}– He($n = 2, 3$) collisions with the

ıigh-energy Glauber approximation. Based on the situation ʼor the Be^{4+} projectile, cf. Figure 15, one would expect that ılso these results are reliable down to energies of 50 keV/u.

3.2.4 C^{q+} – He collisions

ʒingle and double electron transfer in 0.05 – 5 keV/u C^{4+}– Ie collisions has been studied [32] with an MO expansion nethod. Total transfer and state resolved cross sections are ɡiven. There is general agreement with an earlier AO expan- ıion study but disagreement with an earlier MO expansion ıtudy, see the discussion in ref. [32].

The C^{5+}– He system has been studied anew with the AO ɔxpansion scheme [33]. This study is similar to an earlier nvestigation [22] but it adds the transfer-excitation pro- ɔess, which competes with double electron transfer, and also ıdopts a more realistic exponentially screened potential for .he projectile ion. An overview of the calculated cross sec- ıions is given in Figure 17. The cross sections are seen to

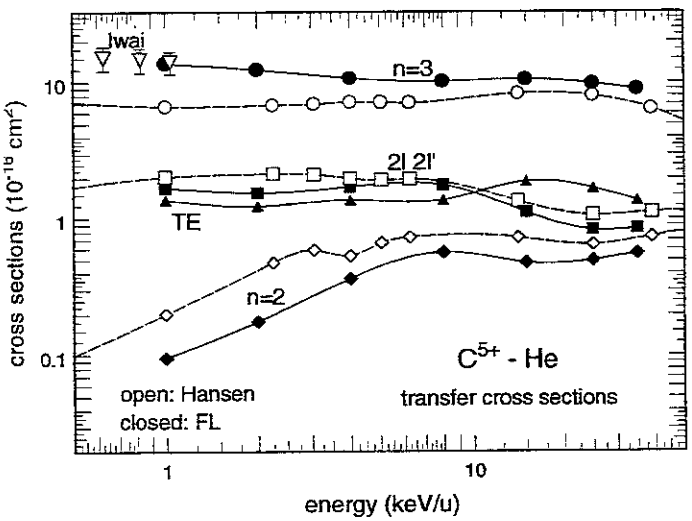

ʔIG. 17: Calculated electron cross sections in C^{5+}– He collisions, ırom close-coupling calculations with AO expansions [33] (closed ɜymbols) and [22] (open symbols), for single electron transfer to ɪ=2,3 states, for double electron transfer to $2\ell 2\ell'$ states, and for ıransfer-excitation (TE) configurations. Data is by Iwai et al. 34] (inverted triangles).

ɔe different, up to a factor of two, between the two calcula- ıions. There is a much larger difference in the partial trans- ʼer cross sections, notably for the single transfer channel to ɔhe C^{4+} 3*s* state. For the partial transfer cross sections in ɔhe double transfer channel for which there is data, the in- ɔlusion of transfer-excitation channels in ref. [33] leads to ɔlose agreement with data, see the discussion in ref. [33].

Partial transfer cross sections for a number of one- and ɜwo-electron transitions in C^{6+}– He collisions have been de- ɜermined with the AO expansion model [19]. Single transfer ɔo the dominant channel of C^{5+} (n=3) up to the n=7 shell ıas been included in this work.

3.2.5 N^{+} – He collisions

N^{+}– He collisions at energies of 0.03 – 7 keV/u have been ɜtudied with the MO expansion method [35]. Electron transfer cross sections have been determined for the projectile in its ^3P ground state and in its ^5S excited state. The agreement with data for the projectile in its ground state is rather good, and another set of data with a mixture of the two projectile states is explained. Also the projectile excitation cross section to its ^3D state is determined.

3.2.6 O^{5+} – He collisions

The O^{5+}– He collision system has been studied [36] at 0.06 – 11 keV/u with the MO expansion model. The authors show that single electron transfer to the O^{4+} ($2s3\ell$) states dominates at these energies. They also asses the magnitude of transfer channels ($2p3\ell$) that are accompanied by projectile excitation, and the cross section for excitation of the projectile.

4 Summary and Conclusions

In the past two years, there have been more than 30 new theoretical investigations on slow collisions between plasma impurity ions and H or He gases. They are done with the close-coupling method using molecular-orbital or atomic-orbital expansion schemes, the latter including Gaussian basis sets, or with purely classical (CTMC) descriptions. There is particularly much work on systems with Be^{q+} and B^{q+} ions. As highlights in these investigations we note the following:

- a few investigations on lowly charged systems for which total transfer cross sections *cannot* be derived from equicharged systems;
- a few studies have been undertaken at very low, near-thermal energies;
- some of these investigations include the determination of transfer cross sections into high-n shells of the ions; this has been done, in one instance, even with a molecular-orbital expansion;
- in some investigations which include large basis sets, the target gas has been investigated also in an initially excited state; the scaling of cross sections in these systems, which is based on CTMC work, has been confirmed, except at low energies;
- there is more work now on electron excitation in these systems; structures in the excitation cross section at low energies appear now to be confirmed by a few independent calculations.

Despite of all this progress, the data basis for the systems of interest is still far from being complete. In slow collisions, theory still finds it hard to determine ionization cross sections reliably. The data basis is particularly weak at very low energies. But even in the keV/u energy region, total transfer cross sections are not well established for some specific systems like B^{2+}– He.

In some of the investigations which are specifically done for the needs of the plasma physics community, the authors present their results but barely discuss them. In some investigation, the calculations are not described to all details.

Moreover, some of the investigations of the past two years have looked into the same systems independently. Therefore, some effort is needed to evaluate the results of all these works. This report is one step in this direction but its scope has been limited to a few prominent example systems. More work is needed to gain the full benefit, from all of these investigations, for the atomic data basis for fusion purposes.

Acknowledgements

We gratefully acknowledge support by the National Institute for Fusion Science Nagoya, Japan, where most of the calculations by the authors were performed. We also acknowledge the assistenance of the authors who sent preprints of their respective works, especially works that are now published in the special issue of Physica Scripta, volumn T62, as well as the active encouragement by R.K. Janev who has inspired much of that work.

References

[1] R. Hoekstra, in *The Physics of Electronic and Atomic Collisions*, eds. L.J. Dubé et al., AIP Conf. Proc. **360**, American Institute of Physics, Woodbury, N.Y., 1995, p. 547.

[2] R.K. Janev, HP. Winter, W. Fritsch, chapter 13 in *Atomic and Molecular Processes in Fusion Plasmas* (ed. R.K. Janev), Plenum, New York (1995), p. 341.

[3] H. Tawara, NIFS report NIFS-DATA-12, National Institute for Fusion Science, Nagoya, Japan, 1991.

[4] W. Fritsch, in *VIth Int. Conf. on the Physics of Highly Charged Ions* (eds. P. Richard et al.), AIP Conf. Proc. **274**, New York 1993), p. 24.

[5] R.A. Phaneuf, R.K. Janev, H. Tawara, M. Kimura, P.S. Krstic, G. Peach, M.A. Mazing, *Atomic and Plasma-Material Interaction Data for Fusion (Nucl. Fusion Supplement*, **3** (1992) 105.

[6] L.F. Errea, J.D. Gorfinkiel, C. Harel, H. Jouin, A. Macias, L. Méndez, B. Pons, A. Riera, Physica Scripta **T62** (1996) 33.

[7] R.K. Janev, E.A. Solov'ev, G. Ivanovski, Physica Scripta **T62** (1996) 43.

[8] D.R. Schultz, P.S. Krstić, C.O. Reinhold, Physica Scripta **T62** (1996) 69.

[9] N. Toshima, H. Tawara, NIFS reportNIFS-DATA-26, National Institute for Fusion Science, Nagoya, Japan, 1995.

[10] P.S. Krstić, M. Radmilovic, R.K. Janev, *Atomic and Plasma-Material Interaction Data for Fusion (Nucl. Fusion Supplement*, **3** (1992) 113.

[11] J.P. Hansen, A. Dubois, Physica Scripta **T62** (1996) 55.

[12] N. Shimakura, S. Suzuki, Y. Murakami, J.P. Gu, G. Hirsch, R.J. Buenker, K. Kimura, I. Shimamura, Physica Scripta **T62** (1996) 39.

[13] M. Pieksma, M. Gargaud, R. McCarroll, C.C. Havener, Phys. Rev. A **54** (1996) R13.

[14] B. Herrero, I.L. Cooper, A.S. Dickinson, D.R. Flower, J. Phys. B **28** (1995) 4607.

[15] P.C. Stancil, B. Zygelman, Phys. Rev. Lett. **75** (1995) 1495.

[16] B. Saha, Phys. Rev. A **51** (1995) 5021.

[17] W. Fritsch, J. Phys. B **27** (1994) 3461.

[18] H.O. Folkerts, F. Bliek, R. Hoekstra, J. Phys. B **27** (1994) 3475.

[19] W. Fritsch, Nucl. Inst. Meth. in Physics Research B **98** (1995) 246.

[20] Y.D. Wang, N. Toshima, C.D. Lin, Physica Scripta **T62** (1996) 63.

[21] W. Fritsch, Physica Scripta **T62** (1996) 59.

[22] J.P. Hansen, K. Taulbjerg, Phys. Rev. A **47** (1993) 2987.

[23] F. Martin, A. Riera, M. Yanez, Phys. Rev. A **34** (1986) 4675.

[24] W. Fritsch, *Proc. 8th Int. Conf. on the Physics of Highly Charged Ions*, Omiya 1996, to be published in Physica Scripta.

[25] L. Salasnich, F. Sattin, Phys. Rev. A **51** (1995) 4281.

[26] W. Fritsch, JET report JET-R(94)05 (1994) 1.

[27] A. Igarashi, T. Shirai, Physica Scripta **T62** (1996) 95.

[28] M. Kimura, S. Suzuki, N. Shimakura, J.P. Gu, G. Hirsch, R.J. Buenker, I. Shimamura, Phys. Rev. A **54** (1996) in press.

[29] L.D. Gardner, J.E. Bayfield, P.M. Koch, I.A. Sellin, D.J. Pegg, R.S. Peterson, M.L. Mallory, D.H. Crandall, Phys. Rev. A **20** (1979) 766.

[30] C.W. Sherwin, Phys. Rev. **57** (1940) 814.

[31] A. López-Castillo, F.R. Ornellas, Phys. Rev. A **51** (1995) 381.

[32] L.F. Errea, B. Herrero, Méndez, A. Riera, J. Phys. B **28** (1995) 693.

[33] W. Fritsch, C.D. Lin, Phys. Rev. A in press.

[34] T. Iwai, Y. Kaneko, M. Kimura, N. Koboyashi, S. Ohtani, K. Okuno, S. Takagi, H. Tawara, S. Tsurubichi, Phys. Rev. A **26** (1982) 105.

5] M. Kimura, J.P. Gu, G. Hirsch, R.J. Buenker, Phys. Rev. A **51** (1995) 2063.

5] N. Shimakura, S. Yamada, S. Suzuki, M. Kimura, Phys. Rev. A **51** (1995) 2989.

REARRANGEMENT REACTIONS IN ION-ION AND ION-ATOM COLLISIONS: RESULTS AND PROBLEMS

L.P.Presnyakov and H.Tawara***
*Lebedev Physical Institute, Moscow 117924, Russia
**National Institute for Fusion Science, Nagoya 464-01, Japan

Abstract

Recent experimental and theoretical results are discussed for ionic collisions with large cross sections at intermediate and small energies of the relative motion. Single- and double-electron removal from H^- ions in slow collisions with other ions is considered in more details. The theoretical methods are discussed from the viewpoint of general requirements of scattering theory.

Introduction

In hot hydrogenic plasmas with an impurity content of heavier elements, the emission spectrum and the distribution of the impurity ionization stages are largely determined by electron impact processes. There are, however, particular instances where transitions are caused preferentially by atom, proton and other ion impacts. In additional to modifying the plasma characteristics, such transitions have a special utility as diagnostics probes of the heavier component of the plasma. The importance of the proton impact processes has been pointed out by Seaton [1] and Dalgarno [2] long ago. The role of ion-atom collisions in fusion and astrophysical plasmas is also well understood, especially for

emissivity and energy loss from the plasmas and for the NBI problems (see, for example [3-4]).

The ion-ion collisions may be important if their cross sections are large. The typical examples are the processes involving the negative ions in collisions with other ions (both positively and negatively charged). In collisions between two highly charged ions, the cross sections may be large for symmetric resonant and for quasi-resonant processes.

In the present paper, we discuss single- and double-electron detachment in collisions of H^- ions with HCl,

$$H^- + X^{q+} \text{-------} H^0 + ... \qquad (1)$$

$$H^- + X^{q+} \text{-------} H^+ + ... \qquad (2)$$

with other H^- ions,

$$H^- + H^- \text{---------} H^0 + H^- + e \qquad (3)$$

$$H^- + H^- \text{---------} H^0 + H^0 + 2e \qquad (4)$$

and quasi-resonant charge transfer,

$$X^{q+} + Y^{(q-1)+} \text{------} X^{(q-1)+} + Y^{q+} \qquad (5)$$

$$Y^{q+} + X^{(q-1)+} \text{-------} Y^{(q-1)+} + X^{q+} \qquad (6)$$

at intermediate and small energies of the relative motion. Both experimental and theoretical results are considered. In order to illustrate one of the theoretical methods used, we discuss also single- and double-ionization of He atom under heavy-ion impact,

$$He + X^{q+} \text{-----} He^+ + ... \qquad (7)$$

$$He + X^{q+} \text{ ----- } He^{2+} + ... \qquad (8)$$

The rest of the paper is as follows. The part 1 contains a description of the recent experimental data jointly with theoretical calculations. The main attention is taken to the physical mechanisms of the processes. The part 2 is devoted to discussion on the theoretical methods involved.

1. Experimental Data and Theoretical Calculations

At present time, only a few sets of experimental data are published on ion-ion collisions, however, they demonstrate the most interesting features of the processes. The theory of ion-ion collisions is a natural continuation of the general theory of atomic collisions in which " fast" and "slow" collisions are analyzed with the help of one-center (atomic)and two-center (molecular) approaches, respectively. The theoretical analysis below is based on the references [5-9] and [14-16], and the original experimental data are taken from the references [14-19].

1.1. Single- and double-electron detachment in collisions of H^- ions with multiply charged ions

The experimental data are published for single-electron removal only. Medium-energy collisions with rare-gas ions ($q < 9$) have been investigated by Salzborn's group [15], and slow collisions with He^+ by Brouillard's group [17-18] and by Peart and Bennet [19]. The data jointly with theoretical calculations for single-electron removal at intermediate energies [15] and for single- and double-electron detachment at slow collisions [5] are given in Fig.1. Altogether, the resulting curves help to understand the physical mechanisms of the processes. At fast collisions, the one-

center approach with non-stationary continuum-distorted waves [11,15] shows that the leading mechanism is through- and over-barrier transmission of the electron in the time-dependent field of the projectile. The main process is the electron transition into continuum. At slow collisions, however, is charge transfer with capturing the electron into Rydberg states of the projectile. The two-center approach [5-6] based on the exact analytic solution of the quasi-molecular problem (eigenfunctions and eigenstates) for the model Hamiltonian describes pseudo-crossings and other characteristics of the regions of non-adiabatic transitions. Very large values of the single-electron cross sections at very small velocities have a simple kinematic explanation: in the Coulomb attraction field, the effective impact parameter is larger than the distance of the closest approach. The double-electron capture can be considered as a product of two single-electron ones because the non-adiabatic regions for transitions of "inner" and "outer" electron are well separated spatially. Thus, the problem is reduced to calculations of the transition amplitudes in H^0 -HCI collisions. The scaled velocity in Fig.2 is appropriate for charge-transfer (slow collisions). For fast collisions, detachment into continuum predominates, and the scaled velocity should be $v/q^{0.5}$ [11,15]. Smallness of the ratios of double-to-single electron detachment (Fig.2) shows that highly charged ions could be used for neutralization of H^- beams with great efficiency because the single-electron cross sections are very large.

1.2. Mutual neutralization in collisions of two negative ions: single- and double-electron processes

In this case, the experimental data are available for both reactions, (3) and (4) at center-of-mass energies between 2.5 and 100 keV [14]. The calculations have been done also for both processes at the energies from 2.5 eV to 300 keV [5,14]. At small velocities

[5], the leading mechanism is the initial-state promotion into continuum. When R is equal or less than 36 a.u., there is promotion into so-called one-electron continuum, after intersection with the ground state of the $H\text{-}H^-$ system. (It is worth to note that the negative hydrogen-molecule ion has no stable states, and was never observed as a molecule.) At the distance of about 18 a.u., the H^- level intersects the ground- state level of the neutral Hydrogen molecule, and goes into two-electron continuum. The physical picture of the single- and double-electron removal is exactly the same as described for medium velocities (see [14] references therein to earlier works of other authors). In present paper, we employ just another way for the calculations of the autoionization widths on the base of the two-center model Hamiltonian [5] instead of the modified perturbation theory [14]. The calculations for the "outer" electron detachment have been done with using the Coulomb-repel trajectory, and for the "inner" one, the straight-line path is appropriate. The results are given in Fig.3 for cross sections and in Fig.4 for the ratios. It is of interest the ratio maximum follows from the calculations of the double-electron detachment [14] due to transitions to double-electron continuum. When we compare pure experimental results, the ratio curves is much more smooth.

1.3. Quasi-resonant charge transfer between positively charged ions

Using a crossed-beams technique, the Salzborn's group [16] have measured absolute cross sections for the quasi-resonant charge transfer reaction,

$$C^{2+} + B^{+} \text{ ------ } C^{+} + B^{2+} - dE, \qquad (9)$$

by coincident detection of the product ions for CM-energies between 1.3 and 160 keV. The inverse reaction,

$$B^{2+} + C^{+} \text{ ------- } B^{+} + C^{2+} + dE, \qquad (10)$$

was also investigated in the energy range between 2.5 and 80 keV. In this case, the energy difference (so called resonance defect) was very small, dE = 0.77 eV. The theoretical calculations [16] are in good agreement with the experimental data.

The results for the direct reaction (9) and for the inverse one (10) are given in Figs. 5 and 6, respectively. The calculations are based on the same principles of the theory of non-adiabatic collisions as it was pointed out above: a) establishing the regions of non-adiabatic transitions, b) analysis of matrix elements and other parameters in those regions, and c) solving the close-coupling equations for the transition amplitudes. The problems a) and b) were solved analytically, and c) by means of numerical methods. The possible role of metastable ions in the beams was also investigated. The main conclusions are as follows. The direct reaction (9) and the inverse (10) are not connected to each other by the statistical-weight ratio of the ground states of the colliding ions. It means that the different channels are responsible for the direct and inverse reactions. In this case of many-electron ions, the reaction (9) involves mainly the singlet ground states of both ions, whereas the reaction (10) populates also the triplet (metastable) state of the B^{+} ion. For these processes, Coulomb repel is important at energies below 0.5 keV. Large values of the cross sections indicate importance of the quasi-resonant processes for determining the characteristics of hot plasmas.

1.4. Ion-atom collisions: single- and double-ionization of He by heavy ion impact

Concluding the brief overview of the experimental data available jointly with their theoretical interpretation, we discuss also the ratios of the cross sections of the processes (8) and (7). The corresponding cross sections and their ratios have been calculated recently [8] for projectiles with the charge values, q, from q=6 to q=90, at energies between 3 and 1300 MeV/amu. For these calculations, a new modification of the non-stationary continuum-distorted wavefunctions [8] has been introduced. The results were obtained with the help of the second-order DWA with kinematic relativistic corrections. It is a typical example of fast collisions. The results show that the model of "independent electrons" (or "independent events") can be used also for fast collisions. Fig.7 represents the calculated ratios jointly with the experimental data obtained in several groups. The list of references to the experimental works and more earlier theoretical calculations is given in [8].

2. Importance of Internal Theoretical Criteria

We discussed above almost all the experimental results on ion-ion collisions available up to now (October 1996). The experimental data are limited, and the theory plays the essential role in the field. General requirements to the final results are the same for all branches of the theory of atomic collisions:

- well established range of applicability,
- estimated accuracy,
- description of existing experimental data, and (that is extremely important)
- prediction of the future experimental results.

In all the cases, the analytic formulas and scaling laws provide a lot of valuable information on the physical pictures of the processes, even if those analytic expressions are approximate or derived as fitting from the numerical calculations.

Two quantum approaches are promising at present: the close coupling (CC), and non-traditional methods of continuum-distorted wavefunctions (CDW). In the CC-approach, the following elements should be provided:

- symmetry properties in basis wavefunctions,
- unitarity of S-matrix (Hermitian character of the system of coupled equations),
- correct boundary conditions for rearrangement collisions (so called translation factors as the first approximation to the Jacobi coordinates),
- completeness of the basic set including the continuum states (in practice it means solving integro-differential equations instead of using pseudo-states),
- analysis of the partial cross sections for estimation of the accuracy,
- parametrization of the equations and/or solutions in an analytic form for the development of scaling laws.

The CDW-approach subjects to similar criteria, and should describe the asymptotic properties of the processes with respect to the natural physical parameters. Unification of both CC- and CDW- approaches promises interesting new results in the theory.

Conclusions

Discussions above show that practical collaboration of several experimental and theoretical groups (say, NIFS - Lebedev Institute - Giessen University) helps much in obtaining new results. In the present paper, we paid less attention to very important problem of accuracy of the data discussed because of good agreement between

the experiment and theory. Such comparison represents a very important criterion, especially for the theory, however, it is one of criteria. Other important criteria are listed in part 2 of the present paper.

The authors are grateful to many colleagues for effective collaboration during the research work and for discussions: Prof. E. Salzborn, Drs. F.Melchert and S.Krudener (Giessen University), Dr. I.Tolstikhina (NIFS), Drs. D.Uskov, V.Shevelko and A.Ulantsev (Lebedev Institute).
L.P.P. acknowledges support by ISTC (project # 0-76), INTAS (project 94-4698), and RFBR (project 96-02-1600-a). (project 96-02-16090-a).

References:

1. M.J.Seaton, Proc.Phys. Soc. 68, 457 (1955)
2. A.Dalgarno, Proc. Roy. Soc. A262,131 (1961)
3. R.Janev, L.Presnyakov, and V.Shevelko, Physics of Highly Charged Ions, Springer, Heidelberg-New York, 1985
4. H.Tawara, NIFS-DATA-25 (National institute for Fusion Science, 1995)
5. L.P.Presnyakov and H.Tawara, paper TH-52 at HCI-96 (Omiya); submitted to Phys. Scripta
6. L.P.Presnyakov and H.Tawara, paper 10F09 at ICPP-96 (Nagoya)
7. L.P.Presnyakov, paper MO-30 at HCI-96; submitted to Phys. Scripta
8. L.P.Presnyakov, H.Tawara, I.Yu.Tolstikhina, and D.B.Uskov, J.Phys.B 28, 785 (1995)
9. L.P.Presnyakov, H.Tawara, and D.B.Uskov, Nucl.Instr. Meth.B98,332 (1995)
10. L.P.Presnyakov, Phys.Rev.A2, 1720 (1970)
11. L.P.Presnyakov and D.B.Uskov, in Proc. P.N.Lebedev

Institute, edited by I.I.Sobelman (Nova Science Publishers, NY 1987) vol.179, p.137
12. L.Hostler and R.H.Pratt, Phys. Rev. Lett.,10, 469 (1963)
13. L.P.Presnyakov, in V.Galitsky, E.Nikitin and B.Smirnov, Theory of Atomic Particle Collisions, Suppl.6, Moscow, Nauka, 1981,p.231 [in Russian]
14. F.Melchert, R.Schulze, S.Krudener, S.Meuser, E.Salzborn, D.B.Uskov, A.D.Ulantsev and L.P.Presnyakov, J.Phys. B28,3299 (1995)
15. F.Melchert, M.Brenner, S.Krudener, R.Schulze, K.Huber, E.Salzborn, D.B.Uskov and L.P.Presnyakov, Phys.Rev.Lett., 74, 888 (1995)
16. C.Brandau, F.Melchert, S.Krudener, S.Meuser, A.Pfeifer, K.vDiemar, T.Bartsch, E.Salzborn, D.B.Uskov, A.D.Ulantsev and L.P.Presnyakov, J.Phys. B28, L579 (1995)
17. M.Terao, S.Szucs, M.Cherkani, F.Brouillard and J.R.Allan, Europhys. Lett., 1, 123 (1986)
18. M.Terao et al, Z.Phys.D, 319, (1988)
19. B.Peart and M.A.Bennet, J.Phys.B27, 2551 (1995)
20. R.K.Janev and D.C.Belic, J.Phys B15, 3479 (1982)

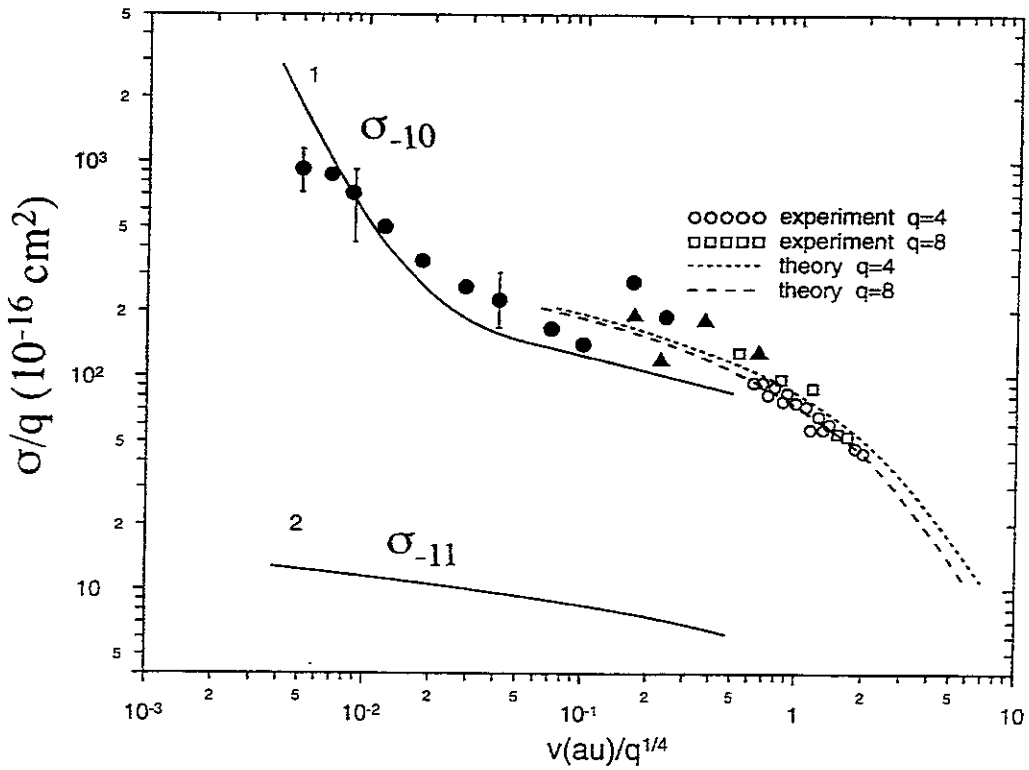

Fig.1.

Scaled cross sections of single- and double-electron removal in collisions of H^- with HCl versus scaled velocity of the relative motion. Curves (1) and (2) are calculations [5] work for the single- and double-electron processes, respectively. Open circles and squares are experimental data [15], dashed curves are calculations [15]. Full circles [17-18] and full triangles [19] are experimental data under He^{2+} impact.

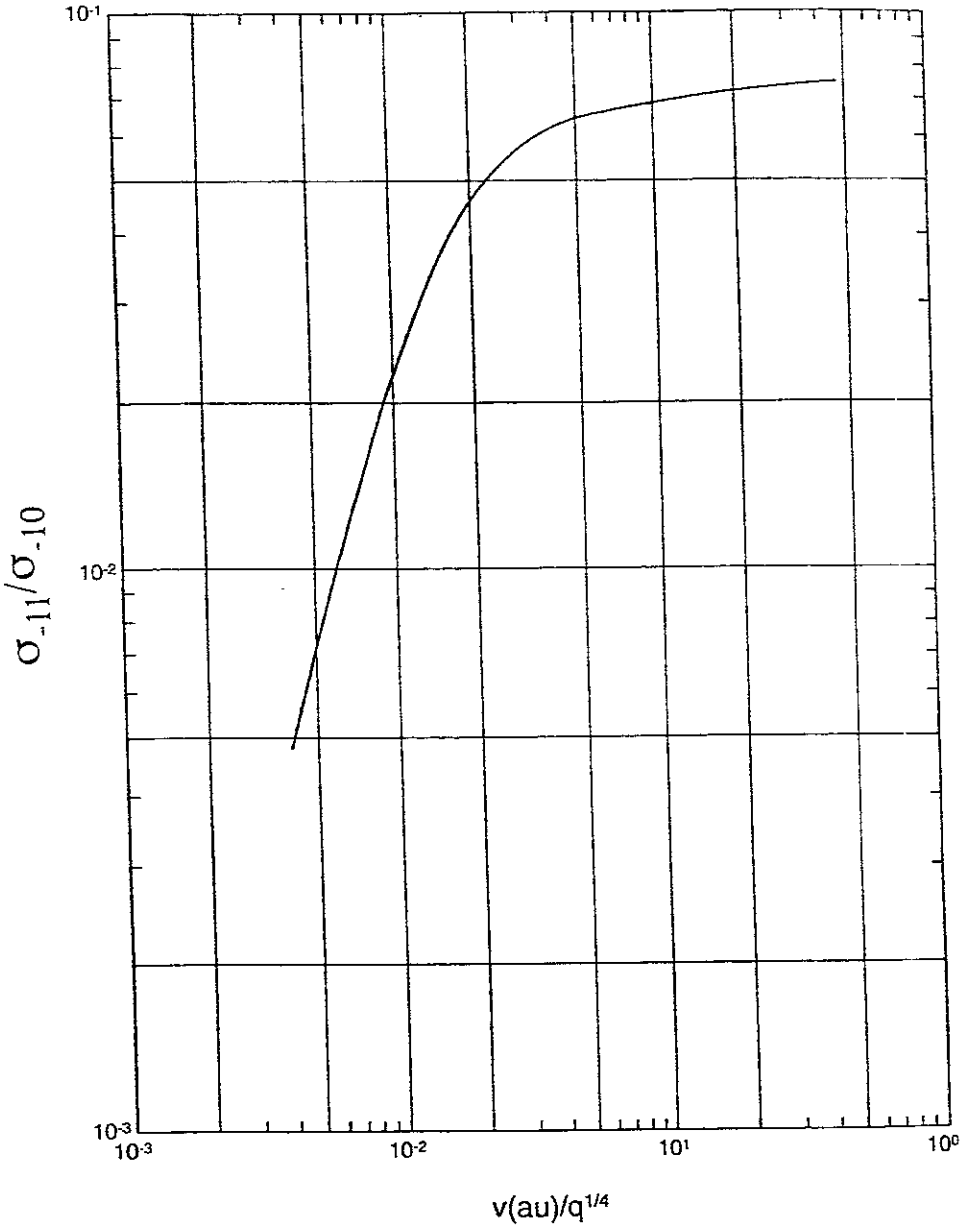

Fig.2.
Ratios of double-to-single electron removal according to curves (2) and (1) in Fig.1.

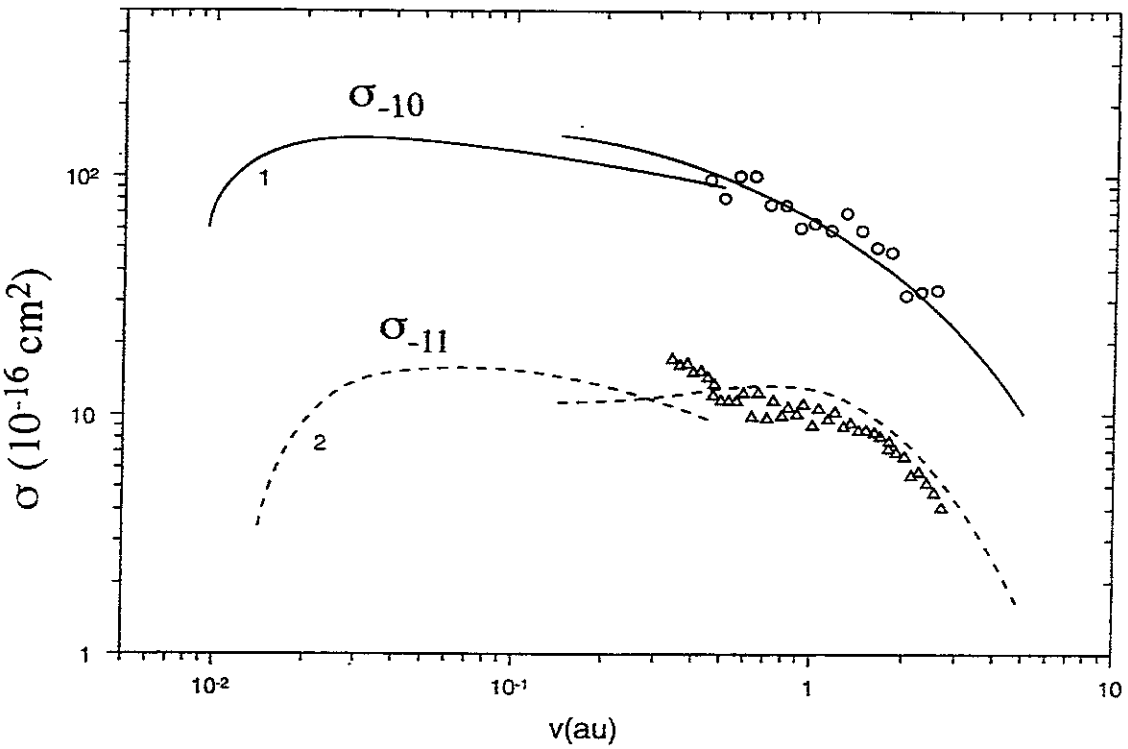

Fig.3.
Single- and double-electron detachment cross sections in collisions of two H^- ions versus velocity of the relative motion. Curves (1) and (2) are calculations [5]. The middle-energy experimental data and theoretical curves are taken from Ref.[14].

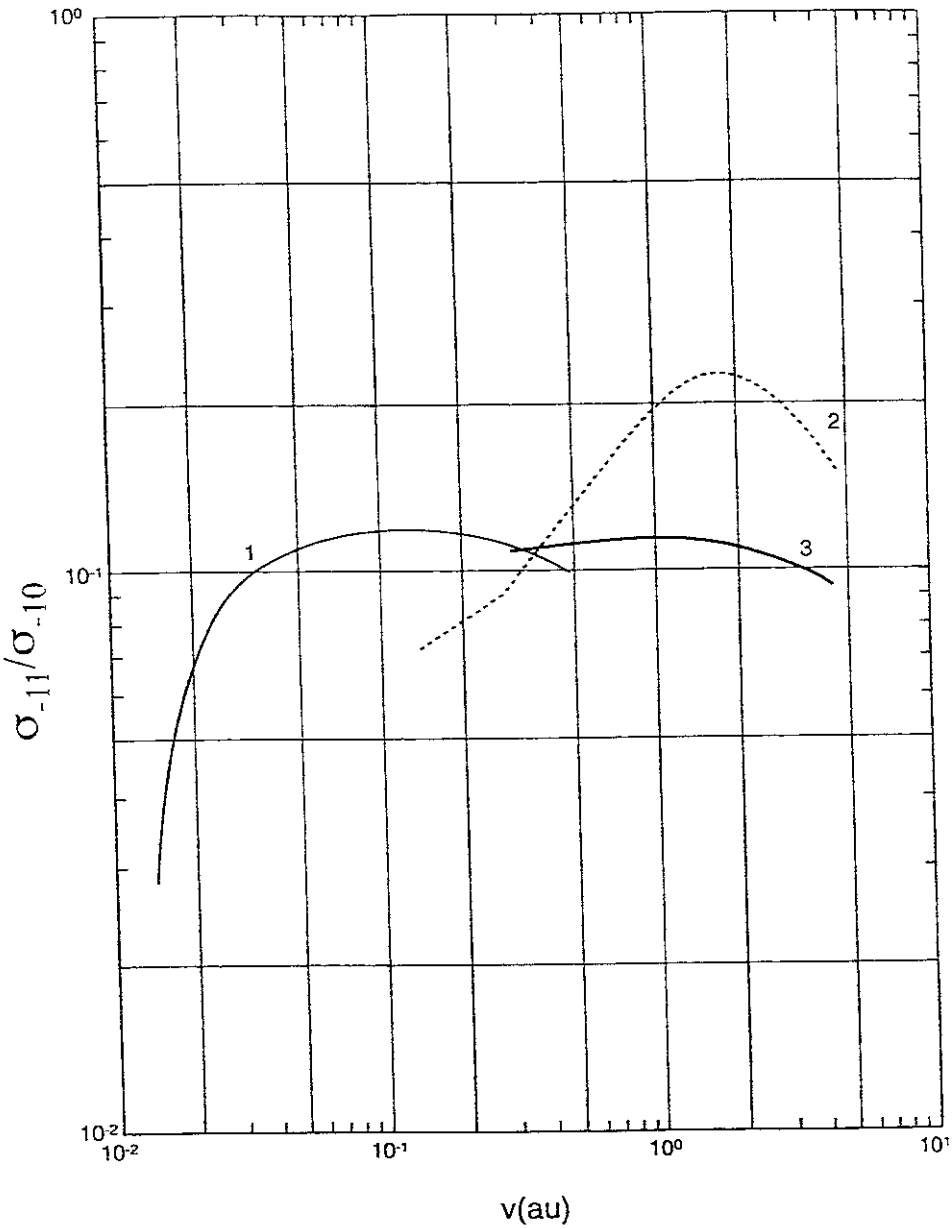

Fig.4.

Ratios of double-to-single electron detachment resulting from Fig.3.

Curve (1) represents results of the present calculations. Curves (2) and (3) are derived from calculations [14] and experimental data [14], respectively.

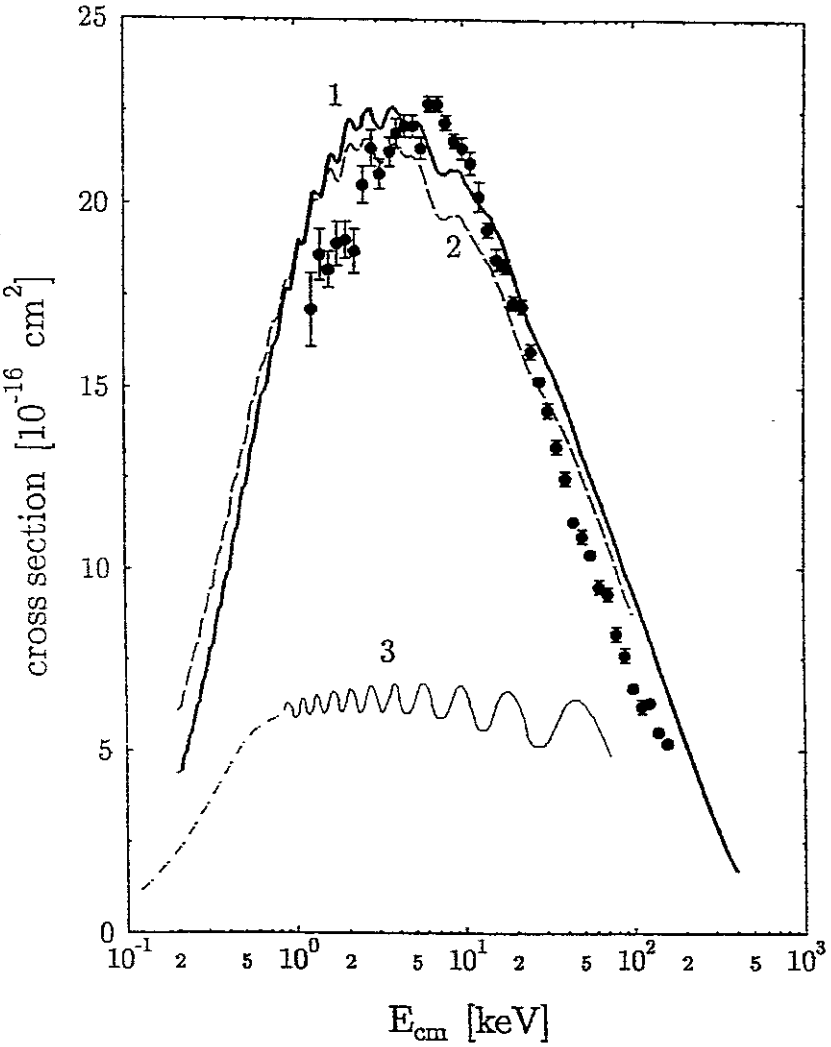

Fig.5.

Cross sections for the direct reaction (9) from ref. [16]: (•),experimental data; curve 1, the theoretical result; curve 2, theory assuming 20 per cent concentration of C^{2+} metastable ions in the beam;curve 3, previous calculations [20].

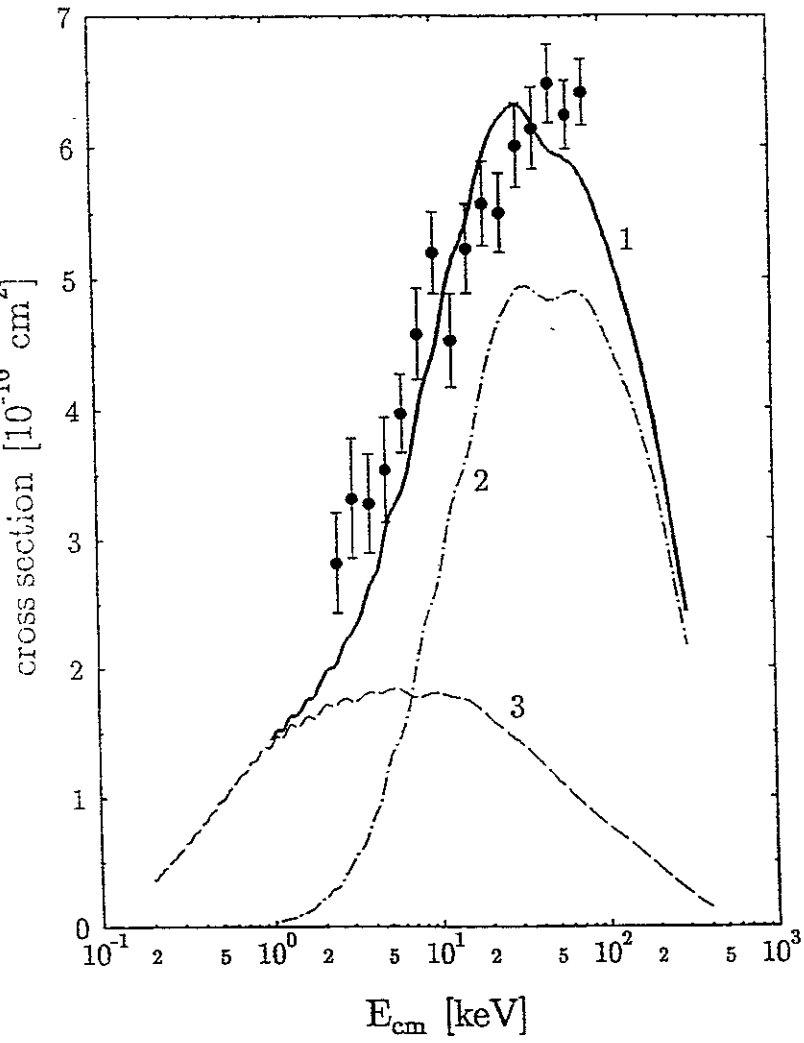

Fig.6.
Cross sections for the inverse reaction (10) from ref.[16]: (•), experimental data; curve 1, the theoretical result; curve 2, capture to the triplet metastable state of B^+; curve 3, capture to the ground singlet state of B^+.

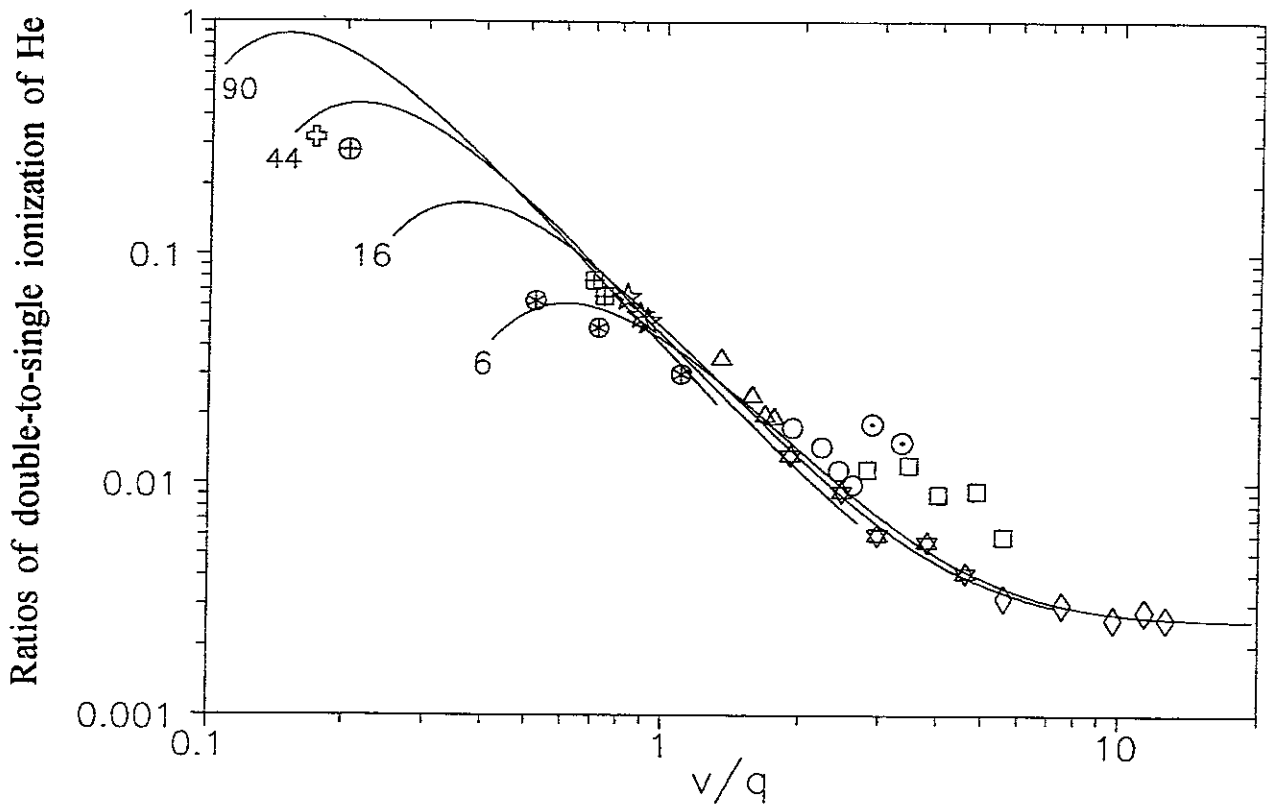

Fig.7.
Ratios of double-to-single ionization of He by several ions as a function of v/q (in atomic units). Full curves, theory (the q- values are indicated). Experimental data: open circles, C^{6+} , star within circle, U^{90+}. For other details and references, see [8].

Multicharged Ion-induced Emission from Metal- and Insulator Surfaces related to Magnetic Fusion Research

HP. Winter
Institut für Allgemeine Physik, Techische Universität Wien, A-1040 Wien, Austria
Fax-No. --43 1 5864203; email <winter@iap.tuwien.ac.at>

Survey

The edge region of magnetically confined plasmas in thermonuclear fusion experiments couples the hot plasma core with the cold first wall. We consider the dependence of plasma-wall interaction processes on edge plasma properties, with particular emphasis on the role of slow multicharged ions (MCI). After a short survey on the physics of slow MCI - surface interaction we discuss recent extensive studies on MCI-induced electron emission from clean metal surfaces conducted at impact velocities << 1 a.u., from which generally reliable total electron yields can be obtained. We then demonstrate the essentially different role of the MCI charge for electron emission from metallic and insulator surfaces, respectively. Furthermore, we present recent results on slow MCI-induced "potential sputtering" of insulators which, in contrast to the well established kinetic sputtering, already occurs at very low ion impact energy and strongly increases with the MCI charge state.

Lecture Notes prepared for
International Symposium on Atomic and Molecular Processes in Fusion Plasmas
National Institute for Fusion Science, Nagoya/Japan (Sept. 17 - 19, 1996)

1. Role of the Edge Plasma for Plasma-Wall Interaction

The socalled edge plasma (boundary plasma) connects the hot core (central plasma) of magnetically confined fusion plasmas with the cold solid surface ("first wall") of the plasma vacuum vessel. Properties of the edge plasma are strongly affected both by the core plasma and the material and geometry of the first wall. The edge plasma, in turn, is of relevance for the power balance of the central plasma and strongly influences the plasma-wall interaction, in particular the erosion of, deposition on and particle emission from the first wall. The edge plasma may be roughly divided into two zones, the "radiating layer" and the "scrape-off layer" ("SOL") /1/. The radiating layer, which typically extends some tens of centimeters inside the separatrix (last closed magnetic flux surface), is the region where collision processes involving bound electrons strongly influence the local particle momentum and -energy balances. The SOL, on the other hand, corresponds to the region outside of the separatrix where the magnetic field lines are open and thus terminate on material surfaces, at which all processes covered by the global term "plasma-wall interaction" will take place. The plasma is very efficiently neutralized upon its interaction with material surfaces, causing neutral gas formation near the exposed structures. The non-removed fraction of this neutral component is reionized in the plasma mainly by electron-impact ionization, with the such produced ions again getting converted via neutralization to energetic neutrals, etc. This multiple neutralization at the surface and re-ionization in the plasma is referred to as "recycling". The kinetic energy of plasma ions diffusing toward the first wall is enhanced by the plasma sheath potential V_s, which is formed near any material wall /2/:

$$V_s = 0.5.(kT_e/e).\ln\{2\pi(m_e/m_i)(1 + T_i/T_e)(1-\gamma)^{-2}\} \qquad (1)$$

For an isothermic hydrogen plasma ($T_e \approx T_i$) V_s typically amounts to $3kT_e/e$ (T_e, T_i: plasma electron- and -ion temperatures /1/). V_s also depends on particle-induced electron emission from the first wall (the respective total electron yield is designated by γ in equ. (1), see below). The sheath potential influences the efficiency of plasma ions for releasing impurities from solid surfaces by sputtering and desorption. The impurities diffuse into the radiating layer and the plasma core, where they will cause enhanced radiation power loss and thermonuclear fuel dilution.

Optimization of the boundary plasma properties constitutes one of the major tasks which need to be mastered along the road toward development of future thermonuclear fusion reactors. To this goal, up till now the "limiter"- and the "divertor" concepts have been pursued (cf. fig. 1).

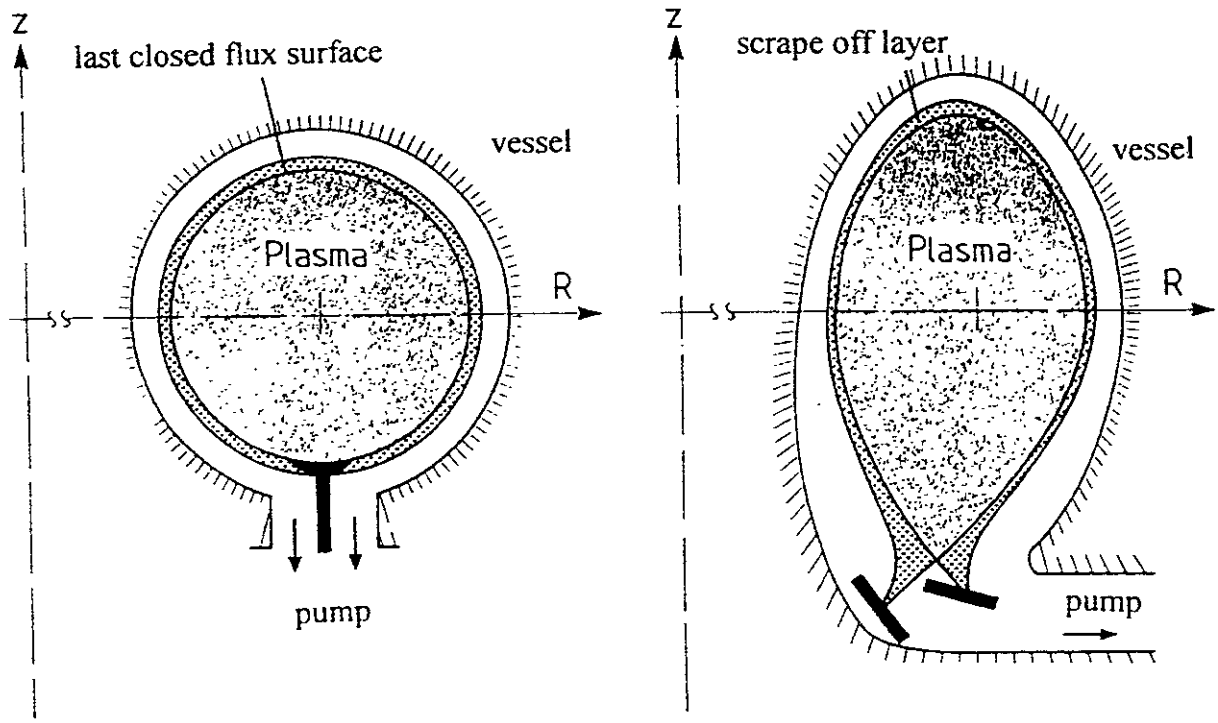

Fig. 1: Schematic of plasma boundary - limiter (left) and divertor (right) /1/.

In the limiter concept an aperture is inserted into the plasma region, at which the processes of plasma-wall interaction will be concentrating. The divertor concept, on the other hand, involves suitable shaping of the external magnetic field lines to divert some magnetic flux bundles away from the main plasma into a separate chamber in which the plasma-wall interaction can be spread out onto a larger material surface. To keep the power load on the strongly exposed first wall components at a tolerable level, various measures or a combination of them are being considered /1/:

- Small glancing angles of magnetic field lines on the surface (ca. 1°).
- Spatial sweeping of the separatrix to reduce the average load.
- High recycling regime with large plasma temperature gradient near surface.
- Enhanced radiation cooling of the plasma boundary.
- Increase of energy transfer via charge-exchange in the plasma boundary.
- Gas-target regime involving dominant volume-recombination processes.

Due to its small spatial extension (typically micrometers) the sheath region is essentially collisionless. Fig. 2 from /2/ shows the potential drop ($V_s<0$!) across the sheath region for different plasma ion species and ratios of ion- to electron temperatures. In fig. 2 the influence of the secondary electron yield (designated by δ and including electron reflection; in this paper we will generally use the symbol γ for any particle-induced electron yield) for the sheath potential V_s has been indicated. For a given electron temperature T_e at the plasma sheath entrance, the relation between the electron energy flux density Γ_e and the net electron (particle) flux density P_e across the sheath can be expressed by an energy-transmission coefficient τ_e in the form /1, 2/:

$$\Gamma_e \approx \tau_e.P_e.kT_e;\ \tau_e \approx 2/(1-\gamma) - eV_{sf}/kT_e \qquad (2)$$

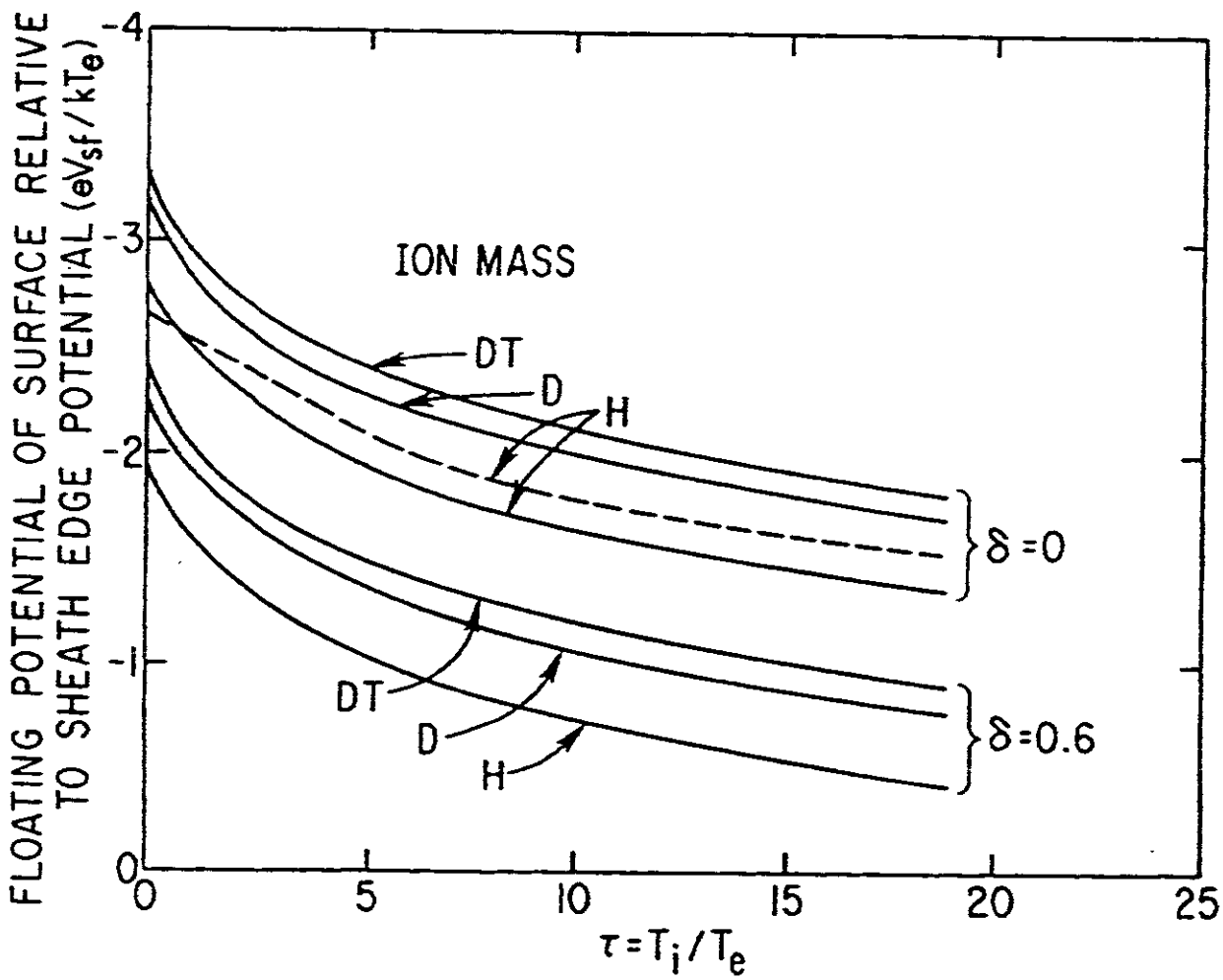

Fig. 2: Dependence of sheath potential on T_e, T_i, ion species and secondary electron emission /2/.

Equ. (2) shows how electron emission from the first wall modifies the transmission coefficient τ_e and thus the global plasma energy balance. Electron emission (which can also be induced by heavy particle impact) from first wall components "is often omitted from the discussion of boundary plasma physics since, according to present knowledge, it will be suppressed for magnetic field lines incident at the nearly glancing angles required for adequate power distribution in a thermunuclear fusion reactor" /1/. Neglecting electron emission due to impact of hydrogen ions on clean metal surfaces is in order since the respective total electron yields at impact energies of relevance (up to some hundreds of eV) are well below unity (cf. fig. 3 from /3/). However, this is neither true for oxidized surfaces (see also fig. 3), which are of interest in present day fusion experiments in connection with first-wall coating and -oxygen gettering /4/, nor is it really true for impact of multiply charged ions (MCI) on both metallic and insulating surfaces (see chapter 4). Furthermore, MCI-induced erosion of insulator surfaces due to the recently studied process of "potential sputtering" will be introduced and discussed in chapter 5.

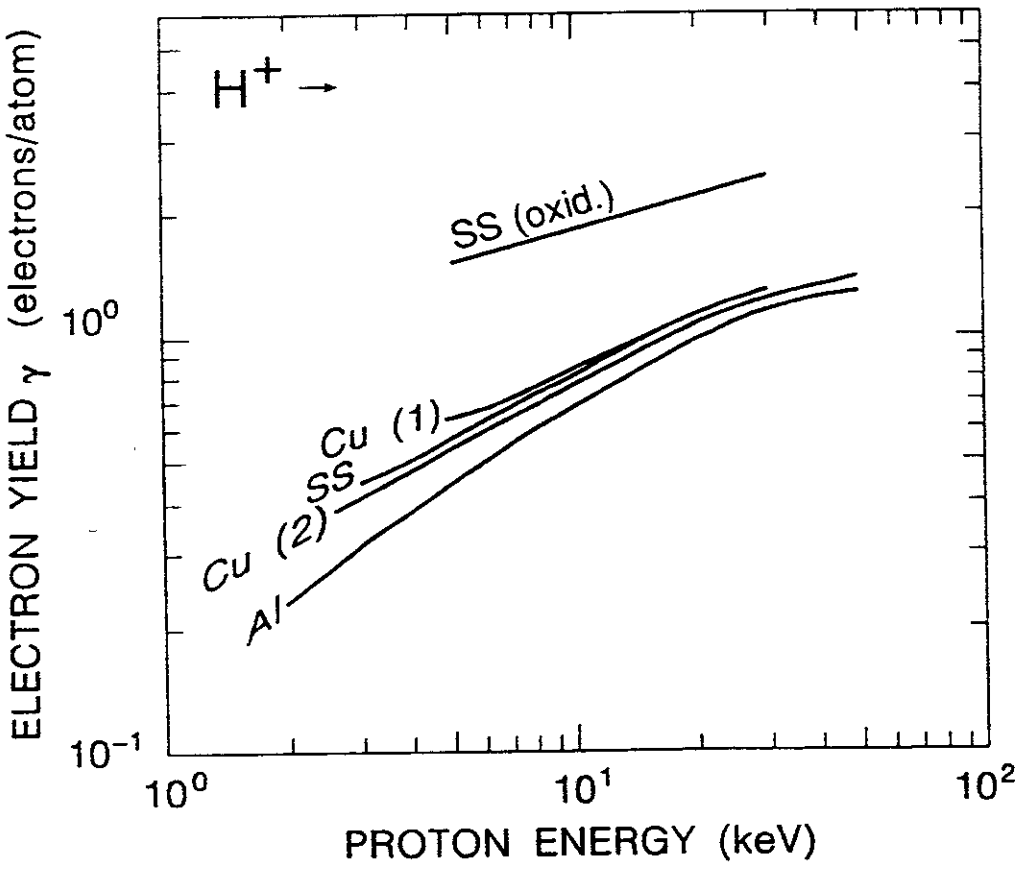

Fig. 3: Proton-induced electron emission from clean and oxidized metal surfaces /3/.

2. Slow Multicharged Ion-Surface Collisions - Basics

2.1 Introduction

When regarding the interaction of slow MCI with solid surfaces and the adjacent subsurface layers of metals, semiconductors or insulators, we have to take into account all electronic processes between states of the respective projectile and the surface. With "slow" we refer to impact velocities below one atomic unit (corresponding to 2.18×10^6 m/s or a projectile energy of 25 keV per atomic mass unit). At such low impact velocities electronic transitions between the projectile and the target surface are generally much faster than significant changes of the projectile distance from the surface. Furthermore, any so-called "kinetic effects" (i.e. caused by the projectiles kinetic energy) remain less important than the influence of the projectiles potential energy which is deposited upon surface impact. This potential energy is equal to the total ionization energy which had been spent for generating the original MCI from its neutral atomic ground state. Due to primarily technical reasons, earlier collision studies involving MCI have generally been conducted at relatively higher kinetic energies where possible potential effects were superimposed and usually dominated by the kinetic effects. With the nowadays available multicharged ion sources (see chapter 3) one can produce slow MCI beams in such a way that in surface collisions the dissipated potential ion energy of an MCI greatly exceeds its kinetic energy. The resulting "potential effects" depend critically on the respective target surface conditions, since the latter strongly influence the nature of electronic transitions between projectile- and surface states. Therefore, meaningful investigations of such potential effects call for well defined projectile- and target surface conditions in ultra-high vacuum (UHV) environment, as well as for appropriate surface definition, -preparation and -analysis as common to experimental surface physics. Processes occuring in the course of MCI-surface collisions are closely related to ion-induced desorption, secondary ion emission and low-energy ion reflection from surfaces, all of which are highly relevant for surface analysis.
In studies on the impact of slow MCI on metal surfaces, a new kind of short-lived (transient) atomic state, the so-called *"hollow atom"*, has been identified. This name refers to projectiles with empty inner shells but filled outer shells such that transient neutral atoms are created. Formation of hollow atoms is initiated by multiple-electron capture if the projectile is still above the surface. They then collapse at and below the surface under the influence of dynamic screening and eventually become fully de-excited inside the solid.

The hollow atom state has raised considerable interest in the physics community /5-7/ and established a new field of research in atomic collision physics. Related studies have been greatly facilitated by the availability of novel powerful MCI sources which will be shortly reviewed in chapter 3.1.

2.2 Simple Scenario for Slow MCI - Surface Impact Phenomena

Current views on the interaction of slow MCI with a metal surface evolved during the last decade from numerous experimental and theoretical studies of the respective total electron yields, slow electron number statistics, fast Auger electron energy distributions, scattered projectile charge states and -energies, and soft X-ray emission. The appropriate scenario (cf. fig. 4) can be divided into four stages, covering the projectile's approach toward the surface (A), its close contact with the surface (B, C), and finally its subsequent penetration into the target bulk (D) or backscattering into vacuum.

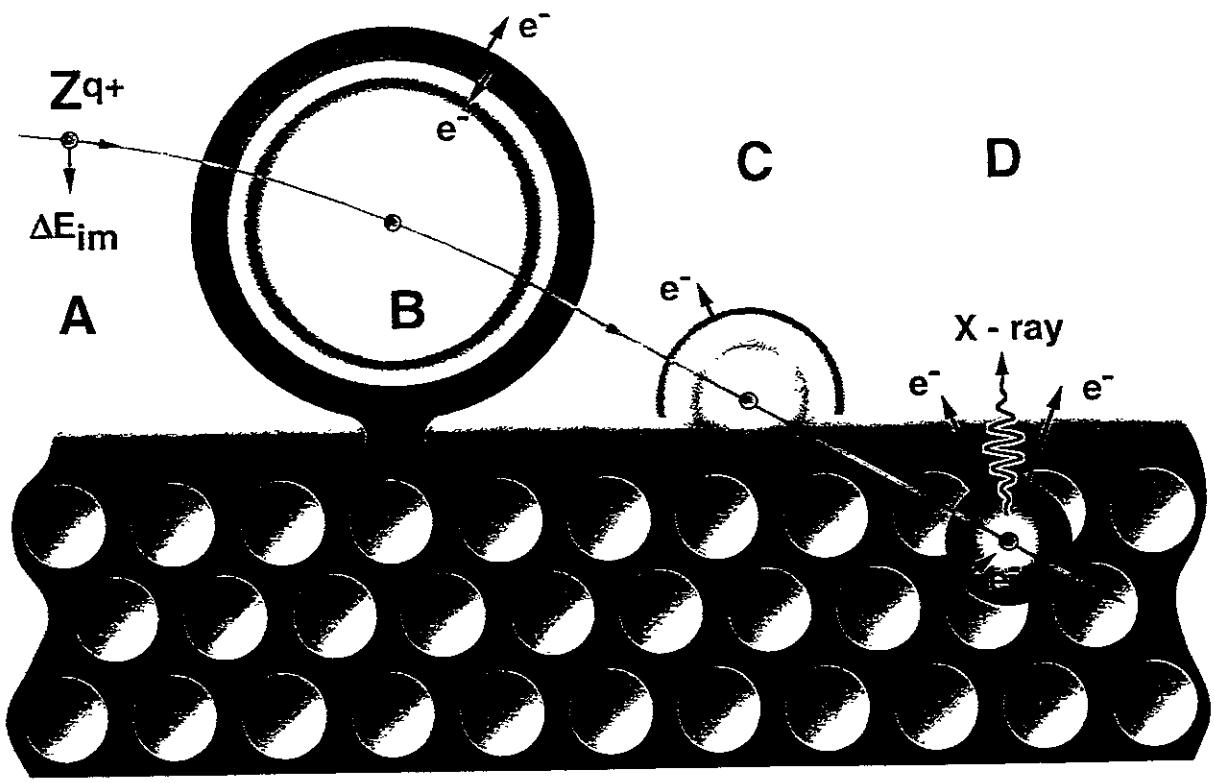

Fig. 4: Development of a "Hollow Atom" during impact of a slow MCI on a metal surface

The above-surface stage (A) of hollow atom formation can be described within the so-called "classical over-the-barrier"- (COB) model /8,9/. Above the metal surface the MCI induces a collective response of the free metal electrons which at sufficiently large distance can be replaced by the classical image potential. The latter accelerates the MCI towards the surface and thus sets a lower limit for the effective projectile impact velocity, with a correspondingly upper limit for the MCI above-surface interaction time. The image interaction shifts up and Stark-mixes the projectile electron states, and also increases the potential barrier between the MCI and the surface. Below a critical distance which in first approximation depends on the metal work function and the MCI charge state, electrons from the solid can be captured into highly excited projectile states (resonant neutralisation-RN). These processes go on until complete neutralization of the MCI is achieved, corresponding to formation of the "primary hollow atom" (fig. 4, stage B). The resulting hollow atoms are subject to rapid autoionization (AI) but remain dynamically neutral because of the ongoing RN. Simply speaking, with its further surface approach the levels of the hollow atom will be shifted because of image interaction and screening of the projectile charge by the already captured electrons. Both AI and level shifting give rise to slow electron emission from the projectile (see chapter 4). Increasingly stronger bound projectile states will become populated as they fall into resonance with occupied electron states in the surface. On the other hand, electrons in up-shifted states may be recaptured into the metal via resonant ionization (RI). This interplay of different electronic transitions will continue until close contact with the surface, and will be accompanied by both electron emission and gradual shifting of electrons into lower n-shells of the projectile (fig. 4, stage C). All involved projectile states become filled and again depopulated within a few femtoseconds and are therefore of a highly transient nature. At close contact with the surface, screening by surface electrons will cause "peeling-off" of the still bound outer-shell electrons. Relaxation of the thereby formed "secondary hollow atoms" will proceed below the surface via three competing processes (fig. 4, stage D). At low impact velocity, Auger neutralisation (AN) can populate the still present projectile inner shell vacancies, whereas at higher impact velocity the latter can also be directly filled via quasi-molecular transitions in close collisions with target atoms. The resulting sub-surface AN accounts for the bulk of observed fast projectile Auger electrons which, however, are always much less abundant than the emitted slow electrons (see below).

In competition to Auger electron emission, in MCI with higher Z transient inner shell vacancies may also de-excite by characteristic projectile X-ray emission. Auger electron- as well as soft X-ray emission occur predominantly already below the surface, where the projectile shielding by free metal electrons strongly influences all electronic transitions (see fig. 4, stage D). Many-electron processes like multiple electron capture may play an increasingly more important role with higher initial charge of the projectile. In addition to the fast Auger electron emission, a considerably larger number of slow electrons is emitted mainly before and at close surface contact (see fig. 4, stages B, C). The latter stages are also relevant for elastic and inelastic MCI scattering, as well as for MCI-induced sputtering and -secondary ion emission (chapter 5).

2.3 Relation of MCI-Surface Collisions to other Fields

MCI can carry along a rather large amount of potential energy (e.g. 250 keV for Ne-like Th^{80+}). Transfer of such a large energy onto a relatively small surface area of about 100 $Å^2$ within the rather short time of $\leq$100 fs corresponds to the immense power density of $\geq 10^{14}$ W/cm^2, which can give rise to various, still largely unexplored non-linear processes.

Many electrons are extracted from the surface and captured by the MCI, thus producing transient "hollow" atoms whose outer Rydberg orbitals are filled while the inner shells stay temporarily empty. The high potential energy of MCI is released mainly via emission of electrons. As MCI deposit their potential energy in a very small region, the corresponding high-energy concentration may also cause characteristic surface modifications.

The above described processes are of interest, e.g., in the following fields.

* Astrophysics and cosmology (MCI induced desorption from interplanetary and interstellar clusters and grains).
* Atomic physics of multiply excited species ("Hollow Atom Spectroscopy").
* Information technology (high-density storage media based on MCI induced micro structures).
* Plasma chemistry and -technology.
* Semiconductor industry (novel cleaning procedures, preferential removal of insulating layers).
* Thermonuclear fusion reactor development (plasma wall interaction and forced radiation cooling in the plasma edge region, cf. chapter 1).

3. Experimental Investigation of MCI-Surface Interaction

In this chapter we shortly inform on some important ingredients for experimental studies in the field of slow MCI-surface interactions. Production of appropriate MCI beams relies on the availability of suitable multicharged ion sources (chapter 3.1). MCI-induced electron emission is studied primarily with respect to the total electron yield (chapter 3.2.1) and the kinetic energy distribution of ejected electrons (chapter 3.2.2). The special demands for investigating MCI-induced secondary ion emission and "potential sputtering" are described in chapter 3.3. For all above fields of study the preparation and characterization of clean solid surfaces under proper ultra-high vacuum conditions is of central importance.

3.1 High-Performance MCI Sources

3.1.1 *ECRIS* - Electron Cyclotron Resonance Ion Source

An ECRIS capable of efficient MCI production /10/ consists of the main components as shown in fig. 5. A discharge chamber filled with the working gas (pressure of typically $\leq 10^{-5}$ mbar; for ion production from non-volatile substances see below) is immersed in a "min-B" magnetic field geometry (i.e. the magnetic field strength increases from the center outward) which provides the necessary ion confinement. The magnetic fields are generated by sets of solenoids (which for larger set-ups may be super conducting) combined with multipolar magnetic fields produced by high current-carrying conductors ("Joffe bars") or, for more compact constructions, permanent magnets (Sm-Co, Fe-Nd-B).

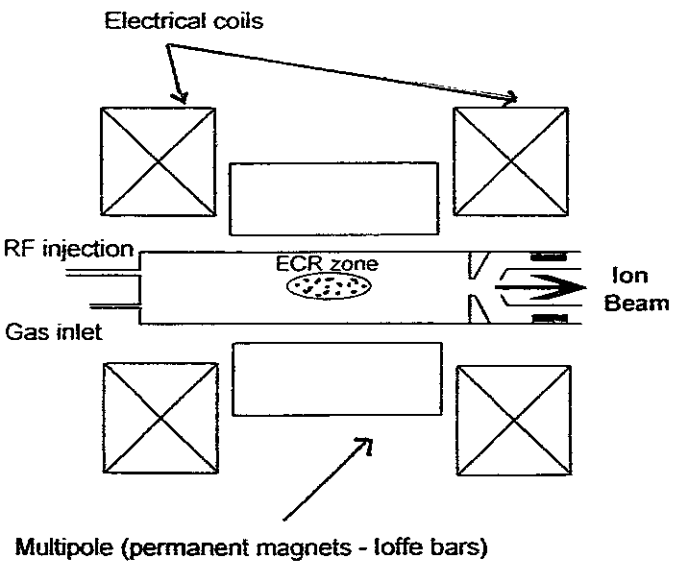

Fig. 5: Main components of an ECRIS for MCI production

Microwaves with a frequency of presently up to 28 GHz are fed into the discharge chamber. They produce a plasma wherein the electrons are preferentially heated by electron cyclotron resonance (ECR) when drifting through the so-called ECR zone (cf. fig. 5) where the electron cyclotron frequency $\nu_{ec} = e.B/2\pi.m_e$ matches the applied microwave frequency (e and m_e are electron charge and -mass, respectively, and B is the local magnetic field). In this way the electrons can reach rather high energies (up to hundreds of keV) and thus ionize efficiently even highly charged ions, which themselves stay rather cold. This provides effective step-by-step electron impact ionization conditions up to high q values and permits extraction of high-quality MCI beams. Different techniques have been developed for producing MCI from solid compounds, e.g. sputtering or melting from suitable electrodes situated next to the ECR zone, or vaporisation from a crucible inside the discharge chamber. Stable operation of ECRIS calls for preferential replenishment of the plasma electrons. In early ECRIS this has been achieved by a first discharge stage with a relatively higher gas pressure, but more recently by electron delivery from hot filaments or ion-induced electron emission from oxide-coated inner walls or from negatively biased probes with respect to the ECR plasma. Modern ECRIS operate typically with ECR frequencies of 10 - 15 GHz at a power level of several 100 W, and produce c.w. beams with, e.g., 4 μA of Ar^{16+} or 12 μA of U^{33+} /10/. The kinetic energy spread of the extracted ions is typically between 5 and 10 eV times charge state q. Ion beam emittances $\varepsilon_{95\%}$ (i.e. covering 95% of the total ion current) are below 100 π.mm.mrad.

Of special interest to experimentalists is the actual trend to rather compact, all-permanent magnet ECRIS, which need only astonishingly low microwave power. For example, "Nanogan 10 GHz" /11/ can produce 10 eμA of Ar^{8+} with only 1 W microwave power, which is available from low-cost solid-state microwave transmitters. Evacuation is provided from the ion extraction region such that no vacuum pump on the high voltage terminal is necessary.

3.1.2 *EBIS* - Electron Beam Ion Source

While ECRIS produce MCI from magnetically confined plasmas, EBIS devices utilize high-density electron beams for both ion confinement and -ionization [12]. An appropriate electron beam (see fig. 6; typical length about 1 m, diameter some tens to hundreds μm, current densities of some hundreds to several thousands A/cm^2) is guided by a strong magnetic field of typically 1 T inside a series of drift tubes connected to variable potentials.

This magnetic field is produced by a long (usually superconducting) solenoid. The electron beam, by virtue of its strong negative space charge, provides excellent confinement for the positive ions as long as suitable positive potential wells are applied on both ends (cf. fig. 6).

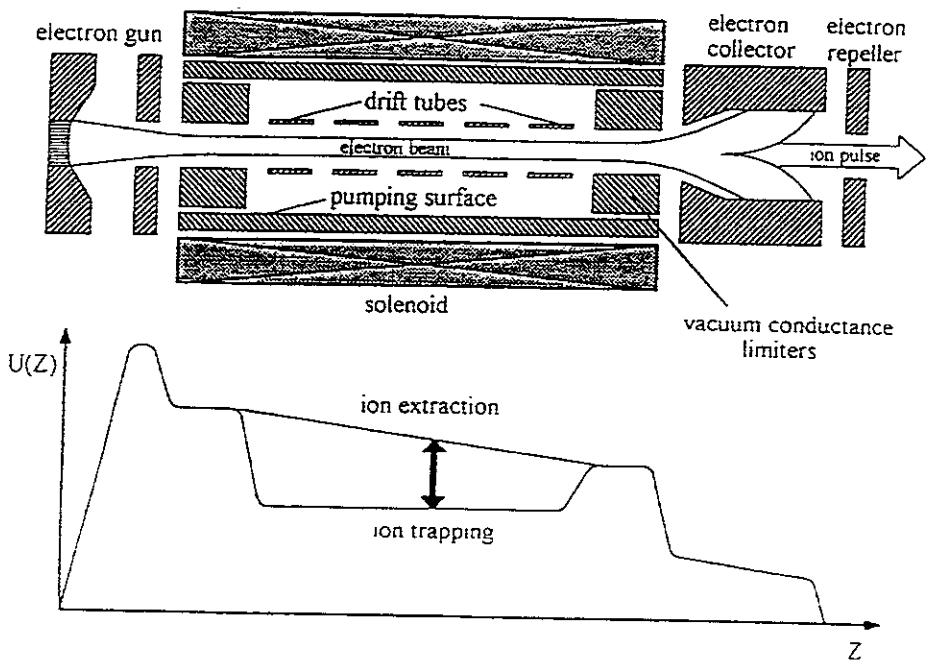

Fig. 6: Main components of an EBIS for MCI production

The confinement can last for a few milliseconds up to many seconds, until the full space-charge compensation of the electron beam is reached. Ions brought into the electron beam during the confinement time, either by gas injection or from suitable external beam sources, will be ionized in a step-by-step manner. The lower the surrounding background gas pressure, the more efficiently the ionization proceeds. The background pressure can be kept below 10^{-10} mbar by cryo-pumping on the inner walls of the superconducting solenoid. As a special feature, at any time during ion confinement only narrow groups of MCI charge states are present. With EBIS used in short-pulsed fashion, desired MCI are extracted by rapidly lowering one of the axial potential barriers (extraction time typically 5 - 50 µs). In this mode an EBIS is also excellently suited as MCI injector for heavy ion synchrotrons. On the other hand, it may be run c.w. in the so-called "leaky mode", where it delivers less highly charged ions than in the (short) pulsed mode. Existing EBIS are capable of producing up to fully stripped Xe^{54+} ions (about 10^4 per pulse), or fully stripped Ar^{18+} (about 10^8 per second; /13/).

Typical EBIS emittances of ≤10 π.mm.mrad are considerably smaller than for ECRIS (see above). Technical details on the construction and operation of cryogenic EBIS are found in /14/.

3.1.3 *EBIT* - Electron Beam Ion Trap

EBIS and EBIT feature as their common working principle the step-by-step ionization of ions trapped in the space charge of dense electron beams. However, the EBIT /15/ involves a much shorter electron beam than an EBIS (only a few cm), which is both easier to realize and probably more stable, thus giving rise to a comparably more efficient ion confinement. The EBIT has originally been conceived for studying the X-ray radiation from trapped MCI. The respectively most advanced setup ("superEBIT" at Lawrence Livermore National Laboratory) involves a 200 keV electron beam and permits studies on electron impact excitation and -ionization for up to H-like U^{91+} /6/. It is also possible to extract the MCI along the electron beam direction, in order to form a free MCI beam as first demonstrated in /16/. In this case ion charge spectra and MCI yields can be obtained similar as from EBIS (see above). For production of MCI from non-gaseous compounds, respective singly charged ion species can be injected in a similar way as for EBIS. In summary, EBIT are very compact devices (comparable in size, technology and costs to a medium-performance electron microscope), which can produce up to fully stripped ions of practically all elements.

3.2 Experimental Studies of MCI-induced Electron Emission

3.2.1 Total yield and number statistics of slow electrons

The total electron yield γ (mean number of electrons emitted per single projectile impact) is usually determined by measuring the fluxes of both the incoming projectiles I_p and the emitted electrons $I_e = \gamma.I_p/q$, respectively (so-called current measurement). With charged projectiles this can be accomplished in a straightforward manner by measuring target currents with and without permitting the electrons to leave the target via appropriate target biasing with respect to its environment. The large majority of MCI-induced electrons (typically ≥95 %) are emitted with a kinetic energy of below 50 eV (see chapter 2). Precautions have to be taken against possible disturbances from charged particle reflection, secondary ion emission and, in particular, spurious electron production due to reflected or scattered atoms, ions or electrons.

In general, for such measurements projectile currents of typically above one nA are necessary. Very highly charged ions (typically q>20) are usually not available in such large quantities. An alternative technique for determination of the total electron yield γ involves the electron emission statistics (ES), i.e. the probabilities W_n for ejection of 1,2,...,n electrons per incident projectile /17, 18/, where

$$\sum_{n=0}^{\infty} W_n = 1 \qquad (3)$$

The relation between γ and W_n is then given by

$$\gamma = \sum_{n=1}^{\infty} n \cdot W_n \qquad (4)$$

A set-up for measuring ES induced by slow MCI is shown in figs. 7a,b: Incoming MCI can be accelerated or decelerated by a five-cylinder lens assembly to any desired nominal impact energy, before hitting the target surface under normal incidence.

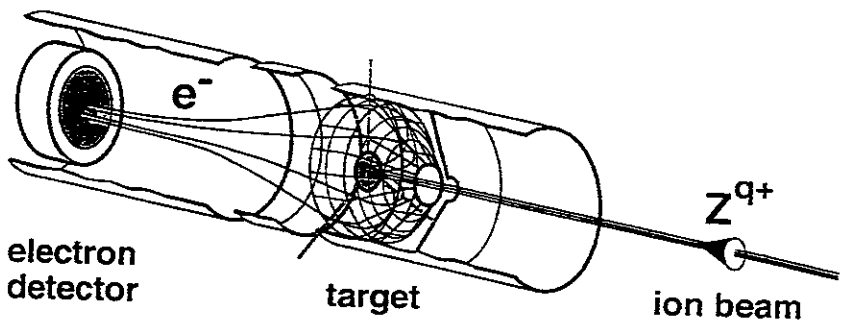

Fig. 7a: Detector for measuring the number statistics (ES) of MCI-induced electron emission.

The lowest accessible impact energy is determined by the projectile image charge acceleration toward the surface. Almost all electrons with energies below typically 50 eV entering from the target into the 2π half solid angle are deflected by a highly transparent conical electrode, extraction from there and guided onto a surface barrier detector biased with $U_e \geq 20$ kV with respect to the target. Typical ejected electron trajectories have been indicated in figs. 7a,b. Electron emission events induced by one impinging projectile particle will be finished within less than 10^{-11} s, which is much shorter than the resolution time of common detection electronics ($\geq 10^{-8}$ s).

Thus, n electrons emitted due to impact of one projectile are registered like *one* electron of $n \cdot U_e$ keV rather than a number n of U_e keV-electrons.

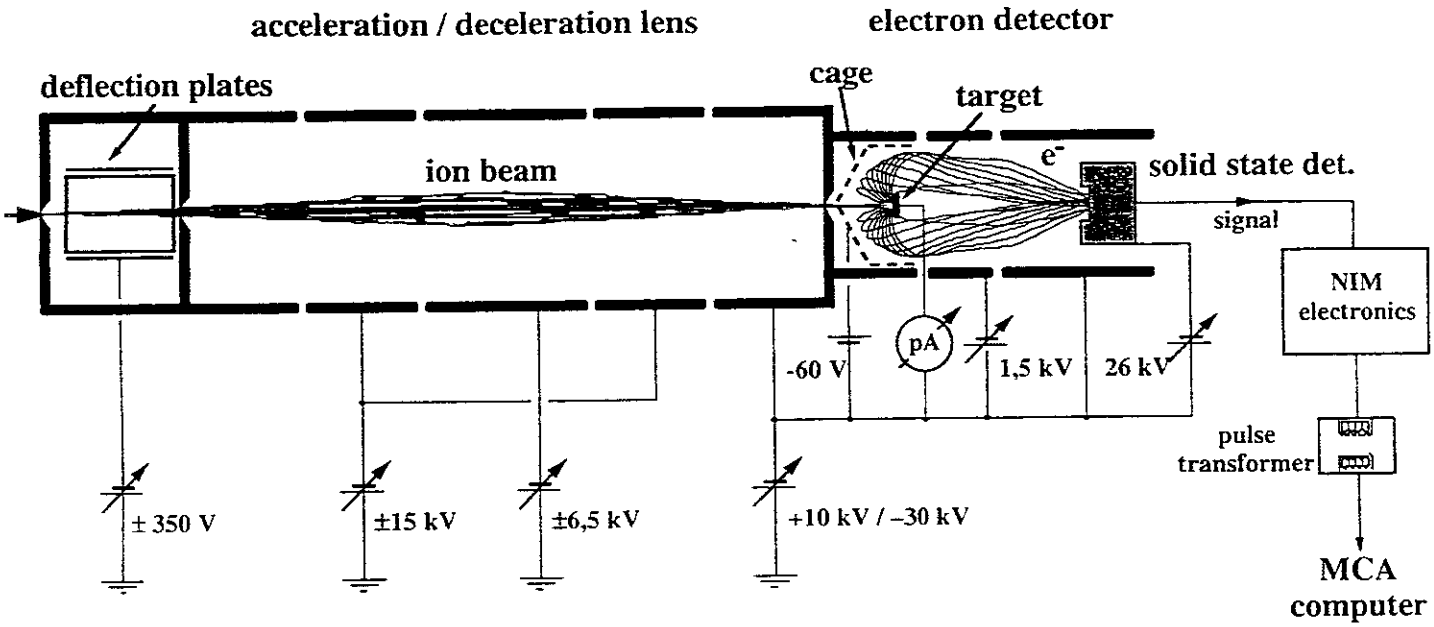

Fig. 7b: Setup for measuring ES for MCI impact energies up to 40 q.keV

The area below the nth peak of the resulting electron "energy" spectra (c.f. fig. 8a) is directly related to the probability W_n for emission of n electrons. The probability W_0 that no electron is emitted cannot be determined directly, but may practically be neglected for yields $\gamma \geq 3$. As described in detail in refs. /17, 18/, least-squares fits of linear combinations of Gaussian peaks to the measured pulse height spectra deliver the actual emission probability distributions W_n (see fig. 8b), from which total electron yields are obtained via equ. (4). The ES technique requires ion fluxes at the target surface of not more than 10^4 projectiles/s and is therefore ideally suited for comparably tiny MCI beams from EBIS and EBIT. In addition, charging-up of insulator surfaces under MCI bombardment is completely avoided (cf. chapter 3.3). Since MCI-induced potential electron emission depends strongly on the MCI charge state, with respective ES spectra one can distinguish different MCI species in "mixed" ion beams with equal charge-to-mass ratios /19/. The ES method also yields the electron number statistics which provides unique information on the respective interaction processes, i.e. both the total number of electrons involved in a particular emission process and the mean "single emission probability" for these electrons, since only a fraction of electrons extracted from the solid can actually escape into vacuum.

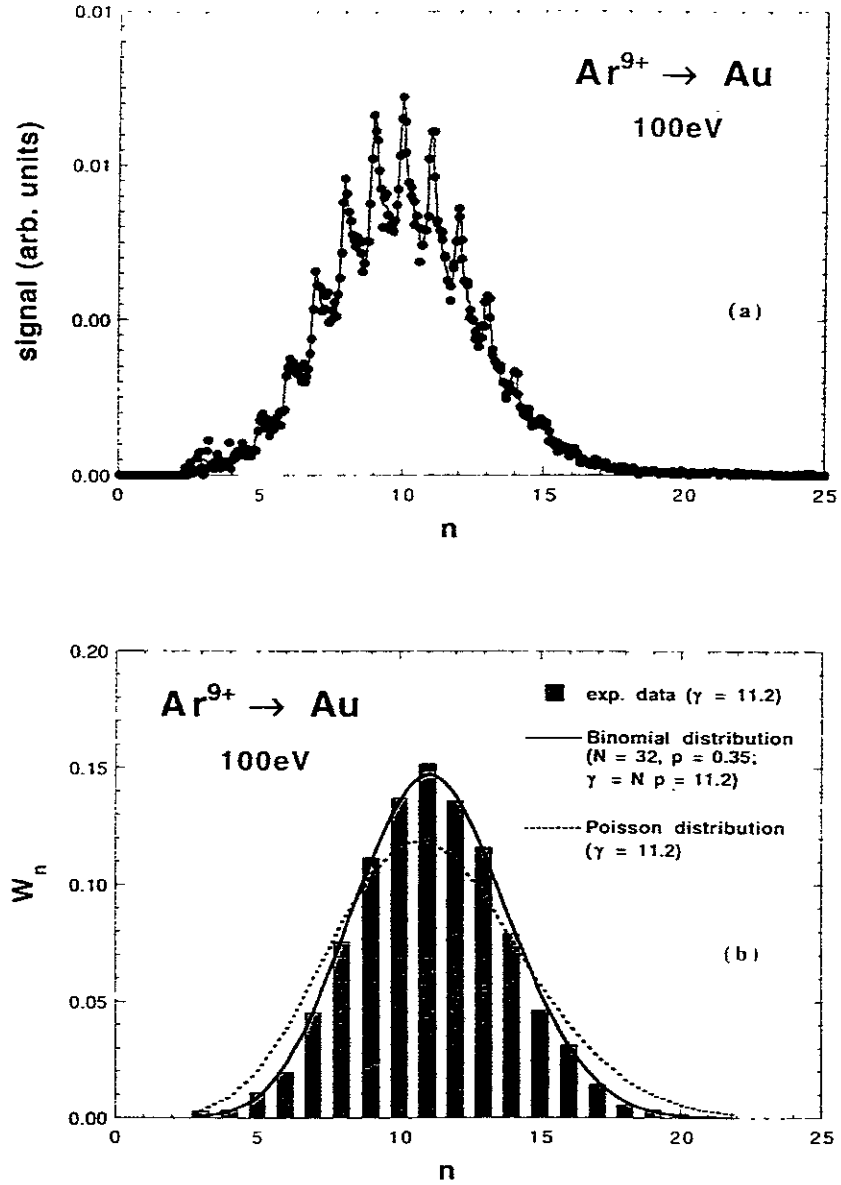

Fig. 8: Measured (a, top) and evaluated (b) electron number statistics (ES) for impact of 100 eV Ar^{9+} ions on clean gold. Evaluated ES best-fits a binomial statistics (cf. chapter 4.1)

3.2.2 Measurement of Electron Energy Distributions

For kinetic energy analysis of ejected electrons various types of electrostatic spectrometers are suitable. Each species consists essentially of two plates for producing a well defined electric field. The names of these spectrometers refer usually to the shape of their plates (parallel plate-, cylindrical mirror-, cylindrical plate- and spherical plate spectrometer, respectively). Fig. 9. shows schematically a "tandem parallel-plate spectrometer" within an UHV collision chamber for studying fast Auger electrons induced by MCI from clean solid surfaces (N. Stolterfoht et al., Hahn-Meitner-Institut Berlin, Germany).

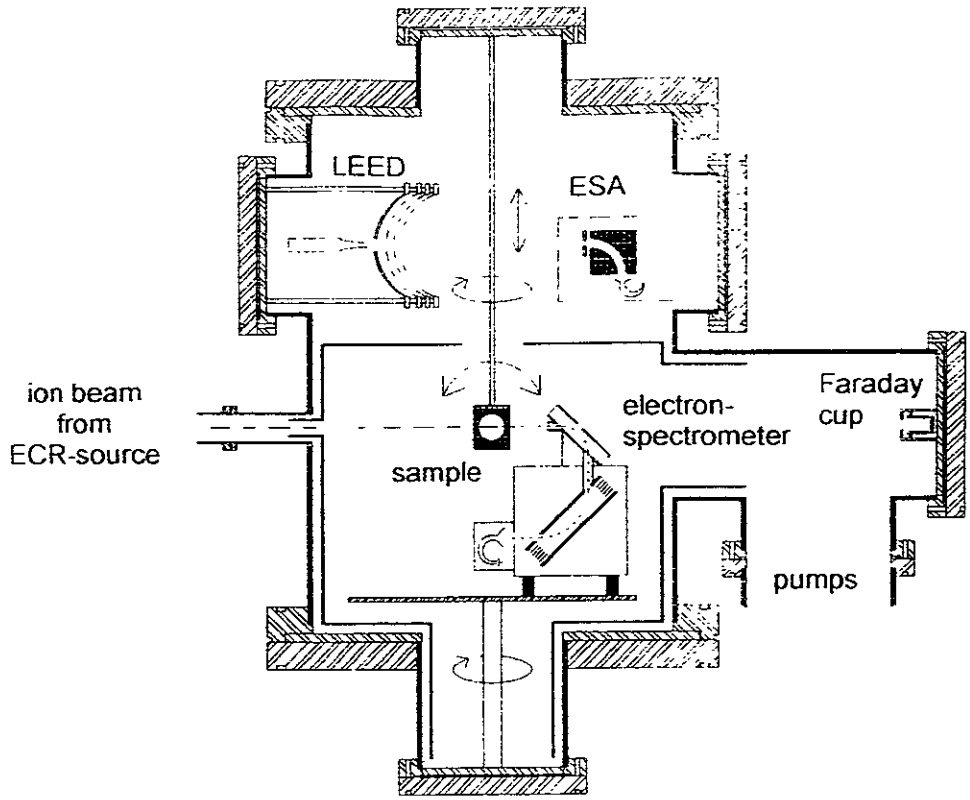

Fig. 9: Tandem parallel-plate spectrometer in UHV collision chamber for studies on MCI induced fast Auger electron emission from surfaces.

An important quantity of a spectrometer is itsacceptance angle defined as the product of its polar and azimuthal acceptance angles. Another important feature is the relative energy resolution $\Delta E/E$ defined as accepted energy interval ΔE divided by electron energy E. The quality of a spectrometer is determined by the focusing power, as electron spectrometers can focus in different orders. Various aspects have to be considered when choosing a certain spectrometer type. Favourable features are high resolution, efficiency and simplicity of design. High resolution is required when individual Auger electron lines are to be measured (see chapter 4.2). Natural line widths and separations of adjacent lines are of the order of 1 eV. Accordingly, for electrons with an energy of typically 1 keV, resolutions $\Delta E/E$ of $\leq 10^{-3}$ are required, which can be realized by reduction of the spectrometer slits or electron deceleration. The latter method takes advantage of the fact that $\Delta E/E$ is usually constant so that the reduction of E also decreases ΔE. The deceleration method is preferrable since the loss in spectrometer efficiency is relatively low and, furthermore, allows for varying ΔE during the measurements.

A measure for the efficiency is the luminosity of the spectrometer which is proportional to the product of the solid angle and the accepted area of the source. Both the solid angle and the accepted source area are determined by the focusing power of the spectrometer. Significant experimental problems are posed by stray electrons reaching the detector and by spurious electric and magnetic field. For high resolution measurements it is required to reduce the earth magnetic field by a factor of about 100. This can be achieved by a Mu-metal shield placed inside the scattering chamber. Similarly, spurious electric fields must be avoided. They are generally produced by electrons collected at insulating ("dirty") surfaces. Such fields are critical near the target region as they can produce energy shifts of the electrons of several eV. In chapters 4.2 and 4.3 some typical Auger electron spectra will be exhibited.

3.3 Studies on MCI-induced Sputtering and Secondary Ion Emission from Insulator Surfaces

3.3.1 Secondary Ion Emission

Secondary ion emission yields can be measured simply with a quadrupole mass spectrometer for positive and negative ions (see fig. 10). Relative ion yields (i.e. counts per primary ion) can be determined in a fixed geometry, and the respective absolute secondary ion yields are derived from the acceptance geometry, based on the quadrupole solid angle of acceptance and the angular distribution of the secondary ions. From the accuracies of primary and secondary ion current measurements and by taking into account possibly different ejection characteristics, a conservative estimate leads to total errors of the absolute secondary ion yields of $\leq 50\%$. Great care is necessary for avoiding artifacts due to surface charge-up effects in ion impact on insulator surfaces /20/. The targets can be heated to become sufficiently conductive, or flooded with low energy electrons to compensate positve charge on the surface. For example, at room temperature a LiF(100) surface can become charged-up to such an extent that it acts as an electrostatic mirror for the ion beam. However, by increasing the temperature the charging-up und ion bombardment decreases and at a temperature of more than 350 ^{o}C no change in the yield of emitted positively and negatively charged secondary ions can be observed anymore /20/. Therefore, all data for LiF(100) described in chapter 5 have been measured at a temperature of 400 ^{o}C, where LiF is a good ionic conductor and its stoichiometric surface is restored because radiation induced lattice defects will be annealed.

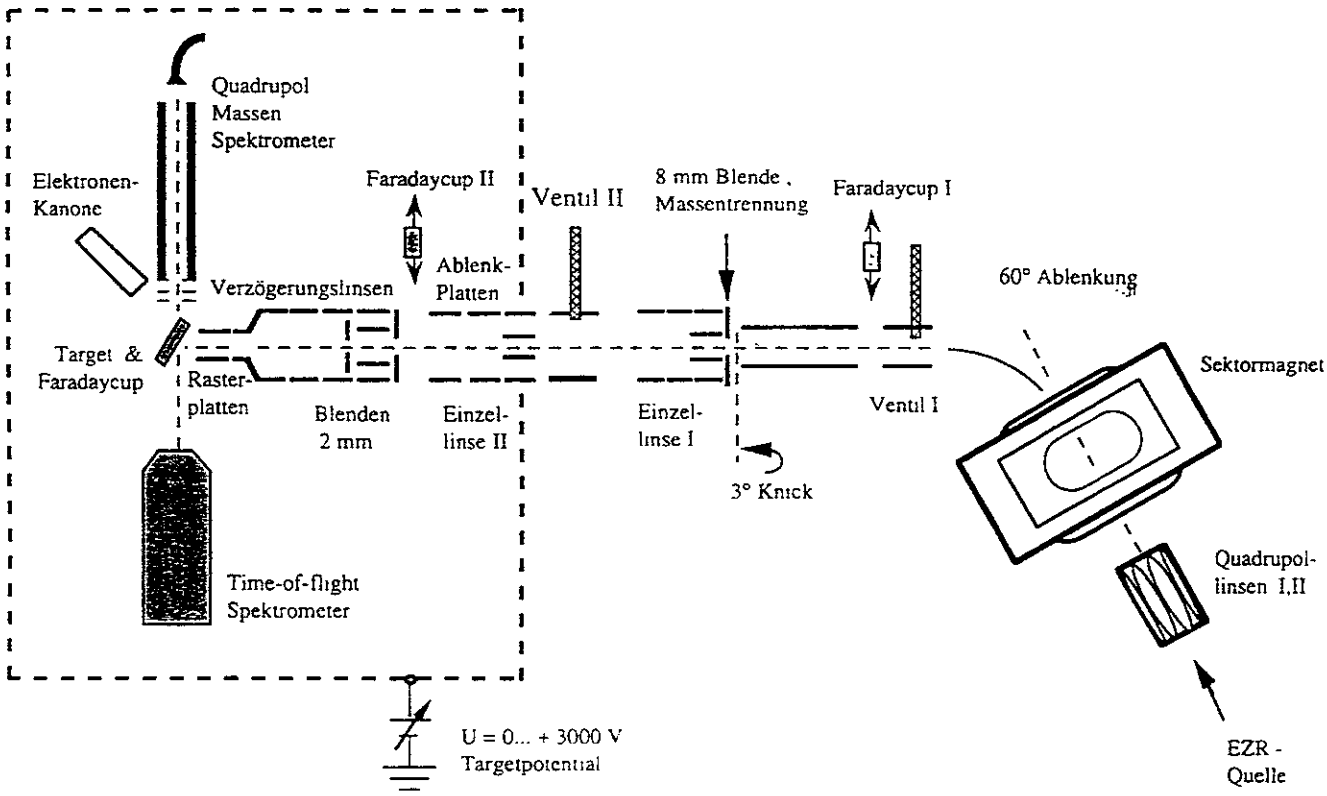

Fig. 10: Setup for studying MCI-induced "potential sputtering" and -secondary ion emission from atomically clean surfaces.

Similar heating experiments have also been performed with thin LiF film targets /21/. The emission of Li^+, F^+ and F^- was studied at target temperatures of 20 and 400 °C with and without electron flooding. Since the apparent yields can depend on surface charging-up as well as changes in surface composition related to different sample treatment, the following test procedure has been adopted. As a first step, the ratio of Li^+ and F^+ yields was monitored to control the surface composition. Since both ion species are positively charged, this ratio should be independent of the electric potential of the surface, and each change of this ratio should indicate a change in surface composition.
Constant surface composition was achieved only for carefully annealed (400 °C) surfaces. The ratio of Li^+ and F^- was taken to monitor any charging-up of the surface. This ratio increases if the target is positively charged-up, since then Li^+ will be repelled from and F^- attracted by the surface. The ratio of Li^+ and F^- yields turned out to be slightly larger for a cold target than for a hot one, which indicates that even thin LiF films are slightly charged-up at room temperature under ion bombardment.

Changes of these ratios increase with decreasing impact energy because then the energy distribution of secondary ions is shifted towards lower energy, and slower ions are more likely to "feel" an electric field at the surface which can influence the respective yields more substantially. The conclusion drawn from these tests was that keeping LiF at 400 °C is a sufficient and convenient method to get rid of electric charging-up. The experiments also showed that artifacts in ion yield measurements can be introduced very easily and great experimental care is needed to avoid wrong measurements. On the other hand, measurements for insulator targets which need to be kept at low temperature, have to be performed by flooding the target with low energy electrons.

3.3.2 Measurement of Total Sputter Yields from Thin Films by means of the Quartz Microbalance

Quartz crystals are widely used for determination of the area mass and hence the thickness of deposited material. They can therefore also be utilized for measuring the rate for removal of deposited material (i.e. the sputtering yield), which so far has mainly been studied with other techniques such as conventional microbalances or catcher foils analyzed by Rutherford back-scattering. The use of quartz crystals for sputter yield measurements encounters several problems. The rates of material removal and hence the frequency changes are rather low compared to most deposition applications, requiring high frequency stability of the crystal and of the oscillator circuit, as well as high accuracy and resolution of the frequency measurement. Furthermore, a substantial amount of energy is deposited by the primary particles on the sputtered surface, causing problems due to thermal drift. In many deposition applications, the energy deposition per incident atom is only a few eV (sublimation energy plus heat radiation from the evaporation source), while for MCI impact the energy deposited per sputtered atom is rather in the range of up to a few hundred eV. Other problems may arise from the sensitivity of the resonance frequency on quartz surface stress.

The application of the quartz microbalance for sputtering investigations has now been improved such that mass changes of $\leq 10^{-3}$ monolayers of thin films evaporated on temperature-stabilized SC-cut quartz crystals are detectable /22/. Quartz crystal targets for measuring sputter yields (see fig. 11) were provided with evaporating Au contacts on a thin Cr adhesion layer. For sputtering of LiF and NaCl (see chapter 5.2) thin films of approximately 100 nm were evaporated from a Mo boat onto the frontal contact.

Measurements on Au were directly performed at the Au contact of the quartz crystal. Deposition of these contacts and their coating with LiF- and NaCl thin films was done in a separate high vacuum coating system at approximately 150 °C substrate temperature and deposition rates in the order of 1 nm/s. For sputtering measurements on Si and SiO_2 pure Cr contacts were used to avoid formation of Au silicide. Si was deposited in situ from an electron-beam heated crucible, whereas GaAs was deposited in a MBE system and transported in air to the UHV set-up.

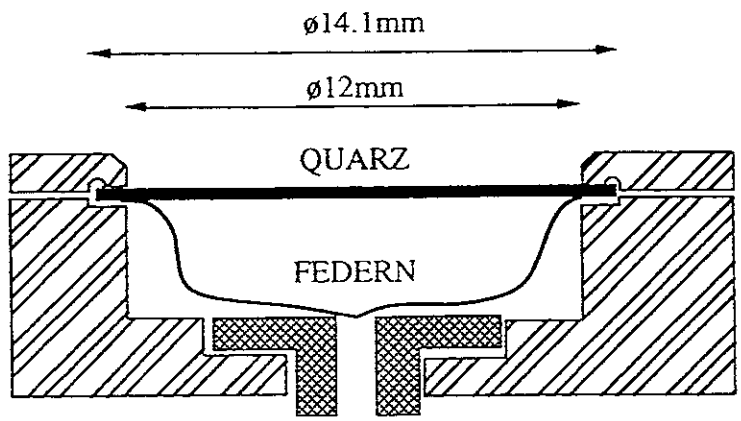

Fig. 11: Geometry of oscillator quartzes applied for sputtering measurements.

Before measurements all target surfaces have been cleaned by sputtering and heating. To check cleanliness, quality and stoichiometry of thin films from alkali halides, secondary ion mass spectroscopy and Auger electron spectroscopy have been used in situ. Two types of plano-convex (6 MHz, 14 mm diam.) quartz crystals have been used, which mainly differed in their crystallographic orientation: The AT-cut (YXl)-35.25° (rotation symbol after /23/) is the standard orientation used for deposition monitors, but has the disadvantage of being sensitive to radial stress with a relative frequency change of 2.75×10^{-11} m^2/N /24/. The SC-cut (YXwl)+21.93°,-33.93° is insensitive to radial stress but has a lower piezoelectric coupling factor than the AT-cut. It also needs special oscillator electronics to suppress an unwanted vibration mode with a frequency approximately 10% above the main resonance. Both crystals are operated in the lowest thickness-shear mode (i.e. a standing transversal wave, with the wave vector perpendicular to the crystal surface), which has extrema of resonance frequency at approximately 80 °C for the AT-cut quartzes, and around room temperature and at 160 °C for SC-cut quartzes.
To avoid first order thermal effects, the crystal holder was resistively heated to this temperature.

Since AT-cut crystals exhibit an additional temperature sensitivity due to thermal stresses, the ion beam was scanned over most of the 10×10 mm^2 contact surface of the crystal to avoid localized heating, which would cause frequency jumps if the ion beam is switched on and off.
On the SC-cut it is sufficient to have constant ion current density in the "active" (vibrating) area of the crystal. There, ion beams were scanned over 5×5 mm^2 only which allowed higher current densities than with the AT-cut.
The electronics consisted of a home-built gain-controlled oscillator circuit and a HP 5372A frequency analyzer with temperature-stabilized crystal timebase. The whole system provided a frequency noise level of approximately 10 mHz (RMS) with AT- and 1 mHz (RMS) with SC-cut crystals, respectively.
Since the deposited films are very thin compared to the thickness of the quartz crystal, it is sufficient to use the simple equation

$$\frac{\rho_F \, \Delta l}{\rho_Q \, l_Q} = -\frac{\Delta f}{f} \qquad (5)$$

for determination of the mass loss from the relative change of frequency $\Delta f/f$. $\rho_F \Delta l$ denotes the change of mass per area, and ρ_Q and l_Q are the density and thickness of the quartz crystal, respectively.
To determine the total sputter yield in dependence of the MCI kinetic energy, one has to consider two important facts which can be of strong influence. The first point concerns the measurement of the primary ion current which has to be performed with a biased Faraday Cup to avoid errors due to ion induced electrons. Secondly, the energy dependent primary ion deposition in the first monolayers at low ion doses influences the frequency change in the opposite direction to the sputtering effect, until steady state conditions are reached.
E.g., for 100 eV Ne^+ bombardment of LiF it has been found that the system reached steady-state conditions (i.e. no more significant changes in the sputtering rate within the accuracy limit of 10 %) after a dose of $1x10^{16}$ ions/cm^2, which corresponded to the removal of two monolayers.

4. Studies on MCI-induced Electron Emission

4.1 Slow Electron Emission from Metal Surfaces

For MCI charge states up to q=6 Hagstrum /25/ found a linear dependence of the total electron yield on the projectile's potential energy, i.e. the sum of the q first ionization potentials. Further investigations with MCI of q≤7 were performed by Arifov et al. /26/ who interpreted their results by cascades of stepwise resonance neutralization- and autoionization processes undergone by the projectile in front of the surface, each of these steps giving rise to ejection of electrons with, on the average, kinetic energies of about 15 eV. For still higher MCI charge states the former linear relationship between the total electron yield and the MCI potential energy was found to break down /27, 28/. However, up to q=80 no saturation of the total electron yield as a function of charge state has been found, so far /29/. A large set of absolute total electron yields measured by means of the statistical method (cf. chap. 3.2.1; q≤80) is shown in fig. 12.

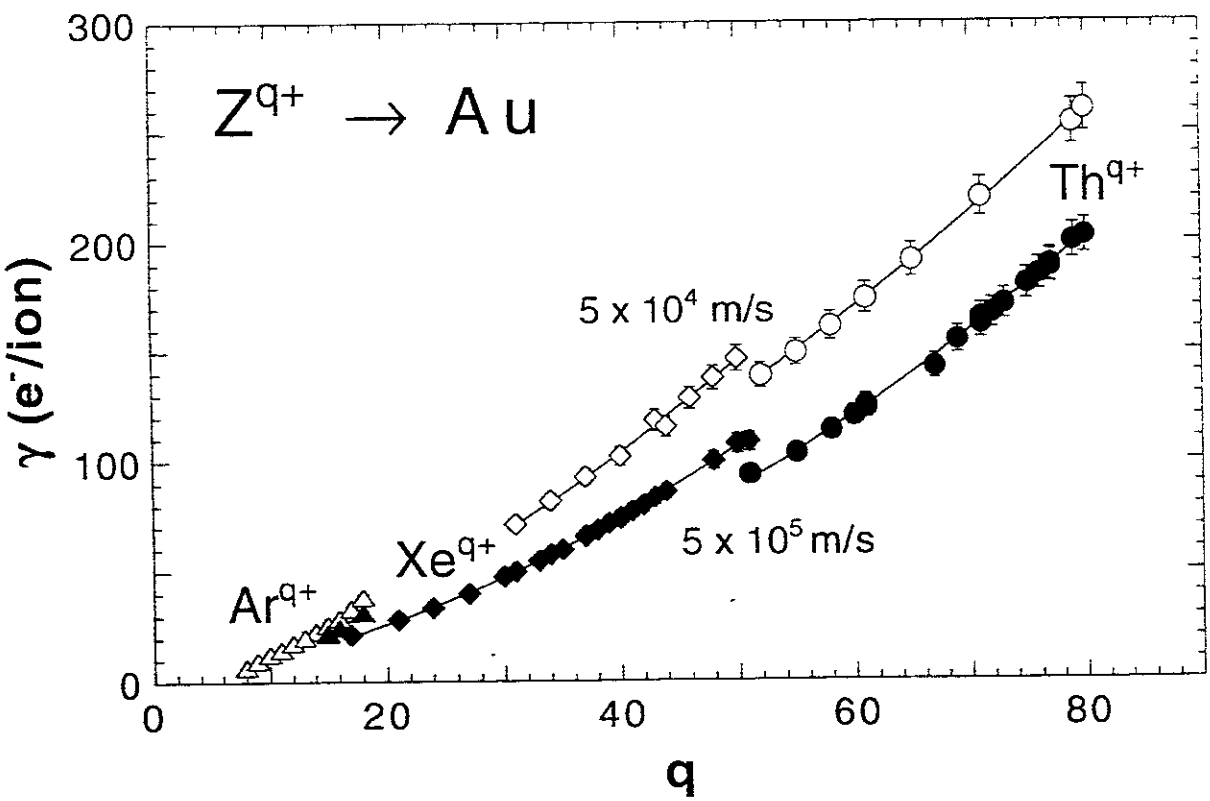

Fig. 12: Total electron yields for impact of slow MCI on clean polycrystalline Au /29/.

At the lowest impact velocity, as given by the image-charge self-acceleration of the projectile, e.g. for impact of Th^{79+} on clean gold about 290 electrons are ejected. It has been found that these total electron yields exhibit the following general dependence on the impact velocity. Starting from low collision velocity the electron yield drops continuously towards a minimum value and rises again due to an increase of the kinetic electron emission, as shown in fig. 13 for impact of C^{5+}, N^{5+} and O^{5+} on clean gold /30/. The KE threshold velocity v_{th} is reached at ca. $2x10^5$ m/s. Above it a contribution due to kinetic emission starts to rise practically linearly with the excess impact velocity. The overall behaviour of the total electron yield γ can thus be represented empirically by the relation:

$$\gamma(v) = \gamma_{PE} + \gamma_{KE} = \frac{c}{\sqrt{v}} + \gamma_{\infty} + k \cdot (v - v_{th}) \cdot \theta(v - v_{th}) \qquad (6)$$

where θ denotes the unit step function and c, γ_{∞} and k are constants depending on the collision systems under consideration.

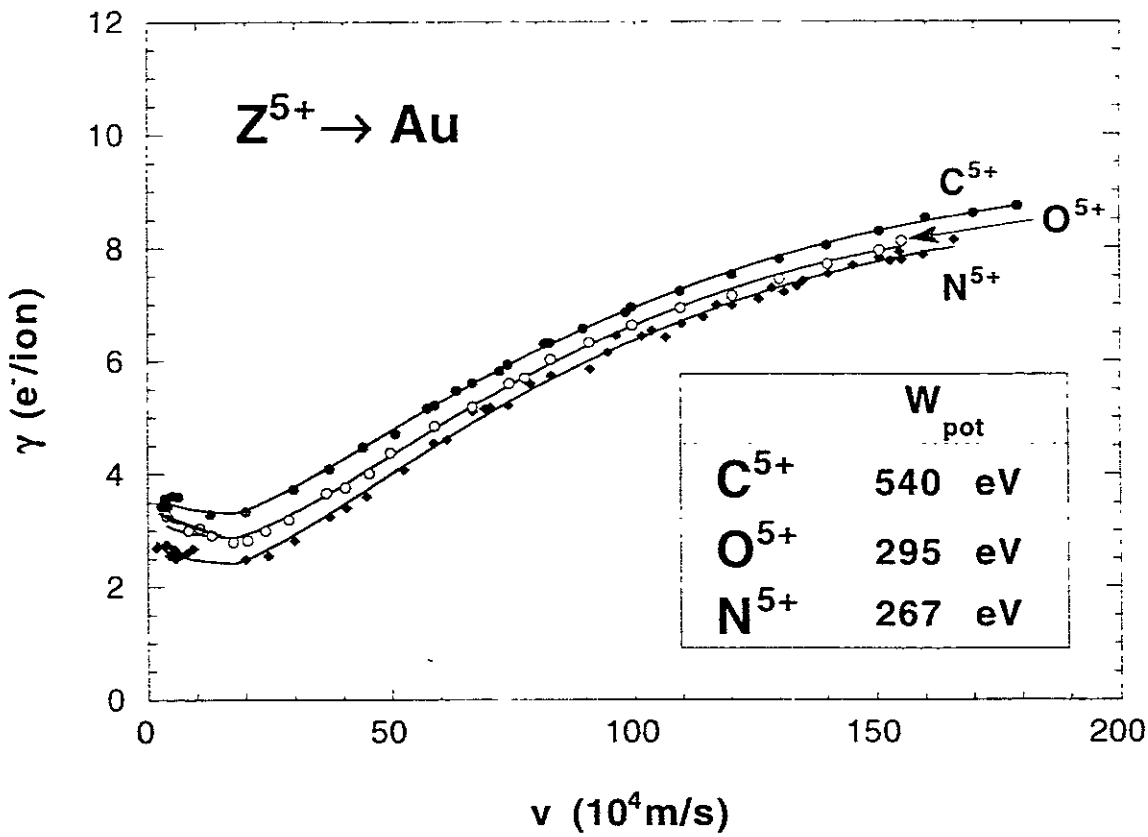

Fig. 13: Total electron yields for impact of Z^{5+} (Z = C, N, O) on clean polycrystalline Au over wider impact velocity range /30/.

The increase of the electron yield for lower velocities (cf. Fig. 13) is attributed to the fact that the slower the ions the more time is available for the above-surface neutralisation and de-excitation processes leading to electron emission before the projectiles hit the surface. Of course, the velocity v should be taken as the effective velocity including the image charge acceleration, therefore no singularity appears at zero nominal impact velocity. Further insight into the origin of the emitted electrons is provided by comparing the measured electron emission statistics with model probability distributions /31/. For this purpose, the assumption is made that the electrons are emitted statsitically independent from each other with equal single emission probabilities p. In this case the probability for the emission of n electrons is given by the binomial distribution which contains a number N for the total ensemble of involved electrons as second parameter. Thus, by best-fitting binomial distributions to the measured statistics, the respective single emission probability p and the number N of electrons which are actually involved in MCI-surface interactions giving rise to potential emission (PE) are determined.

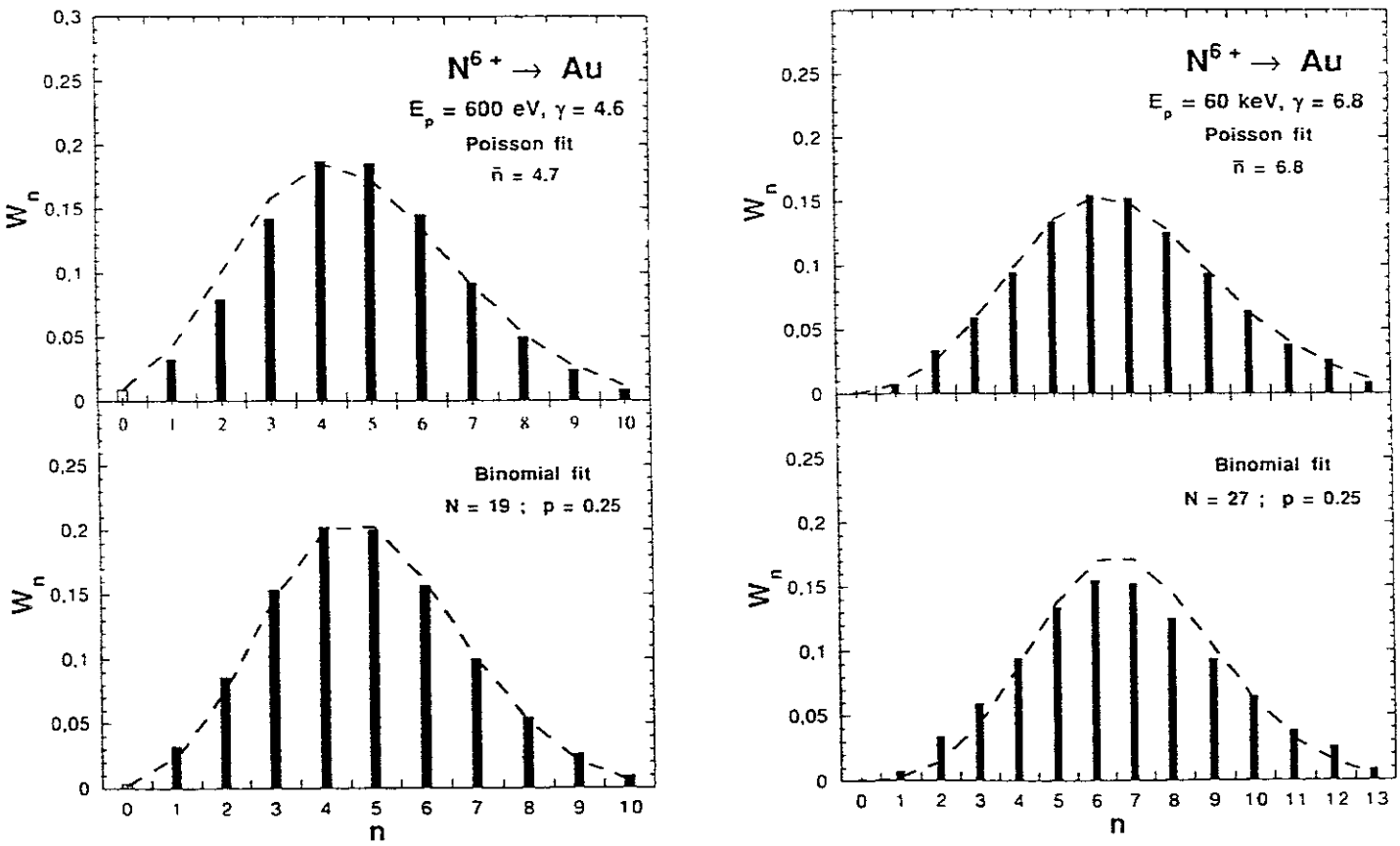

Fig. 14: ES for impact of N^{6+} on clean polycrystalline Au
for low (left) and higher (right side) impact energies /31/.

In Fig. 14 the comparison of a measured statistical distribution with its best-fitted binomial distribution are shown for 600 eV N^{6+} ions impinging on a Au surface. The statistics in the number of observed electrons indeed follows closely the binomial distribution. This is an indication that most of the electrons are ejected above and at the surface: Emission below the surface would involve strongly differing escape probabilities and thus cause a deviation from the binomial distribution. The electron ensemble size is about N=19 electrons which are involved in the emission process, and their mean escape probability is $p \approx 0.25$. There is another indication that most of the slow electrons are ejected above and at the surface, namely the dependence of the yield on the time available in front of the surface. This time is limited by the image charge acceleration which causes a finite impact velocity even if the projectile ion beam has been prepared with almost zero velocity far from the surface. Correspondingly, a levelling off of the total electron yield is observed when going to very low impact velocities /29/. The impact energy gain caused by image charge acceleration can directly be extracted from the experimental dependence of γ vs. v, and more clearly from γ versus 1/v. Corresponding results are in accordance with the prediction of the staircase model of stepwise neutralization up to charge states as high as q=80.

In order to extract information about the above-surface neutralization steps of highly charged projectiles, the measured total electron yields have been compared with results from elaborate model calculations based on the over-the-barrier model /8, 9/. Qualitatively, the increase of γ towards low impact velocities covered by the term containing the constant c in equ. (6) is attributed mainly to Auger- (AI) cascades which can evolve the longer the more time is available in front of the surface. The velocity-independent part of the PE denoted by the constant γ_∞ in equ. (6) is largely attributed to electron promotion and screening effects. However, dependencies of the electron yield on the projectile species, e.g. for Ne^{10+} vs. Ar^{10+} vs. Xe^{10+}, cannot be accounted for by the over-the-barrier model /8, 9/, indicating that the so far given description of MCI surface interaction is still only approximate.

Considering the above-surface phase only, it is difficult to understand the large number of electrons emitted. E.g., the result that about 20 electrons are involved in the emission process for 600 eV N^{6+} ions impinging on a Au surface would imply that all these electrons were ejected in the short time interval of 10^{-14} s above the surface, i.e. the respective rates for PE have to be as large as 2×10^{15} s^{-1}.

Typical Auger processes are significantly slower except when all involved electrons are initially in the same n-shell (Coster-Kronig transitions) - a situation unlikely for hollow atoms in front of the surface. However, such high rates have recently been calculated for electron emission following Auger capture into screened projectiles inside a metal /32/. This suggests that PE occurs to a large extent only when the projectile is very close to the surface where it is effectively screened by metal electrons. In the close vicinity of the surface it makes in fact no sense to distinguish between electrons in the conduction band and those captured by the projectile: The ionic core is "dressed" by the conduction band electrons, and consequently atomic Auger transition rates are expected to become similar as the Auger neutralization rates. It should also be noted that at higher impact energies a sub-surface contribution to PE due to secondary electron emission has been inferred from measurements for N^{q+} impact on single-crystalline metal surfaces /33/, by regarding the dependence of the total electron yield on the azimuthal angle. Pronounced variations of the total electron yield for different crystallographic directions could not be easily explained by assuming that all the observed electrons are ejected above the surface. An alternative explanation is that upon surface impact of the hollow atom the projectile screening becomes so effective that the respective AI rates are sufficiently high such to provide the almost impact velocity-independent PE contribution γ_∞ in equ. (6).

4.2 Fast Auger Electron Emission from Metal Surfaces

Final relaxation of projectiles which after their above- and at-surface phases are still in highly excited states has to take place below the surface. This implies that a major fraction of the potential energy of the highly charged ions is carried into the solid, which should also have important consequences for MCI induced material modifications. Filling of the innermost projectile vacancies (K-vacancies for bare or hydrogen-like projectiles) results in the emission of KLL Auger electrons and can be regarded as the last step in this relaxation. In view of realistic Auger decay rates a full relaxation of the multiply excited hollow atoms via Auger cascades is very unlikely within the short time available in front of the surface (see above). More detailed analysis of KLL Auger spectra with respect to this question /34, 35/, involving N^{6+} projectiles colliding on a Au surface, showed that a structure at the low-energy side of the KLL peaks increased with decreasing collision energy.

This structure was ascribed to above-surface emission which already implied that the major fraction of fast Auger electrons is emitted from below the surface. It should be stressed, however, that these fast Auger electrons always constitute a very small fraction (typically below five percent) of the total number of emitted electrons which in their majority are much slower (cf. chapter 4.1). Evidence for sub-surface emission of fast Auger electrons has been also been obtained /36/ from Auger electron spectra measured at different ion impact- and take-off angles, by exploiting the fact that for initially bare projectiles two KLL Auger processes will take place subsequently (cf. fig. 15). Electrons from the second transition are more strongly attenuated than those from the first one if electron emission takes place inside the bulk. Clearly the relative intensity of the peak from the second Auger process decreases with increasing impact angle, i.e. for deeper penetration of the projectiles.

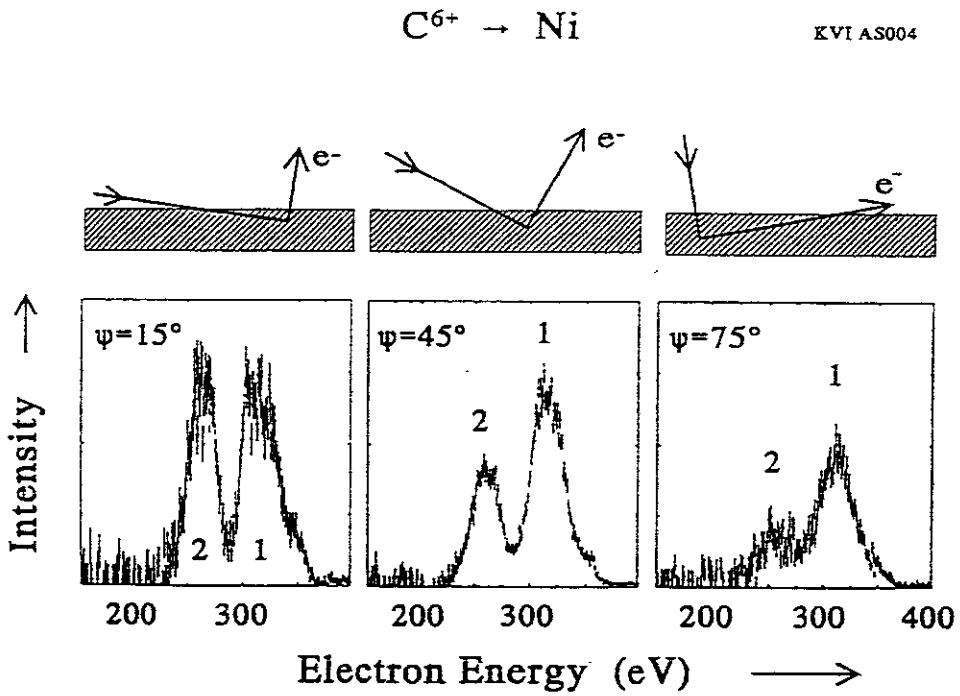

Fig. 15: Auger electron spectra for C^{6+}-Ni(110) impact measured at different impact and take-off angles /36/.

At sufficiently low collision energies and angles of incidence the major fraction of all projectiles is reflected from the uppermost surface layer. In that case one can be sure that KLL Auger electron emission takes place above or in the topmost layers of the surface. In fig. 16 Auger electron spectra are shown for N^{6+} collisions on Al(110), measured at an angle of incidence of 2.5° for different impact velocities /37/.

At low impact velocity one can see a pronounced structure on the low energy side, which by means of Hartree-Fock calculations has been identified as being due to decay of neutral nitrogen atoms with only two electrons in the L-shell, whereas the broad structure can be ascribed to the decay of configurations with a larger number of L-electrons. A more detailed analysis of the sharp peak, based on its Doppler shifting and relative intensity at various collision energies, supports the above-surface nature of this structure whereas the electrons related to the broad structure are emitted already in the uppermost surface layers. The course of the sharp "above-surface" peak intensity vs. the inverse ion impact velocity also indicates that it is subject to the image charge self-acceleration of the projectile, in a similar way as for emission of the slow above-surface electrons (cf. chapter 4.1).

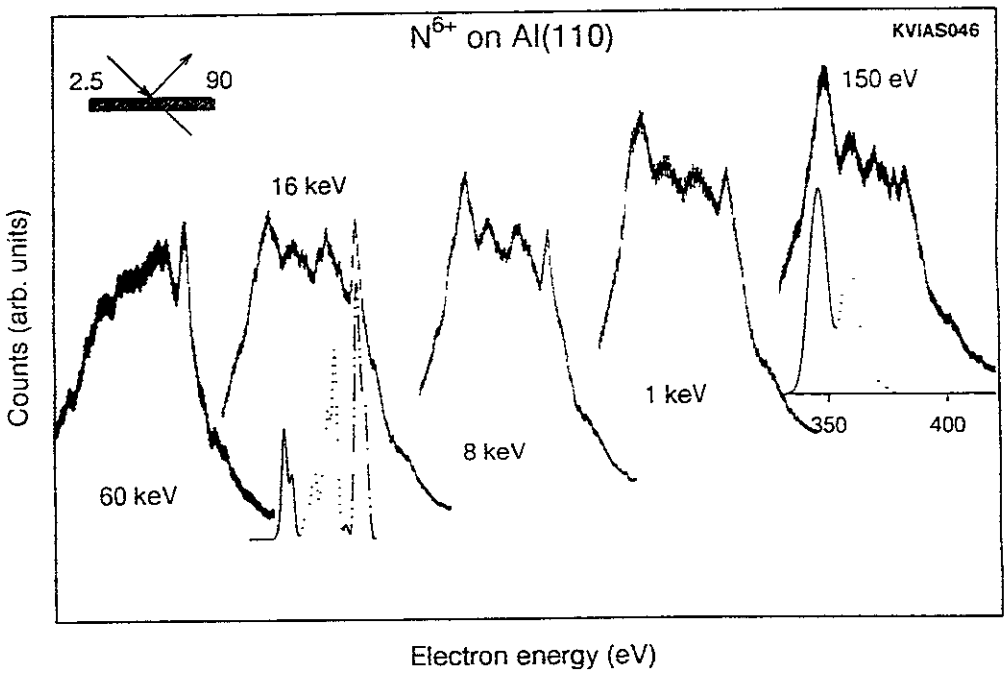

Fig. 16: Auger electron spectra for impact of N^{6+} on Al(110) measured at different impact velocities /37/.

Above the surface the projectile L-shell can be filled only via a relatively slow cascading-down from higher n-shells. Filling becomes much faster if the close collision region is reached, which results in KLL transitions from L-shells filled with more than two electrons. If the time above the surface decreases for higher collision energy, a sharp structure appears at the high energy side of the spectrum due to Auger electron transitions with a completely filled L-shell, caused by transfer of electrons between inner shells of target and projectile.

4.3 Electron Emission from Insulator Surfaces

Interaction of MCI with insulating surfaces is generally difficult to investigate because of charging-up of the target. An exception are alkalihalides, which at elevated temperatures feature a sufficiently high ion conductivity, preventing charging-up by the impinging ion beam (see chapter 3.3.1), whereas they can be regarded as insulators from an electronic point of view. Recently, studies of the interaction of MCI with LiF surfaces have exhibited clear differences to results for MCI collisions with metal- or semiconductor targets, which can be expected since electrons are not as abundantly available and much less mobile than in free electron metals. In Fig. 17 the occupied, un-occupied and forbidden electron energy states of LiF are compared with those of a typical metal as Au. Whereas in metals the conduction band is divided at the Fermi level in electronic bands of occupied and unoccupied states, in LiF the $F^-(2p)$ electrons form a completely occupied valence band with binding energies of about 12 eV (bulk value; surface value can somewhat differ).

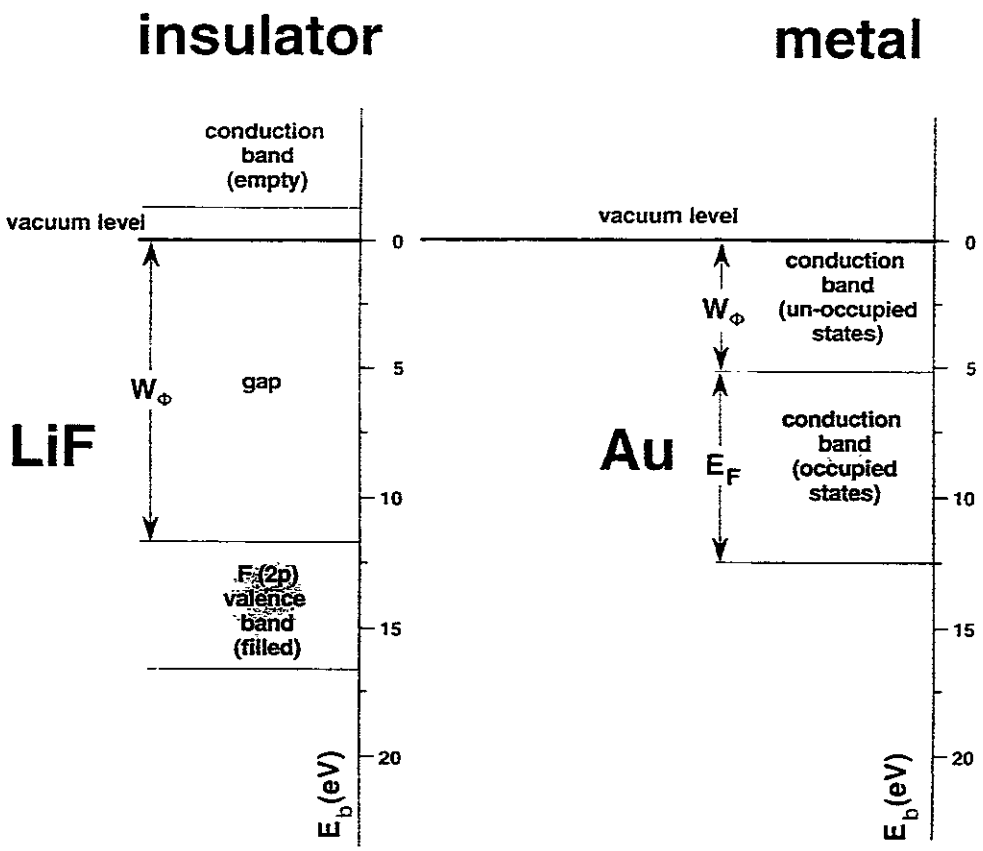

Fig. 17: Surface-densities of states for LiF (left side) vs. Au (right side).

This valence band exhibits a flat dispersion curve, indicating large effective electron masses and a localization of the 2p-electrons at the fluorine atoms in the lattice. A broad energy gap of about 14 eV (bulk value) extends well above the vacuum level toward the first empty allowed states. Not only the electronic structure but also the dielectric response of LiF clearly differ from a perfect conductor. The classical over-barrier condition has been reconsidered by taking into account a dynamic image potential, which involves the frequency-dependent permittivity $\varepsilon(\omega)$ of LiF between about $\varepsilon(0) = 8.6$ (static value) and $\varepsilon(\infty) = 1.9$ (optical value) /38/.

4.3.1 Low Energy Electron Emission from Insulator Surfaces

It has been shown in /39/ that electron yields from LiF due to potential emission significantly differ from that obtained for, e.g., a Au surface. Fig. 18 demonstrates measured yields for N^{q+} ions interacting with LiF as a function of the impact energy.

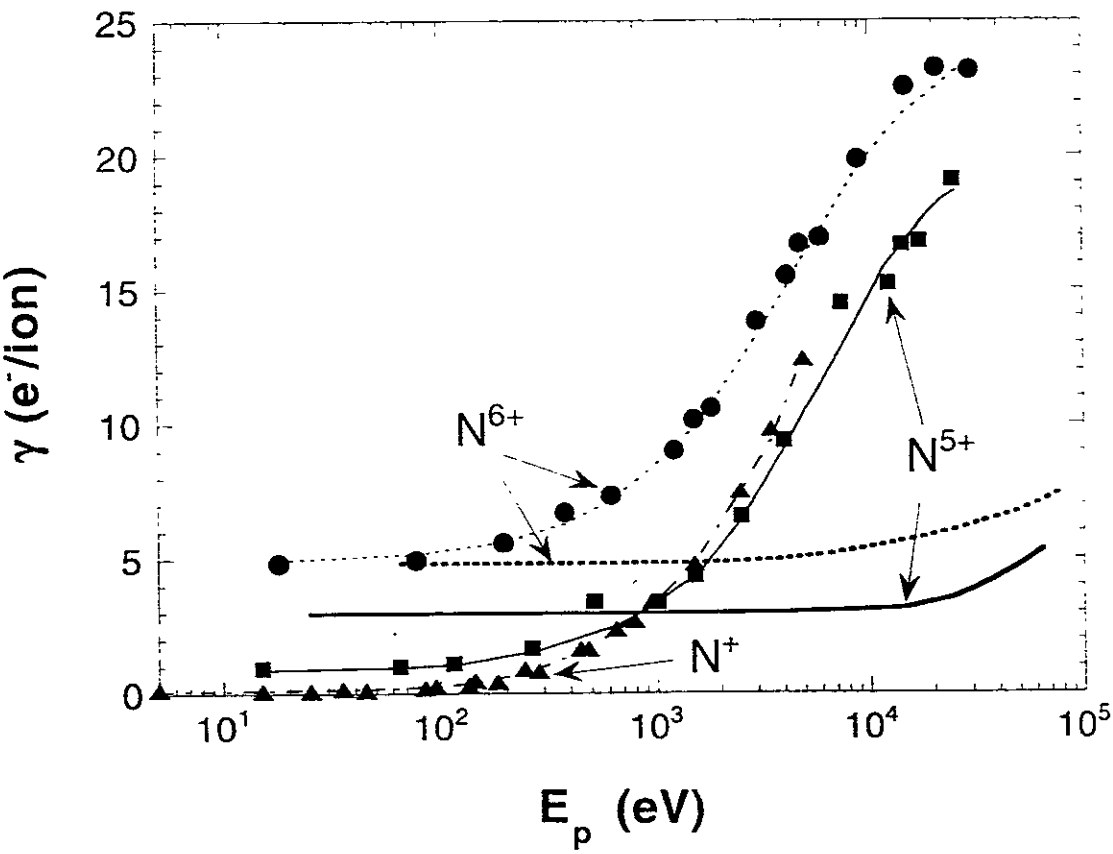

Fig. 18: Total electron yields for impact of N^{q+} (q = 1, 5, 6) on poly-crystalline LiF and Au, respectively, vs. impact energy /39/.

A detailed analysis of these yields demonstrates that besides contributions from PE also ion-induced kinetic emission and secondary electron emission in the target bulk have to be taken into account. The comparably lower yield for N^{5+} for LiF as compared with a Au target can be ascribed to a drastic reduction of the "above-surface" production of low energy electrons. The fact that a similarly lower yield is not observed for N^{6+} projectiles can be explained by the contribution from secondary electrons below the surface induced by high energy KLL-Auger projectile electrons arising in the course of K-vacancy filling. Another indication for the absence of major "above-surface" electrons can be obtained from the electron number statistics. In fig. 19 respective data are shown for impact of N^{5+}/N^{6+} on LiF. For higher energies the fit with a binomial distribution, which worked quite successfully for the Au target, does not agree at all for the LiF target. The Polya distribution gives a much better fit, which can be ascribed to an important contribution by electron emission from below the surface /39/, since the inelastic mean free paths of low energy electrons are considerably larger in insulators than in metals.

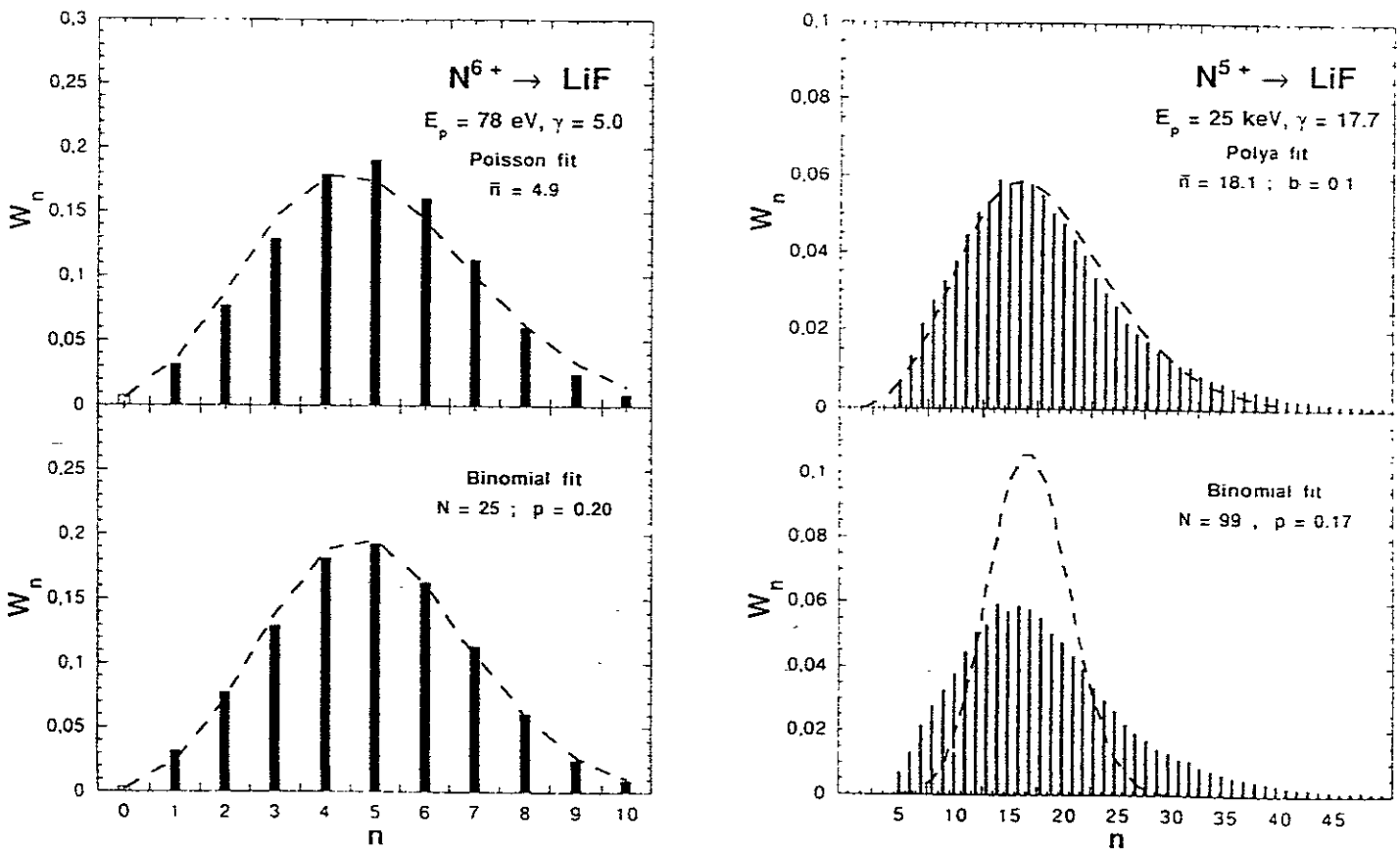

Fig. 19: ES for impact of slow and fast multicharged nitrogen ions on polycrystalline LiF, best-fitted to model distributions /39/.

4.3.2 Fast Auger Electron Spectra from Insulator Surfaces

Fig. 20 shows KLL spectra obtained for impact of N^{6+} on a LiF(100) surface /40/, which can be compared with respective data for a metal surface as shown in fig. 16. Here, the prominent peak on the left side is missing which for the metal target shows up for low-energetic KLL Auger electrons. However, for both targets a sharp peak appears with increasing collision energy on the high energy side. The two peaks have been associated with competing mechanisms for filling the projectile L-shell, as described in chapter 4.2. One of them proceeds via Auger cascades and starts as soon as the hollow atom is formed.

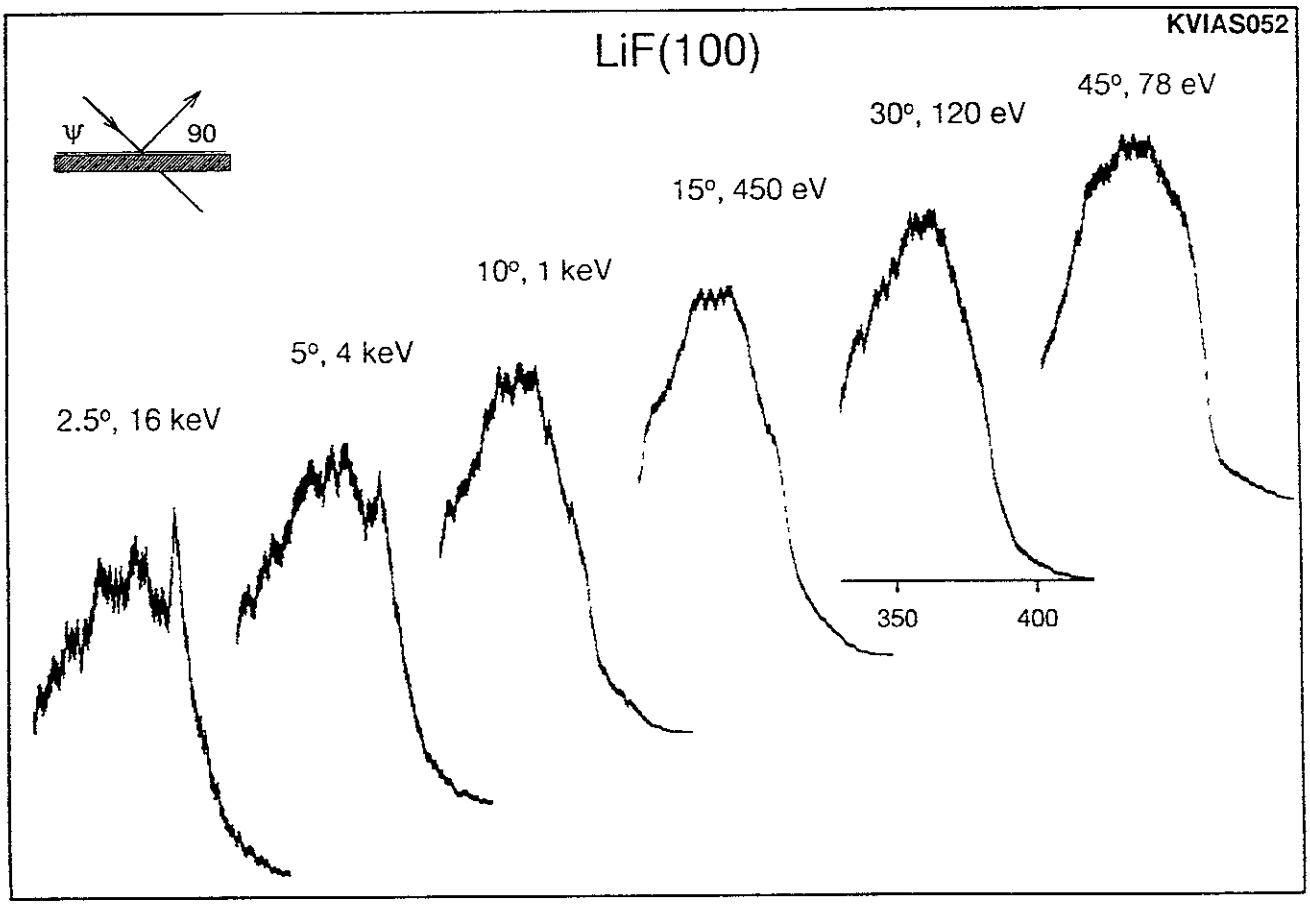

Fig. 20: KLL Auger electron spectra for impact of N^{6+} on LiF(100) /40/.

The associated L-shell filling rate is small compared to typical KLL Auger rates. KLL decay will thus occur readily after the second L-electron has been captured (low energy peak). However, as soon as the ion experiences closer collisions with target atoms, the L-shell can be much more rapidly filled by direct transfer of target core electrons.

This process is rather localized and the associated filling rate is therefore proportional to the ion-target atom collision frequency. For sufficiently high projectile velocities the L-shell becomes completely filled before KLL decay can actually start to take place (high energy peak). As seen in fig. 20, the latter mechanism is also active for LiF, whereas a slow L-shell filling by the Auger cascades is absent. This can in principle be explained [281, 283] by assuming that no hollow atoms are formed above the surface, just as one would expect from LiF being an insulator (cf. above). The large binding energy and small mobility of the LiF valence band electrons block multiple-electron capture from a single lattice site. It has been shown, however, that hollow atom formation takes place if the electron transfer can start from different surface sites, e.g. for grazing MCI incidence at higher projectile impact velocity.

5. MCI induced Emission of Atoms and Secondary Ions from Insulator Surfaces

5.1 Introduction

Figs. 21a,b from /41/ show total sputter yields vs. ion impact velocity for bombardment of various materials relevant for fusion technology. For impact energies of interest for fusion edge plasmas (≤ 1 keV, cf. chapter 1), the yields for hydrogen-ion induced sputtering stay well below 0.1 atoms/ion, and yields for self-sputtering are still below one.

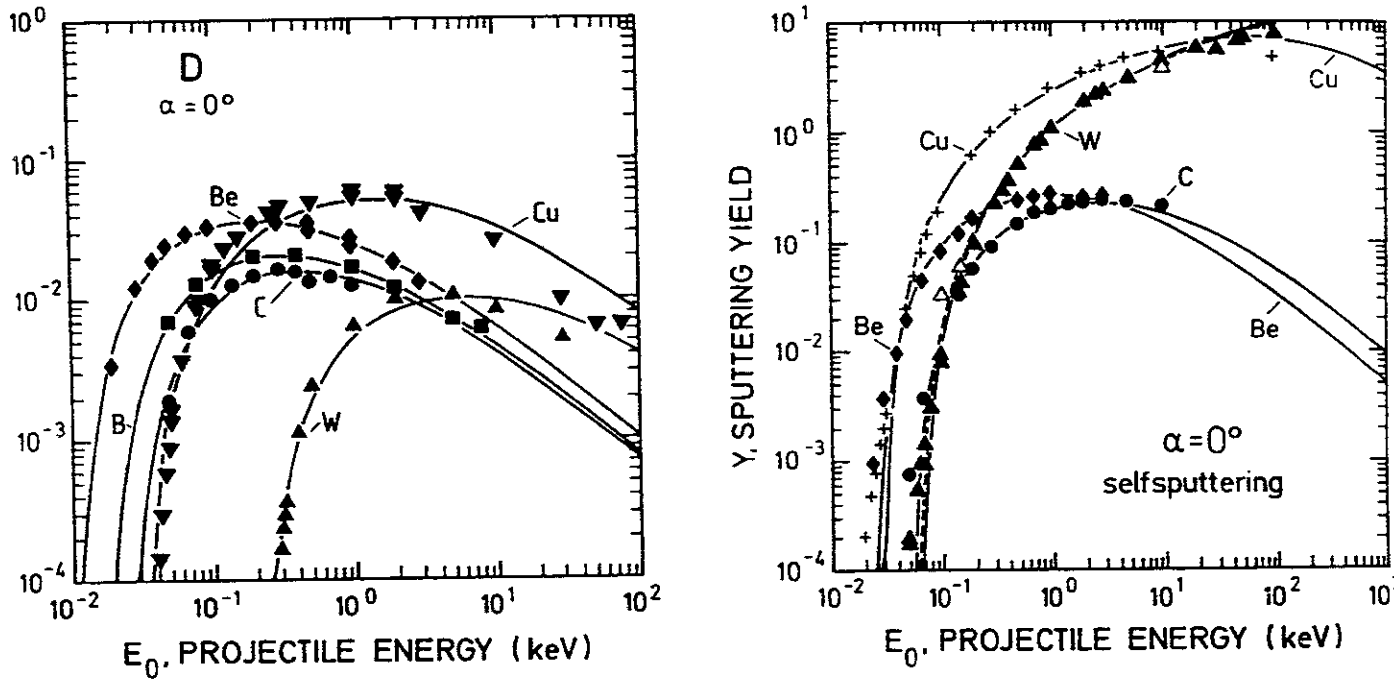

Fig. 21: Sputter yields Y vs. projectile energy E_o for bombardment of materials by deuterons (left side), and for self-sputtering (from /41/).

In investigations of secondary ion emission from insulators bombarded by MCI an apparently strong dependence of the SI yield on the ion charge state /42/ has been explained by the socalled Coulomb explosion model /43/. More recently, MCI induced secondary ion emission- and total sputter yields have been investigated for different atomically clean surfaces of metals (Au), insulators (LiF, NaCl, MgO, SiO_2) and semiconductors (Si, GaAs) /21, 22, 44/. The respective experimental set-up and techniques have already been described in chapter 3.3 (cf. figs. 10 and 11). The primary ion impact energy has been kept below one keV, to separate the specific role of the projectile potential energy in these processes.

The MCI current density was always below 10 nA/cm^2 and the residual gas pressure in the target chamber remained in the low 10^{-10} mbar range.
Interest in MCI as projectiles for insulator sputtering is related to the possibly much higher sputtering yields at low impact energy than for metal surfaces. This so-called "soft sputtering" might be of interest for removing insulating materials from metal substrates without producing radiation defects in the latter. The relevant processes involved in the conversion of projectile potential energy at the surface into kinetic energy of the desorbed and/or sputtered secondary ions and atoms has been a controversial issue. So-called DIET-processes (Desorption Induced by Electronic Transitions) have mainly been studied by impact of photons (PSD for photon stimulated desorption) or electrons (ESD for electron stimulated desorption) on surfaces /45/. In principle, the latter processes should also play a role in MCI-induced sputtering of insulators because of the related high potential projectile energy. The role of the MCI charge state in relation with the ionization energy of the respective atoms for desorption and sputtering should be especially visible at very low impact velocity where any processes due to kinetic effects are suppressed. The already mentioned "Coulomb explosion" model /43/ for sputtering of insulators by MCI assumes the ejection of positively charged microscopic domains from the surface in the course of step-by-step neutralization of the MCI resulting in electron depletion in the near-surface region. In /46/ it has been demonstrated that bombardment of Si with singly charged ions results in a sputter yield larger by a factor of two than for impact of the related neutral atoms. In contrast to these results, in bombardment of Si by 20 keV Ar^{q+} ($q \leq 9$) only the secondary ion yield increased noticeably with the MCI charge, whereas the total sputter yield remained practically independent of q /28, 47/.

5.2 Secondary Ion Emission from LiF

Relative ion yields for F^-, F^+ and Li^+ in dependence on the kinetic energy and charge of Ar^{q+} ions impinging on LiF have been measured /21, 22/. It should be mentioned from the outset that the yields for charged secondary particles are by about three to four order of magnitude smaller than those for the neutral species and therefore represent only a negligible contribution to the respective total sputter yields. However, interesting conclusions can be drawn on the physical processes for production of secondary ions.

In fig. 22 the F^- yield is shown vs. Ar^{q+} impact energy. Within the experimental uncertainty, no clear dependence on primary ion charge can be seen. Below 100 eV impact energy the measurable yield decreases with the latter by two orders of magnitude. In contrast to this behaviour, the yield for F^+ (fig. 23) is strongly affected by the projectile charge. If q increases from 2 to 9, the F^+ yield increases by two orders of magnitude at all kinetic energies applied, but its dependence on the impact energy is much weaker than for F^-.
For Li^+ (fig. 24) the situation is again different: At high kinetic energy practically no influence of the ion charge is observed, whereas at low energy the yield strongly depends on q.

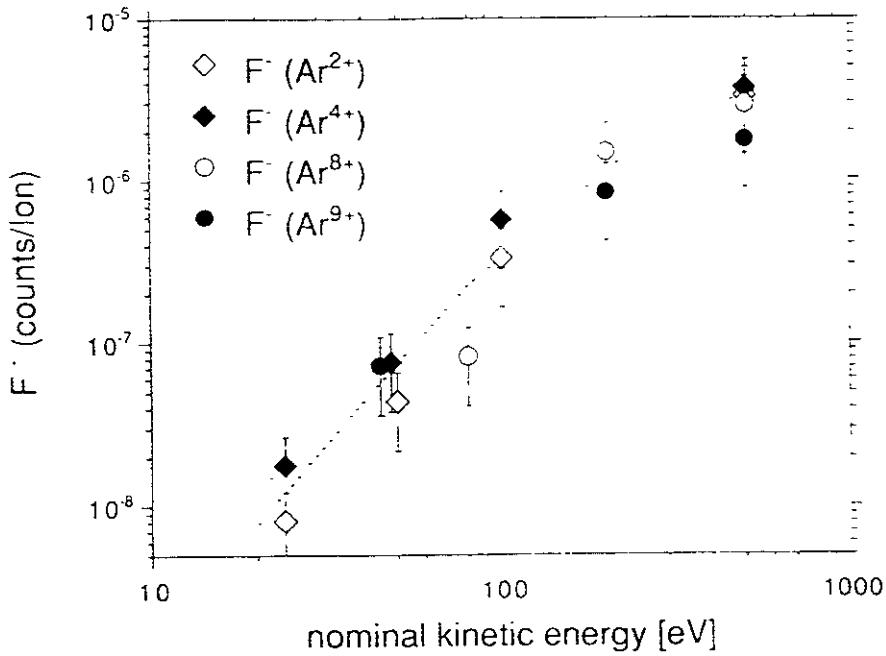

Fig. 22: Dependence of F^- secondary ion yield on projectile charge for impact of Ar^{q+} ($q \leq 9$) on polycrystalline LiF /21/.

It has been shown that at hyper-thermal ion impact energies (<100 eV; /20, 48/) interatomic Auger processes between the projectile and the $F^-(2p)$ valence band of crystalline LiF initiate the F^+ production. At higher impact energies F^+ emission can also be started by electron promotion due to close collisions of projectile ions and target atoms /49/. Due to the low current density (about $1 nA/cm^2$) the emitted ions can only be ejected in single projectile collisions, and for low projectile charge the neutralization of four F^- ions by electronic transitions is impossible.

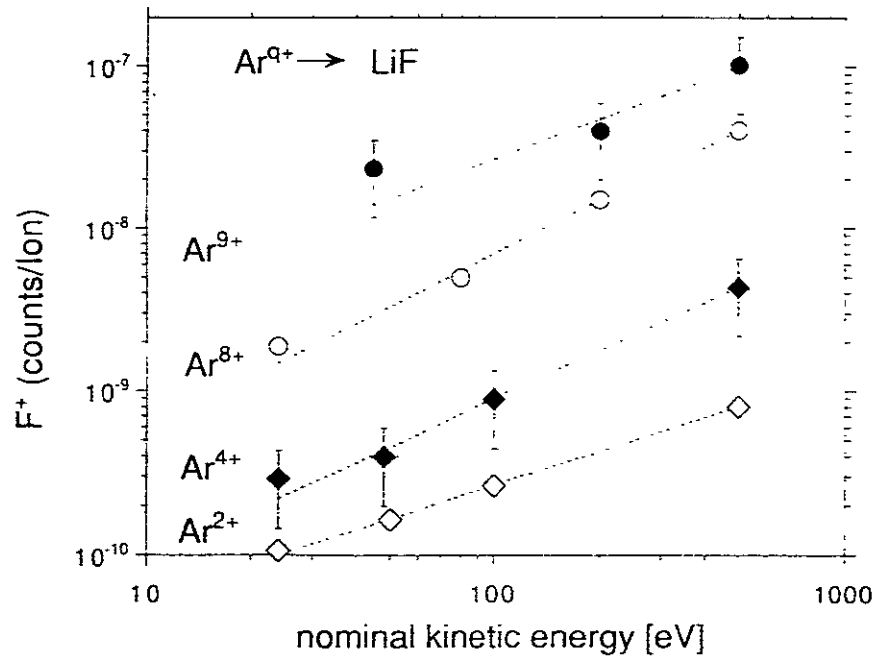

Fig. 23: Dependence of F^+ secondary ion yield on projectile charge for impact of Ar^{q+} ($q \leq 9$) on polycrystalline LiF /21/.

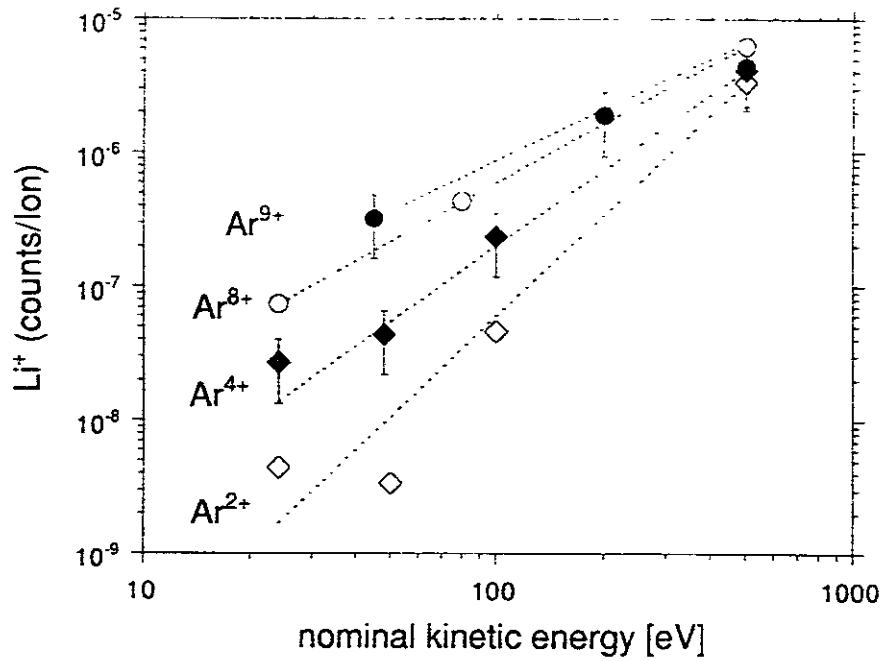

Fig. 24: Dependence of Li^+ secondary ion yield on projectile charge for impact of Ar^{q+} ($q \leq 9$) on polycrystalline LiF /21/.

For Ar^{2+} impact two resonance neutralisation (RN) processes can take place in the front of the surface, or one RN and one Auger neutralisation (AN) process after ion penetration, creating at most one F^+ ion and three F^o neutrals, which is not sufficient to initiate the F^+ desorption. Results for Ar^{2+} indicate an increase of F^+ emission in comparison with Ar^+, the latter one carrying insufficient potential energy for initiating one AN process at the LiF surface.
The data also show that a minimum kinetic energy for the projectile is needed to induce F^+ desorption by momentum transfer. It can be concluded that a distortion of the LiF lattice by momentum transfer from the projectiles makes desorption of F^+ possible if at least two or three neutralized next-neighbour F-atoms are provided, but F^+ production remains very unlikely in comparison with emission of F^- and Li^+. A rough estimate shows that in neutralization of Ar^{9+} about 40 holes per impinging ion can be created in the LiF valence band. Since for an impact energy of about 100 eV the ion can only penetrate at most two monolayers into the LiF bulk, all holes will be formed at the surface which causes a locally strongly distorted, electron-depleted surface region around the impact site. The electron depletion may enhance direct F^+ emission by Coulomb repulsion /50/ from the positively charged surface region. However, the drastic increase of F^+ emission with the MCI charge at low ion impact energy can only be understood by the respectively enhanced AN and a therefrom resulting increased number of sites for direct F^+ emission.
Emission of F^- is induced by momentum transfer from the projectiles. For singly charged primary ions it has been shown that the energy distributions of secondary ions are typical for collisionally induced sputtering /51/. Further indication for such kinetic sputtering of the F^- is the impact energy dependence of the related yield, which resembles those for metal sputtering (cf. fig. 21), and that the F^- yield is practically independent on the primary ion charge.
The Li^+ yield depends strongly on ion impact energy only for impact of Ar^+ and Ar^{2+}. At higher q Li^+ emission becomes possible by Coulomb repulsion without momentum transfer, because of the increased neutralization of four neighbouring F^- lattice ions /50/. However, at higher impact energy for all charge states the influence from momentum transfer becomes more important than the contribution from potential sputtering, and therefore the strong significance of the MCI charge state q disappears. As a general feature, potential energy effects dominate the secondary ion emission from LiF only at impact energies below 100 eV, whereas at higher impact energy kinetic sputtering will always impose the comparably more important influence.

5.3 Potential Sputtering from Insulator Surfaces

Total sputter yields have been measured for bombardment of thin LiF films by Ar^{q+} (q = 1÷9), utilizing the quartz microbalance technique (/22, 44/, see chapter 3.3.2). The observed yield dependence on the projectile impact energy has been plotted in fig. 25a for different projectile charge. Yields clearly increase with q and for given q stay approximately constant up to 100 eV impact energy, but then increase gradually with further increasing impact energy. This influence of the projectile potential energy becomes more visible from fig. 25b, where the MCI kinetic energy has been corrected for image charge acceleration (see chapter 4). At low impact energy the total sputter yield reaches typically one emitted LiF molecule per 100 eV potential energy.

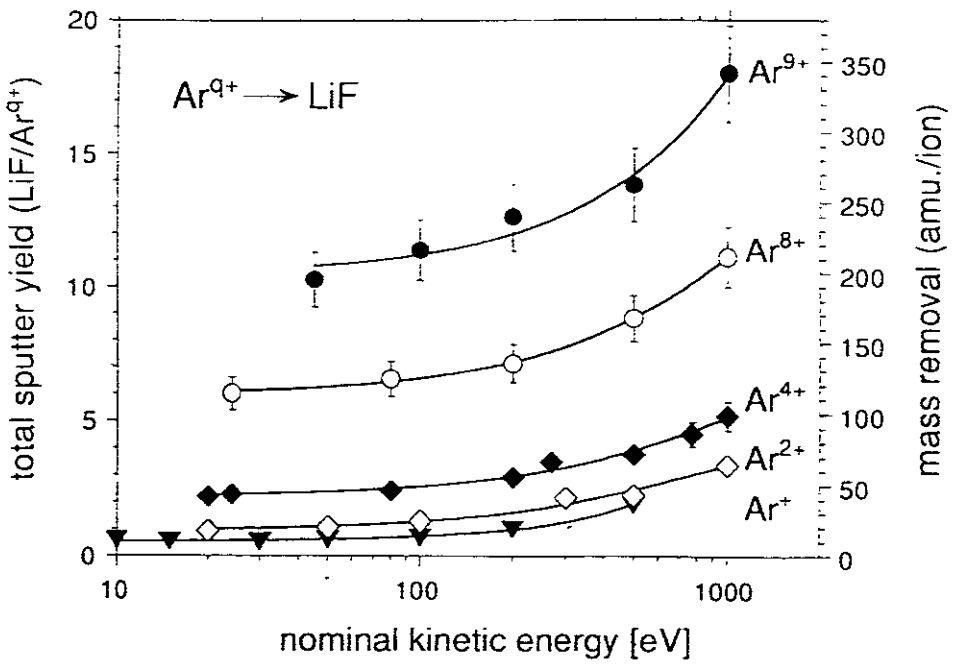

Fig. 25a: Total sputter yields for Ar^{q+} bombardment of polycrystalline LiF vs. impact energy, for different ion charge states q /22, 44/.

These results can be explained by considering the neutralization of slow MCI on a LiF surface (see chapter 4.3), together with the broadly accepted mechanisms responsible for ESD and PSD from alkalihalides. Neutralization and de-excitation of impinging MCI above, at and below the LiF surface will produce holes as well as free electrons in the $F^-(2p)$ valence band.

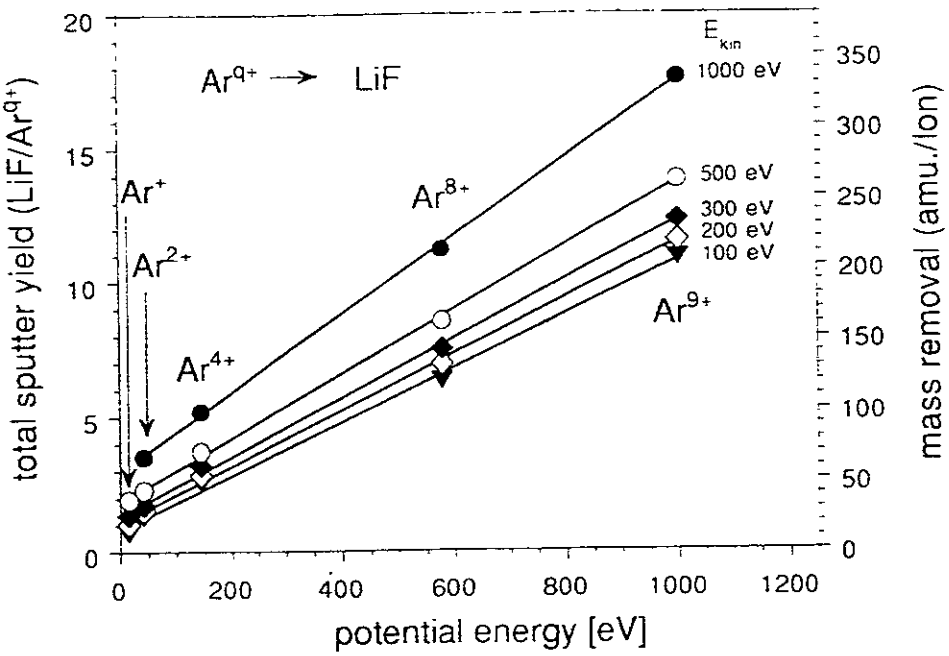

Fig. 25b: Total sputter yields for Ar^{q+} bombardment of polycrystalline LiF vs. MCI potential energy, for different impact energies /22, 44/.

ESD and PSD of neutral particles from alkalihalide surfaces /45/ are initiated by electron-hole pair creation due to interaction of electrons or photons with the solid. Holes formed inside the F^-(2p) valence band are called "hot holes" and can diffuse very rapidly until becoming trapped by impurities or by forming "V_k-centres" (i.e. F_2^- molecular ions adjacent to two anion sites). These V_k-centres can trap available electrons and form "self-trapped excitons" /52/, which at room temperature will immediately decay into two "colour centres", i.e. a "H-centre" (F_2^- molecular ion at anion lattice site) and a "F-centre" (electron localized at the next or second next anion site). H-centres and F-centres created in the bulk can diffuse to the surface, where the H-centre decays by emitting a F^o atom and the F-centre may neutralize a Li^+ cation. The such created Li atoms at the surface will form a metallic overlayer which at room temperature stops further progress of ESD or PSD, but will be evaporated at surface temperatures above 150 °C.

For neutral particle desorption induced by hyperthermal MCI impact on LiF the following model can be adopted. If the MCI approaches the LiF surface, holes in the F(2p) valence band will be created by RN.

"Cold holes" localized at the Fermi edge in the first surface layer will form V_k-centres, with the resulting highly excited projectiles being de-excited by AN- and AI processes, which leads to electron emission as described in chapter 4.3.1. If a projectile penetrates the surface layer still in its ionized or highly excited state, interatomic AN and RN will take place and further neutralize and/or de-excite the projectile, thus producing more electron-hole pairs. "Hot holes" will be formed with higher probability because of the larger electron density in the centre of the valence band. The situation is similar to ESD where decay into H- and F-centres followed by desorption of F^o (and at elevated temperature also Li^o, see above) takes place. At low impact energy all defects are created still in the near-surface region, and diffusion processes are of minor importance. However, in contrast to ESD, for MCI impact no Li overlayer is formed because already at low impact energy the projectile provides sufficient momentum transfer for removing the rather weakly (van der Waals) bound Li atoms from the LiF surface, even at room temperature. Therefore, for MCI impact stoichiometric desorption can be assumed, whereas for ESD at room temperature a Li-enriched surface is produced because only the halogen atoms are ejected. Increase of the MCI impact energy will enhance the efficiency of hole formation in a similar way as for impact of singly charged ions. Slow-MCI induced electron emission is related to the MCI potential energy /39/ as in the case "potential sputtering", with one important difference: Increase of the Ar^{q+} charge from 8 to 9 produces one L-shell vacancy in the projectile. The MCI induced electron yield does not follow the respective large jump in ion potential energy, since a major share of the additional potential energy is used up for producing one fast (ca. 200 eV) Auger electron in filling the Ar^{9+} L-shell vacancy. In contrast to this, the total yield for "potential sputtering" of LiF rises further on, more or less linearly with the projectile potential energy (cf. fig. 25b), which is due to the ESD contribution from the Ar^{9+} related LMM Auger electron (cf. chapter 4.3.1).
In summary, absolute total sputter yields of alkalihalides result primarily from electron-hole pair formation in the LiF valence band after electron capture by Ar^{q+}. Up to q=9 no evidence for a so-called "Coulomb explosion" mechanism /43/ on the total sputter yield has been found. Very recently, however, similar measurements as above have been made for considerably higher MCI charge states, in cooperation with N. Stolterfoht et al. at HMI Berlin, Germany.

Fig. 26 shows some still preliminary results which indicate a considerably stronger increase of the total sputter yield with further enhanced MCI charge (i.e. potential energy) than extrapolated from Ar^{q+} impact up to q=9.
Whether this is actually an indication for onset of "Coulomb explosion" or still in line with our above presented ideas has to await further studies.

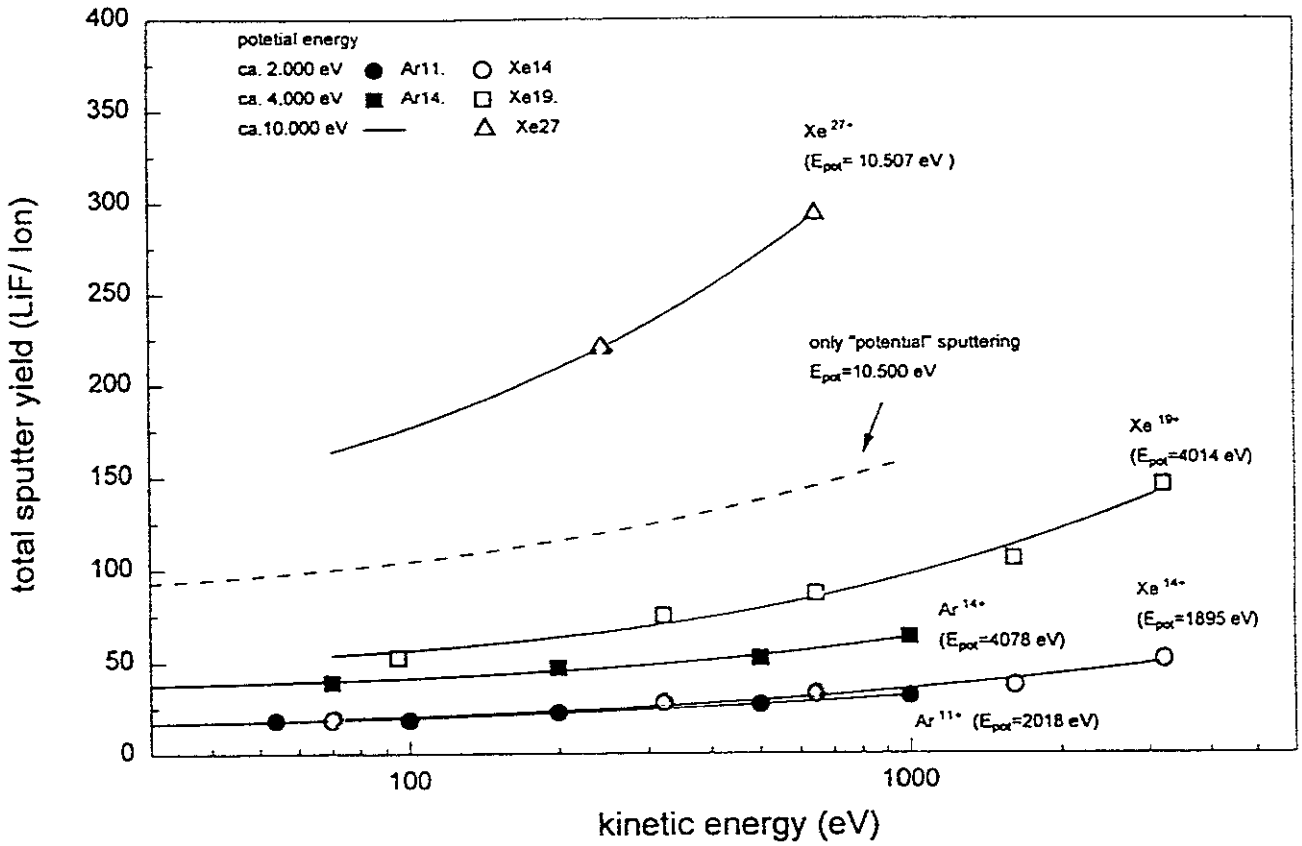

Fig. 26: Total sputtering yields for impact of Ar^{q+} (q = 11, 14) and Xe^{q+} (q = 14, 19, 27) on polycrystalline LiF (cf. text).

Some other target species have also been studied for potential sputtering effects. NaCl showed similar results as LiF, with the absolute sputter yields being slightly lower /22, 53/. On the other hand, bombardment of GaAs, MgO and Si showed no marked influence of the projectile charge on the sputter yields, and for Au the expected independence on q could be demonstrated /22, 53, 54/. For stoichiometric SiO_2 (i.e. the face of the oscillator quartz) a small increase of the sputter yield with q has been found (see fig. 27). However, even slight oxygen deficiency at the SiO_2 surface immediately stopped any influence of the the projectile charge on the measured sputtering yields.

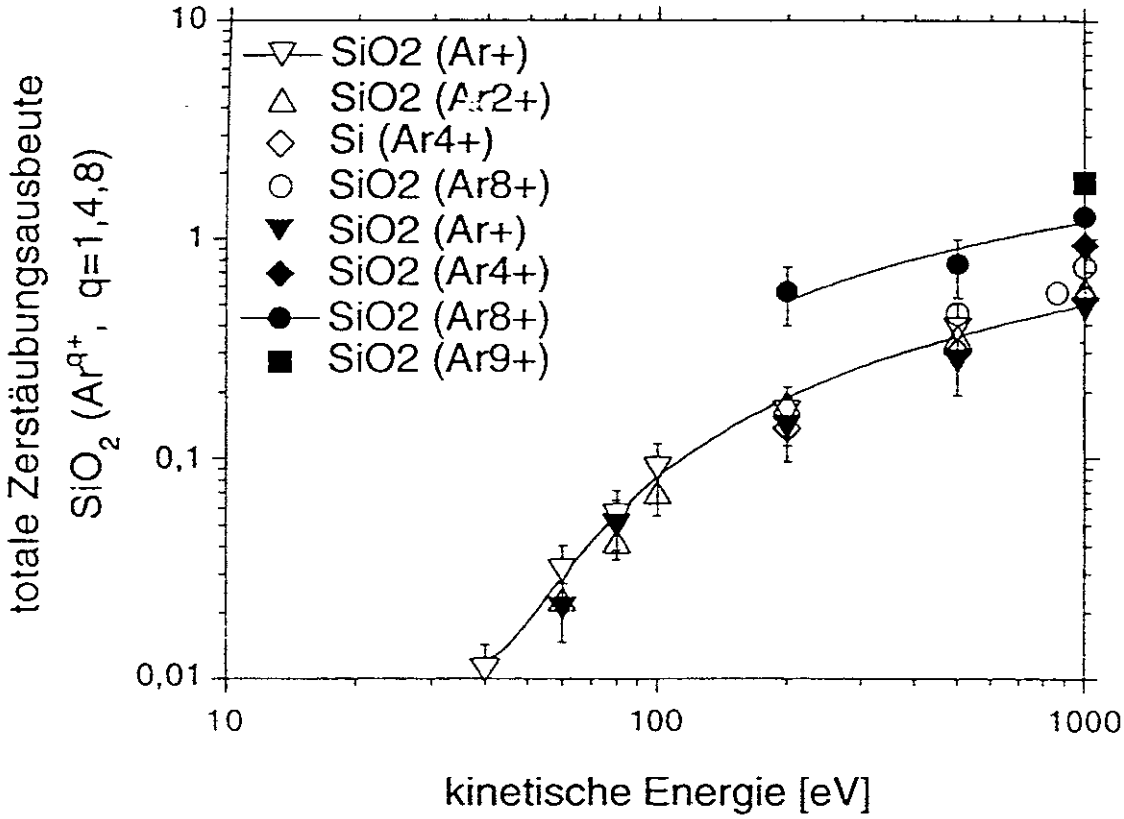

Fig. 27: Dependence of total sputter yields on projectile charge for impact of Ar^{q+} ($q \leq 9$) on a SiO_2 crystal surface /22, 55/.

This behaviour is due to the fact that sputtering of SiO_2 causes preferential oxygen sputtering, which blocks the initially observable potential sputtering effects already after a few monolayers have been removed. Clearly, further experiments along these lines are needed to reveal the mechanisms responsible for potential sputtering of oxide- and other insulator surfaces.

Summary and Outlook

In this review we have presented and discussed recently measured absolute total yields for multicharged ion-induced emission of slow electrons, and for MCI induced sputtering of both neutral and ionized target particles, all for clean insulator surfaces. These results have been compared with similar data obtained for MCI bombardment of clean metal surfaces, and they can be explained in line with the latter results by additionally taking into account the specific role of electronic transitions induced by the impinging MCI near, at and just below the insulator surface. In fig. 28 we summarize the dependence of total slow electron yields on the respectively available potential energy, for a number of multicharged projectiles. If the specific role of projectile inner shell vacancies for the involved emission processes is properly taken into account, it is apparent from fig. 28 that one needs typically 100 eV of potential energy for releasing one electron from a clean metal surface.

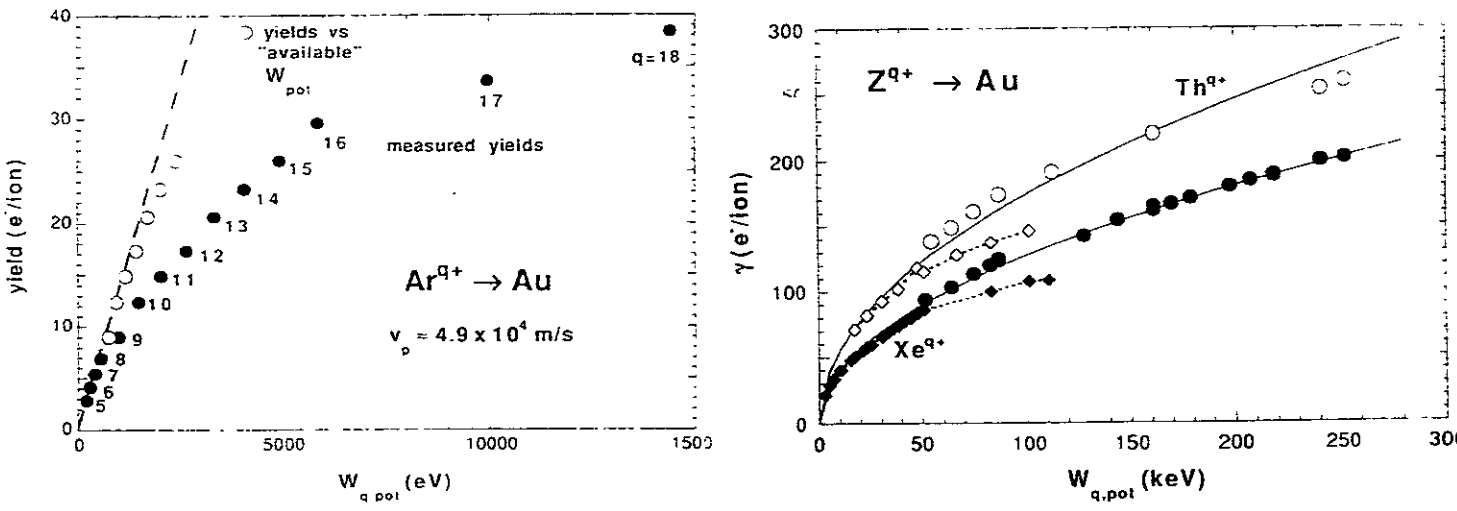

Fig. 28: Dependence of total slow electron yield on projectile potential energy for bombardment of clean polycrystalline gold by various MCI.

For insulator surfaces, however, the situation is considerably more complex. In fact, fig. 18 and results of similar studies for impact of other multicharged ions on LiF show that the projectile potential energy is only really important at relatively low impact velocity.

Kinetic effects start to become important already at much lower impact velocity than for clean metal surfaces, and further above the respective KE threshold the total electron yields become soon completely dominated by KE. We clearly need further measurements, also involving other insulator surfaces, before similar as for clean metal surfaces reliable empirical rules for the dependence of the respective total electron yields on projectile kinetic- and -potential energies can be formulated. However, from the results known so far it is already clear that electron emission from insulator surfaces can be much more important than for metal surfaces in the kinetic projectile energy range which is relevant for fusion edge plasmas. This is especially true if one takes into account the additional acceleration of multicharged ions through the plasma sheath. In a similar way, inspection of figs. 25b and 26 shows that for particular insulator surfaces less than 100 eV of projectile potential energy are necessary to sputter-off single target molecules. Also here further studies are necessary to support these very first absolute measurements, and to extend them toward other target species of possible relevance for fusion reactor technology. At present, many important questions regarding suitable first wall materials for magnetic fusion experiments and the development of future magnetic fusion reactors are yet unresolved. There is considerable interest in insulating material films for first wall coating, conditioning, etc. The influence of such materials for a decrease of the sheath potential, at least in low-B field regions, and the resulting effects on edge plasma conditions definitely deserve further studies in the fields presented in this lecture.

Acknowledgments

Most of the work presented in these lecture notes has been carried out at the author's institute in two research groups under the leadership of Drs. F. Aumayr and P. Varga, the cooperation of whom is gratefully acknowledged. Support for these studies has been provided by Austrian Fonds zur Förderung der wissenschaftlichen Forschung, Austrian Ministry for Science, Traffic and Fine Arts via the Austrian Academy of Sciences, and by Friedrich Schiedel-Stiftung für Energietechnik.
The author also gratefully acknowledges all informations displayed in these notes on relevant work carried out by many colleagues in other research institutions.

References

[1] D. Reiter, in Physical Processes of the Interaction of Fusion Plasmas with Solids, (W.O. Hofer and J. Roth edrs.) Academic Press, New York 1996.

[2] P.C. Stangeby and G.M. McCracken, Nuclear Fusion **30** (1990) 1225.

[3] J. Schou, loc.cit. in ref. /1/.

[4] J. Winter, loc.cit. in ref. /1/.

[5] R. Morgenstern, and J. Das, Europhysics News **25**, 3 (1994).

[6] R. E. Marrs, P. Beiersdorfer, and D. Schneider, Physics Today **10**, 27 (1994).

[7] I. Hughes, Physics World **4**, 43 (1995).

[8] J. Burgdörfer, in *Fundamental Processes and Applications of Atoms and Ions* C. D. Lin, Edr. (World Scientific, 1993).

[9] C. Lemell, H. Winter, F. Aumayr, J. Burgdörfer, and F. W. Meyer, Phys.Rev.A **53**, 880 (1996).

[10] G. Melin, and A. Girard, in *Accelerator based Atomic Physics* J. Austin and S. Shafroth, Edr. (Am.Inst. of Physics, 1996).

[11] G. Sortais, Nucl.Instrum.Methods B **98**, 508 (1995).

[12] E. D. Donets, in *The Physics and Technology of Ion Sources* I. G. Brown, Edr. (John Wiley, New York, 1989) chapt. 12.

[13] E. D. Donets, HCI-92, P. Richard, M. Stöckli, C. L. Cocke, C. D. Lin, Eds., HCI-92 (AIP Conf. Proc., Manhattan, Kansas, 1992), vol. 274, p. 663.

[14] M. Stoeckli, in *Accelerator based Atomic Physics* J. Austin and S. Shafroth, Edr. (Am.Inst. of Physics, 1996).

[15] R. E. Marrs, M. A. Levine, K. D. A, and J. R. Henderson, Phys.Rev.Lett. **60**, 1715 (1988).

[16] D. Schneider, M. W. Clark, B. Penetrante, J. McDonald, D. DeWitt, and J. N. Bardsley, Phys.Rev.A **44**, 3119 (1991).

[17] G. Lakits, F. Aumayr, and HP. Winter, Rev.Sci.Instrum. **60**, 3151 (1989).

[18] F. Aumayr, G. Lakits, and HP. Winter, Appl.Surf.Sci. **47**, 139 (1991).

[19] F. Aumayr, H. Kurz, HP. Winter, D. Schneider, M. A. Briere, J. W. McDonald, C. E. Cunningham, and HP. Winter, Rev.Sci.Instrum. **64**, 3499 (1993).

[20] P. Varga, and U. Diebold, in *Low Energy Ion-Surface Interaction* J. W. Rabalais, Edr. (Wiley, New York, 1994).

[21] T. Neidhart, F. Pichler, F. Aumayr, HP. Winter, M. Schmid, and P. Varga, Nucl.Instrum.Meth.Phys.Res.B **98**, 465 (1995).

[22] T. Neidhart, Thesis, TU Wien (1995)

[23] IEEE Standard on Piezoelectricity, IEEE New York (1978).

[24] E. P. EerNisse, J.Appl.Phys. **43**, 1330 (1972).

[25] H. D. Hagstrum, Phys.Rev. **91**, 543 (1953).
H. D. Hagstrum, Phys.Rev. **96**, 325 (1954).

[26] U. A. Arifov, E. S. Mukhamadiev, E. S. Parilis, and A. S. Pasyuk, Sov.Phys.Tech.Phys. **18**, 240 (1973).

[27] M. Delaunay, M. Fehringer, R. Geller, D. Hitz, P. Varga, and HP. Winter, Phys.Rev.B **35**, 4232 (1987).

[28] S. T. de Zwart, Thesis, University of Utrecht, (1987).

[29] H. Kurz, F. Aumayr, D. Schneider, M. A. Briere, J. W. McDonald, and HP. Winter, Phys.Rev.A **49**, 4693 (1994).

[30] M. Vana, Thesis, TU Wien (1996).

[31] M. Vana, F. Aumayr, C. Lemell, and HP. Winter, Int. J. Mass Spectr. Ion Proc. **149/150**, 45 (1995).

[32] A. Arnau, R. Köhrbrück, M. Grether, A. Spieler, and N. Stolterfoht, Phys.Rev.A **51**, R3399 (1995).

[33] I. G. Hughes, J. Burgdörfer, L. Folkerts, C. C. Havener, S. H. Overbury, M. T. Robinson, D. M. Zehner, P. A. Zeijlmans van Emmichhoven, and F. W. Meyer, Phys.Rev.Lett. **71**, 291 (1993).

[34] F. W. Meyer, S. H. Overbury, C. C. Havener, P. A. Zeijlmans van Emmichhoven, J. Burgdörfer, and D. M. Zehner, Phys.Rev.A **44**, 7214 (1991).

[35] J. Das, L. Folkerts, and R. Morgenstern, Phys.Rev.A **45**, 4669 (1992).

[36] J. Das, and R. Morgenstern, Comments At.Mol.Phys. **29**, 205 (1993).

[37] J. Limburg, J. Das, S. Schippers, R. Hoekstra and R. Morgenstern, Surface Science **313**, 355 (1994)

[38] E.O. Pahlik and W.R. Hunter, Edrs., *Handbook of Optical Constants of Solids*, Academic, New York 1985).

[39] M. Vana, F. Aumayr, P. Varga, and HP. Winter, Europhys. Lett. **29**, 55 (1995).
M. Vana, F. Aumayr, P. Varga, and HP. Winter, Nucl. Instrum. Meth. Phys. Res. B **100**, 284 (1995).

[40] J. Limburg, S. Schippers, R. Hoekstra, R. Morgenstern, H. Kurz, M. Vana, F. Aumayr, and HP. Winter, Phys.Rev.Lett. **75**, 217 (1995)

[41] W. Eckstein and V. Phillipps, loc.cit. in ref. /1/.

[42] S. S. Radzhabov, R. R. Rakhimov, and P. Abdusalumav, Isv.Akad.Nauk SSSR Ser.Fiz. **40**, 2543 (1976).

[43] I. S. Bitensky, M. N. Murakhmetov, and E. S. Parilis, Sov.Phys.Tech.Phys. **24**, 618 (1979).
I. S. Bitensky, and E. S. Parilis, J. de Physique (Paris) **C2**, 227 (1989).

[44] T. Neidhart, F. Pichler, F. Aumayr, HP. Winter, M. Schmid, and P. Varga, Phys.Rev.Lett. **74**, 5280 (1995).

[45] N. H. Tolk, M. M. Traum, J. C. Tully, and T. E. Madey, Edr., *Desorption induced by electronic transitions DIET I*, vol. 24 (Springer, Berlin, 1983).

[46] A. J. Eccles, J. A. van den Berg, A. Brown, and C. Vickerman, Appl.Phys.Lett. **49**, 188 (1986).

[47] S. T. de Zwart, T. Fried, D. O. Bourma, R. Hoekstra, A. G. Drentje, and A. L. Boers, Surf.Sci. **177**, L939 (1986).

[48] T. Neidhart, M. Schmid, and P. Varga, Springer Ser. Surf.Sci **31**, 129 (1993).
T. Neidhart, M. Schmid, and P. Varga, in *Ionization of Solids by Heavy Particles* R. Baragiola, Edr. (Plenum Press, New York, 1993) 129.

[49] Z. Sroubek, and H. Oechsner, Surf.Sci. **311**, 263 (1994).

[50] T. Green, M. E. Riley, and M. E. Coltrin, Phys.Rev.B **39**, 5397 (1989).

[51] Z. Postawa, J.Chem.Phys. **96**, 3298 (1992).

[52] R. Williams, Phys.Rev.B **33**, 7232 (1986).
R. Williams, and K. Song, J.Phys.Chem. **51**, 679 (1990).

[53] M. Sporn, Diploma Thesis, TU Wien (1995).

[54] T. Neidhart, F. Pichler, F. Aumayr, HP. Winter, M. Schmid, and P. Varga, 3S´95, P. Varga, F. Aumayr, Edrs., 3S´95 Symposium on Surface Science Kitzsteinhorn, Salzburg, Austria, 1995), p. 74.

[55] G. Libiseller, Diploma Thesis, TU Wien (1996)

Molecule-Surface Interaction Processes of Relevance to Gas Blanket Type Fusion Device Divertor Design

K. J. Snowdon*

Department of Physics, University of Newcastle, Newcastle upon Tyne, NE1 7RU, U.K.

and

H. Tawara*

National Institute for Fusion Science, Nagoya 464-01, Japan

Abstract

The mechanisms which may lead to the departure of molecular species from surfaces exposed to low energy (0.1 - 100 eV) particle or photon and electron irradiation are reviewed. Where possible, the charge and electronic state, angular, translational and internal energy distributions of the departing molecules are described and the physical origin of the nature of those distributions identified. The consequences, for the departing molecules, of certain material choices become apparent from such an analysis. Such information may help guide the choice of appropriate materials for plasma facing components of gas-blanket type divertors such as that recently proposed for the International Thermonuclear Experimental Reactor (ITER).

Key Words: surfaces, molecules, dissociation, molecular desorption, molecular scattering, recombinative molecular desorption

*email: k.j.snowdon@ncl.ac.uk

tawara@dptawara.nifs.ac.jp

1. Introduction

Next-generation fusion devices such as the International Thermonuclear Experimental Reactor (ITER) will make use of so-called divertors to divert and exhaust plasma edge impurities which would otherwise have a detrimental effect on device operation. It has been estimated that power densities in the divertor of the ITER reactor will be of the order of 35 MWm^{-2} [1]. Although remarkable progress has been made in the development of divertor plate materials and cooling concepts [2], it would seem necessary to reduce peak heat loads to less than 10 MWm^{-2}. The current strategy is to operate the divertor under conditions of high density and rely on gas phase atomic and molecular processes to spread the heat load over the entire divertor structure [1]. Plasma temperatures at the divertor plate surfaces of around 1 eV and neutral particle densities up to 10^{15} cm^{-3} are then envisaged [1]. Under these conditions, the role of vibrationally excited H_2 and H_2^- in defining the divertor plasma properties is likely to be crucial [3].

Existing divertor modelling codes, while already exceedingly complex, do not yet take proper account of many atomic, molecular and particle-surface processes. This is particularly true of processes at the low temperatures and high neutral particle densities proposed for the new divertor designs [4,5]. We quote as examples processes involving highly vibrationally excited molecules and molecular ions, exothermic ion-molecule reactions and molecule formation and dissociation processes on surfaces [5]. Little quantitative data is available for several of these processes, particularly the particle-surface processes, for divertor relevant materials at the low collision energies of interest for ITER. In an attempt to partially redress this deficit, we briefly review and attempt to assess the likely relative importance of those *particle-surface processes* spanning the translational energy regime 0.1 - 100 eV which may lead to the release of molecular species from surfaces, and therefore be of relevance to the currently proposed divertor concept. In so doing, we will in general avoid the use of terms such as physical and chemical sputtering, radiation enhanced sublimation and evaporation and disruption erosion. These processes and their implementation in modelling codes have been reviewed, e.g. in [6] and the deficits noted.

In this paper we will use the language of surface science and base our discussion on clearly definable microscopic physical processes. We will draw the bulk of our information from surface science investigations performed under well controlled conditions. Such detailed (often ultra high vacuum) experiments are particularly suited to identifying, isolating and understanding individual processes, the discussion of which forms the bulk of this paper. Clearly though, the question arises as to the *relevance* of knowledge gained from such 'ideal' experiments to the conditions which might exist at the surface of a divertor plate of a fusion device. It would seem reasonable to suppose that *mechanisms* will be 'portable' and relevant to 'real' surfaces. More problematic is the identification of the mechanisms which are likely to dominate under operational conditions. In this respect it is important to note that it is possible to predict reaction rates in the harsh environment of an industrial catalytic reactor (high temperature and pressure) using data from measurements of the behaviour of the reactants on well-defined single crystal surfaces under UHV conditions [7]. This is possible because on an atomic scale, real surfaces can be thought of as 'assembled' from a small number of the most thermodynamically favourable well-ordered surface configurations separated by steps and defects whose catalytic activity can be characterised in single-crystal experiments. And even where a large number of distinct, potentially 'active' sites exist on a surface, diffusion processes can lead to only a restricted subset of these being responsible for the actual release of species into the gas phase. If the same can be said of divertor surfaces, then the potential is there, not only to apply our general understanding of mechanisms for predictive purposes, but also to use data obtained under an appropriate mix of 'ideal' conditions to simulate the behaviour of 'real' divertor surfaces.

2. Mechanisms Leading to Molecule Release from Surfaces

Most of the detailed information available on the interaction of neutral and ionised species with surfaces in the low energy regime comes from studies at the extremes of the energy regime of interest in this review (0.1 - 100 eV). At low translational energies (below ~1 eV), quantum state specific supersonic neutral beam experiments have provided a very detailed picture of the dynamics of the interaction of H, D, H_2, D_2 and some heavier molecules such as NO with well

characterised surfaces. Above ~100 eV, experiments with both ionised and neutral molecular beams have provided detailed insights into charge transfer processes and molecular dissociation, again at well characterised crystal surfaces under UHV conditions. Very little information is available which bridges the energy gap between the practical upper limit of supersonic beam experiments and the practical lower limit of most ion beam based experiments. However, the situation is rapidly changing, motivated in part by the needs of the fusion community and the technological interest in techniques for low damage, low temperature epitaxial thin film growth, the optimisation of high temperature catalytic processes and in the dry processing of microelectronic devices.

A plethora of processes can lead to the release of molecular species from surfaces. These are illustrated schematically in fig. 1 and described individually in the following sub-sections. Particles can be thermally desorbed. Particles may simply be scattered, or they may leave as a consequence of the exothermicity of a chemical reaction, in response to momentum transfer by energetic particle irradiation, and via a variety of direct and substrate mediated electronic processes induced by incident electrons and photons. Molecular species may, in principle, be rotationally, vibrationally and translationally 'hot' (or cold!), reflecting the detailed dynamics of the ejection, reflection or desorption process.

Particles may also depart from the surface in an electronically excited or ionised state. The initial *creation* of such a state may (as in the case of certain electron and photon induced desorption mechanisms) be intimately related to the ejection process itself. However, the *probability of survival* of such a state, at least for particle ejection from *metal* surfaces, can be qualitatively understood by reference to fig. 2. If, in the near surface region, the ionisation level of the particle lies energetically above the Fermi level of the metal, the probability that the particle leaves the surface as an ion may be quite high. Similarly, if the affinity level of the particle lies close to or below the Fermi level over the range of particle-surface separations where the electron tunnelling probability is high, the probability of negative ion emission could also be high. However, for hydrogenic species near metal surfaces with work functions of ≈5 eV (i.e., for all but alkali or alkali-covered metals), simple image potential considerations lead us to expect the ionisation level

to lie well below, and the affinity level well above, the Fermi level. In this case the probability P_s of survival of a non-equilibrium product is given roughly by a formula of the type derived (originally in terms of velocities) by Hagstrum [8], viz.

$$P_s \propto \exp(-\tau_n/\tau_e)$$

where τ_e represents the electron transfer time of ~1 fs at metal surfaces and τ_n the timescale for the departure of the particle from the surface. Even for the fastest particles of interest in this review (100 eV low mass particles), the exponential dependence of P_s on the ratio τ_n/τ_e leads to the establishment of near-equilibrium [9] level populations on the departing particle and consequently, to very low ionised or electronically excited particle fractions. However, for contaminated and graphite surfaces (where τ_e may be much larger) and alkali metal surfaces (where the affinity level of the ad-particle lies energetically close to, or below, the Fermi level, and therefore the assumptions underlying the derivation of the above equation are no longer valid), high negative ion fractions have been reported (e.g. up to 10 % H^- from a graphite surface [10]).

To provide an overview, we have attempted in the following sub-sections to illustrate each of the processes shown in fig. 1 with suitable examples from the literature. We have restricted ourselves to a discussion of the angular, translational energy and internal energy distributions. The particle charge and electronic state distributions are not individually addressed. They are in all cases influenced by the above-mentioned adiabaticity considerations. It has not been our intention to provide a complete review of all published work. Instead, our central aim has been to introduce and explain the general concepts and to illustrate as clearly as possible the physical processes which are believed to be operative. It is our hope that through an understanding of those molecular release mechanisms, it may be possible to suppress the contribution of 'troublesome' processes in a fusion device via an appropriate choice of, for example, the plasma facing material or surface operating temperature.

2.1 Thermal Desorption of Molecularly Adsorbed Species

Despite being in thermodynamic equilibrium with a surface, a molecularly adsorbed species may nevertheless thermally desorb (fig. 1a). The surface binding energy of individual molecules may be overcome by the transfer of sufficient energy from the phonons of the substrate to the molecule-surface vibrational co-ordinate. It might be expected that the dynamical parameters of such desorbing molecules would reflect the temperature of the surface, i.e. that the angular distribution would be cosine, the velocity distribution Maxwellian and the rotational and vibrational population distributions would follow the Boltzmann law. That this is in general unlikely to be the case was argued quite early by Comsa [11]. A glance at a two dimensional representation (fig. 3) of a possible potential energy surface (PES) for a diatomic molecule interacting with a surface makes the reason for such doubts immediately clear. The existence of a region of *elevated potential energy*, such as an *adsorption barrier* in the final section of the *desorption path* (region a of fig. 3), can clearly lead to the transformation of a thermally activated desorption process into an apparently exothermic process. The translational energies of desorbing molecules reflect the detailed dynamics of 'rolling off' this barrier. Any curvature in the exit path for the desorption process, as present in fig. 3, could clearly lead to vibrational excitation of the desorbing species which would then, for the same reason, bear little or no relation to the temperature of the surface. The same general comments apply to molecules which are formed via the recombination of surface adsorbed species (region c on the PES of fig. 3) and equilibrate totally or partially in the molecular adsorption region of the PES (region b on the PES of fig. 3) before desorption occurs.

2.2 Prompt Molecular Desorption following Surface Recombination (L-H) Reactions

If the region b on the PES of fig. 3 is absent (i.e. a stable molecularly chemisorbed species does not exist), recombination reactions of surface equilibrated, adsorbed species (so-called Langmuir-Hinshelwood reactions, fig. 1b) may lead to the prompt desorption of molecules from the surface. Again the comments of the previous sub-section apply. A now classic example of non-cosine angular distributions and non-equilibrated velocity distributions following such a thermally

induced surface recombination reaction was investigated by Comsa and David [12] for the recombinative desorption of H_2 and D_2 from Cu(100) and Cu(111) surfaces (fig. 4a,b).

The dynamics of the desorption process has in this case been investigated in considerable detail by Küchenhoff et al. [13] using the model potential energy surface of fig. 5. This study was prompted by the above results and by the non-Boltzmann vibrational population distributions (table 1) observed for the recombinative desorption of H_2 and D_2 from Cu(110) and Cu(111) by Kubiak et al. [14]. In the latter experiments the vibrational population of the $v = 1$ state was found to exceed that expected from a Boltzmann distribution at the surface temperature by up to two orders of magnitude. That the barrier for *ad*sorption, at least for the Cu(111) surface, is indeed late* and the exit path for the *de*sorption process indeed curved has recently been verified by *ab initio* calculations of the potential energy surface within the local density functional generalised gradient approximation by Hammer et al. [15].

Enhanced vibrational populations have also been observed for the desorption of D_2 from Pd(100) by Zacharias [16]. Both the latter experiment and that of Kubiak et al. [14] for H_2 and D_2 desorption from Cu(110) and Cu(111) found non-Boltzmann rotational state distributions characterised by mean energies considerably less than $kT_{surface}$.

2.3 Prompt Molecular Desorption following Gas-Surface Recombination (E-R) Reactions

The direct reaction of a particle from the gas phase with a surface-adsorbed species can lead to the abstraction of the adsorbed species from the surface (so-called Eley-Rideal reactions, fig. 1c). The observation by Hall et al. [17] and Eenshuistra et al. [18] of highly vibrationally excited

---

* A 'late barrier' is one which is located at a small molecule-surface separation but a large atom-atom separation in the molecule. The intra-molecular bond is therefore broken 'late' in the interaction of the molecule with the surface.

hydrogen molecules emanating from a metal box containing hydrogen in the presence of a heated filament (up to v=9 in [17]) lead to the inference that this process was occurring. The first well controlled experiments involving the formation of hydrogen molecules via this process were reported by Rettner [19]. Using atomic deuterium beams with translational energies of 0.07 eV and 0.36 eV incident on an atomic hydrogen covered Cu(111) surface, Rettner obtained the angular distributions of released HD shown in fig. 6 [20]. The beams were incident at 60° to the surface normal. The dependence of the shape of the angular distribution on incident beam translational energy is clear evidence for a direct process in which the incident particle has not yet equilibrated completely, if at all, with the surface. The mean translational energy of the HD product was 1.1 ± 0.2 eV, independent of the emission angle within 20° of the surface normal [20]. The dependence of the mean rotational energy on vibrational state is reproduced in fig. 7 and the vibrational state distribution is shown in fig. 8 [20]. These results reveal that hardly any energy has been transferred to the crystal lattice in the interaction. The degree of rotational excitation was found to decrease with increasing vibrational excitation, reflecting the partition of a fixed total energy (incident translational energy E_T^i plus reaction exothermicity of ΔE_{ex} ~2.3 eV [21]) among the product degrees of freedom viz.

$$E_T^i + \Delta E_{ex} = E_T^f - E_V^f + E_R^f.$$

The reaction exothermicity is given by the difference between the energy gained by formation of the H_2 (or HD or D_2) bond, $E_{H\text{-}H}$, and the energetic cost of breaking the H- (or D-) surface bond, $E_{H\text{-}S}$, viz.

$$\Delta E_{ex} = E_{H\text{-}H} - E_{H\text{-}S}.$$

The energy in the product vibrational degree of freedom is therefore restricted to the range

$$E_V^f < E_T^i + E_{H\text{-}H} - E_{H\text{-}S}$$

by energy conservation considerations. The only conceivable explanation for the observation of $H_2(v=9)$ *in the experiment of Hall et al.* [17] is, therefore, that the adsorbed atomic hydrogen was in a weakly bound sub-surface site, was only very weakly bound to the surface [22], or the adsorbate-surface bond was highly vibrationally excited. For energetic hydrogen impact (E_T^i large), the nature of the binding site or degree of adsorbate vibrational excitation will be of little importance in determining the energetics of the product vibrational excitation, as the above inequality implies.

The cross section for the abstraction reaction was found by Rettner and Auerbach [20] to be ~3.8 $\pm 0.5 \times 10^{-16}$ cm^2/adsorbed atom for incident D-atom energies of 0.07 - 0.36 eV. This is roughly four times the geometrical cross-section of HD, suggesting that the incident atom may (contrary to the simplified picture depicted in fig. 1c) first hit the surface before reacting with the adsorbate.

The results obtained by Rettner et al (fig. 8 [20]) appear at first sight to be incompatible with the *Boltzmann-like* vibrational population distribution of H_2 effusing from the heated filament sources of Hall et al. [17] and Eenshuistra et al. [18] *at low vibrational quantum numbers v.* However, it must be remembered that in the latter experiments the effusing flux will contain a mixture, not only of species which were created on the inner walls of the container and which escape from the box following few, if any, quenching collisions, but also species which have been partially- and totally-equilibrated in gas-phase collisions and collisions with the walls of the container. In the experiment of Rettner et al., the desorbed particles reach the detector directly. Furthermore, *all the desorbed particles* in those experiments, independent of the vibrational quantum state, *appear to arise from E-R reactions.* The lack of a significant contribution to the desorption flux of hydrogen arising from L-H reactions is not difficult to rationalise, despite the high surface concentration of adsorbed hydrogen. If the surface temperature were high enough for L-H reactions to occur on this surface (≈300 K [20]), such reactions would quickly deplete the concentration of adsorbed hydrogen, making the probability for a direct interaction between a gas

phase hydrogen atom and an adsorbed hydrogen atom very small. Raising the surface temperature to increase the surface diffusion rate therefore represents an effective means to suppress the production of highly vibrationally excited hydrogen in surface abstraction reactions.

Valuable theoretical insights into the E-R reaction mechanism have been provided by Jackson and Persson [21] and Kratzer and Brenig [22]. A two-dimensional cut of the model PES used by the latter authors for the reaction of gas phase H with H adsorbed on a tungsten surface is reproduced in fig. 9. The gas phase hydrogen atom approaches from the upper right hand corner of the PES and the H_2 molecule leaves through the narrow. vertical exit channel on the left. The atom from the gas phase is *accelerated* before hitting the adsorbed atom. The observed high vibrational excitation was found by Kratzer and Brenig [22] to be a consequence of this acceleration and the high curvature of the PES compared to the PES for the L-H reaction (fig. 5). The influence of the kinetic energy of the impinging H-atom on the probability of populating a given vibrational state is reproduced in fig. 10 [22]. We observe there an increasing population of the higher vibrational states with increasing kinetic energy over the range 0.05 eV to 0.3 eV. The authors also report [22] a decrease in the number of reactive collisions with increasing incident atom kinetic energy or increasing attraction of the impinging atom to the surface and attribute this observation to the increasing difficulty at shorter interaction times for the system to find its way into the narrow exit channel in fig. 9. It remains to be clarified whether these trends would persist for non-normal incidence, and yet higher impact energies of relevance to future divertor designs (up to ~100 eV).

Several experiments at higher incident particle energies have been performed. An attempt by Jiang et al. [23] to observe product ions from E-R type reactions between incident 10 eV N^- ions and CO adsorbed on Ni(100) and Cu(100) was unsuccessful. However, one of the first clear demonstrations of the E-R mechanism was provided by the observation by Kuipers et al. [24] of the protonation of 1 - 9 eV $N(C_2H_4)_3N$ incident on a hydrogen-covered Pt(111) surface. The product ion yield was found to increase with the kinetic energy of the incident molecule, a result believed to reflect the translational energy dependence of the initial ionisation step of the incident molecule rather than the efficiency of the abstraction reaction itself [24]. More recently, Yang et al. [25] have observed recombination reactions between incident 30 - 250 eV Cs^- ions and surface

species (Si and O) for scattering from a Si(111) surface in the presence of adsorbed H_2O. They invoke a substantial influence of momentum transfer between the incident molecule and the surface atom in forming the product molecule.

It is presently unclear whether the formation of hydrocarbon molecules following the exposure of graphite and carbon containing materials to hydrogen [26] proceeds via the L-H or E-R mechanisms, an intermediate case [27], or a combination of these.

2.4 Desorption and Sputtering Induced by Incident Atomic and Molecular Species

Incident atomic and molecular species can simply displace adsorbed species, with part of the adsorption energy of the incident particle being carried away by the displaced desorbing species [28]. Energetic atomic and molecular impact can lead, via direct momentum transfer, to the initiation of chemical reactions on surfaces [29] with the possible liberation of a molecular product. For example, the impingement of Xe atoms at energies in excess of 4 eV on a coadsorbed monolayer of CO and O_2 on Pt(111) leads to the release of CO_2 from the surface [30]. The data is consistent with a 'hot atom' mechanism whereby the impacting Xe atoms dissociate the molecularly adsorbed O_2, producing energetic O-atoms. These are then believed to possess sufficient kinetic energy to surmount the activation barrier for the reaction with adsorbed CO, leading to the formation of CO_2, which desorbs [30]. Alternatively, the impacting heavy particle may set the adsorbed molecules in motion, allowing direct reaction of CO and O_2 [30].

Pre-existing molecules may also be simply desorbed from surfaces [31] following either the direct impact of incident energetic particles or momentum transfer from secondary particles which have been set in motion by the initial energetic particle impact. Diebold et al. [32] have measured cross sections in the range of 10^{-15} cm^2 for desorption of neutral CO from a Ni(111) surface exposed to rare-gas ion (He^+, Ne^+, Ar^+ and Kr^+) bombardment at impact energies from 10-500 eV.

At yet higher incident particle energies (which are not the subject of this review), an extensive literature exists (see e.g. [33] and refs. therein). However, the validity of the binary collision approximation, which forms the basis of commonly used computer programmes to simulate *physical sputtering* at higher energies (such as TRIM [34] and MARLOWE [35]), becomes questionable at low energies. The need for molecular dynamics simulations in the low energy regime has been noted already by Reiter [6]. However, such simulations require reliable potentials, not just for perfect surfaces, but also for step and kink atoms and defect inundated surface morphologies. A limited number of molecular dynamics simulations do exist for the near threshold physical sputtering regime. Amirav and Cardillo [36] have shown that P_2 and P_4 molecules are efficiently sputtered from the surface of InP(100) by 16 eV Xe atoms. Molecular dynamics simulations have also shown that 6 - 30 eV argon atoms can induce efficient sputtering of materials such as nickel [37].

Low energy neutral and ionised particle impact can lead to electronic excitation [38,39], which introduces the possibility of a variety of ejection mechanisms which are discussed in more detail in the next section (2.5). These 'electronic' mechanisms may in principle act alone, or in addition to the role of direct momentum transfer by collisions. Their importance on metallic substrates is strongly suppressed, as explained in the beginning of section 2. of this paper, because electronic excitations are efficiently quenched on the timescale required for the departure of low energy atomic and molecular species from surfaces.

2.5 Desorption Induced by Electron and Photon Irradiation

In principle, both substrate atoms and adsorbates may be desorbed from surfaces by electron and photon irradiation (fig. 1d). The desorption may occur via a direct process, in which the initially bound configuration of the particle-surface system is directly excited by the incident electron or photon, or via a substrate-mediated process, where the first step involves the creation of a localised or non-localised electronic excitation of the substrate. These processes are illustrated schematically in fig. 11.

In the so-called Menzel-Gomer-Redhead (MGR) mechanism [40], a direct transition from a bonding to an antibonding electronic configuration is induced (fig. 11a). Provided the upper state lifetime is comparable to or longer than the time required for the particle to escape from the immediate vicinity of the surface, desorption occurs. As we have just indicated, this mechanism is generally inefficient on metal surfaces, as the upper state lifetime is typically of the order of femtoseconds while the nuclear motion occurs on the timescale of molecular vibrations, namely 10-100 fs.

In the Antoniewicz mechanism [41], a direct transition from the ground state to a bound upper state is induced by the incident radiation. If the topography of the upper state is such that the particle is accelerated *toward* the surface, the system may find itself in an unbound vibrational state upon relaxation (fig. 11b). The probability of desorption from metals may be significantly higher than that for the MGR mechanism as the Antoniewicz mechanism can take advantage of the strongly repulsive inner wall of the lower state to 'compensate' for a short propagation time on the upper state.

In the mechanism suggested by Knotek and Feibelman [44], a core hole is generated on a near surface atom by the incident electron or photon (fig. 11c). Relaxation of this initial excitation via Auger decay could leave a surface species in a singly or doubly ionised state (for intra- and interatomic Auger decay respectively) which may be antibonding with respect to the surrounding atoms. As before, if this excitation is not quenched on the time-scale for nuclear motion, the species may be ejected from the surface.

The adsorption of an incident electron or photon can also result in the production of electron-hole pairs in the conduction band of the solid. The resulting energetic electrons (sometimes referred to as 'hot' electrons [43]) may scatter through higher lying negative-ion-like resonance's of the adsorbate-substrate system (fig. 11d). This *indirect* process [43] looks formally just like the Antoniewicz mechanism (fig. 11b), as the addition of an image potential-like contribution

$$V_{im} = -1/4z,$$

(to describe the presence on the adsorbed particle of an additional electron) to the initial state potential curve, leads to an upper to lower state relative topography just like that assumed by the Antoniewicz mechanism. The efficiency of the desorption mechanism again depends critically on the residence time of the electron in the upper state. Under very high fluence conditions, achievable in the laboratory for example via the use of intense femtosecond laser pulses, a sufficiently high density of 'hot' electrons may be produced to enable several such electron scattering events to occur [44]. Transitions to the upper state provide the 'kicks' necessary for the adsorbate to climb the vibrational ladder and permit desorption to occur.

Strong evidence exists that multiple electronic transitions indeed lead to desorption from metals exposed to high pulsed laser fluences [44]. However, even 'off-normal' events in the divertor of a fusion device, which are estimated [45] to deliver 2-10 MJ/m^2 in 0.1-3 ms to plasma facing surfaces, fall a factor of at least 10^6 short of the energy densities delivered in the above-mentioned pulsed laser experiments. This rules out any need to consider multiple electronic transition type desorption mechanisms in contributing to the desorption flux in a fusion device.

2.6 Scattering

The scattering of low energy neutral and ionised molecular species from surfaces (fig. 1e) may be accompanied by charge transfer, fragmentation, rotational and vibrational excitation and deexcitation, and abstraction and desorption of surface species. At the very lowest energies of interest here (~0.1 eV), only molecular rotations and substrate phonons may be excited, provided the incident molecule is neutral and in its vibrational ground state. As the kinetic energy is increased, the details of any attractive part of the interaction are expected to become less important and the collision will become more impulsive in nature. At the same time, vibrational excitation, electron-hole pair excitation and finally ionisation and dissociative scattering become energetically permissible. These, and a host of other phenomena which lie outside the scope of

this article, have been reviewed recently by Amirav [46], Ceyer [47], Gerber [48], Rettner and Auerbach [49] and others [50-53].

Angular distributions of scattered molecules depend sensitively on the incident beam translational energy, incidence angle and charge state. For neutral N_2 scattering from a W(110) surface at 800 K, the width (FWHM) of the angular distribution decreases from $32 \pm 2°$ at an incident beam energy of 0.09 eV to $19 \pm 1°$ at 1 eV [49] (fig. 13). The scattering potential is, however, essentially 'flat' and the incident molecule experiences quasi-specular reflection, often shifted toward grazing exit angles reflecting a preferential loss of energy from the surface normal component of the particle motion [46]. As the incident particle kinetic energy or surface normal energy is increased yet further, the scattering potential becomes more corrugated, resulting again in broader angular distributions [54,55]. This effect is seen in fig. 14 for the scattering of O_2 from Ag(111) [54]. The dependence on incident beam energy of the angular distributions of CO^+ scattered from Pt(100) is shown in fig. 15 [56]. The authors suggest that the acceleration of the beam toward the surface in the attractive part of the molecule surface interaction potential leads to a strong enhancement in the loss of surface normal energy via the excitation of phonons.

During scattering, a fraction of the incident beam kinetic energy may be transferred to the rotational and vibrational degrees of freedom of the molecule and the vibrational degrees of freedom of the substrate. Rotational state distributions for NO following scattering from Ag(111) at a surface temperature of 750 K are shown as a function of the energy of the incident beam in fig. 16 [49]. The effect of the incidence energy on the vibrational populations is shown in fig. 17 [49]. Van den Hoek et al. [57] have performed molecular dynamics simulations of the partition of energy between these degrees of freedom for O_2 scattering from a Ag(111) surface over a range of incidence energies between 1 eV and 3 keV (fig. 18). However, generalisations to other systems are difficult, as the results obtained will depend on the precise details of the interaction potential and the geometric arrangement of the surface atoms.

An extensive theoretical analysis by Gross et al. [58] has shown that vibrational excitation can arise purely from scattering on the electronically adiabatic ground state PES in the so-called

entrance channel of the PES (region a of fig. 3), particularly if the entrance channel exhibits curvature (as in fig. 3) and the vibrational frequency of the molecule changes upon the molecule approaching the surface. If the system were to access for a short time an electronic configuration different from that in the entrance channel (such as the molecular chemisorption region 'b' of the PES in fig. 3) or electronically non-adiabatic processes occur, vibrational excitation may also result [59,60]. The mechanism of vibrational excitation in the former case, where a transient change in the electronic configuration occurs, is similar to that which leads to vibrational excitation in the Antoniewicz mechanism of desorption discussed earlier (section 2.5 and fig. 11b). Without the support of multi-dimensional calculations on reliable potential energy surfaces, it does not at present seem possible to distinguish the various possible origins of vibrational excitation observed in experiments.

At incident neutral molecule translational energies exceeding the molecule dissociation energy, the dissociative scattering channel will compete with the sticking, chemisorption and non-dissociative scattering channels. Experiments on molecular dissociation induced by 'impulsive' collisions with chemically inert solid surfaces have been performed, e.g. by Gerber and Amirav [61]. Classical trajectory studies on *planar*, rigid surfaces by the same authors showed that energy transfer to the rotational degree of freedom is very efficient [61]. The angular momentum J acquired by the molecule upon impact leads to a reduction in the depth of the unperturbed intramolecular potential $V_0(r)$, viz.

$$V_J(r) = V_0(r) + J^2/2\mu r^2$$

where μ is the reduced mass of the molecule and r the internuclear separation. Dissociation may occur at low J with the assistance of vibrational excitation, which although less efficient [61], may suffice to overcome the centrifugal barrier. At sufficiently high J, the molecular potential $V_J(r)$ becomes purely repulsive and dissociation proceeds unhindered. This result was also shown to hold for *corrugated* surfaces by van den Hoek and Kleyn [57] in the afore-mentioned classical simulation of O_2 scattering from Ag(111). In a further classical trajectory study by the same group, this time for 70 eV O_2 scattering from Pt(111), Kirchner et al. [62] showed that early in

the interaction, approximately twice as much energy was transferred from the translational to the rotational as to the vibrational degree of freedom, independent of the final outcome of the scattering event. Later in the trajectory, those molecules which finally dissociate were found to possess much more vibrational than rotational energy, while those which do not dissociate have roughly the same amount of energy in vibration and rotation.

As the collision energy is increased, the surface appears more corrugated. For 70-200 eV H_2 scattering from Ag(111) at not too large angles of incidence to the surface normal, the dissociation probability was found by van Slooten et al. [63] to exhibit $E_i\theta_s^2$ scaling, where E_i denotes the incident beam energy and θ_s the total scattering angle of the dissociatively scattered H-atoms. This could be understood by assuming that most collisions were governed by the interaction of an incident dumbbell or ellipsoid shaped molecule with a *single* surface atom [64].

If the incidence angle is increased sufficiently toward grazing, shadowing effects eventually become important at all energies. The lateral corrugation of the interaction potential may still be large, but the trajectory of the molecule comes to be dominated by the surface normal directed forces experienced by the molecule in passing over the 'peaks' of the corrugated molecule-surface interaction potential. The classical trajectory calculations of Van den Hoek et al. [57] show that for grazing incidence of 1 eV - 3 keV O_2 on Ag(111) and constant surface normal energy of 11.7 eV, both the total energy loss and the dissociated fraction goes through a maximum at several 10's of eV incident beam energy before becoming independent of energy beyond several 100 eV. These conclusions will of course loose their validity if the surface is atomically rough on length scales smaller than the trajectory length of the molecule in the surface interaction region.

If the incident molecule is positively ionised, and charge transfer to non-bonding states of the neutral molecule is energetically possible, dissociative scattering may occur. On the other hand, charge capture to bound states may be accompanied by vibrational excitation. A concrete example is provided by the H_2^- molecule. Upon approach to a metal surface, both the bound singlet $X^1\Sigma_g^+$ and unbound triplet $b^3\Sigma_u^-$ states of H_2 are probably populated by charge transfer [65] (fig. 19). Adiabaticity arguments (see the beginning of section 2.) suggest that charge transfer will occur as

the molecule approaches the surface. The branching ratio for these two charge transfer channels is unknown in the energy range of interest here. However, at beam energies of several keV and glancing incidence (surface normal energies of the order of 1 eV), detailed measurements of H_2^+ and D_2^+ scattering from Cu(111) seem to suggest that between 30% and 80% of the beam may be non-dissociatively scattered [66]. Positive and negative product ion fractions for 400 eV H_2^+ and H_3^+ irradiation of graphite at surface normal energies of around 50 eV have been reported by Tsumori et al. [10] and positive and neutral product fractions for 0.2-1 keV H_3^+ irradiation of Ni(111) at normal energies of 2-10 eV by Willerding et al. [67].

Incident neutral molecules or initially ionised molecules which neutralise to a bound state can still dissociatively scatter, even under conditions where the purely collisional mechanisms discussed earlier are not important. Fast neutral H_2 (at keV energies) in its ground electronic state is efficiently dissociated in grazing collisions with metal surfaces [68,69]. It has been proposed [69] that the dissociative scattering dynamics of fast molecules is influenced by additional (higher lying) potential surfaces of quite different topography to that of the adiabatic ground state, via processes analogous to those discussed already for desorption in section 2.5. If we convert the experimentally measured total translational energy losses to losses per unit time in the interaction region [69], we discover that keV energy molecules dissipate energy at rates in the 0.1-1 eV/fs regime. Most of the energy appears to be transferred to the metal conduction electrons via an efficient electron-hole pair excitation mechanism [70]. The resulting 'hot' electrons are therefore continuously available to populate higher lying electronic states of the molecule-metal system. Classical simulations of this process have successfully reproduced the essential features of experimental data for a large number of dissociatively scattered diatomic and polyatomic molecules [71]. The same mechanism predicts a high vibrational excitation of non-dissociatively scattered molecules, a prediction which awaits experimental verification. However, such 'hot' electron mediated processes can only dominate for fast grazing trajectories on reasonably planar surfaces where the molecule can both efficiently excite electron-hole pairs and coincidentally spend several vibrational periods in the near-surface region. At the (presumably) rough surfaces of a fusion device, such events are unlikely to be of any significance.

3. Conclusion

The microscopic mechanisms responsible for the formation of molecules on surfaces and for their departure from surfaces are reasonably well understood. This is particularly so for metal surfaces. Although the rotational, vibrational and electronic state populations of departing molecules exhibit complex system-specificity's and surface structure dependencies, two generalisations do seem possible *for metal surfaces* at least:

- the fast (10's of fs) electronic relaxation times characteristic of conduction band electrons in metals imply that at the low ejection velocities of interest here, the product state distributions will generally be dominated by dynamical processes involving the *lowest lying adiabatic electronic state* of the system, and
- product angular, translational, vibrational and rotational distributions are unlikely to be thermal distributions characterised by the temperature of the surface.

A recommendation which emerges from our current understanding of particle-surface processes in the 0.1-100 eV impact energy regime is to use *medium to high-Z metals* for the surfaces of divertor structures exposed to the low energy particle irradiation characteristic of the proposed ITER divertor operation mode. With this choice, penetration and 'physical sputtering' of surface material will be minimised. At sufficiently elevated surface temperatures, surface damage could be self-annealing on the microscopic scale relevant to the processes discussed in this paper. This would lead to the properties of the surface being more consistent and predictable. In addition, thermal desorption of adsorbed H_2 or diffusion of any adsorbed atomic hydrogen, followed by L-H surface recombination reactions, could occur. This mode of operation would help to keep the concentration of surface and sub-surface hydrogen low, which would help keep the vibrational excitation of the desorbing H_2 low. In contrast, the choice of a 'low' surface temperature would permit, in the absence of efficient particle induced desorption processes, a high concentration of atomic hydrogen to become established at the surface. This would increase the chance of Eley-Rideal reactions and the probability that any desorbing H_2 is highly vibrationally excited. The ultimate choice of the operating temperature may therefore depend on whether or not the

presence in the divertor plasma of highly vibrationally excited hydrogen is beneficial or detrimental to the successful operation of the gas blanket concept.

Acknowledgements

We wish to thank the National Institute for Fusion Science in Nagoya and the British Council in Tokyo for the generous support provided to KJS at NIFS while preparing the bulk of this article, Ms M. Kato (NIFS) for copious quantities of green tea and Dr. Ratko Janev (IAEA Wien) for discussions and encouragement.

References

[1] K. Borrass et al. , The ITER Divertor Concept, 1994

[2] Y. Kubota, N. Noda, A. Sagara, N. Inoue, K. Akaishi, J. Yamamoto, O. Motojima, to be published

[3] R. K. Janev, in 'Proceedings Intern. Symp. Atomic and Molecular Processes in Fusion Plasmas', ed. H. Tawara, NIFS-DATA-Series Report ..... (1996)

[4] D. R. Schultz, in 'AIP Conference Proceedings 322, Atomic Processes in Plasmas, 9th APS Topical Conf., San Antonio, Texas, 1993', ed. W. L. Rowan (AIP Press, New York 1995) p.3

[5] Summary Report of the IAEA Advisory Group Meeting on 'Atomic, Molecular and Particle-Surface Interaction Data for Divertor Physics Design Studies', ed. R.K. Janev (1995)

[6] D. Reiter, in 'Atomic & Plasma-Material Interaction Processes in Controlled Thermonuclear Fusion', ed. R. K. Janev & H. W. Drawin (Elsevier, 1993) p. 243

[7] P. Stoltze, J. K. Nørskov, J. Catalysis 110 (1988) 1

[8] H. Hagstrum, in 'Inelastic Ion-Surface Collisions', ed. N. H. Tolk, J. C. Tully, W. Heiland, C. W. White (Academic Press, NY, 1977) p.1

[9] K. J. Snowdon, Nucl. Instrum. Meth. Phys. Res. B 33 (1988) 365

[10] K. Tsumori, W. R. Koppers, R. M. A. Heeren, M. F. Kadodwala, A. W. Kleyn, J. H. M. Beijersbergen, Int. Symp. Production & Neutralization of Negative Ions & Beams (Brookhaven, 1995 and AIP Conference Proc., to be published)

[11] G. Comsa, J. Chem. Phys. 48 (1968) 3235

[12] G. Comsa, R. David, Surf. Sci. 117 (1982) 77

[13] S. Küchenhoff, W. Brenig, Y. Chiba, Surf. Sci. 245 (1991) 389

[14] G.D. Kubiak, G.O. Sitz, R.N. Zare, J. Chem. Phys. 83 (1985) 2538

[15] B. Hammer, M. Scheffler, K. W. Jacobsen, J. K. Nørskov, Phys. Rev. Lett. 73 (1994) 1400

[16] H. Zacharias, Appl. Phys. A 47 (1988) 37

[17] R. I. Hall, I. Cadez, M. Landau, F. Pichou, C Schermann, Phys. Rev. Lett. 60 (1988) 337

[18] P. J. Eenshuistra, J. H. M. Bonnie, J. Los, H. J. Hopman, Phys. Rev. Lett. 60 (1988) 341

[19] C. T. Rettner, Phys. Rev. Lett., 69 (1992) 383

[20] C. T. Rettner, D. J. Auerbach, Surf. Sci. 357/358 (1996) 602

[21] B. Jackson, M. Persson, J. Chem. Phys. 96 (1992) 2378; J. Chem. Phys. 102 (1994) 1078; Chem. Phys. Lett. 237 (1995) 468

[22] P. Kratzer, W. Brenig, Surf. Sci. 254 (1991) 275

[23] C.-G. Jiang, H. Namba, M. Nagasaka, N. Kosugi, S. Murakami, H. Tochihara, Y. Murata, J. Phys. Soc. Japan 53 (1984) 1797

[24] E. W. Kuipers, A. Vardi, A. Danon, A. Amirav, Phys. Rev. Lett. 66 (1991) 116

[25] M. C. Yang, H. W. Lee, H. Kang, J. Chem. Phys. 103 (1995) 1

[26] J. Roth, E. Vietzke, A. A. Haasz, in 'Atomic and Plasma-Material Interaction Data for Fusion', Suppl. to Nucl. Fusion 1 (1991) 63

[27] J. Harris, B. Kasemo, Surf. Sci. 105 (1981) L281

[28] C. T. Rettner, J. Lee, J. Chem. Phys. 101 (1994) 10185

[29] M. B. Lee, Q. Y. Yang, S. L. Tong, S. T. Ceyer, J. Chem. Phys. 85 (1986) 1693, S. T. Ceyer, Science 249 (1990) 133

[30] C. Åkerlund, I. Zoric, B. Kasemo, J. Chem. Phys. 104 (1996) 7359

[31] J. D. Beckerle, Q. Y. Yang, A. D. Johnson, S. T. Ceyer, J. Chem. Phys. 86 (1987) 7236

[32] U. Diebold, W. Möller, P. Varga, Surf. Sci. 248 (1991) 147

[33] J. Roth, in 'Atomic & Plasma-Material Interaction Processes in Controlled Thermonuclear Fusion', ed. R. K. Janev & H. W. Drawin (Elsevier, 1993) p. 381

[34] J. Biersack, W. Eckstein, Appl. Phys. A 34 (1984) 73

[35] M. T. Robinson, I. M. Torrens, Phys. Rev. B 9 (1974) 5008

[36] A. Amirav, M. J. Cardillo, Surf. Sci. 198 (1988) 192

[37] H. Metiu, A. E. DePristo, J. Chem. Phys. 91 (1989) 2735

[38] J. A. Schultz, P. T. Murray, R. Kumar, Hsin-Kuei Hu, J. W. Rabalais, in 'Desorption Induced by Electronic Transitions DIET I', Ed. N. H. Tolk, M. M. Traum, J. C. Tully, T. E. Madey, Springer Series in Chemical Physics, Vol. 24 (Springer-Verlag, Berlin, 1983) p. 191.

[39] H. Metiu, J. W. Gadzuk, J. Chem. Phys. 74 (1981) 2641

[40] P. E. Redhead, Can. J. Phys. 42 (1964) 886
D. Menzel, R. Gomer, J. Chem. Phys. 41 (1964) 3311

[41] P. Antoniewicz, Phys. Rev. B21 (1980) 3811

[42] P. J. Feibelman, M. L. Knotek, Phys. Rev. B18 (1978) 6531

[43] J. W. Gadzuk, L. J. Richter, S. A. Buntin, D. S. King, R. R. Cavanagh, Surf. Sci. 235 (1990) 317

[44] J. A. Misewich, T. F. Heinz, D. M. Newns, Phys. Rev. Letts. 68 (1992) 3737

[45] R. Janev, in 'Atomic & Plasma-Material Interaction Processes in Controlled Thermonuclear Fusion', ed. R. K. Janev & H. W. Drawin (Elsevier, 1993) p. 27

[46] A. Amirav, Comments At. Mol. Phys. 24 (1990) 187

[47] S. T. Ceyer, Ann. Rev. Phys. Chem. 39 (1988) 479

[48] R. B. Gerber, Chem. Rev. 87 (1987) 29

[49] C. T. Rettner, D. J. Auerbach, Comments At. Mol. Phys. 20 (1987) 153

[50] J. A. Barker, D. J. Auerbach, Surf. Sci. Reports 4 (1984) 1

[51] V. Celli, D. Evans, in 'Dynamics of Gas-Surface Interactions', eds. G. Benedek, U. Valbusa, Vol. 21, Springer Series in Chemical Physics 2 (Springer-Verlag, Berlin, 1982)

[52] M. J. Cardillo, Ann. Rev. Phys. Chem. 32 (1981) 331

[53] J. C. Tully, Acc. Chem. Res. 14 (1981) 188

[54] M. E. M. Spruit, P. J. Van den Hoek, E. W. Kuipers, F. H. Greuzebroek, A. W. Kleyn, Phys. Rev. B 39 (1989) 3915

[55] C. T. Rettner, E. K. Schweizer, Surf. Sci. 203 (1988) L677

[56] H. Akazawa, Y. Murata, J. Chem. Phys. 92 (1990) 5551

[57] P. J. van den Hoek, A. W. Kleyn, J. Chem. Phys. 91 (1989) 4318

[58] A. Gross, W. Brenig, Chem. Phys. 177 (1993) 497

[59] J. W. Gadzuk, Comments At. Mol. Phys. 16 (1985) 219

[60] D. M. Newns, Surf. Sci. 171 (1986) 600

[61] R. B. Gerber, A. Amirov, J. Phys. Chem. 90 (1986) 4483

[62] E. J. J. Kirchner, U. van Slooten, E. J. Baerends, A. W. Kleyn, J. Chem. Phys. 97 (1992) 3821

[63] U. van Slooten, D. Andersson, A. W. Kleyn, E. A. Gislason, Chem. Phys. Lett. 185 (1991) 185

[64] U. van Slooten, D. R. Andersson, A. W. Kleyn, E. A. Gislason, Surf. Sci. 274 (1992) 1

[65] U. Imke, K. J. Snowdon, W. Heiland, Phys. Rev. B 34 (1986) 41

[66] A. Nesbitt, R. Harder, A. Golichkowski, G. Herrmann, K. J. Snowdon, Chem. Phys. 179

(1994) 215

[67] B. Willerding, K. J. Snowdon, W. Heiland, Z. Phys. B 59 (1985) 445

[68] K. Schmidt, H. Franke, A. Naermann, W. Heiland, J. Phys.: Condens. Matter 4 (1992) 9869

[69] R. Harder, A. Nesbitt, A. Golichowski, G. Herrmann, K. J. Snowdon, Surf. Sci. 316 (1994) 47

[70] A. Bilic, B. Gumhalter, W. Mix, A. Golichkowski, S. Tzanev, K. J. Snowdon, Surf. Sci. 307-309 (1994) 165

[71] K. J. Snowdon, R. Harder, A. Nesbitt, Surf. Sci. 363 (1996) 42

Tables

Table 1. Comparison of the calculated [13] vibrational populations of the $v = 1$ and 2 levels of H_2 and D_2 following desorption by the Langmuir-Hinshelwood reaction mechanism with those expected from a Boltzmann distribution the surface temperature and with those observed in the experiments of Kubiak et al. [14].

State	Molecule	Theory	Boltzmann	Cu(111)	Cu(110)
$P(v = 1)$	H_2	0.04	0.0009	0.08 ± 0.03	0.05 ± 0.01
$P(v = 1)$	D_2	0.19	0.0060	0.35 ± 0.20	0.24 ± 0.20
$P(v = 2)$	H_2	1×10^{-4}	8×10^{-7}	< 0.01	< 0.01
$P(v = 2)$	D_2	3.3×10^{-3}	3.6×10^{-5}	< 0.04	< 0.04

Fig. 1. Schematic illustration of processes which may in principle lead to the emission of molecular species from surfaces: a) thermal desorption of molecularly adsorbed species; b) prompt desorption following surface recombination of adsorbed species (Langmuir-Hinshelwood reaction); c) prompt desorption following the direct reaction of a species from the gas phase with a surface adsorbed species (Eley-Rideal reaction); d) direct (right) or substrate mediated (left) desorption induced by incident heavy particles, electrons and photons; e) direct scattering of molecules incident from the gas phase, possibly accompanied by fragmentation. Although surface species are shown here as ad-particles on planar surfaces, our discussion refers equally to rough surfaces and to species located at step edges and within the surface layer.

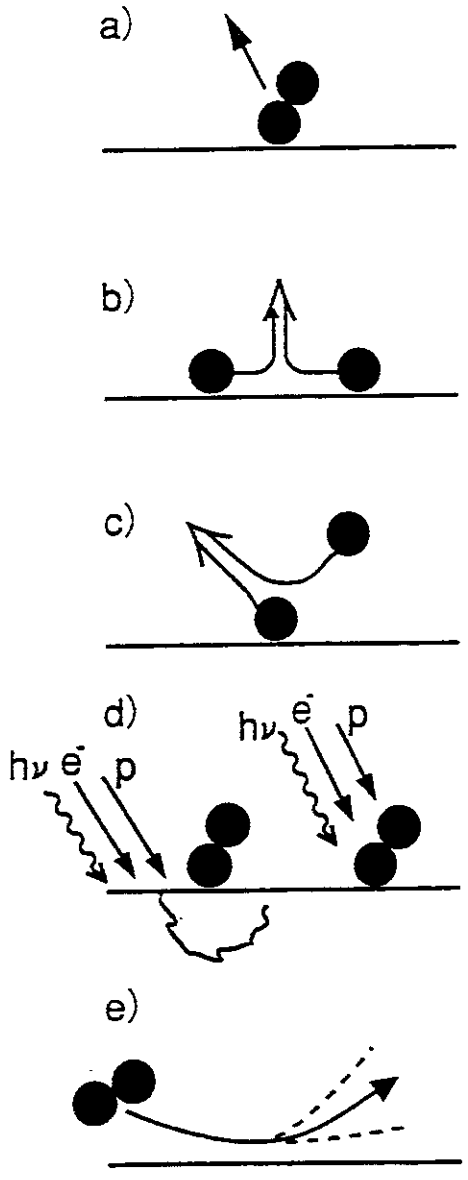

Fig. 2. Schematic illustration of the shift and broadening experienced by atomic or molecular ionisation and affinity levels in the vicinity of a metal surface (ε_F is the Fermi level of the metal, I and A the ionisation and affinity levels of the atom or molecule; for simplicity of representation, the ad-particle potential is shown as a single Coulomb-like well).

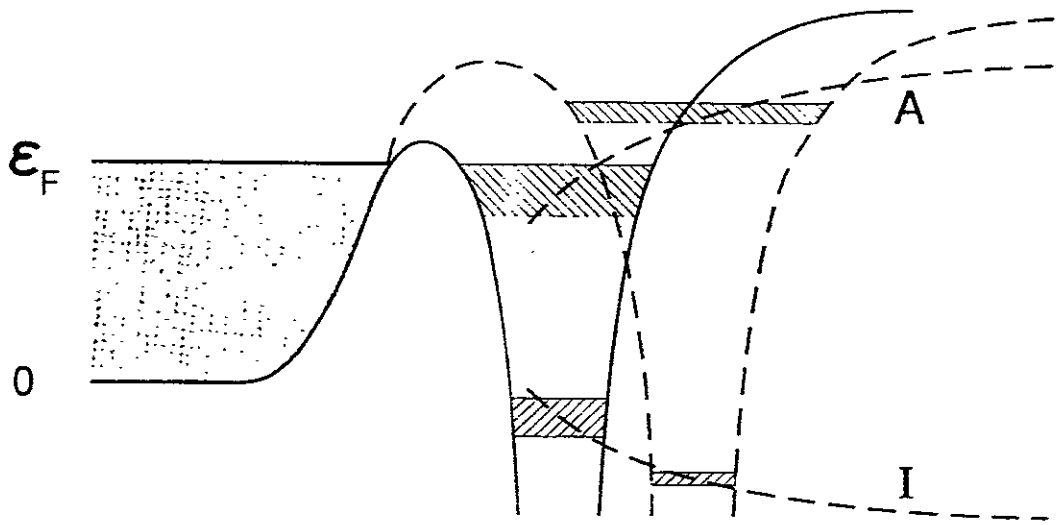

Fig. 3. Contour plot of the potential energy surface (PES) for a diatomic molecule interacting with a surface as a function of the separation x of the atoms in the molecule and the distance z of the molecule centre of mass from the surface. Region a of the PES represents the gas phase molecule in the initial (final) stage of adsorption (desorption). Region b represents a molecularly chemisorbed species. Region c represents the dissociative chemisorption of the molecule on the surface. We emphasise that the shape of such potential energy surfaces depend on the chemical nature of the constituents of the molecule, the location of the molecule with respect to the nearby surface atoms, the chemical nature and geometrical arrangement of the surface atoms and the molecular orientation with respect to the surface.

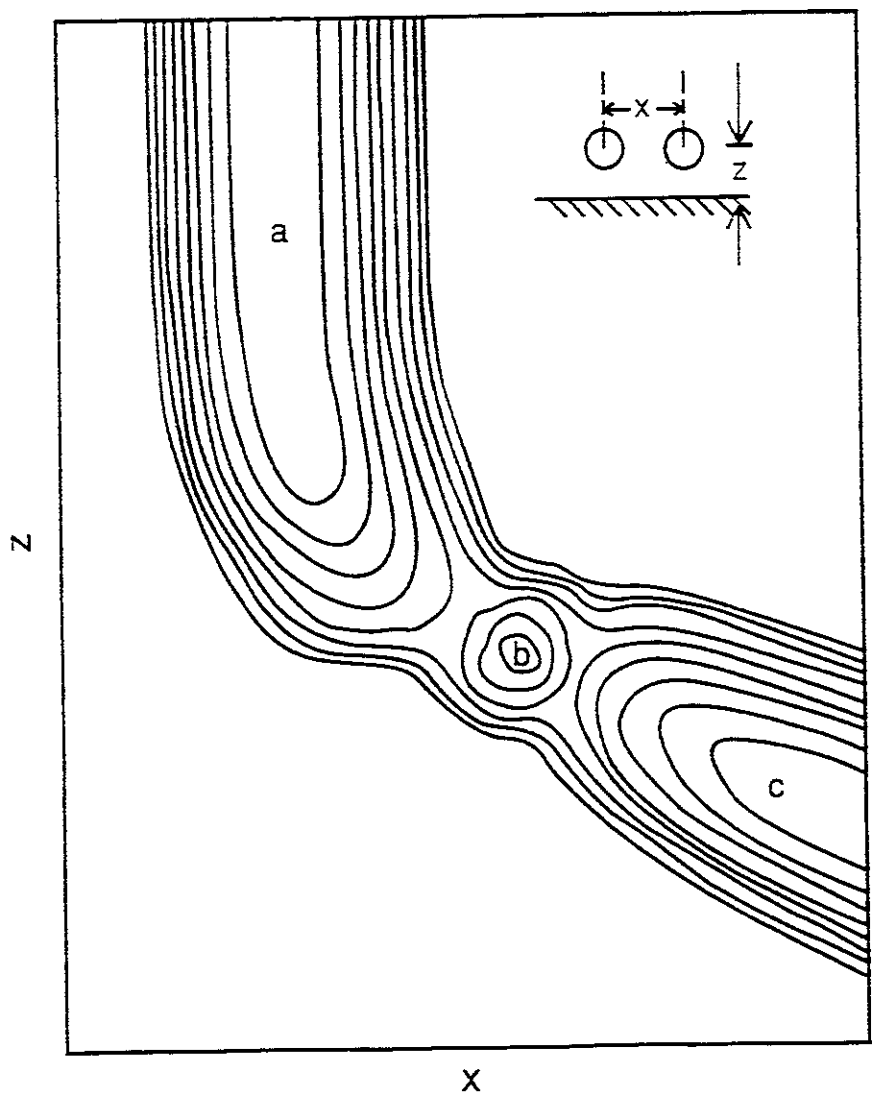

Fig. 4. a) Normalised flux of D_2 molecules desorbing from Cu(100) (×) and b) mean energy of D_2 molecules desorbing from Cu(100) (×) and Cu(111) (o) as a function of the polar angle of desorption ϑ (adapted from fig. 3 of [12], with permission).

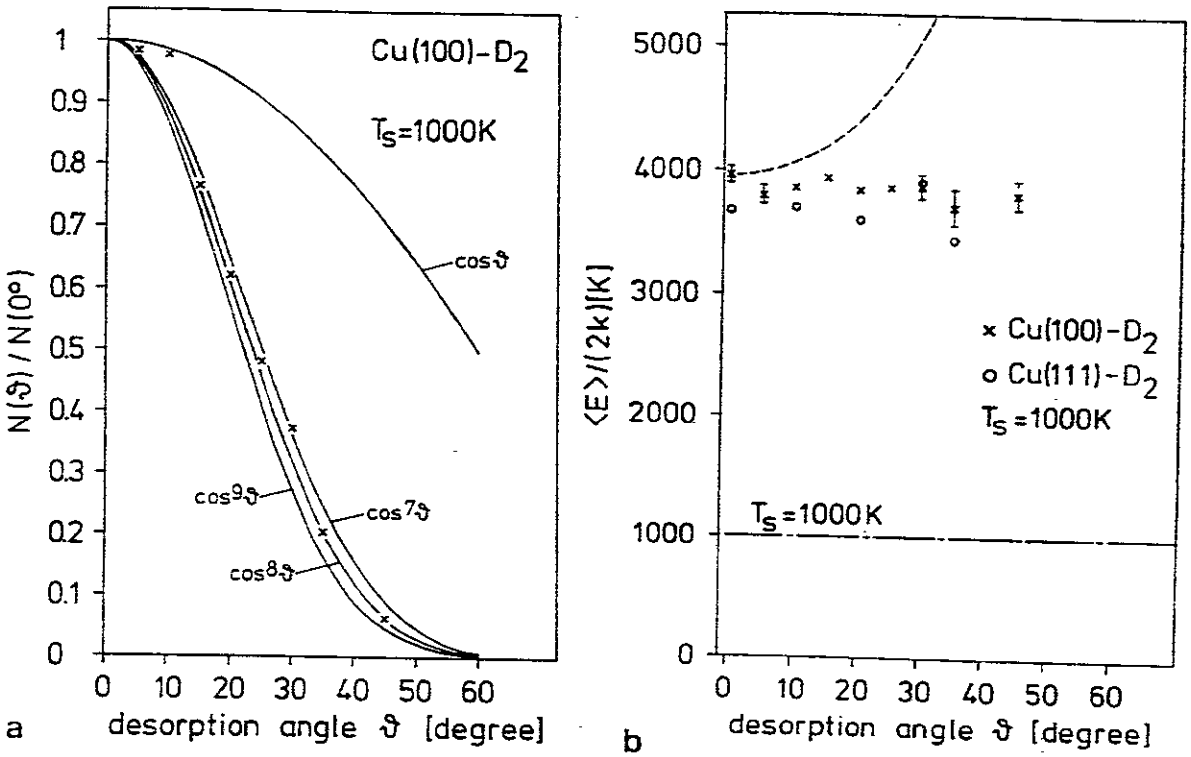

Fig. 5. Model PES for H_2 interacting with Cu as a function of the co-ordinates x and z (see caption to fig. 3). The separation of two contour lines is 0.1 eV (fig. 1a of [13], with permission).

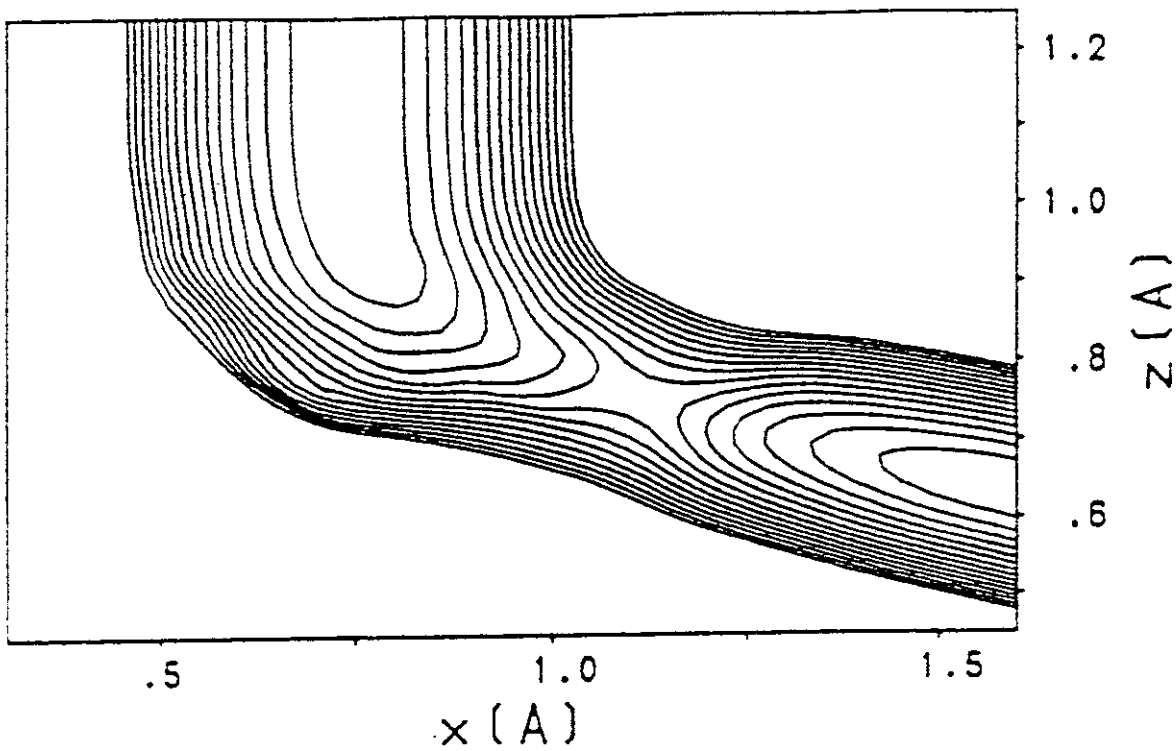

Fig. 6. Angular distribution of HD molecules desorbed from a H-covered Cu(111) surface at 100 K exposed to D-atom beams of kinetic energies of 0.07 eV (■) and 0.37 eV (●) incident at 60° to the surface normal. The solid curves are drawn to guide the eye (fig. 2 of [20], with permission).

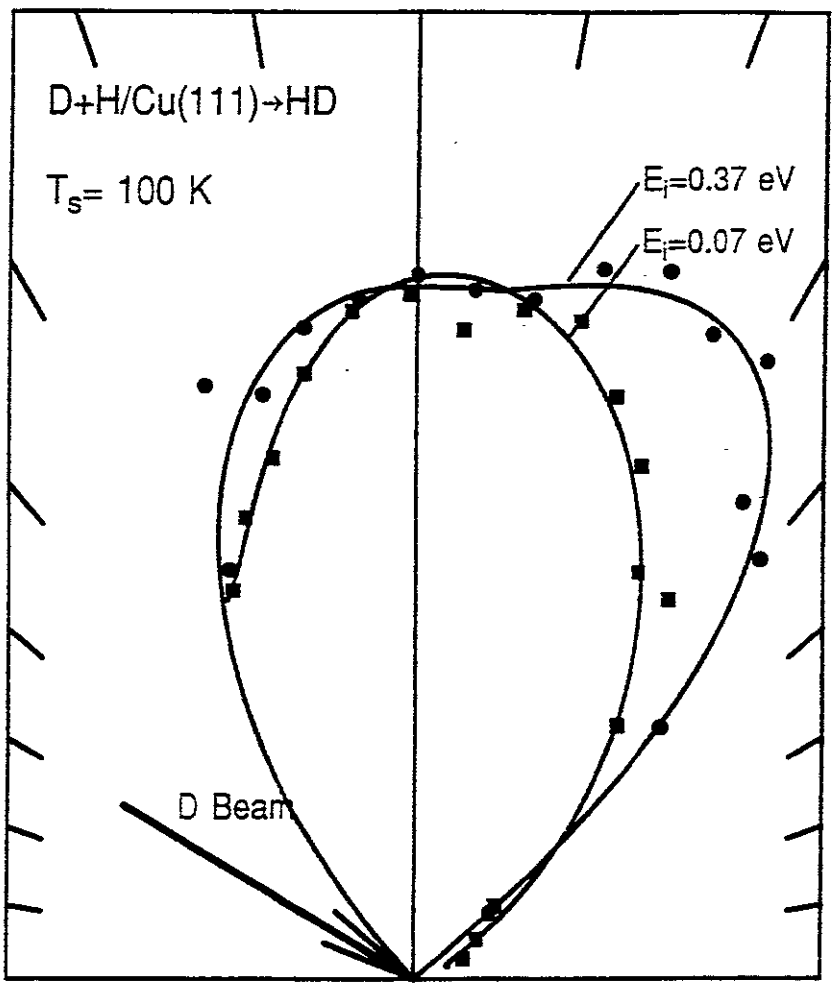

Fig. 7. Vibrational state dependence of the mean rotational energy of HD molecules produced via the reaction of incident D-atoms with a H-covered Cu(111) surface at 100 K. The mean translational energy was measured to be 1.1 ± 0.2 eV (fig. 8a of [20], with permission).

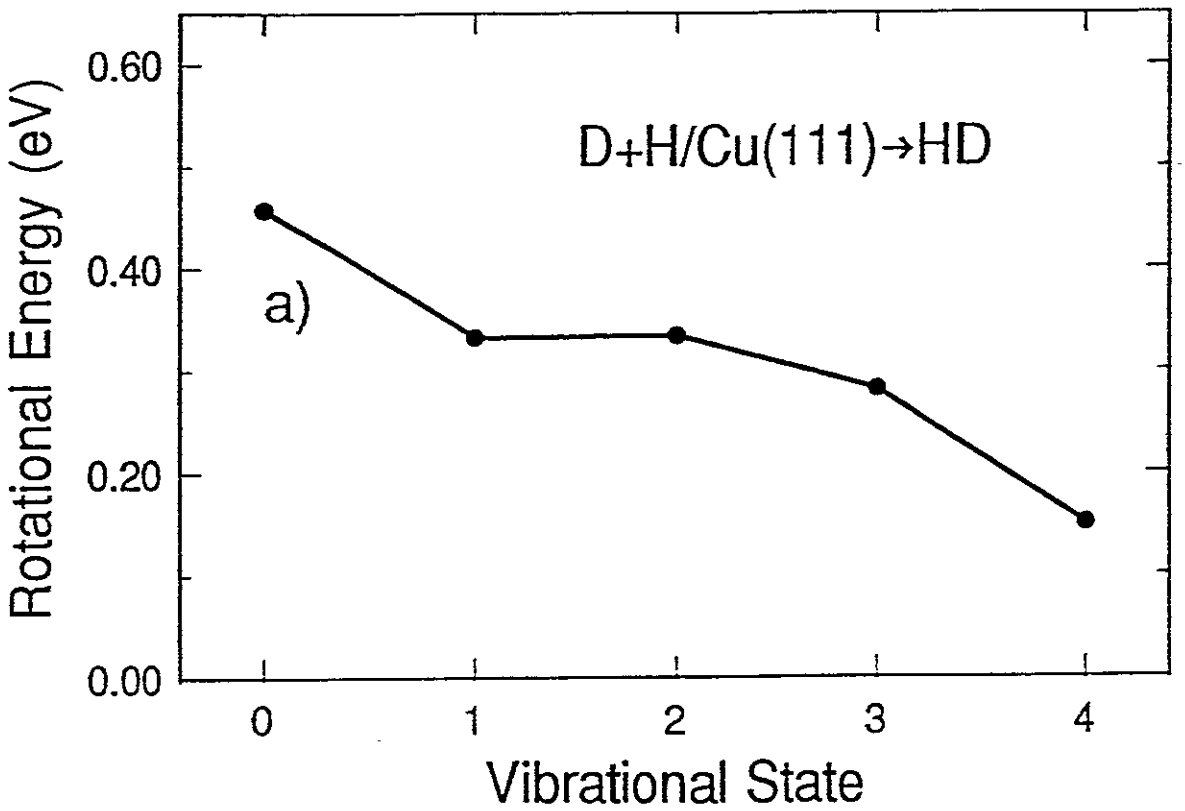

Fig. 8. Vibrational state (flux) distributions of HD molecules produced via the reaction of incident D-atoms with a H-covered Cu(111) surface at 100 K. The mean translational energy was measured to be 1.1 ± 0.2 eV (adapted from fig. 7a of [20], with permission).

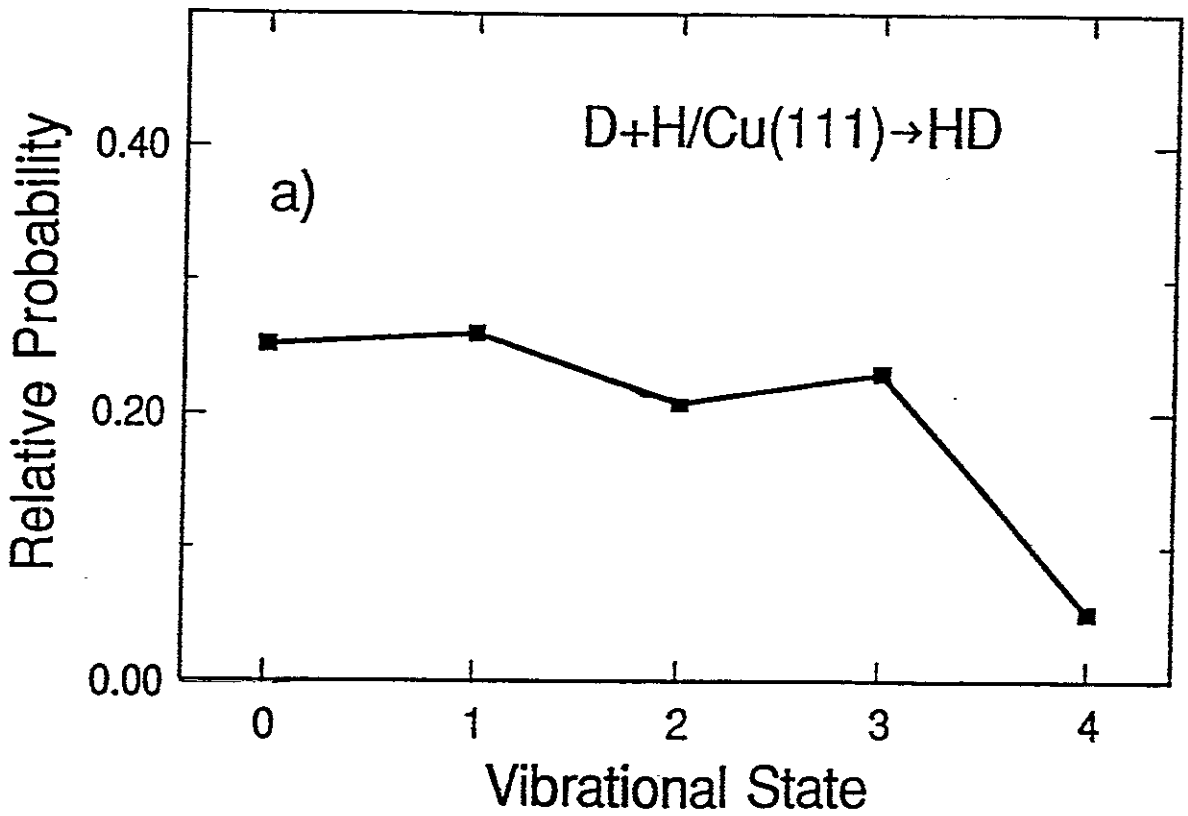

Fig. 9. Model PES for the Eley-Rideal reaction of a gas phase H-atom (incident along the surface normal) with an H-atom adsorbed on a tungsten surface. Contour lines are drawn in steps of 0.5 eV as a function of the distance z between the centre of mass of the molecule and the surface and the separation x of the two H-atoms (fig. 1 of [22], with permission).

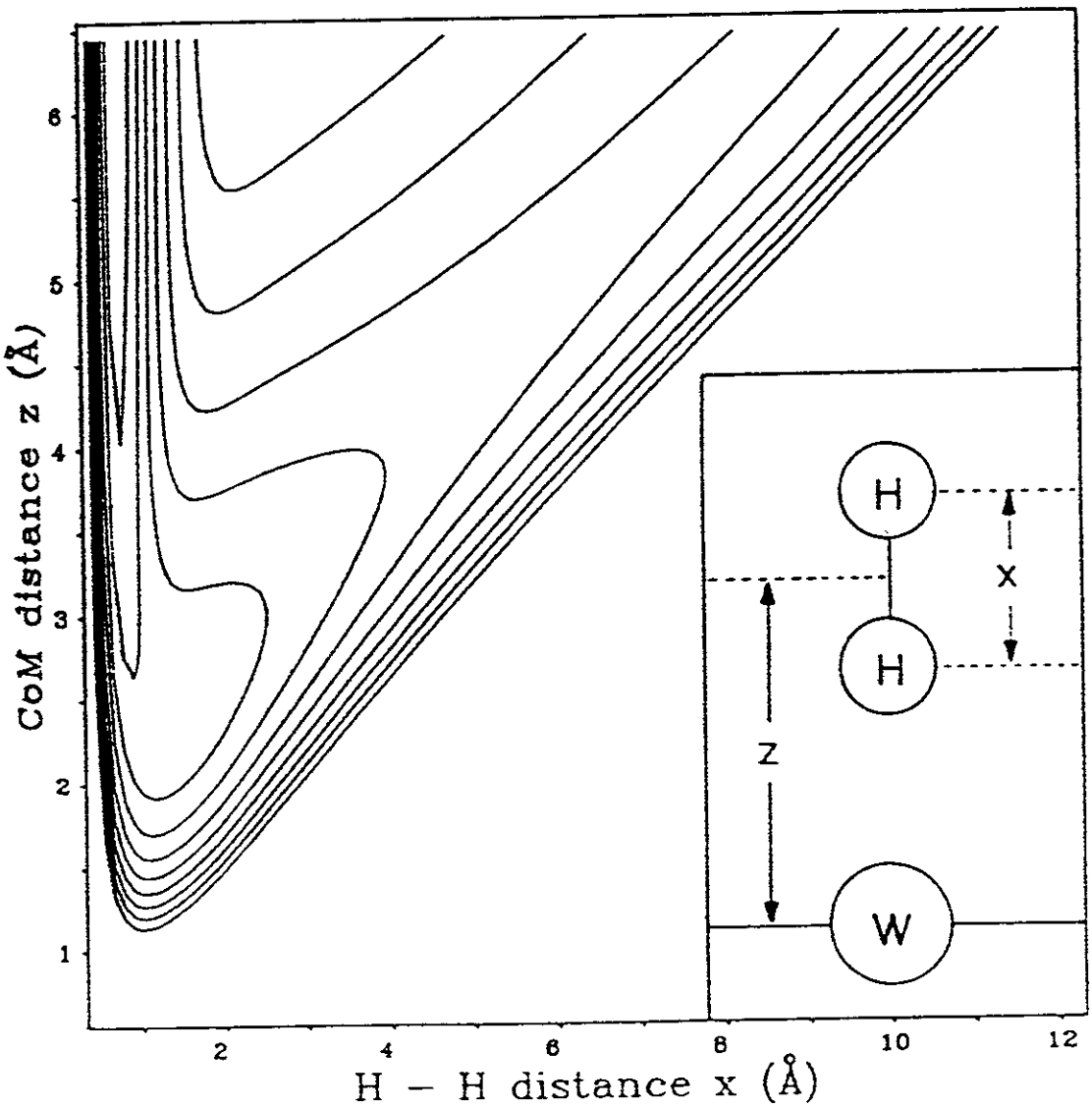

Fig. 10. Probability of occupation of the $v = 0$ (o), $v = 1$ (◊), $v = 2$ (Δ), $v = 3$ (+), $v = 4$ (×) and $v = 5$ (•) vibrational states of H_2 desorbed from a tungsten surface via the Eley-Rideal reaction mechanism as a function of the kinetic energy of the normally incident H-atom for the PES shown in fig. 9 (fig. 2 of [22], with permission).

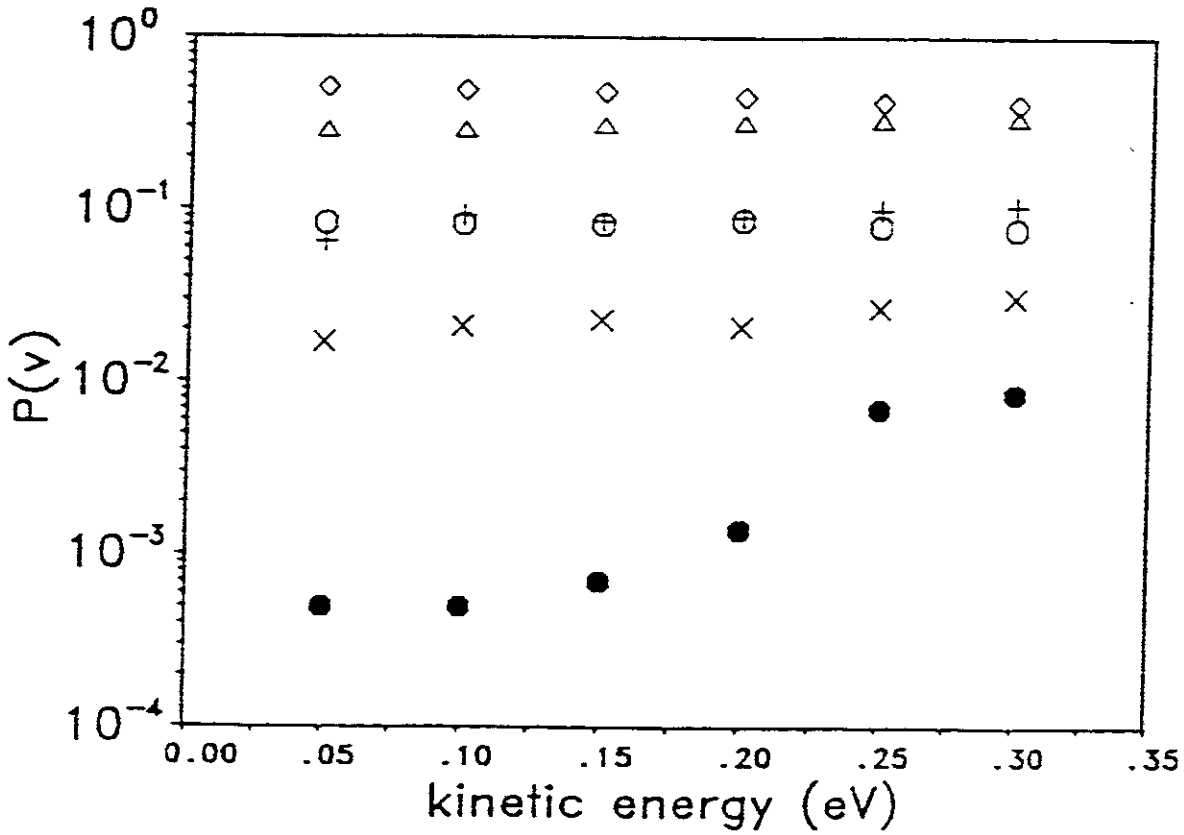

Fig. 11. Schematic illustration of processes which may lead to desorption of molecular species from surfaces following electron or photon irradiation: a) direct excitation to an unbound state (Menzel-Gomer-Redhead mechanism [40]); b) direct excitation to a bound state followed by acceleration toward the surface and subsequent deexcitation (Antoniewicz mechanism [41]); c) excitation of a core hole by the incident electron or photon, followed by Auger decay of the initial excitation, leaving the resulting ionised species in a non-bonding configuration allowing desorption to occur (Knotek-Feibelman mechanism [42]); d) electron-hole pair creation by adsorption of the incident radiation leads to 'hot' electrons which if scattered through negative-ion like resonance's of the adsorbate may lead to vibrational excitation and desorption via one [43] or more [44] excitation-deexcitation cycles of the type illustrated by the potential curves in b).

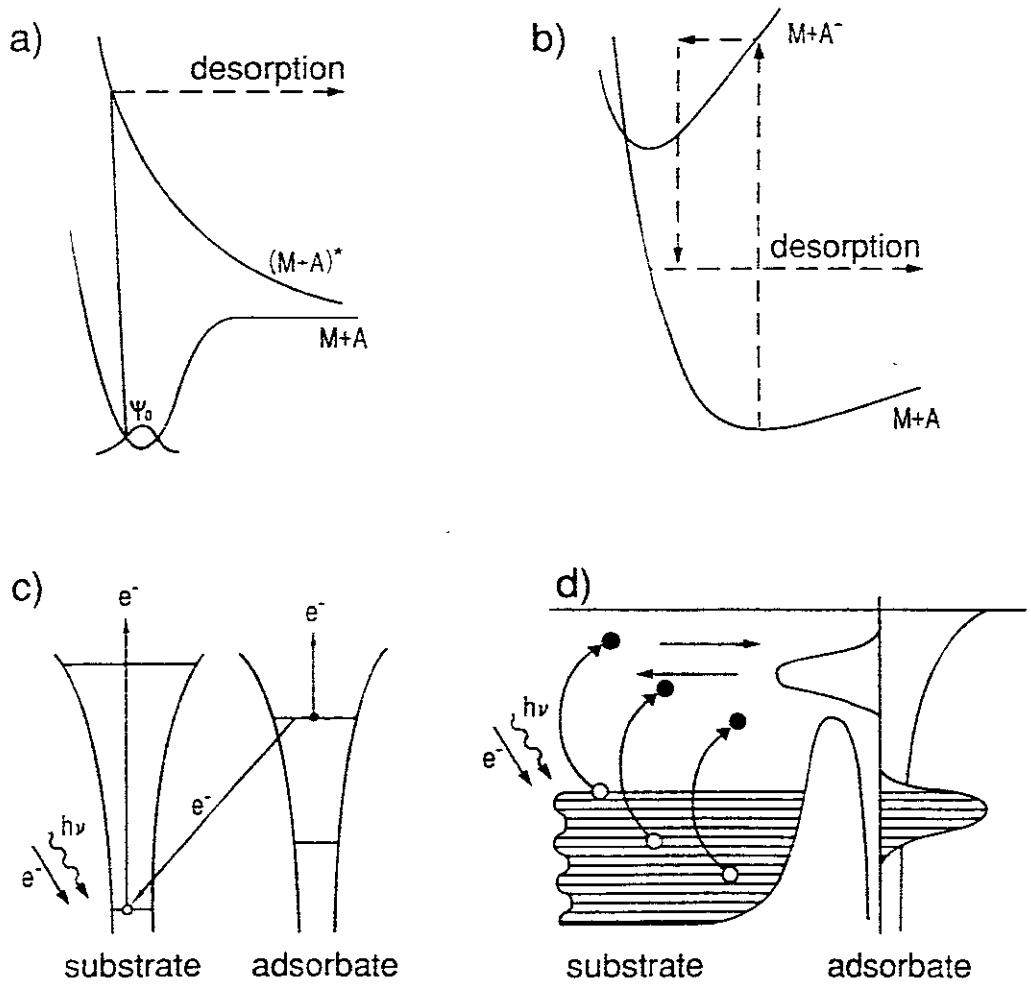

Fig. 12. Angular distributions of N_2 scattered from a W(110) surface at a temperature of 800 K. The beam was incident at 45° to the surface normal with translational energy a) 0.09 eV and b) 1 eV. In b) the angular distribution for He is also shown (adapted from fig. 4 of [49], with permission).

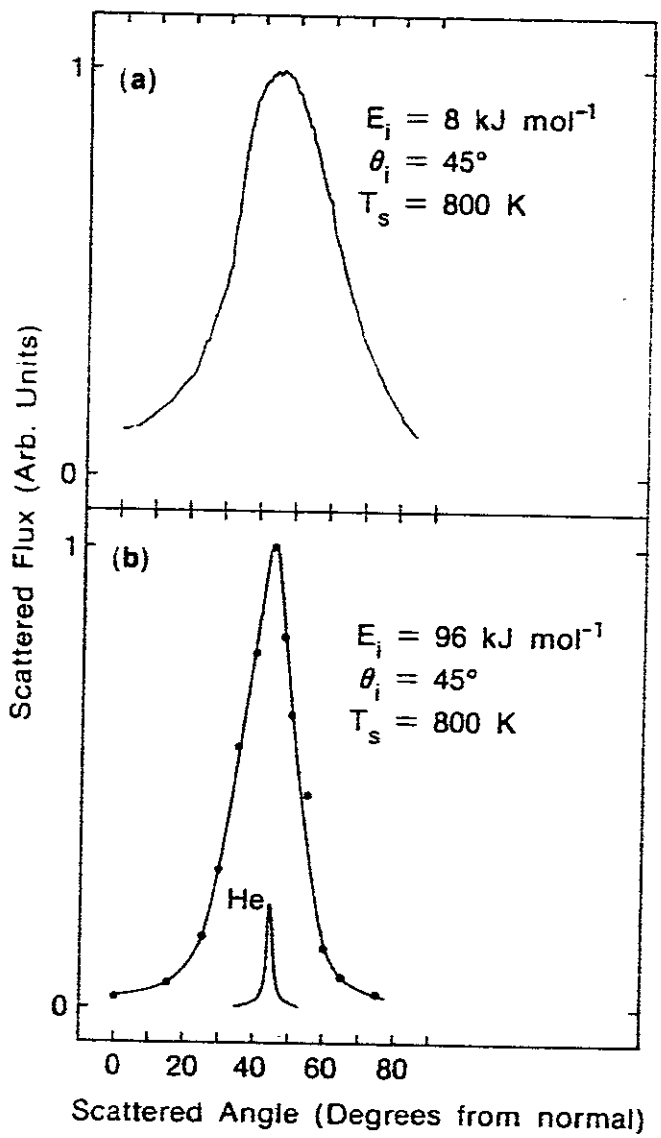

Fig. 13. Topographical representation of the intensity of scattered O_2 as a function of departure angle θ_f (see inset) and flight time between the crystal and the detector for incident beam energies E_i = 1.56, 1.16 and 0.91 eV and incidence angles θ_i (see inset) of 38°, 43° and 52°. $E_n = E_i\cos^2\theta_i$ is the normal energy of the incident beam to the surface in each case. Contour lines are drawn at 30%, 50%, 70% and 90% of the peak maximum (fig. 1 of [54], with permission).

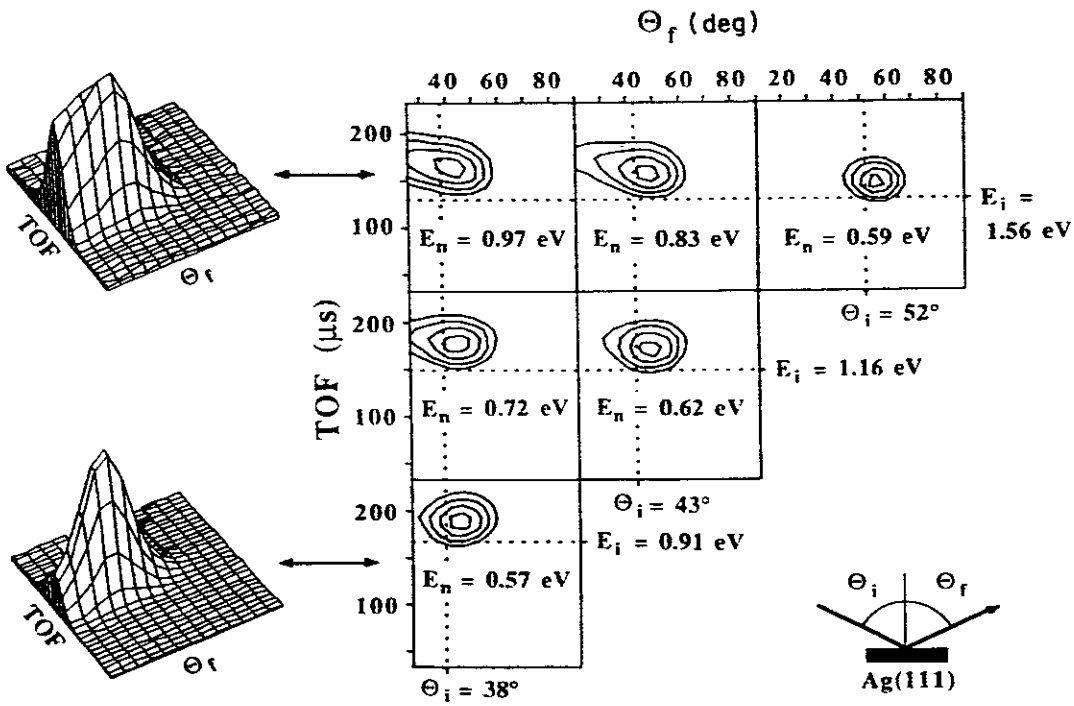

Fig. 14. Angular distributions of CO^- scattered from a Pt(100) surface. The beam was incident at 60° to the surface normal with translational energies of 30, 50, 70 and 100 eV (fig. 14 of [56], with permission).

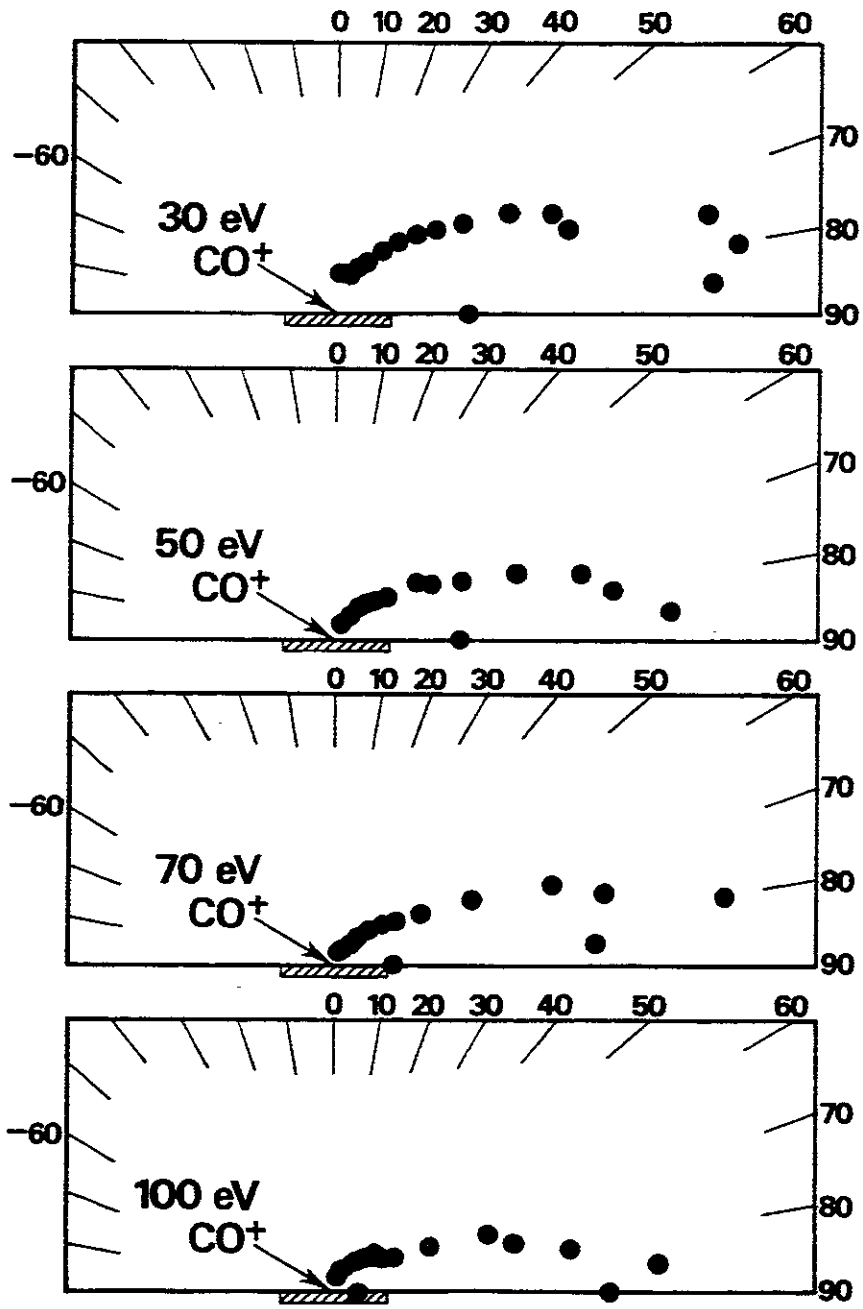

Fig. 15. Rotational state distributions for NO scattered from a Ag(111) surface at 750 K. The beam was incident at 15° to the surface normal with translational energies of 0.85 eV (upper curve) and 0.09 eV (lower curve) (fig. 2 of [49], with permission).

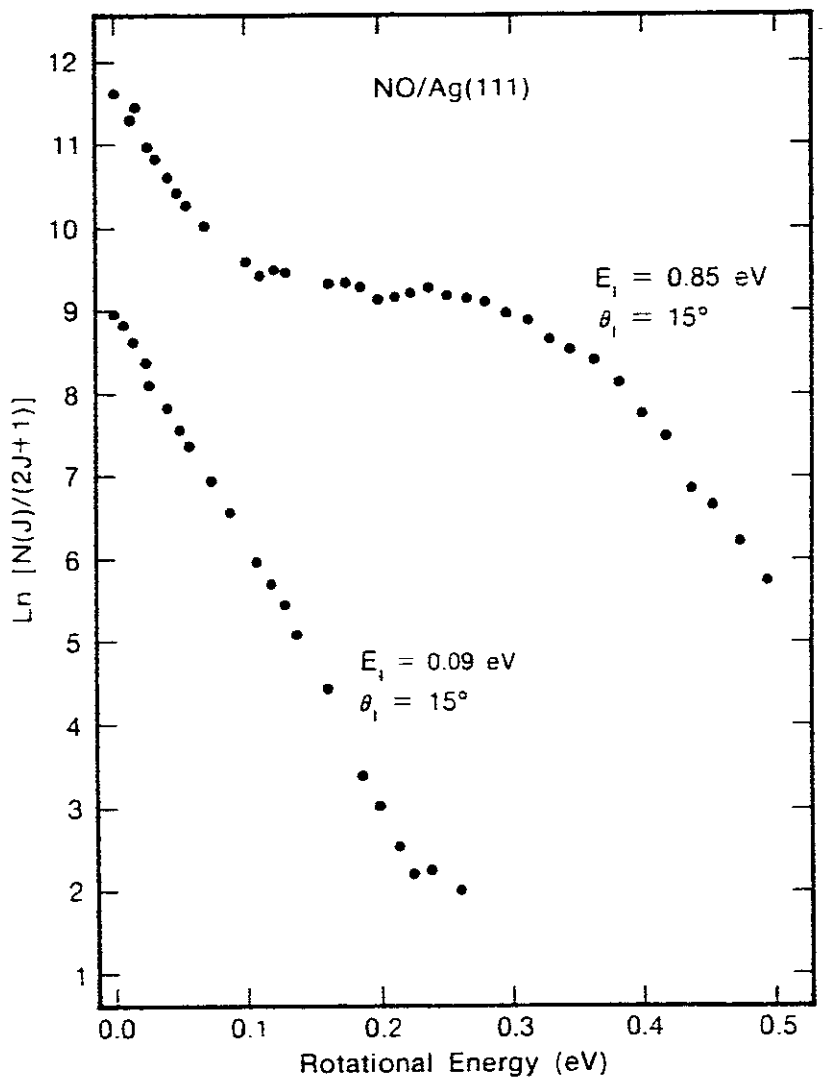

Fig. 16. Dependence on surface normal energy E_n of the population ratio NO(v = 1)/NO(v = 0) for NO scattered from a Ag(111) surface at 760 K and incidence angles θ_i to the surface normal of 15°, 30° and 45° (fig. 3 of [49], with permission).

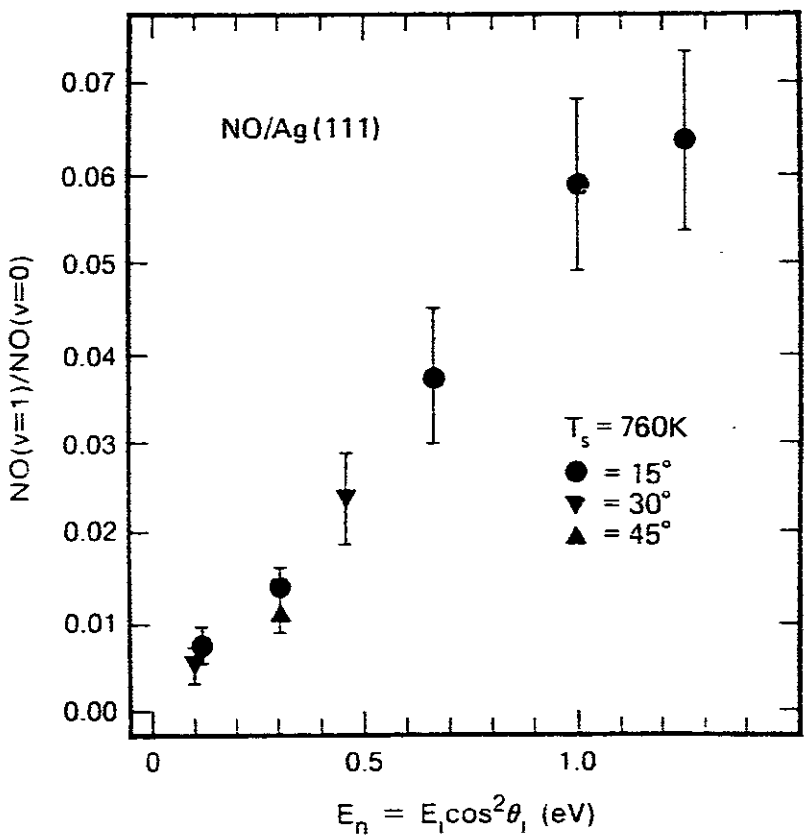

Fig. 17. Molecular dynamics calculation of the total energy loss ΔE_{tot} (for non-dissociated molecules), energy loss to the solid ΔE_{solid} and energy loss to internal degrees of freedom ΔE_{int} as a function of total incident molecule energy for O_2 scattering from Ag(111) for a surface normal energy E_n = 11.7 eV (adapted from fig. 9 of [57], with permission).

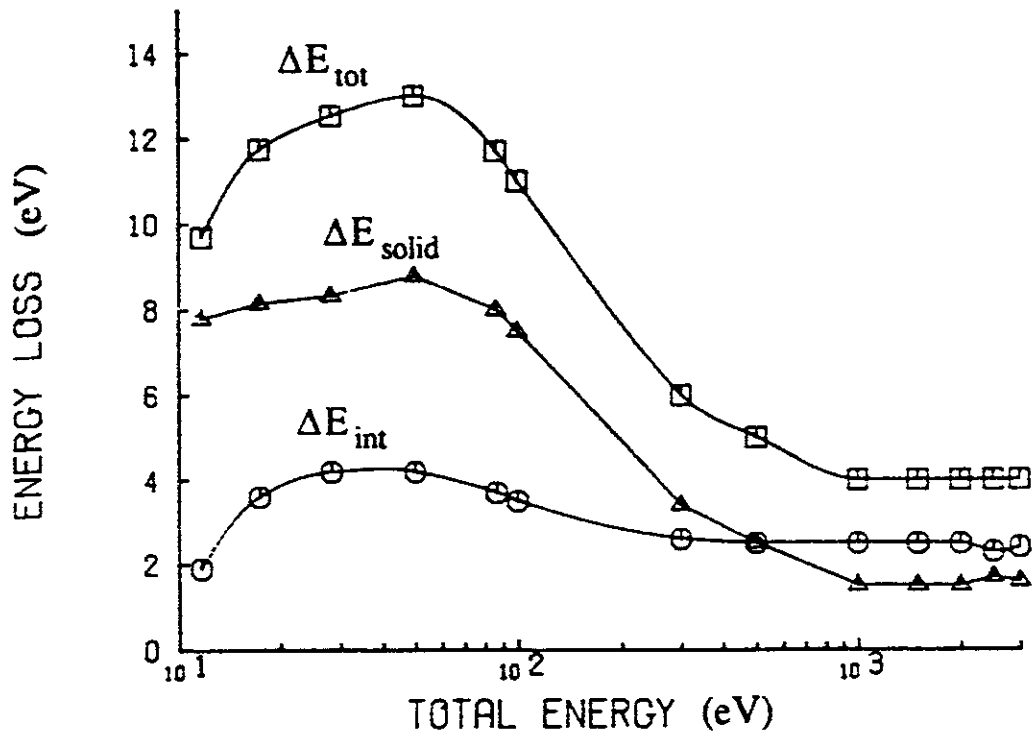

Fig. 18. Charge transfer (left) from the surface of a solid (here Al) to an incident ionised molecule (here H_2^+) can lead to (right) dissociative scattering or non-dissociative scattering, accompanied by vibrational excitation.

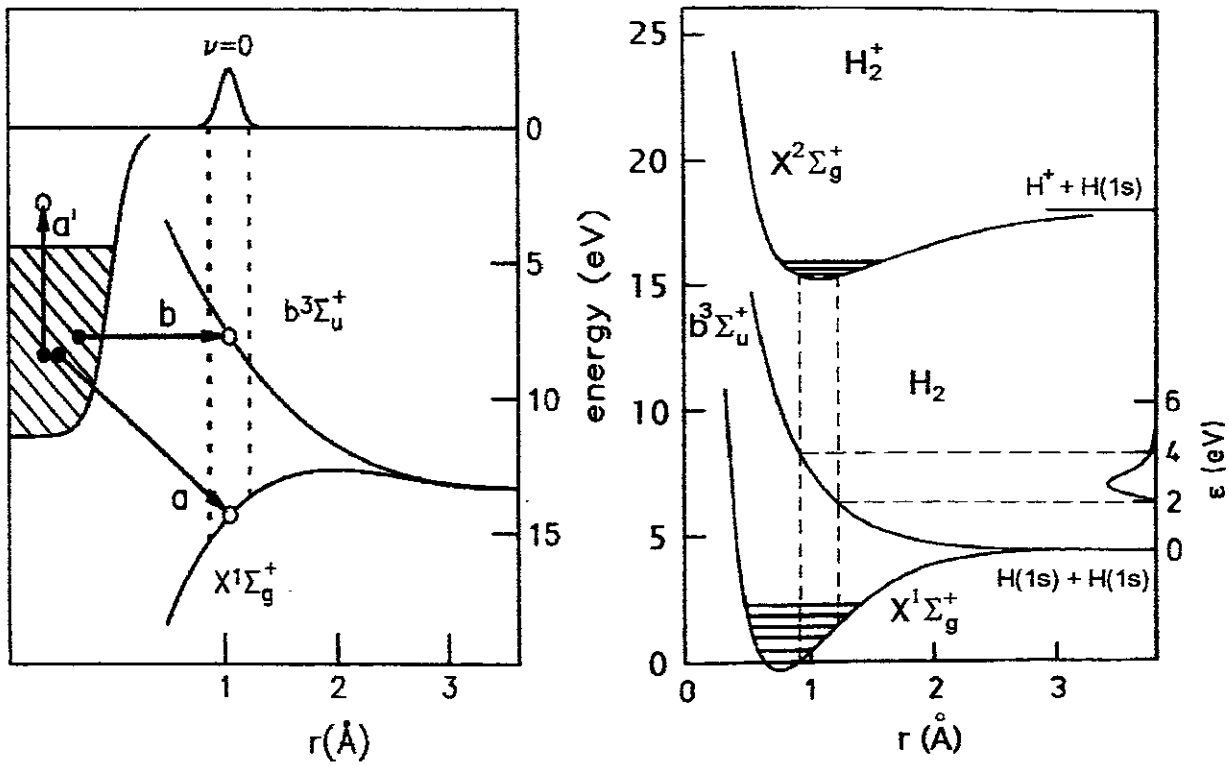

Appendix : list of posters

Electron Impact Ionization of the Hydrogen-like Ions B^{4+}, C^{5+}, N^{6+} and O^{7+}

K. Aichele, U. Hartenfeller, D. Hathiramani, G. Hofmann, V. Schäfer, M. Steidl, M. Stenke, R. Völpel and E. Salzborn
Institut für Kernphysik, Strahlenzentrum, Justus-Liebig-Universität Giessen, D-35392 Giessen, Germany

The electron impact ionization of atoms and ions is a topic of fundamental importance in modern physics. Electron impact ionization cross sections are especially desired for studying plasma-, fusion,- and astrophysics. Atomic hydrogen and hydrogen-like ions provide the simplest systems for electron impact ionization, because only direct ionization is possible for these three body systems with long-range Coulomb interactions. Much theoretical work has been done in this field since Thomson's first calculation [1]. Early calculations often led to strongly varying results. Therefore, semi-empirical formulas, e.g. the Lotz-formula [2], or scaling laws were often used for the prediction of the cross sections.

The measurements of the absolute electron impact ionization cross section for the ions B^{4+}, C^{5+}, N^{6+} and O^{7+}, were performed at the Giessen experimental crossed-beams set-up which has been described in detail earlier [3]. The ions were produced in a 10 GHz electron-cyclotron-resonance ion source and extracted at energies of q × 10 keV. After magnetic analysis of the desired mass to charge ratio and a collimation to typically 2 × 2 mm^2, the ion beam was crossed with an intense electron beam with energies of up to 6.5 keV. The product ions were separated from the parent ion beam by a magnet and detected in a single-particle detector. The parent ion beam was collected in a wide faraday cup. Employing the dynamic crossed-beams technique [4], absolute cross sections were obtained by moving the electron beam up and down through the ion beam.

The small cross sections, typically 10^{-20}cm, were measured for electron energies from below threshold up to 6.5 keV. The results were compared with distorted-wave calculations (DWA) by Younger [5] and the semi-empirical Lotz-formula [2]. For C^{5+} and N^{6+} also comparison with a binary-encounter approximation calculation by Salop was made [6]. Furthermore, we compared our cross sections with experimental data obtained from an EBIS experiment by Donets [7]. In all cases, the DWA calculations and the Lotz-formula were in very good agreement with our data. Donets' data, however, were often higher than our data and the theoretical predictions.

In order to test Thomson's scaling law [1] the measured cross sections and other available cross sections for hydrogen-like ions [8,9] and atomic hydrogen [10] were scaled by the square of the ionization energy and plotted against the electron energy in threshold units.

The scaling law predicts a general function for the scaled cross sections and our data agree very well with this prediction. For low atomic numbers Z (1-3) the scaled cross sections are smaller because of the partial screening of the nuclear charge. All scaled cross sections converge to the Bethe limit [11].

[1] J. J. Thomson, *Phil. Mag.* **23** (1912) 449
[2] W. Lotz, *Z. Phys.* **216** (1968) 241
[3] G. Hofmann, A. Müller, K. Tinschert and E. Salzborn, *Z. Phys. D* **16** (1990) 113
[4] A. Müller, K. Tinschert, C. Achenbach, E. Salzborn and R. Becker, *Nucl. Instr. Meth. in Phys. Res B* **10/11** (1985) 204
[5] S. M. Younger, *J. Quant. Spectrosc. Radiat. Transfer Vol.* **26** (1981) 239
[6] A. Salop, *Phys. Rev. A* **14** (1976) 2095
[7] E. D. Donets and V. P. Ovsiannikov, *Zh. Eksp. Teor. Fiz.* **80** (1981) 916
[8] B. Peart, D. S. Walton and K. T. Dolder, *J. Phys. B: At. Mol. Phys.* **2** (1969) 1347
[9] K. Tinschert, A. Müller, G. Hofmann, K. Huber, R. Becker, D. C. Gregory and E. Salzborn, *J. Phys. B: At. Mol. Opt. Phys.* **22** (1989) 531
[10] M. B. Shah, D. S. Elliot and H. B. Gilbody, *J. Phys. B: At. Mol. Phys.* **20** (1987) 3501
[11] H. Bethe, *Ann. Phys.* **5** (1930) 325

Double electron capture by impact of bare heavy ions on He targets. Contribution of final excited states.

H.F. Busnengo[†¶], A.E. Martínez[†‡], R.D. Rivarola[†‡],
R. Gayet[♠] y J. Hanssen[♣]

† *Instituto de Física Rosario CONICET-U.N.R.*
‡ *Facultad de Ciencias Exactas, Ingeniería y Agrimensura U.N.R.*
¶ *Facultad de Ciencias Bioquímicas y Farmacéuticas U.N.R.*
♠ *Université de Bordeaux I, France*
♣ *Université de Metz, France*

Abstract

In the present work the double electron capture process is analized within the independent electron approximation (IEA). Total cross sections for capture to the groud state and singly and doubly excited final states are calculated for several bare heavy projectiles on $He(1s^2)$ targets. The theoretical calculations are carried out using the *Continuum Distorted Wave-Eikonal Initial State* (CDW-EIS) and the *Continuum Distorted Wave-Eikonal Final State* (CDW-EFS) approximations.

Previous results corresponding to the CDW-EIS and *Continuum Distorted Wave* (CDW) models obtained using the IEA, which only consider capture to the final ground state of the projectile, are in good agreement with the experimental total cross sections corresponding to capture to any final state. However, for the case of multicharged projectiles, it is necessary to evaluate the contribution coming from capture to excited final states. Using the CDW approximation it has been found that for He^{2+} ions, the contribution of the final excited states is small but it is very important for the cases of Li^{3+} and B^{5-} projectiles. The total cross sections obtained in the present work are compared with experimental data and with previous theoretical results.

Polarization of X-ray Line Emission : a diagnostic of the angular distribution of electron in tokamaks and other hot plasmas

J. DUBAU

UPR-176-CNRS, DARC, Observatoire de Paris, 92195 Meudon, France

An ion excited by an electron beam usually emits linear polarized light due to the anisotropy of the excitation process. The most important isoelectronic sequences are those with closed shell ground state, such as $1s^2$, He-like ions, $1s^22s^22p^6$, Ne-like ions, etc. These ground states have only one level $J = 0$ and one sublevel $M_J = 0$ which is spherical symmetric and therefore does not depend on the choice of the quantization axis z-axis. The anisotropy and the energy of the projectile electron is partly transfered to the excited state which radiates an anisotropic and polarized line. It is then possible to use this property to derive a plasma diagnostics of the angular and energy distribution of the electrons from the polarization measurements of the lines.

Atomic calculations and discussions of the electron diagnostics have already been performed for He-like ions [1-4]. This diagnostic has been used for He-like Al for the detection of electron anisotropy in laser produced plasma [5].

We consider Ne-like Germanium as an example but, of course, other Ne-like ions have similar properties. The choice of the atomic element depends on the Bragg cristal available to obtain the line spectra and on the energy of the anisotropic electron which we wish to analyze : heavier is the element higher is the energy which is required to obtain a Ne-like spectra. This element could be inserted in the tokamak as a foil and evaporated by a laser.

The atomic data necessary to construct a theoretical model for Ne-like Germanium are presented. They concern mainly the collisional excitation and desexcitation between the first 37 levels (145 sublevels) belonging to the configurations $2s^22p^6$, $2s^22p^53l$, $2s2p^63l$. The most promising lines for tokamaks are the 8 intense X-ray lines around 9 Å issued from $2s^22p^53s$, $2s^22p^53d$, $2s2p^63p$. Their polarizations and intensities have a very different behavior as function of the electron energy.

Ne-like Germanium is also an important ion for the X-ray laser where the 196 Å lasing line has been measured -53 % polarized [6].

References

[1] A.S. Shlyaptseva, A.M. Urnov, A.V. Vinogradov, Lebedev Physical Institute Preprints **193** and **194** (1981)
[2] M.K. Inal, J. Dubau, J. Phys. B **20**, 4221 (1987) ; Phys. Rev. A **47**, 4794 (1993).
[3] Y. Itikawa, R. Srivastava, K. Sakimoto, Phys. Rev.A **44**, 7195 (1991).
[4] M.K. Inal, J. Dubau, J. Phys. B **22**, 3329 (1989).
[5] J.C. Kieffer, J.P. Matte, H. Pépin, M. Chaker, Y. Beaudouin, T.W. Johnston, C.Y. Chien, S. Coe, G. Mourou, J. Dubau, Phys. Rev. Lett. **68**, 480 (1992).
[6] T. Kawachi, K. Murai, G. Yuan, S. Ninomiya, R. Kodama, H. Daido, Y. Kato, T. Fujimoto, Phys. Rev. Lett. **75**, 3826 (1995).

Static and Dynamic Characteristics of Plasma Detachment in Gas Target Scheme

N. Ezumi [a], M. Tanaka [a], S. Mori [b], N. Ohno [a], M. Takagi [a], S. Takamura [a], H. Suzuki [c]

[a] Department of Energy Engineering and Science
[b] Department of Electrical Engineering
Graduate School of Engineering, Nagoya University, Nagoya, 464-01, Japan
[c] National Institute for Fusion Science, Nagoya, 464-01, Japan

Heat flux flowing into divertor plate has been assumed to several tens MW/m^2 for next generation fusion reactors such as ITER (International Thermonuclear Experimental Reactor). It is difficult to develop a new material withstanding such a high heat load for a long time. Then, ITER EDA (Engineering Design Activity) considers removing such a high plasma heat flux from divertor plate by strong plasma-neutral interactions. These interactions will be accompanied by decreasing not only plasma temperature but also its momentum. In several tokamaks, plasma detachment has been observed, but the detail physics are not so clear that studies of plasma detachment is in urgent need of divertor physics R & D. We have carried out a simulated gas target divertor experiment in the linear plasma device (TPD-I device) to investigate fundamental physics of plasma detachment. The TPD-I device has a high heat flux ($<0.7MW/m^2$) and high density ($n_e<1.0\times10^{20}$ m^{-3}) plasma in steady state. So far, we have already succeeded in obtaining the detached plasma there, and we are also developing a heat pulse generation by modulating the discharge power supply.

In the present paper, we would like to discuss the dependence of plasma detachment on the plasma density and neutral gas species by comparing the experimental observation with the numerical simulation predicted with two dimensional fluid code (B2 code). Furthermore, we will give preliminary data on dynamic response plasma detachment by heat pulse. In the case of high plasma density n_e ($> 5\times10^{18}$ m^{-3}), helium plasma has been observed to be detached from the end target plate by feeding helium gas. However, in a low plasma density n_e($<$ 5×10^{17} m^{-3}), such a plasma detachment is not observed even under a substantially high neutral pressure. The existence of threshold value of plasma density to occur the plasma detachment is thought to come from the fact that the electron energy is mainly lost by the energy exchange between electrons and ions. The latter loses their energy through charge exchange process. The e-i energy exchange is proportional to the square of plasma density. Furthermore, heat pulse experiments have been indicating an importance of relation between energy relaxation time and pulse width. In addition, we have observed the quite different effects of feeding different target gases (H_2, Ar) into the helium plasma on plasma detachment.

Electron Impact Ionization of Titanium Ions

U. Hartenfeller, K. Aichele, D. Hathiramani, G. Hofmann, V. Schäfer, M. Steidl, M. Stenke and E. Salzborn
Institut für Kernphysik, Strahlenzentrum, Justus-Liebig-Universität Giessen, D-35392 Giessen, Germany

A better understanding of atomic collision processes involving low-charged ions is important for the modeling of edge plasmas in fusion research [1]. Our present measurements extend the available data base for single and multiple ionization of titanium ions.
In a crossed-beams experiment [2] absolute cross sections $\sigma_{q,q+n}$ have been measured for the reaction $e+Ti^{q+} \rightarrow Ti^{(q+n)+}+(n+1)e$. Apart from $\sigma_{1,2}$, $\sigma_{2,3}$ [3,4] and $\sigma_{5,6}$ [5] the following cross sections have been measured for the first time:

single ionization:	$\sigma_{1,2}$	$\sigma_{2,3}$		$\sigma_{4,5}$	$\sigma_{5,6}$	$\sigma_{6,7}$	$\sigma_{7,8}$
double ionization:	$\sigma_{1,3}$	$\sigma_{2,4}$	$\sigma_{3,5}$	$\sigma_{4,6}$	$\sigma_{5,7}$	$\sigma_{6,8}$	
triple ionization:	$\sigma_{1,4}$	$\sigma_{2,5}$	$\sigma_{3,6}$				
quadruple ionization:	$\sigma_{1,5}$	$\sigma_{2,6}$					

The animated crossed-beams method [6] has been employed and the measurements have been performed using two electron guns covering the energy ranges from thresholds up to 1 keV [7], and up to 6.5 keV [8], respectively.
The titanium ions were produced in a 10 GHz electron cyclotron resonance ion source [9] feeding a bundle of titanium wires axially to the ECR plasma. We observed some fractions of metastable ions in the primary ion beam which led to an ionization signal below the thresholds of the respective ground states.
The measurements for single ionization show contributions from excitation-autoionization processes which are described well by distorted-wave calculations [5]. The semi-empirical Lotz formula [10], however, underestimates the measured cross sections in most cases. Besides contributions from excitation-autoionization we also observed sharp structures in some cross sections resulting from resonant capture of the incident electron with subsequent double autoionization (REDA processes).
The cross sections for multiple ionization show considerable contributions from inner shell processes involving 2p electrons. The comparison of this data with semi-empirical formulae [11,12] shows that there is no satisfactory theoretical description for multiple ionization available until now.

[1] *Atomic and Molecular Processes in Fusion Plasmas*, edited by R. K. Janev, (Plenum, NY 1995)
[2] G. Hofmann, A. Müller, K. Tinschert and E. Salzborn, 1990 *Z. Phys. D* **16** 113
[3] M. J. Diserens, A. C. H. Smith, M. F. A. Harrison; *J. Phys. B: At. Mol. Phys* **21** (1988) 2129
[4] D. W. Mueller, T. J. Morgan, G. H. Dunn, D. C. Gregory, D. H. Crandall; *Phys. Rev. A* **31** (1985) 2905
[5] S. J. Chantrenne, D. C. Gregory, M. J. Buie, M. S. Pindzola; *Phys. Rev. A* **41** (1990) 140
[6] A. Müller, K. Tinschert, C. Achenbach and E. Salzborn, *Nucl. Instr. Meth. in Phys. Res. B* **10/11** (1985) 204
[7] R. Becker, A. Müller, A. Achenbach, K. Tinschert and E. Salzborn, *Nucl. Instr. Meth. in Phys. Res. B* **9** (1985) 385
[8] M. Stenke, K. Aichele, D. Hathiramani, G. Hofmann, M. Steidl, R. Völpel and E. Salzborn, *Nucl. Instr. Meth. in Phys. Res. B* **98** (1995) 573
[9] M. Liehr, M. Schlapp, R. Traßl, G. Hofmann, M. Stenke, R. Völpel and E. Salzborn, *Nucl. Instr. Meth. in Phys. Res. B* **79** (1993) 697
[10] W. Lotz, *Z. Phys.* **216** (1968) 216
[11] V. P. Shevelko and H. Tawara, *J. Phys. B* **28** (1995) L589
[12] V. Fisher, Yu Ralchenko, A. Goldgirsh, D. Fisher and Y. Maron, *J. Phys. B* **28** (1995) 3027

Electron Impact Ionization of Molybdenum Ions

D. Hathiramani, K. Aichele, G. Hofmann, M. Steidl, M. Stenke, R. Völpel and E. Salzborn
Institut für Kernphysik, Strahlenzentrum, Justus-Liebig-Universität Giessen, D-35392 Giessen, Germany

For the modeling of fusion plasmas, electron impact ionization cross sections for ions of metallic plasma impurities are needed. The use of molybdenum as a material for divertor plates is under consideration, so data for Mo^{q+} ions are of particular importance for plasma radiative cooling studies [1]. In the case of molybdenum, there are only a few theoretical calculations and experimental measurements available of electron impact ionization cross sections. Therefore, we performed absolute cross section measurements for electron impact single and multiple ionization of Mo^{q+} ions for energies from threshold to 6.5 keV.

single ionization:	σ_{12}	σ_{23}	σ_{34}	σ_{45}	σ_{56}	σ_{67}	σ_{78}	σ_{89}
double ionization:	σ_{13}	σ_{24}	σ_{35}	σ_{46}	σ_{57}	σ_{68}		
triple ionization:	σ_{14}	σ_{25}	σ_{36}	σ_{47}				

The measurements were performed using the Giessen electron-ion crossed-beams setup [2]. The molybdenum ions were produced by a 10 GHz Electron-Cyclotron-Resonance (ECR) ion source [3] using an insertion technique. An acceleration voltage of 10 kV was applied. After magnetic separation of the desired mass to charge state ratio the ion beam was crossed with an intense electron beam. For these measurements two electron guns were employed. One electron gun for energies up to 1 keV [4] and the other with an energy range between 0.2 and 6.5 keV [5]. Absolute cross sections were obtained by employing the dynamic crossed-beams technique [6].

Our results corresponds well with the single ionization measurements for Mo^{+} by Man et al. [7] and for Mo^{4+} and Mo^{5+} by Bannister et al. [8], respectively. For all measured single ionization cross sections CADW calculations were carried out [9]. The comparison between the experimental data and the calculations shows that excitation-autoionization from the ground state as well as from metastable states strongly contributes to the cross sections. The multiple ionization cross sections are compared with the semi-empirical formulae by Fisher et al. [9] and Shevelko et al. [10], respectively. These formulae in some cases overestimate the measured cross section by a factor of 2.

[1] *Atomic and Molecular Processes in Fusion Plasmas*, edited by R. K. Janev, (Plenum, NY 1995)
[2] G. Hofmann, A. Müller, K. Tinschert and E. Salzborn, 1990 *Z. Phys. D* **16** 113
[3] M. Liehr, M. Schlapp, R. Traßl, G. Hofmann, M. Stenke, R. Völpel and E. Salzborn, *Nucl. Instr. Meth. in Phys. Res. B* **79** (1993) 697
[4] R. Becker, A. Müller, A. Achenbach, K. Tinschert and E. Salzborn, *Nucl. Instr. Meth. in Phys. Res. B* **9** (1985) 385
[5] M. Stenke, K. Aichele, D. Hathiramani, G. Hofmann, M. Steidl, R. Völpel and E. Salzborn, *Nucl. Instr. Meth. in Phys. Res. B* **98** (1995) 573
[6] A. Müller, K. Tinschert, C. Achenbach and E. Salzborn, *Nucl. Instr. Meth. in Phys. Res. B* **10/11** (1985) 204
[7] K. F. Man, A. C. H. Smith and M. F. A. Harrison, *J. Phys. B* **20** (1987) 1351
[8] M. E. Bannister, F. W. Meyer, Y. S. Chung, N. Djuric, G. H. Dunn, M. S. Pindzola and D. C. Griffin, *Phys. Rev. A* **52** (1995) 413
[9] D. Hathiramani, K. Aichele, G. Hofmann, M. Steidl, M. Stenke, R. Völpel, E. Salzborn, M. S. Pindzola, J. A. Shaw, D. C. Griffin and N. R. Badnell, *Phys. Rev. A* **54** (1996) 587
[10] V. Fisher, Yu.Ralchenko, A. Goldgirsh, D. Fisher and Y. Maron, *J. Phys. B* **28** (1995) 3027
[11] V. P. Shevelko and H. Tawara, *J. Phys. B* **28** (1995) L589

Z- and n-dependencies for autoionizing widths of 1s2*lnl'* states for Li-like ions

U.I.Safronova
Institute Spectroscopy, Russian Academy of Sciences, Troitsk, 142092, Russia

Autoionizing widths of 1s2*lnl'*(n=4 - 10, *l'*=0-3) configurations for Li-like ions with Z=6-54 were calculated by using the perturbation theory method (Z-expansion). Relativistic effects are taken into account by the Breit-Pauli operators. Non-monotonous Z- and n-dependencies with maximums and minimums. were discovered and studied for autoionizing widths of considered states.

Fig.1 demonstrates an example of our calculations. We represented Z-dependencies of autoionizing widths for odd parity complex states with J=7/2 and n=4, 6, 8, 10. The next designations are used: A'=1s2p(^{1}P)nd, I'=1s2p(^{3}P)nd, H'=1s2s(^{1}S)nf, Q'=1s2s(^{3}S)nf; numbers after letters mean (2S+1)(2L+1)(2J+1). Details of our calculations are given in Ref.1. We can see from Fig.1 that Z-dependence of auotoionizing widths does not become simple with n.

1. Safronova,U.I., Shlyaptseva, A.S. and Golovkin, I.E., Physica Scripta **52,** 277 (1995)

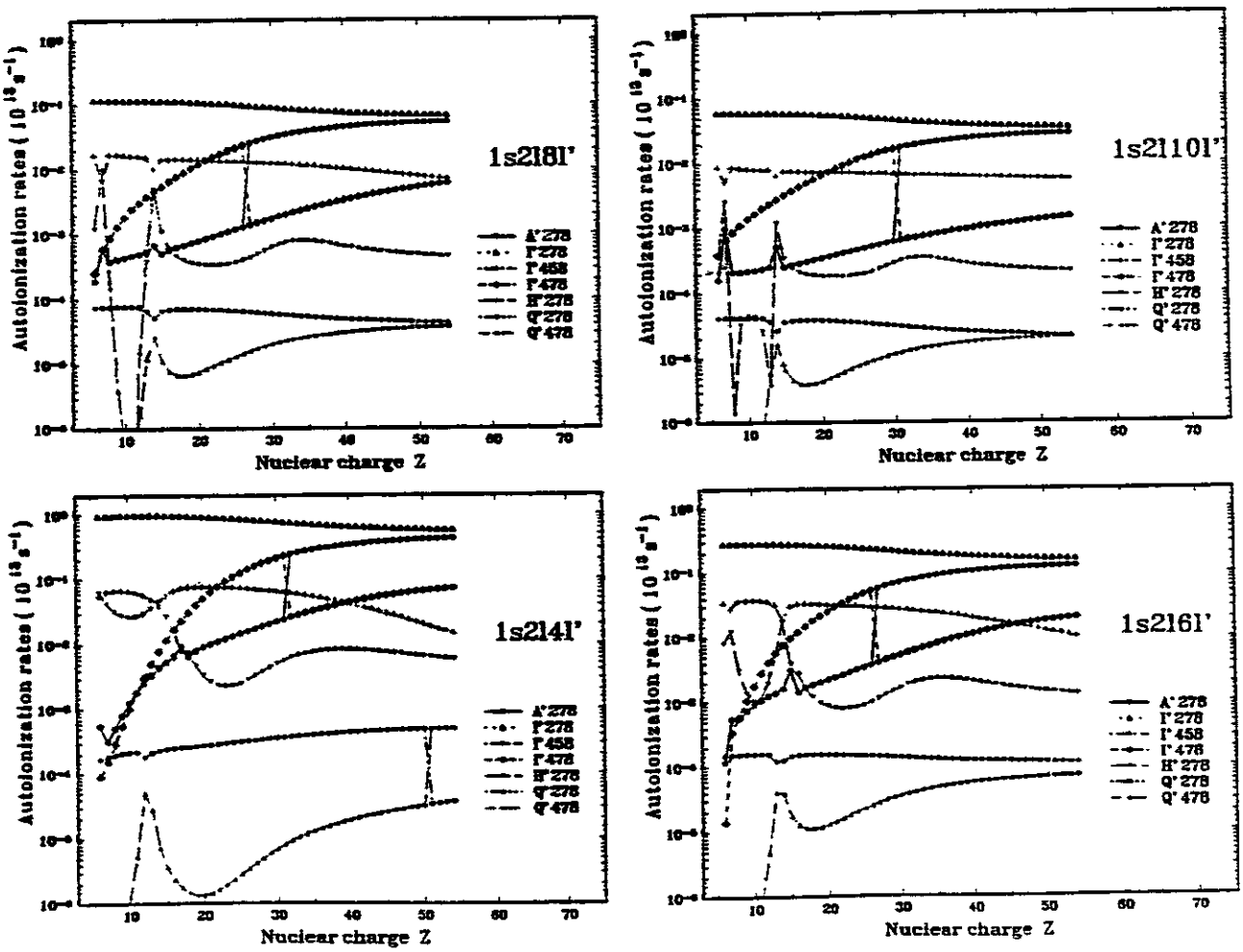

Two-electron processes in collisions between negative carbon clusters and argon atoms

C.P.Safvan, V.R. Bhardwaj, A.K.Gupta and D.Mathur*

Tata Institute of Fundamental Research, Homi Bhabha Road, Bombay 400 005
**Nuclear Physics Division, Bhabha Atomic Research Centre, Bombay 400 085*

Abstract

Studies of the interactions between multi-electron systems, continue to pose considerable challenges. We present here result of systematic experimental investigations of multielectron processes in collisions between small negatively charged carbon clusters and neutral atoms. In the present we focus attention on C_n^--Ar collisions in which the carbon cluster looses two electrons. The energy imparted to the cluster anion goes into both the electronic and nuclear degrees of freedom. Consequently, the resulting positively charged ions have the form C_m^+, where m=n implies a non dissociative channel wherein the collisional energy transfer is exclusively into the electronic degrees of freedom. On the other hand, we also detect channels where m<n, implying dissociative channels where the energy transferred has been redistributed into both the electronic and nuclear degrees of freedom.

Our experiments have been conducted over the collision energy range 20-50 keV using an accelerator coupled to a crossed beams apparatus incorporating a quadrupole mass spectrometer and a high resolution post-collision energy analyser.

Experimental results for C_2^-, C_4^-, and C_6^- are presented. The dissociation channels present complex dynamics which are not amenable to simple interpretations in terms of conventional even-odd propensity rules.

Development of Diagnostic Beams for Alpha Particle Measurement on LHD and ITER

M. Sasao, A. Taniike, I. Nomura, M.Wada*, H.Yamaoka**, M.Sato***

National Institute for Fusion Science
*Department of Electronics, Doshisha Univ., **RIKEN, and ***Himeji Technical Univ.

The velocity distribution of alpha particles in a plasma has been thought to be one of the key items on a burning experiment. Several proposals have been made to measure it. One of them is an alpha particle measurement by using the double charge exchange process[1,2,3]. An alpha particle is neutralized through a two-electron transfer process as

$$^4He^{++} + A^{q+} \longrightarrow {}^4He^0 + A^{(q+2)+} \qquad (1)$$

where $^4He^0$ escapes from a plasma, and is detected by an energy analyzer. Here A^{q+} represents a beam particle, which should be a helium or heavier atom.

A measurement system applicable to the LHD or ITER project is examined using a high-energy neutral beam in combination with a neutral-particle analyzer. As has been pointed out in the earlier works [1,2], beam energy in the range of that of the alpha particles is preferable. The escaped neutral particles should be detected at a forward angle, in order to make the relative velocity between the donor atom and the alpha particle small enough. It is considered that the relevant charge exchange cross section (1) decreases rapidly when the relative energy is greater than 200 keV. In the present work, only helium and lithium beams are considered, since a heavier particle beam requires a higher acceleration voltage to achieve the same beam velocity.

The attenuation of the beam in the plasma of $T_e(r)= 10\ \text{keV} \times \{1-(r/a)^2\}^2$ is evaluated, including electron impact ionization, ion impact ionization and charge exchange processes. Here, contamination by impurity ions of 0.3% O^{8+} and 0.03% Fe^{26+} is assumed. The ionization cross section by naked impurity ions $\sigma_i^{imp}(v)$ is assumed to be proportional to that by protons of the same velocity, and given by

$$\sigma_i^{imp}(v) = z^2 \sigma_i^{p}(v).$$

The main contribution to beam attenuation results from ionization processes associated with impact by plasma ions and impurity ions. The penetration of a beam greatly depends on the beam velocity and plasma density. More than several % of the He^0 beam particles may survive at the center when the beam velocity is greater than $0.6\ v_\alpha$ ($E_b \geq 1$ MeV for a $^3He^0$ beam), and the plasma density less than $2 \times 10^{20}/m^3$. On the other hand, tolerable penetration of a Li^0 beam occurs only when the beam velocity is greater than $0.8\ v_\alpha$ ($E_b \geq 3.4$ MeV for the $^6Li^0$ beam) and the plasma density less than $10^{20}/m^3$[4]..

If the port-through current density 1 mA/cm^2 with a cross section of 10 cm x 10 cm, the counting rate would then be sufficient to measure the neutral particle spectra with good statistics for both cases. The alpha particle spectrum can be obtained by dividing neutral particle counts by the local beam particle density and the two electron transfer cross section, and by making corrections for beam attenuation and detection efficiency[4].

References

[1] D.E.Post et al., Fusion Technology 1 (1987), 355
[2] M.Sasao et al., Fusion Technology 10 (1986), 236
[3] M.Sasao et al., Nucl. Fusion 27-2 (1987), 355
[4] M.Sasao et al., Nucl. Fusion 35-12 (1995), 1619

Double Electron Capture and Recombining Processes in Low Temperature Helium Plasma Contacting with Cold Hydrogen Gas

K. Sato, S. Namba, S. Kusakabe, K. Takahara, H. Tawara, T. Katsuta[A)], K. Takiyama[A)], T. Oda[A)], and U. Furukane[B)]

National Institute for Fusion Science, Nagoya 464-01, Japan
A)Dept. Applied Phys. & Chem. Fac. Eng., Hiroshima Univ., Higashi-Hiroshima 739, Japan
B)Fac. Eng, Hiroshima Denki Institute of Technology, Hiroshima 739-03, Japan

abstract

Experimental and theoretical studies of a plasma interacting with cold neutral gases will make useful contributions to elucidate the important atomic processes in divertor plasmas.

We have been spectroscopically studying He plasmas in contact with cold gases at the TPD- I and -II plasma machines at National Institute for Fusion Science. Spectroscopic observations have been made mostly on the recombining plasmas resulting from rapid cooling of the electron temperature due to the contact with cold neutral helium or hydrogen gases. Population inversions have been observed between the He I low-lying levels. Numerical studies have been also made to understand the population inversion mechanisms.

Recently, anomalously intense photon emissions have been observed from He I lines (n=3->n=2) at the early period of cold hydrogen gas injection in our experiment[1]. This phenomenon is understood to be due to the following selective double electron capture process:

$$He^{2+} + H_2 \rightarrow He^{*}(1s\,3l) + 2H^{+} \qquad (1)$$

whose cross sections are very large at low collision energies.

A numerical study based on a collisional-radiative model was also made to analyze the effect of this process on the temporal evolution of the He I and II level populations. The numerical result could explain fairly well the observed temporal evolution of the enhanced He I line intensity (n=3-->n=2), and gave us further results that the level populations of n=2 and 4 are also enhanced, though much smaller than the n=3 level populations. The features were experimentally confirmed.
Further detailed studies in both experiment and theory are under way.

Reference

[1] K. Sato et al. , J. Phys. B: At. Mol. Opt. Phys. 27 (1994) L652

Atomic and molecular data activities at the NDC/JAERI

Toshizo Shirai
Nuclear Data Center (NDC), Japan Atomic Energy Research Institute (JAERI)
Tokai-mura, Ibaraki 319-11, Japan

Compilation and evaluation work has been continued to make the 4th edition of Evaluated Atomic and Molecular Data Library (JEAMDL-4) for fusion in collaboration with the JAERI Research Committee on Atomic and Molecular Data and with researchers of ORNL and NIST under the US-Japan fusion cooperation program.

We have already published a series of compilations [1] of analytical fits to the recommended cross sections for collisions of H, H_2, He, Li atoms and ions with atoms and molecules[2]. A similar work was made for the recommended cross sections for state-selective electron capture in collisions of C^{6+} and O^{8+} ions with atomic hydrogen [3]. All these data sets are stored in the ALADDIN format as a part of JEAMDL.

In relation to the injection of energetic neutral beams into moderate and high density plasmas, theoretical data production was carried out for ionization of excited hydrogen atoms and hydrogenlike ions by high-energy collisions with bare ions by using the continuum distorted wave-eikonal initial state (CDW-EIS) and the plane-wave Born approximations [4,5] and for excitation and ionization of excited helium atoms in collisions with bare ions in the Glauber and CDW-EIS approximations, respectively, besides the Born approximation[6].

For the molecular processes relevant to gas dynamic divertor, a study has been made on ion-molecule reactions in the H_3^+ ($D^+ + H_2$, $D^+ + D_2$, and $H^+ + D_2$) system in the collision energy range of 2.5 to 8.0eV with the trajectory-surface-hopping method on *ab initio* three-dimensional potential energy surfaces[7]. Agreement with the experimental cross sections was obtained for the production of H^+ and HD^+ions in the $D^+ + H_2$ collisions and for the production of D^+ and HD^+ions in the $H^+ + D_2$ collisions in the whole energy range studied here. For the $D^+ + H_2$ and $D^+ + D_2$ collisions, the energy dependence of the experimental cross sections was well reproduced in the present calculation compared with earlier calculations. Although the present calculation overestimated the cross sections for the D_2^+ ion formation in the $D^+ + D_2$ collisions and in the $H^+ + D_2$ collisions above 5eV, the deviations from the experiments were within a factor of two.

We also have undertaken publication of a series of compilations of spectral data for highly ionized atoms: Ti to Cu, as well as Kr and Mo, of special importance for fusion research. All these data will be presented as a monograph[8].

[1] R. Ito, T. Tabata, T. Shirai, and R. A. Phaneuf, JAERI-M 93-117, Data/Code 94-005, 95-008, and 96-024.
[2] C. F. Barnett, ORNL-6089/V1 (1990).
[3] R. K.Janev, R. A. Phaneuf, H. Tawara, and T. Shirai, ADNDT **55**, 201 (1993).
[4] A. Igarashi and T. Shirai, Phys. Rev. **50**, 4945 (1994).
[5] A. Igarashi and T. Shirai, Phys. Rev. **51**, 4699 (1995).
[6] A. Igarashi and T. Shirai, Phys. Scr. **T62**, 95 (1996).
[7] A. Ichihara, T. Shirai, and K. Yokoyama, J. Chem. Phys. **105**, 1857 (1996).
[8] T. Shirai, J. Sugar, and W. L. Wiese, JPCRD Monograph No. 8 (1996) in press.

TWO ELECTRON REARRANGEMENT PROCESSES IN COLLISIONS OF HCI WITH ATOMS.

Uskov D B
P N Lebedev Physical Institute Moscow Russia

The following processes are considered:
i) double electron removal
$He + A^{q+} \rightarrow He + 2e + A^{q+}$, $He + e + A^{(q-1)+}$, $He + A^{(q-1)+}$
ii) double electron ionization, which is the dominant part of the double electron removal at sufficiently large impact velocities
$He + A^{q+} \rightarrow He + 2e + A^{q+}$

The goal of the present work is to establish the asymptotic properties of cross sections for double electron removal and double electron ionization in the limiting case of very large ion charge $q>>1$. The total cross sections of the processes, generally speaking, are the functions of two parameters: collision velocity v and ion charge q. A non-trivial limiting case will be considered, namely 1) $q>>1$, $v/q=const$ 2. $q>>1$, $v^2/q=const$

The latter case is directly related to the well known and quite useful scaling rule, established for a large number of processes (see, for example, ref [2]):
(cross section) is proportional to (ion charge)*function(v^2/q).

The well known definition of the transition amplitude refers to the Dyson's formulation as an infinite sum over all perturbation orders and has the form of power series over parameter $(q/v)^n * f^{(n)}(v)$. This sum is reordered to eliminate v-dependence of f(n) functions. As far as we are interested in the limit $q>>1$, $v/q=const$ we have to do expanding of exp(-iHx/v) to obtain the Magnus [1] sum over the powers of interaction time $(1/v)^n * g^{(n)}(q/v)$. This sum over power series of 1/q is in fact required for the analysis of the limiting case of $q>>1$, $v/q=const$. In the case of Coulomb interaction the higher terms in the sum will have a logarithmic features of the form 1./v*log(v) due to the long-range dipole interaction.

One of the most important characteristics of electron-electron correlation in He is the ratio of single to double photo- and collisional ionization. In the resent paper [3] the ratio of double to single ionization was calculated using expansion over the generalized Volkov-Keldysh states. In the present work the method is extended to take into account the dynamic dumping of the initial atomic state during the collision process [4,5]. It was widely discussed that the experimental data for U^{90+} [6] ions fall off the general trend of both theoretical calculations and scaled experimental data for lower ions. So it is worth noting that the present calculations are in quite good agreement with U^{90+} data.

Acknowledgments
The author appreciates valuable discussions with L Presnyakov, E Salzborn and H Tawara.

1. Magnus W. Comm. Pure and Applied Math 1954 v 7 p. 649.
2. Janev R K, in: Supplement to the Journal Nuclear Fusion v.3 1992 pp.71-79
3. Presnyakov L P, Tawara H, Tolstikhina Yu I, Uskov D B, 1995 J Phys B 28, 785.
4. Presnyakov L P, Uskov D B 1984 Sov Phys - JETP 59 515
5. Uskov HCI-96 , invited talk.
6. Berg et al 1992 Phys Rev A 46 5539
   Berg et al 1992 J Phys B 25 3655

Polar Dissociation of Vibrational Excited and Ground State H_3^+ on He target.

F. B. Yousif, G. Hinojosa, J. de Urquijo, C. Cisneros and I. Alvarez.-
Laboratorio de Cuernavaca, IFUNAM, Apdo. Post.48-3, Cuernavaca 62251, Morelos, México

The polar dissociation of H_3^+ incident on a He target has been studied at different ion source pressures and over a wide range of projectile energies. The contributions of the different vibrational states of H_3^+ to the channel leading to the products $H^+ + H^- + H^+$ has showed a strong dependence with the ion source pressure, thereby allowing us to study the energy spectra of positive and negative ions in coincidence, with the initial H_3^+ (v=0). The basic apparatus used to generate the fast H_3^+ beam is basically described in Ref.1.

The laboratory energy distributions of H^+ in coincidence with H^- at 9 keV of primary beam and at different source pressures are displayed in Fig. 1

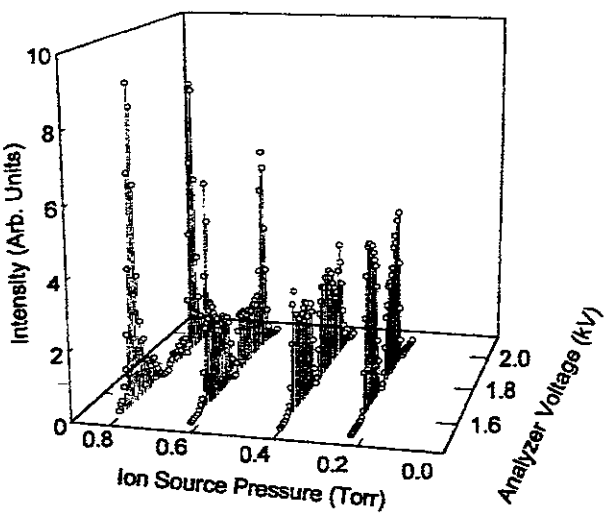

Figure 1.- Energy distribution of H^+ in coincidence with H^- at different ions source pressures.

The results at low pressure (0.23 Torr) in the source,shows a broad H^+ energy distributions whose minimum corresponds to the zero energy loss value, resulting from the polar dissociation of vibrationally excited H_3^+ ions. The results at a source pressure of 0.4 Torr begin to produce the H^+ fragment by H_3^+ (v=0) at the outer part of the wings, since the H_3^+ in their ground state require higher excitation energy to reach the dissociating channel. At a source pressure of 0.62 Torr, the initial H_3^+ ions are almost entirely in the v=0 level, the energy spectrum displays a depleted plateau resulting from the remaining vibrationally excited initial H_3^+ ions, while the pronounced peaks are mainly due to the H^+ fragments coming from initial H_3^+ (v=0)
At 0.8 Torr the H_3^+ beam is almost entirely in its ground state.

From the laboratory energy spectra of H^- and H^+ in coincidence with each other, an accurate c.m. projectile-frame energy distribution can be extracted. In Fig.2 we present the c.m. energy distribution of the H^+ as well as the H^- fragments resulting from the polar dissociating channel in the forward and backward direction taken at 8 keV of the H_3^+(v=0)

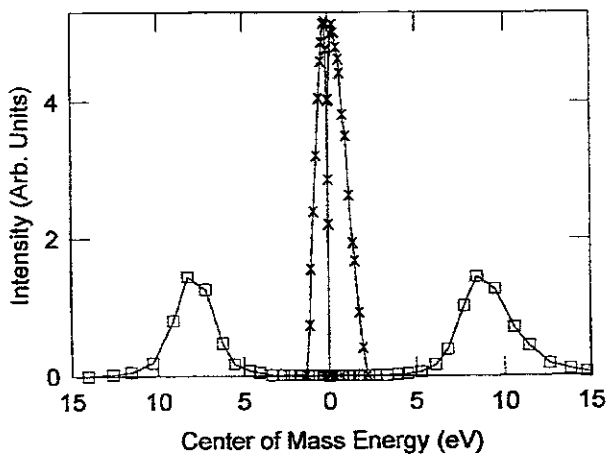

Figure 2 .- Center of mass energy distribution of H^+ and H^- from the H_3^+ polar dissociation on He at 8 keV, in the forward and backward directions. The crosses represents the H^- fragment and the squares the H^+ fragment.

The most probable energies for H^- and H^+ in the forward direction are 0.3 and 7.3 eV respectively, while in the backward direction are 0.25 and 7.3 eV. The fragment protons share equally most of the dissociation energy, which is as much as 25 times the H^- energy. The experimentally measured energy distributions of H^+ and H^- are consistent with the available potential energy curves of H_3^+.

References: 1.- I. Domínguez, H. Martínez, C. Cisneros, J. de Urquijo and I. Alvarez. Phys. Rev. **A50**, 3856 (1994).

Publication List of NIFS-DATA Series

NIFS-DATA-1 Y. Yamamura, T. Takiguchi and H. Tawara,
Data Compilation of Angular Distributions of Sputtered Atoms;
Jan. 1990

NIFS-DATA-2 T. Kato, J. Lang and K. E. Berrington,
Intensity Ratios of Emission Lines from OV Ions for Temperature and Density Diagnostics ; Mar. 1990 [At Data and Nucl Data Tables 44(1990)133]

NIFS-DATA-3 T. Kaneko,
Partial Electronic Straggling Cross Sections of Atoms for Protons;
Mar. 1990

NIFS-DATA-4 T. Fujimoto, K. Sawada and K. Takahata,
Cross Section for Production of Excited Hydrogen Atoms Following Dissociative Excitation of Molecular Hydrogen by Electron Impact ; Mar. 1990

NIFS-DATA-5 H. Tawara,
Some Electron Detachment Data for H^- Ions in Collisions with Electrons, Ions, Atoms and Molecules –an Alternative Approach to High Energy Neutral Beam Production for Plasma Heating– ;
Apr. 1990

NIFS-DATA-6 H. Tawara, Y. Itikawa, H. Nishimura, H. Tanaka and Y. Nakamura,
Collision Data Involving Hydro-Carbon Molecules; July 1990
[Supplement to Nucl. Fusion 2(1992)25]

NIFS-DATA-7 H.Tawara,
Bibliography on Electron Transfer Processes in Ion-Ion/Atom/Molecule Collisions –Updated 1990–; Aug. 1990

NIFS-DATA-8 U.I.Safronova, T.Kato, K.Masai, L.A.Vainshtein and A.S.Shlyapzeva,
Excitation Collision Strengths, Cross Sections and Rate Coefficients for OV, SiXI, FeXXIII, MoXXXIX by Electron Impact ($1s^22s^2$ -$1s^22s2p$-$1s^22p^2$ Transitions) Dec.1990

NIFS-DATA-9 T.Kaneko,
Partial and Total Electronic Stopping Cross Sections of Atoms and Solids for Protons; Dec. 1990

NIFS-DATA-10 K.Shima, N.Kuno, M.Yamanouchi and H.Tawara,
Equilibrium Charge Fraction of Ions of Z=4-92 (0.02-6 MeV/u) and Z=4-20 (Up to 40 MeV/u) Emerging from a Carbon Foil; Jan.1991
[AT.Data and Nucl. Data Tables 51(1992)173]

NIFS-DATA-11 T. Kaneko, T. Nishihara, T. Taguchi, K. Nakagawa, M. Murakami,

M. Hosono, S. Matsushita, K. Hayase, M.Moriya, Y.Matsukuma, K.Miura and Hiro Tawara,
Partial and Total Electronic StoppingCross Sections of Atoms for a Singly Charged Helium Ion: Part 1;Mar. 1991

NIFS-DATA-12 Hiro Tawara,
Total and Partial Cross Sections of Electron Transfer Processes for Be^{q+} *and* B^{q+} *Ions in Collisions with H,* H_2 *and He Gas Targets - Status in 1991-;* June 1991

NIFS-DATA-13 T. Kaneko, M. Nishikori, N. Yamato, T. Fukushima, T. Fujikawa, S. Fujita, K. Miki, Y. Mitsunobu, K. Yasuhara, H. Yoshida and Hiro Tawara,
Partial and Total Electronic Stopping Cross Sections of Atoms for a Singly Charged Helium Ion : Part II; Aug. 1991

NIFS-DATA-14 T. Kato, K. Masai and M. Arnaud,
Comparison of Ionization Rate Coefficients of Ions from Hydrogen through Nickel ; Sep. 1991

NIFS-DATA-15 T. Kato, Y. Itikawa and K. Sakimoto,
Compilation of Excitation Cross Sections for He Atoms by Electron Impact; Mar. 1992

NIFS-DATA-16 T. Fujimoto, F. Koike, K. Sakimoto, R. Okasaka, K. Kawasaki, K. Takiyama, T. Oda and T. Kato,
Atomic Processes Relevant to Polarization Plasma Spectroscopy ; Apr. 1992

NIFS-DATA-17 H. Tawara,
Electron Stripping Cross Sections for Light Impurity Ions in Colliding with Atomic Hydrogens Relevant to Fusion Research; Apr. 1992

NIFS-DATA-18 T. Kato,
Electron Impact Excitation Cross Sections and Effective Collision Strengths of N Atom and N-Like Ions -A Review of Available Data and Recommendations- ; Sep. 1992

NIFS-DATA-19 Hiro Tawara,
Atomic and Molecular Data for H_2O, CO & CO_2 *Relevant to Edge Plasma Impurities*, Oct. 1992

NIFS-DATA-20 Hiro. Tawara,
Bibliography on Electron Transfer Processes in Ion-Ion/Atom/Molecule Collisions -Updated 1993-; Apr. 1993

NIFS-DATA-21 J. Dubau and T. Kato,
Dielectronic Recombination Rate Coefficients to the Excited

States of C I from C II; Aug. 1994

NIFS-DATA-22 T. Kawamura, T. Ono, Y. Yamamura,
Simulation Calculations of Physical Sputtering and Reflection Coefficient of Plasma-Irradiated Carbon Surface; Aug. 1994

NIFS-DATA-23 Y. Yamamura and H. Tawara,
Energy Dependence of Ion-Induced Sputtering Yields from Monoatomic Solids at Normal Incidence; Mar. 1995

NIFS-DATA-24 T. Kato, U. Safronova, A. Shlyaptseva, M. Cornille, J. Dubau,
Comparison of the Satellite Lines of H-like and He-like Spectra; Apr. 1995

NIFS-DATA-25 H. Tawara,
Roles of Atomic and Molecular Processes in Fusion Plasma Researches - from the cradle (plasma production) to the grave (after-burning) -; May 1995

NIFS-DATA-26 N. Toshima and H. Tawara
Excitation, Ionization, and Electron Capture Cross Sections of Atomic Hydrogen in Collisions with Multiply Charged Ions; July 1995

NIFS-DATA-27 V.P. Shevelko, H. Tawara and E.Salzborn,
Multiple-Ionization Cross Sections of Atoms and Positive Ions by Electron Impact; July 1995

NIFS-DATA-28 V.P. Shevelko and H. Tawara,
Cross Sections for Electron-Impact Induced Transitions Between Excited States in He: n, n'=2,3 and 4; Aug. 1995

NIFS-DATA-29 U.I. Safronova, M.S. Safronova and T. Kato,
Cross Sections and Rate Coefficients for Excitation of $\Delta n = 1$ Transitions in Li-like Ions with $6<Z<42$; Sep. 1995

NIFS-DATA-30 T. Nishikawa, T. Kawachi, K. Nishihara and T. Fujimoto,
Recommended Atomic Data for Collisional-Radiative Model of Li-like Ions and Gain Calculation for Li-like Al Ions in the Recombining Plasma; Sep. 1995

NIFS-DATA-31 Y. Yamamura, K. Sakaoka and H. Tawara,
Computer Simulation and Data Compilation of Sputtering Yield by Hydrogen Isotopes ($^1H^+$, $^2D^+$, $^3T^+$) and Helium ($^4He^+$) Ion Impact from Monatomic Solids at Normal Incidence; Oct. 1995

NIFS-DATA-32 T. Kato, U. Safronova and M. Ohira,
Dielectronic Recombination Rate Coefficients to the Excited States of CII from CIII; Feb. 1996

NIFS-DATA-33 K.J. Snowdon and H. Tawara,
Low Energy Molecule-Surface Interaction Processes of Relevance to Next-Generation Fusion Devices; Mar. 1996

NIFS-DATA-34 T. Ono, T. Kawamura, K. Ishii and Y. Yamamura,
Sputtering Yield Formula for B_4C Irradiated with Monoenergetic Ions at Normal Incidence; Apr. 1996

NIFS-DATA-35 I. Murakami, T. Kato and J. Dubau,
UV and X-Ray Spectral Lines of Be-Like Fe Ion for Plasma Diagnostics; Apr. 1996

NIFS-DATA-36 K. Moribayashi and T. Kato,
Dielectronic Recombination of Be-like Fe Ion; Apr. 1996

NIFS-DATA-37 U. Safronova, T. Kato and M. Ohira,
Dielectronic Recombination Rate Coefficients to the Excited States of CIII from CIV; July 1996

NIFS-DATA-38 T. Fujimoto, H. Sahara, G. Csanak and S. Grabbe,
Atomic States and Collisional Relaxation in Plasma Polarization Spectroscopy: Axially Symmetric Case; Oct. 1996

NIFS-DATA-39 H. Tawara (Ed.)
Present Status on Atomic and Molecular Data Relevant to Fusion Plasma Diagnostics and Modeling; Jan. 1997